Synthesis and characterization of new porphyrin-based derivatives for CO and O reduction

Adelais Trapali

To cite this version:

Adelais Trapali. Synthesis and characterization of new porphyrin-based derivatives for CO and O reduction. Coordination chemistry. Université Paris-Saclay; Panepistīmio Krītīs, 2022. English. NNT : 2022UPASF053 . tel-04672713

HAL Id: tel-04672713
https://theses.hal.science/tel-04672713v1

Submitted on 19 Aug 2024

Synthesis and characterization of new porphyrin-based derivatives for CO_2 and O_2 reduction

Synthèse et caractérisation de nouveaux dérivés à base de porphyrine pour la réduction du CO_2 et de l'O_2

Thèse de doctorat de l'université Paris-Saclay et de l'université de Crète

École doctorale n° 571 - Sciences Chimiques : Molécules, Matériaux, Instrumentation et Biosystèmes (2MIB)
Spécialité de doctorat : Chimie
Graduate School : Chimie. Référent : Faculté des sciences d'Orsay

Thèse préparée dans les unités de recherche **Institut de chimie moléculaire et des matériaux d'Orsay** (université Paris-Saclay, CNRS) et **Laboratory of Bioinorganic Chemistry** (Department of Chemistry / University of Crete), sous la direction d'**Ally AUKAULOO**, Professeur, et la direction d'**Athanassios G. COUTSOLELOS**, Professeur

Thèse soutenue à Heraklion, le 27 Juillet 2022, par

Adelais TRAPALI

Composition du Jury

Talal MALLAH Professeur, Université Paris-Saclay	Président
Marine DESAGE-EL MURR Professeure, Université de Strasbourg	Rapporteure & Examinatrice
Panagiotis ANGARIDIS Professeur, Aristotle University of Thessaloniki	Rapporteur & Examinateur
Ioulia SMONOU Professeure, University of Crete	Examinatrice
Maria KANAKIDOU Professeure, University of Crete	Examinatrice
Athanassios G. COUTSOLELOS Professeur, University of Crete	Directeur de thèse
Ally AUKAULOO Professeur, Université Paris-Saclay	Directeur de thèse

THESE DE DOCTORAT

NNT : 2022UPASF053

université
PARIS-SACLAY

ÉCOLE DOCTORALE
Sciences Chimiques : Molécules,
Matériaux, Instrumentation
et Biosystèmes (2MIB)

Titre : Synthèse et caractérisation de nouveaux dérivés à base de porphyrine pour la réduction du CO_2 et de l'O_2

Mots clés : Metallo-porphyrines – Réduction de l'O_2 – Réduction du CO_2 – Tolérance à l'oxygène – Activation de l'H_2O – Métal-oxo

Résumé : Les sources d'énergie à base de carbone représentent la majorité de l'approvisionnement énergétique mondial ; or, leur surexploitation est liée à l'augmentation constante de la concentration atmosphérique de CO_2, qui explique le changement climatique que connaît actuellement la planète Terre. Pour atténuer le changement climatique, l'un des principaux défis scientifiques du 21e siècle est le remplacement des combustibles fossiles par des alternatives neutres en carbone qui peuvent également répondre aux demandes énergétiques du monde moderne. L'élucidation des mécanismes par lesquels la nature active les petites molécules thermodynamiquement stables, par exemple O_2, CO_2 et H_2O, est un objectif recherché pour le développement de dispositifs artificiels dans le but de fournir un approvisionnement en énergie propre.

Dans ce contexte, les trois sujets principaux de cette thèse de doctorat se concentrent sur la conception de métalloporphyrines bio-inspirées et l'évaluation de leur réactivité envers (i) la réduction de l' O_2 moléculaire, (ii) la réduction du CO_2 dans des conditions aérobies, et (iii) l'activation de le H_2O.

Concernant le premier pilier de ce travail de thèse, nous avons caractérisé via des études spectroscopiques UV-Vis, EPR, et rRaman les premiers intermédiaires impliqués dans la réduction de l' O_2 moléculaire catalysée par deux atropisomères de fer-porphyrine fonctionnalisés dans leur seconde sphère de coordination avec des groupes urée comme donneurs de liaisons hydrogène multipoints. Il s'est avéré que les groupes urée améliorent considérablement la stabilité des adduits Fe- O_2 et nous ont permis de déterminer le premier potentiel redox d'un couple fer-porphyrine (S)/(P) par voltamétrie cyclique. De plus, la topologie des fonctions urées a également influencé la stabilité des adduits Fe- O_2 avec des études de spectroscopie UV-Vis à basse température suggérant que deux groupes urées sont nécessaires du même côté par rapport au plan de la porphyrine pour stabiliser plus efficacement les intermédiaires superoxo.

Pour le second sujet de recherche, nous avons décrit une approche différente pour développer des électrocatalyseurs à base de porphyrines de cuivre pour une réduction efficace du CO_2 qui présentent une grande tolérance à la présence d' O_2. Plus précisément, nous avons fonctionnalisé une porphyrine de cuivre avec un groupe pendentif de type méthyl-viologène et avons étudié en premier lieu son activité électrocatalytique vers la réduction du CO_2 et de l' O_2 moléculaire, séparément. Les expériences électrocatalytiques ont non seulement montré que le nouveau catalyseur de cuivre pouvait réaliser la réduction du CO_2 et de l'O_2 individuellement, mais aussi qu'il pouvait maintenir son activité de réduction du CO_2 même dans des conditions aérobies. Ainsi, le groupe pendentif de type méthyl-viologène a rempli son rôle en s'attaquant à la réduction de l' O_2 en même temps que la porphyrine de cuivre catalyse la réduction du CO_2.

Dans la dernière partie de cette thèse, nous avons présenté nos résultats préliminaires sur l'activation de le H_2O par une porphyrine manganèse-imidazole-phénol fusionnée. Ce dérivé a été conçu pour imiter la paire Tyr_{161} / His_{190} dans le photosystème II (PSII) dans le but d'étudier son rôle dans la dernière étape catalytique de la division de l'eau par le complexe d'évolution de l'oxygène (OEC) pendant la photosynthèse oxygénique.

Title : Synthesis and characterization of new porphyrin-based derivatives for CO_2 and O_2 reduction

Keywords : Metalloporphyrins – O_2 Reduction – CO_2 Reduction – Oxygen Tolerance – H_2O Activation – Metal-oxo

Abstract : Carbon-based energy sources comprise the majority of the global energy supply; yet, their over-exploitation is linked to the ever-increasing atmospheric concentration of CO_2, which accounts for the climatic change that planet Earth is currently encountering as a consequence of global warming. To mitigate climate change, one of the primary scientific challenges of the 21st century is the replacement of fossil fuels with carbon-neutral alternatives that can equally meet the energy demands of the modern world. Elucidating the mechanisms through which Nature activates thermodynamically stable small molecules, e.g., O_2, CO_2, and H_2O has been a sought-after goal for developing artificial devices in an attempt to provide a clean energy supply.

In this context, the three main topics of this Ph.D. thesis focus on the design of bio-inspired metalloporphyrins and the evaluation of their reactivity towards (i) reduction of molecular O_2, (ii) reduction of CO_2 under aerobic conditions, and (iii) activation of H_2O.

Concerning the first pillar of this thesis work, we characterized via UV-Vis, EPR, and rRaman spectroscopic studies the first intermediates involved in the reduction of molecular O_2 catalyzed by two iron-porphyrin atropisomers functionalized in their second coordination sphere with urea groups as multi-point hydrogen bonding donors. The urea tweezers were found to greatly enhance the stability of the Fe- O_2 adducts and enabled us to determine the first redox potential of an iron porphyrin (S)/(P) couple via cyclic voltammetry. In addition, the topology of the urea functions also influenced the stability of the Fe- O_2 adducts with low-temperature UV-Vis spectroscopy studies suggesting that two urea groups are needed on the same side with respect to the porphyrin plane to stabilize more efficiently the superoxo intermediates.

In the second research subject, we described a different approach to developing copper porphyrins electrocatalysts for efficient CO_2 reduction that exhibit great tolerance to the presence of O_2. More specifically, we functionalized a copper porphyrin with a pendent methyl-viologen-like group and investigated in the first place its electrocatalytic activity toward the reduction of CO_2 and molecular O_2, separately. Electrocatalytic experiments didn't only show that the new copper catalyst could realize both the reduction of CO_2 and O_2 individually but also that it could maintain its CO_2 reduction activity even under aerobic conditions. Hence the pendent methyl-viologen-like group served its purpose of tackling the reduction of O_2 at the same time that the copper porphyrin catalyzes the CO_2 reduction.

In the last part of this thesis, we presented our preliminary results on H_2O activation by a manganese fused-imidazole-phenol porphyrin. This derivative was designed to mimic the Tyr_{161} / His_{190} pair in photosystem II (PSII) in an effort to investigate its role in the last catalytic step of water splitting by the oxygen evolution complex (OEC) during oxygenic photosynthesis.

universite PARIS-SACLAY

ÉCOLE DOCTORALE
Sciences Chimiques : Molécules,
Matériaux, Instrumentation
et Biosystèmes (2MIB)

Τίτλος : Σύνθεση και χαρακτηρισμός νέων πορφυρινικών παραγώγων για την αναγωγή του CO_2 και του O_2

Λέξεις κλειδιά : Μεταλλοπορφυρίνες - Αναγωγή O_2 - Αναγωγή CO_2 - Ενεργοποίηση H_2O - Μεταλλο-οξο

Περίληψη : Τα ορυκτά καύσιμα αποτελούν την πλειονότητα του παγκόσμιου ενεργειακού εφοδιασμού, ωστόσο, η υπερεκμετάλλευσή τους συνδέεται με τη συνεχώς αυξανόμενη ατμοσφαιρική συγκέντρωση του CO_2, η οποία ευθύνεται για την κλιματική ως συνέπεια της υπερθέρμανσης του πλανήτη. Για το μετριασμό της κλιματικής αλλαγής, μία από τις πρωταρχικές επιστημονικές προκλήσεις του 21ου αιώνα είναι η αντικατάσταση των ορυκτών καυσίμων με εναλλακτικές πηγές ενέργειας φιλικές ως προς το περιβάλλον, οι οποίες μπορούν να καλύψουν εξίσου τις όλο και αυξανόμενες ενεργειακές ανάγκες του σύγχρονου κόσμου. Η αποσαφήνιση των μηχανισμών μέσω των οποίων η Φύση ενεργοποιεί θερμοδυναμικά σταθερά μικρά μόρια, π.χ. O_2, CO_2 και H_2O, έχει αποτελέσει πρωταρχικό στόχο για την ανάπτυξη τεχνητών φωτοσυνθετικών συστημάτων σε μια προσπάθεια παροχής καθαρής ενέργειας.

Σε αυτό το πλαίσιο, τα τρία κύρια θέματα της παρούσας διδακτορικής διατριβής επικεντρώνονται στο σχεδιασμό βιοεμπνευσμένων μεταλλοπορφυρινών και στην αξιολόγηση της καταλυτικής του δράσης ως προς την (i) αναγωγή μοριακού O_2, (ii) αναγωγή CO_2 υπό αερόβιες συνθήκες και (iii) ενεργοποίηση H_2O.

Όσον αφορά τον πρώτο μέρος της παρούσας διατριβής, χαρακτηρίσαμε μέσω φασματοσκοπίας UV-Vis, EPR και rRaman τα πρώτα ενδιάμεσα προϊόντα αναγωγής του μοριακού O_2 καταλυόμενη από δύο ατροποϊσομερή σιδηροπορφυρίνης τροποποιημένα στη δεύτερη σφαίρα συναρμογής τους με ομάδες ουρίας ως δότες δεσμών υδρογόνου. Διαπιστώθηκε ότι οι ομάδες ουρίας ενισχύουν σημαντικά τη σταθερότητα των Fe- O_2 ενδιαμέσων και μας επέτρεψαν να προσδιορίσουμε το πρώτο δυναμικό οξειδοαναγωγής του (S)/(P) ενδιαμέσου μέσω κυκλικής βολταμετρίας. Επιπλέον, μελέτες φασματοσκοπίας UV-Vis σε χαμηλή θερμοκρασία υπέδειξαν ότι απαιτούνται δύο ομάδες ουρίας στο ίδιο επίπεδο του πορφυρινικού δακτυλίου για τη σταθεροποίηση των Fe- O_2 ενδιαμέσων.

Στη δεύτερη ενότητα περιγράψαμε μια διαφορετική προσέγγιση για την ανάπτυξη πορφυρίνων του χαλκού ως ηλεκτροκαταλύτες για την αποτελεσματική αναγωγή του CO_2 παρουσία O_2. Πιο συγκεκριμένα, τροποποιήσαμε μια πορφυρίνη του χαλκού με ομάδες methyl viologen και διερευνήσαμε αρχικά την ηλεκτροκαταλυτική της δράση προς την αναγωγή του CO_2 και του μοριακού O_2, ξεχωριστά. Τα ηλεκτροκαταλυτικά πειράματα έδειξαν ότι η νεοσυντιθέμενη πορφυρίνη του χαλκού μπορούσε να πραγματοποιήσει τόσο την αναγωγή του CO_2 όσο και του O_2 ξεχωριστά, αλλά και ότι μπορούσε να διατηρήσει την καταλυτική της δράση ως προς την αναγωγή του CO_2 ακόμη και υπό αερόβιες συνθήκες. Ως εκ τούτου, οι ομάδες methyl viologen εξυπηρέτησαν τον σκοπό τους δηλαδή να πραγματοποιούν την αναγωγή του O_2 την ίδια στιγμή που η πορφυρίνη του χαλκού καταλύει την αναγωγή του CO_2.

Στο τελευταίο μέρος της παρούσας διατριβής, παρουσιάσαμε τα προκαταρκτικά μας αποτελέσματα σχετικά με την ενεργοποίηση του H_2O από μια πορφυρίνη μαγγανίου που φέρει μια ομάδα ιμιδαζολίου-φαινόλης. Το παράγωγο αυτό σχεδιάστηκε για να μιμηθεί το ζεύγος Tyr_{161} / His_{190} του φωτοσυστήματος II (PSII) σε μια προσπάθεια να διερευνηθεί ο ρόλος του στο τελευταίο καταλυτικό στάδιο της διάσπασης του νερού από το oxygen evolution complex (OEC) κατά την οξυγονική φωτοσύνθεση.

Acknowledgments

First and foremost I am deeply thankful to my two supervisors Prof. Athanassios G. Coutsolelos and Prof. Ally Aukauloo for offering me the opportunity to conduct my Ph.D. thesis in their groups as a joint Ph.D. student but also for their guidance throughout these years. I would also like to express my genuine gratitude to Dr. Charalambidis, Dr. Halime, Dr. Leibl, and Dr. Herrero for always being there to answer my questions and give me fruitful advice.

I am honored and grateful to all the jury members: Prof. Talal Mallah, Prof. Marine Desage-El Murre, Prof. Panagiotis Angaridis, Prof. Ioulia Smonou, and Prof. Maria Kanakidou for accepting to evaluate my thesis.

I am indebted to all the associated members and researchers of both groups: Dr. Sircoglou, Dr. Quaranta, Dr. Gotico, Dr. Amanullah, Dr. Khadraoui, M.Sc. Zhang, M.Sc. Pugliese, M.Sc. Smith, M.Sc. Rashid, Dr. Vo, Dr. Nikolaou, Dr. Charisiadis, Dr. Ladomenou, Dr. Karikis, Dr. Gannoudis, Dr. Landrou, Dr. Panagiotakis, M.Sc. Kandyli, M.Sc. Stoumpidi, M.Sc. Agapaki, M.Sc. Orfanos, Magda Topouza for the friendly, supportive, and cooperative work environment. I am very grateful to all of them.

I would like to thank all of my friends for all the great moments that we shared together. Linh for introducing me to the funny world of LCI and for being one of my best friends here in France. I will come to Poland soon, I promise. Amanda and Greg, two of the most lovely people I have ever met (Αμάντα και εσύ είσαι η καλύτερή μου φίλη!). Asma for always being there for me and having such an amazing time in the lab and also in Tunis! My γλυκάκια μου: Chanjuan who is such an 可爱的 person and always makes me happy; Eva, one of my loveliest friends who is always so supportive. Nicolò for all the funny moments, endless discussions, and support. Laura for having such great picnics together (I can't wait to visit you in Sweden). Aman for his friendship and patience (finally we got the 24/7 pass in CEA). Christian for always supplying me with sachets of sugar and Jean-no for making fun of me for that (little Chrissy, say sugar). Sophie for having so much fun together! Abdoul for taking coffee breaks in the lab. Christina, Semina, Michalis, and Kostas for all these years of friendship and support. And of course Adrien, Arthur, Axel, Adama, Riya, Alberto, and Aristide for always being so nice to hang out with you.

Finally, my special appreciation and my endless gratitude are devoted to the most precious people in my life, my family.

Table of Contents

Chapter I. Oxygen Reduction by Bio-inspired Iron Porphyrins

Chapter II. CO_2 Reduction in the Presence of O_2

Chapter III. Water Activation by a Manganese Fused Imidazole-Phenol Porphyrin Derivative

Abbreviations

Abs.	absorbance
(HP)	hydroperoxo
(P)	peroxo
(S)	superoxo
ACN	acetonitrile
ATP	adenosine 5′-triphosphate
CcO	Cytochrome c oxidase
CCU	carbon capture and utilization
CO_2RR	CO_2 Reduction Reaction
$CoCp_2$	cobaltocene
CODH	CO dehydrogenase
COF	covalent organic framework
CPE	controlled potential electrolysis
CV	cyclic voltammogram
Cyt-P450	cytochrome P450
DMF	dimethylformamide
EMoCS	electrochemical molecular catalyst screening
EPG	edge plane graphite
ET	electron transfer
Fc*	ferrocenium
FDH	formate-dehydrogenase
FE	Faraday efficiency
Ftr	formyltransferase
GC	glassy carbon
GHG	greenhouse gas
HAT	hydrogen atom transfer
Hb	hemoglobin
HCO	Heme-Copper Oxidases
IPCC	intergovernmental panel on climate change
KIE	kinetic isotope effect
LUMO	lowest unoccupied molecular orbital
Mb	myoglobin
mCPBA	meta-chloroperoxybenzoic acid
MFR	methanofuran coenzyme
MO	molecular orbital
MV^{2+}	methyl-viologen
OEC	oxygen evolution complex
ORR	O_2 reduction reaction
PCET	proton-coupled electron transfer
PDB	Protein Data Bank
PROS	partially reduced oxygen species
PSI	photosystem I
PSII	photosystem II
QO	quinol oxidase

RDE	rotating disk electrode
RIXS	resonant inelastic X-Ray scattering studies
***r*Raman**	resonance Raman
rTCA cycle	reverse tricarboxylic acid cycle
SAM	self-assembled monolayers
SCO	spin-crossover
SEC	standard calomel electrode
SECM	scanning electrochemical microscopy
SRRS	surface enhanced resonance raman spectroscopy
TACN:	1,4,7 triazacyclononane,
TBTren	N,N′,N′′-tribenzyltris(aminoethyl) amine
TFA	trifluoroacetic acid
TFE	trifluoroethanol
THF	tetrahydrofuran
TMPA	tris((2-pyridyl)methyl)amine
TOF	turnover frequency
TPP	tetraphenyl porphyrin
WL	Wood-Ljungdahl
XAS	X-Ray absorption spectroscopy

Symbols

A	Ampere
Å:	Angstrom
cm^{-1}	Wavenumber
G	Gauss
I	current
MHz	megahertz
nm	Nanometer
V	Volt
η	overpotential

Chapter I

Oxygen Reduction by Bio-Inspired Iron Porphyrins

1.1 Introduction

1.1.1 Activation and Reduction of Molecular O_2

Dioxygen holds the key to the sustenance and evolution of life. All aerobic organisms, including humans, animals, and plants, leverage its high oxidizing power to supply themselves with the energy needed to develop and evolve. The rich redox chemistry of O_2 spans from the biosynthesis of biomolecules essential for lower and higher forms of life[1] to cellular respiration and oxidative phosphorylation to form adenosine 5′-triphosphate (ATP), the energy currency of the cells[2].

O_2 is the only biradical paramagnetic molecule with a great abundance in Nature which is highly stable and kinetically inert towards the oxidation of organic substrates. The reason lies in the different spin-multiplicity of its triplet ground state and the ground state of organic molecules, usually a singlet, which renders their reaction extremely slow under ambient conditions[3].

Generation of singlet O_2 ($^1O_2$) by the direct excitation of the triplet ground state ($^3\Sigma_g^-$) is a spin-forbidden transition (Fig. 1-1); hence, sensitization of molecular O_2 via a photosensitizer with a suitable excited triplet state is considerably more favorable (type II- photooxidation reaction[4]). Either way, molecular O_2 is promoted to one of its two excited states, $^1\Delta_g$ and $^1\Sigma_g^+$, first and second, respectively. The $^1\Sigma_g^+$ state has an extremely short lifetime in solution (~ps), and therefore it rapidly relaxes to the $^1\Delta_g$ state [5]. According to molecular orbital theory (MO), the $^3\Sigma_g^-$, $^1\Delta_g$, and $^1\Sigma_g^+$ electronic states are described by the same number of electrons as expected, with the two highest in energy electrons occupying the same degenerated orthogonal π* anti-bonding molecular orbital(s). The main difference between the ground and excited states is the arrangement of these two electrons in these two orbitals.

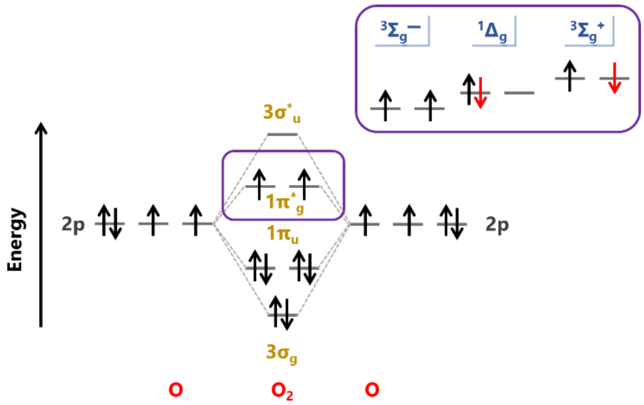

Fig. 1-1 Molecular orbital diagram of O_2 in its ground triplet state ($^3\Sigma_g^-$) and first and second excited states ($^1\Delta_g$ and $^1\Sigma_g^+$, respectively).

As shown in Fig. 1-1, both $^3\Sigma_g^-$ and $^1\Sigma_g^+$ electronic states have their π* anti-bonding orbitals singly occupied. However, in $^3\Sigma_g^-$ electronic state, the spins of two electrons are parallel to each other[6], whereas in the $^1\Sigma_g^+$ electronic state, they are antiferromagnetically coupled.[7] On the

---

[1] Goldfine, H., *J. Gen. Physiol.*, **1965**, 49, 1, 253-274, DOI: 10.1085/jgp.49.1.253.

[2] Babcock, G.T., *PNAS USA*, **1999**, 96, 23, 12971–12973, DOI: 10.1073/pnas.96.23.12971

[3] Wigner, E.P., *Ann. Math.*, **1939**, 40, 1, 149-204, DOI: 10.2307/1968551

[4] Baptista, M.S., Cadet, J., Di Mascio, P., Ghogare, A.A., Greer, A. *et al.*, *Photochem. Photobiol.*, **2017**, 93, 4, 912–919, DOI: 10.1111/php.12716

[5] Wasserman, H.H., Ives, J.L., *Tetrahedron*, **1981**, 37, 10, 1825-1852, DOI: 10.1016/S0040-4020(01)97932-3

[6] Mulliken, R.S., *Phys. Rev.*, **1932**, 32, 2, 186-222, DOI: 10.1103/PhysRev.32.186

[7] Child, W., Mecke, R., *Nature*, **1930**, 125, 599–600, DOI: 10.1038/125599c0

contrary, $^1\Delta_g$ has both electrons paired in a single π* anti-bonding orbital with the second vacant π* molecular orbital lying in the same energy level.[8],[9]

In biological systems, the direct reaction between singlet oxygen and other biomolecules is quite specific and, in the majority, leads to cellular necrosis.[10], [11] Therefore, aerobic life has evolved to activate and reduce molecular O_2 via enzymes that host in their catalytic site complexes of transition metals, e.g., Fe and Cu. Among these natural catalysts, heme-containing enzymes are of utmost importance since they carry out a variety of chemical transformations within the cells, from oxygenation and oxidation of biomolecules to the complete O_2 reduction reaction (ORR) during cellular respiration.

1.1.2 Heme Proteins and Enzymes

The number of different heme-containing enzyme superfamilies found in Nature is quite impressive, to say the least. Among them, oxygenases, peroxidases, catalases, and heme-copper oxidases are the most investigated, and the elucidation of their catalytic mechanisms has been a point of interest for many decades. Oxygenases, for example, activate and reduce molecular O_2 to oxygenate or/and oxidize biological substrates.[12] Peroxidases, on the contrary, realize similar chemical transformations by activating hydrogen peroxide (H_2O_2) instead of O_2.[13], [14] On the other hand, catalases realize the disproportionation reaction of hydrogen peroxide to protect the cells from oxidative stress while heme-copper reductases catalyze the $4e^-/4H^+$ reduction of O_2 to H_2O. [15]

Although these superfamilies cover a broad spectrum of chemical transformations within the cells, they activate and reduce molecular O_2 by following similar pathways. The first step involves the O_2 binding to the ferrous heme center yielding a **(P)Fe-O_2** adduct, where P refers to the porphine ligand. Successive reduction and protonation of **(P)Fe-O_2** leads to the formation of the **(P)Fe^{III}-OOH** intermediate, which in the case of peroxidases is produced via the reaction of the resting state of the enzyme with H_2O_2. Heterolytic or homolytic cleavage of the O-O bond in **(P)Fe^{III}-OOH** results in high-valent iron-oxo species, **($P^{\bullet+}$)Fe^{IV}=O** (Compound I, **Cpd I**) or **(P)Fe^{IV}=O** (Compound II, **Cpd II**), respectively. **Cpd I** and **Cpd II** are primarily responsible for the oxidation and oxygenation of organic substrates. However, in the case of heme-copper reductases, the corresponding **Cpd II**-like intermediate is further protonated and reduced via consecutive proton-coupled electron transfer (PCET) steps to yield H_2O (Scheme 1-1).

---

[8] Herzberg, G., *Nature*, **1934**, 133, 759, DOI: 10.1038/133759a0

[9] Babcock, H. D., Herzberg, L., *Astrophys. J.*, **1948**, 108, 167- 190, DOI: 10.1086/145062

[10] Ronsein, G. E., Oliveira, M. C., Miyamoto, S., Medeiros, M. H. G., Di Mascio, P., *Chem. Res. Toxicol.*, **2008**, 21, 1271–1283, DOI: 10.1021/tx800026g

[11] Stanley, C.P., Maghzal, G.J., Ayer, A., Talib, J., Giltrap, A.M. *et al.*, *Nature*, **2019**, 566, 548–552, DOI: 10.1038/s41586-019-0947-3

[12] Sono, M., Roach, P.M., Coulter, E.D., Dawson, J.H., *Chem. Rev.*, **1996**, 96, 2841–2887, DOI: 10.1021/cr9500500

[13] Li, X., Cong, F., Zhang, S., Zhang, D., Wang, X., *Int. J. Bioorg. Chem.*, **2020**, 5, 1, 10-14, DOI: 10.11648/j.ijbc.20200501.13

[14] Poulos, T.L., *Arch. Biochem. Biophys.*, **2010**, 500, 1, 3–12, DOI: 10.1016/j.abb.2010.02.008

[15] Zamocky, M., Furtmüller, P.G., Obinger, C., *Antioxid. Redox Signal.*, **2008**, 10, 9, 1527-1548, DOI: 10.1089/ars.2008.2046

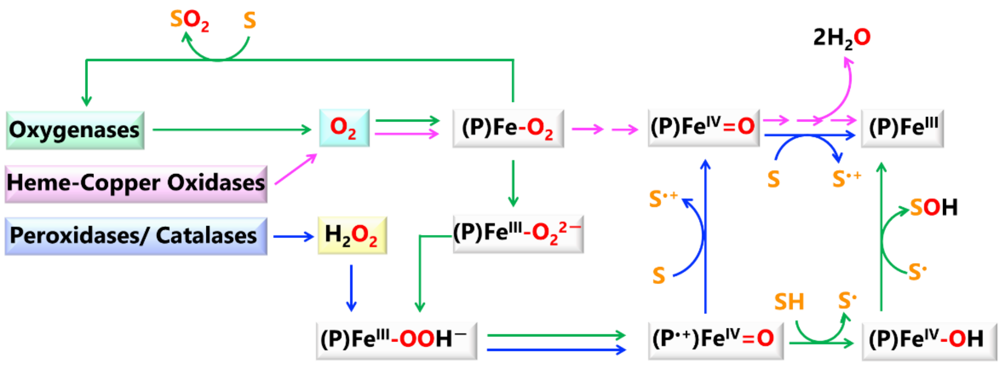

Scheme 1-1 Pathways involved in the activation and reduction of molecular O_2 by heme enzymes.

Gaining insights into the enzymatic pathways of O_2 activation and reduction would enable us to better understand the living world around us and apply the acquired lessons in industrial applications and energy production schemes. Molecular O_2 is indispensably related to the industrial synthesis of bulk and fine chemicals via the selective oxygenation of hydrocarbons [16] and to O_2-based fuel cells technologies that couple the oxidation of fuel, e.g., H_2, with the ORR to generate electricity[17].

1.1.2.1 Oxygen Binding

The initial step of activating and reducing molecular O_2 is its binding to the heme-containing enzymes' active site(s). Although hemoglobin (Hb) and myoglobin (Mb) serve as O_2 carriers heme-proteins, they are ideal models to investigate the molecular and electronic structures of the **(P)Fe-O_2** adduct. Hb and Mb bind O_2 reversibly and are the most well-studied globin proteins. Hb delivers molecular oxygen to the tissues, whereas Mb serves as an O_2 reservoir when Hb fails to meet tissues' demands for O_2 uptake.

Their first structural characterization dates back to 1960 when Perutz[18] and Kendrew[19] solved the first X-ray structures of Hb and Mb, respectively. The obtained crystallographic data revealed an almost identical O_2 binding heme center which was axially ligated with a histidine residue. In addition, a second histidine amino acid was found in the binding pocket of the heme, as shown in Fig. 1-2.

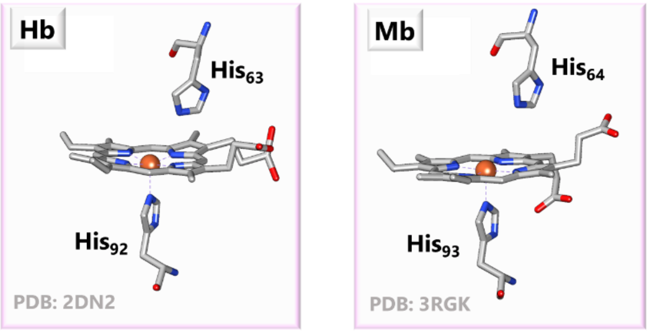

---

[16]Feldman, D., *Des. Monomers Polym.*, **2008**, 11, 1, 1–15, DOI: 10.1163/156855508X292383.
[17]Fan, L., Tu, Z., Chan, S.H., *Energy Rep.*, **2021**, 7, 8421-8446, DOI: 10.1016/j.egyr.2021.08.003
[18]Perutz, M., Rossmann, M., Cullis, A. *et al.*, *Nature*, **1960**, 185, 416–422, DOI : 10.1038/185416a0
[19]Kendrew, J., Dickerson, R., Strandberg, B. *et al.*, *Nature*, **1960**, 185, 422–427, DOI : 10.1038/185422a0

Fig. 1-2 Crystal structures of deoxy-hemes in a) Hb, and b) Mb. Herein they are depicted in a later X-ray structure determined by Tame[20] and Hendrickson[21], respectively. The figures are redrawn using Chimera 1.16 software.

Mössbauer spectroscopy studies have shown that Hb[22], [23], and Mb[24] are high-spin ferrous hemes with a quintet ground state, *viz.*, four unpaired 3d electrons.[25] Theoretical modeling on the deoxy electronic states of heme globins and model compounds have shown that a triplet state with two unpaired electrons lies roughly above the quintet ground state. This slight difference in energy is postulated to make possible the spin transition from the quintet to the triplet state prior to O_2 binding. Interaction between $^3O_2$ and the triplet ground state of the heme would give rise to **(P)Fe-O_2** end-products with an overall spin of S=0 (singlet), S=1 (triplet), or S=2 (quintet) [25], [26],. Nonetheless, among these spin states, only the singlet (S=0) could support the formation of diamagnetic **(P)Fe-O_2** species.

Pauling, Weiss, or McClure/Goddard?

The precise electronic structure of the **(P)Fe-O_2** adducts is still a point of debate, and up to now, three are the prevailing **(P)Fe-O_2** models that could rationalize their diamagnetic behavior. The first possible explanation came from Pauling and Coryell in 1936. [27] According to their model, O_2 binding to the ferrous center gives rise to a **(P)Fe^{II}-O_2** adduct, in which the O_2 ligand has a rather redox innocent character (Fig. 1-3a). On the contrary, in 1964, Weiss [28] proposed that the bound O_2 is singly reduced by the iron porphyrin, leading to a low-spin ferric **(P)Fe^{III}-$O_2^{\bullet-}$** intermediate. The diamagnetism of these species was attributed to the antiferromagnetic coupling between the unpaired electron of the superoxo ligand (S= 1/2) and the one of the Fe^{III} (S=1/2) metal center (Fig. 1-3b). Weiss' proposal and the obtained X-ray structures from Perutz and Kendrew made Pauling reconsider his earlier model in 1964[29]. In his new version, the distal O atom was negatively charged and hydrogen-bonded to a nearby protonated histidine residue, while the Fe-O bond had a rather double bond character (Fig. 1-3d). The "third" possible **(P)Fe-O_2** electronic structure was given by McClure[30] and Goddard[31], who claimed that the bound O_2 is in its triplet ground state (S=1) and couples antiferromagnetically with a Fe^{II} center of intermediate spin (S=1) [**(P)Fe^{II}-$^3O_2$**] (Fig. 1-3c).

---

[20] Park, S-Y., Yokoyama, T., Shibayama, N., Shiro, Y., Tame, J.R.H., *J. Mol. Biol.*, **2006**, 360, 3, 690-701, DOI: 10.1016/j.jmb.2006.05.036.

[21] Hubbard, S.R., Lambright, S.G., Boxer, S.G., Hendrickson, W.A., *J. Mol. Biol.*, **1990**, 20, 215-218, DOI: 10.1016/S0022-2836(05)80181-0

[22] Lang, G., Marshall, W., *J. Mol. Biol.*, **1966**, 18, 3, 385-404, DOI: 10.1016/s0022-2836(66)80032-3.

[23] Gosnerr, U., Grantand, W., Kregzde, J., *Science*, **1964**, 143, 3607, 680-681, DOI: 10.1126/science.143.3607.680

[24] Kent, T.A., Spartalian, K., G.Lang, G., Yonetani, T., Reed, C.A., Collman, P.J., *Biochim. Biophys. Acta- Protein Struct.*, **1979**, 580, 2, 245-258, DOI: 10.1016/0005-2795(79)90137-5

[25] Jensen, K.P., Ryde, U., *J. Biol. Chem.*, **2004**, 279, 15, 14561-14569, DOI: 10.1074/jbc.M314007200

[26] Blomberg, L.M., Blomberg, M.R.A., Siegbahn, P.E.M., *J. Inorg. Biochem.*, **2005**, 99, 4, 949-958, DOI: 10.1016/j.jinorgbio.2005.02.014

[27] Pauling, L., Coryell, C.D., *PNAS USA*, **1936**, 22, 4, 210-216, DOI: 10.1073/pnas.22.4.210

[28] Weiss, J.J., *Nature*, **1964**, 202, 4927, 83-84, DOI: 10.1038/202083b0

[29] Pauling, L., *Nature*, **1964**, 203, 182–183, DOI : 10.1038/203182b0

[30] McClure, D.S., *Radiat. Res. Suppl.*, **1960**, 2, 218-242, DOI: 10.2307/3583598

[31] Goddard, W.A., Olafson, B.D., *PNAS USA*, **1975**, 72, 6, 2335-2339, DOI: 10.1073/pnas.72.6.2335

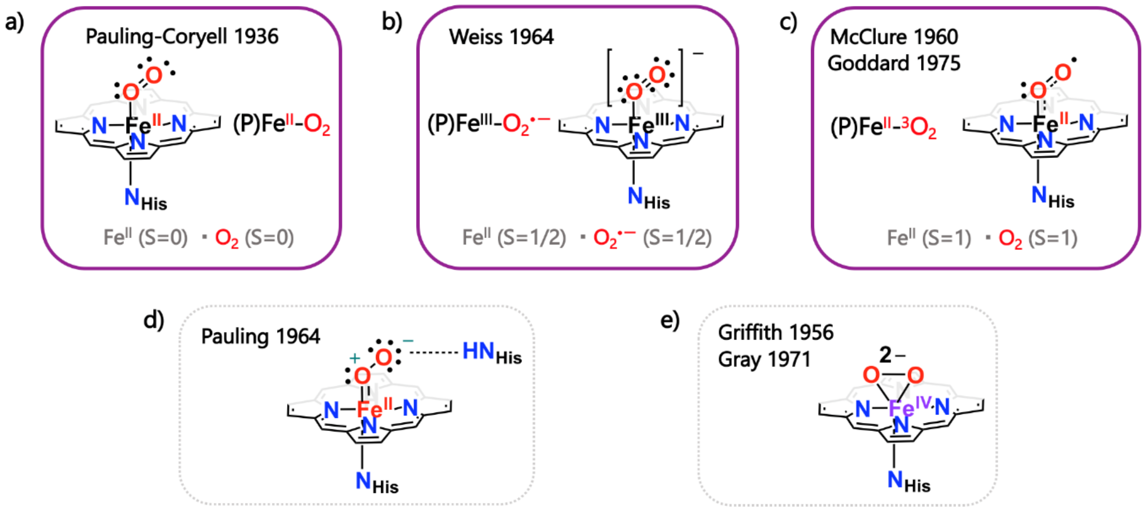

Fig. 1-3 Possible electronic structures of **(P)Fe^{II}-O$_2$** species explaining their diamagnetism. In solid boxes, there are shown the three prevailing models suggested by Pauling-Coryell, Weiss, and McClure/Goddard, respectively.

Experimental evidence supporting the end-on fashion binding of O_2 in **(P)Fe^{II}-O$_2$** species was provided initially by Collman[32], [33] in 1974 and a couple of years later by Shannan[34] and Phillips[35] in the early 80s. Collman and co-workers reported the first X-ray structure of a Fe-O_2 adduct concerning a "picket fence" porphyrin bearing 1-methyl-imidazole as an axial ligand. Shannan and Phillips, on the other hand, determined the crystal structures of Hb-O_2 and Mb-O_2, respectively (Fig. 1-4).

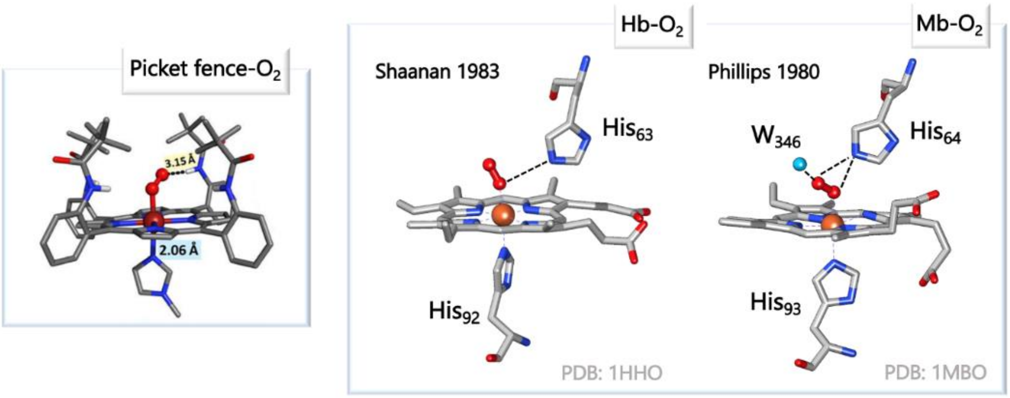

Fig. 1-4 X-ray crystal structures of Fe-oxy intermediate species for a picket fence iron porphyrin and for Hb and Mb. The crystal structure of Hb-O_2 is derived from a later study by Shaanan[36]. The figures are redrawn using Chimera 1.16 software.

The obtained crystallographic data revealed that the O_2 ligand was stabilized on the iron center via hydrogen-bonding interactions, as shown in Fig. 1-4. In the case of Collman's model, the hydrogen bond donor was the -NH group of the *ortho*-pivalamide phenyl ligand, whereas in Hb-O_2 and Mb-O_2 it was the distal non-coordinated protonated histidine residue. The

---

[32] Collman, J.P., Gagne, R.R., Reed, C.A., Robinson, W.T., Rodley, G.A., *PNAS USA*, **1974**, 71, 4, 1326-1329, DOI: 10.1073/pnas.71.4.1326.

[33] Collman, J. P., Gagne, R. R., Reed, C. A., Halbert, T. R., Lang, G., Robinson, W. T., *J. Am. Chem. Soc.*, **1975**, 97, 6, 1427-1239, DOI: 10.1021/ja00839a026

[34] Shaanan, B., *Nature*, **1982**, 296, 683–684, DOI: 10.1038/296683a0

[35] Phillips, S., Structure of oxymyoglobin. *Nature*, **1978**, 273, 247–248, DOI: 10.1038/273247a0

[36] Shaanan, B., *J. Mol. Biol.*, **1983**, 171, 31-59, DOI: 10.1016/s0022-2836(83)80313-1

hydrogen bond formation in the latter was further supported by Schoenborn via neutron diffraction studies.[37]

Concerning now the electronic state of these species, L-edge X-Ray absorption spectroscopy (XAS) studies on the "picket fence" porphyrin revealed a low-spin Fe^{II} (S=0) porphyrin, thus further justifying the model of Pauling[38]. However, K-edge XAS studies for $Hb\text{-}O_2$ revealed two possible electronic structures. In the solid-state, the $Fe\text{-}O_2$ adduct favored the electronic structure proposed by Pauling, while in solution, the one of Weiss *viz*., **$(P)Fe^{III}\text{-}O_2^{\bullet-}$** [39]. Additional evidence of a **$(P)Fe^{III}\text{-}O_2^{\bullet-}$** intermediate came from Solomon [40] via resonant inelastic X-Ray scattering studies (RIXS) and from Grant[41] via Mössbauer spectroscopy. In 2017, Haumann[42] suggested that neither Pauling's nor Weiss' model could represent the **$(P)Fe\text{-}O_2$** electronic structure. Indeed, a series of XAS, X-ray emission spectroscopy (XES) studies, and theoretical calculations revealed that the oxy-Hb/Mb species is better described by the model of McClure/Goddard [**$(P)Fe^{II}\text{-}{}^3O_2$**]. Yet, in 2021, Mössbauer spectroscopic data on oxy-Mb presented by Ohta indicated a **$Fe^{III}\text{-}O_2^{\bullet-}$** electronic state. [43]

Besides the models of Pauling, Weiss, and McClure/Goddard, an additional electronic state for the **$(P)Fe\text{-}O_2$** species has also been proposed independently by Griffith[44] and Gray[45], in which O_2 binds in a side-on fashion to the ferrous center (Fig. 1-3e). However, this configuration is gaining less and less ground since recent computational and experimental studies on oxy-Hb/Mb and model compounds have failed to back up this electronic structure[46], [47]. Even so, it is worth noting that Nam in 2014 reported an X-ray structure of a side-on $Fe^{III}\text{-}O_2$ adduct; yet, for a mononuclear non-heme model. [48] In heme synthetic models, only one example is listed in the literature and it has been evidenced by Nakamoto in the early 80s for a simple FeTPP at 15 K! [49]

Almost a century has passed since the first valence bond model was proposed by Pauling and Coryell, and still, the precise electronic structure of the heme-O_2 adduct remains a mystery. Under ambient conditions, we can imagine that the $Fe\text{-}O_2$ adduct is described at the same time by all of its proposed electronic structures. Yet, depending on the experimental technique and conditions which mainly require cryogenic temperatures, normally one of the electronic states can be trapped and characterized. Whether Pauling, Weiss, or/and McClure/Goddard model describes better the diamagnetic $Fe\text{-}O_2$ adduct may not have been answered yet; the X-ray structures of the oxy-globins and synthetic analogs by Collman[50] have pointed out the

---

[37] Phillips, S., Schoenborn, B, *Nature*, **1981**, 292, 81–82, DOI: 10.1038/292081a0

[38] Wilson, S.A., Kroll, T., Decréau, R.A., Hocking, R.K., Lundberg, M. *et al.*,*J. Am. Chem. Soc.*, **2013**, 135, 3, 1124–1136, DOI: 10.1021/ja3103583

[39] Wilson, S.A., Green, E., Mathews, I.I., Benfatto, M., Hodgson, K.O. *et al.*, *PNAS USA*, **2013**, 110, 41, 16333-16338, DOI: 10.1073/pnas.1315734110

[40] Yan, J.J., Kroll, T., Baker, M.L., Wilson, S.A., Decréau, R. *et al.*, *PNAS USA*, **2019**, 116, 8, 2854-2859 DOI: 10.1073/pnas.1815981116

[41] Gonser, U., Grant, R.W., *Biophys. J.*, **1965**, 5, 6, 823–844, DOI: 10.1016/S0006-3495(65)86754-6

[42] Schuth, N., Mebs, S., Huwald, D., Wrzolek, P., Schwalbe, M. *et al.*, *PNAS USA*, **2017**, 114, 32, 8556–8561, DOI: 10.1073/pnas.1706527114

[43] Yamamoto, Y., Hasegawa, K., Shibata, T., Momotake, A., Ogura, T. *et al., Inorg. Chem.*, **2021**, 60, 2, 1021–1027, DOI: 10.1021/acs.inorgchem.0c03123

[44] Griffith, J.S., *Proc. R. Soc. Ser. A*, **1956**, 235, 1200, 23-26, DOI: 10.1098/rspa.1956.0062

[45] Gray, H.B., *Adv. Chem. Ser.*, **1971**, 100, Bioinorganic Chemistry, Chapter 17, 365-389, DOI: 10.1021/ba-1971-0100.ch017

[46] Chen, H.,Ikeda-Saito, M., Shaik, S., *J. Am. Chem. Soc.*, **2008**, 130, 44, 14778–14790, DOI: 10.1021/ja805434m

[47] Ribas-Ariño, J., Novoa, J.J., *Chem. Commun.,* **2007**, 3160-3162, DOI: 10.1039/B704871H

[48] Hong, S., Sutherlin, K., Park, J. *et al.*, *Nat. Commun.*, **2014**, 5, 5440, DOI: 10.1038/ncomms6440

[49] Nakamoto, K., Watanabe, T., Ama, T., Urban, M.W., *J. Am. Chem. Soc.*, **1982**, 104, 13, 3744–3745, DOI: 10.1021/ja00377a044

[50] Jameson, G.B., Molinaro, F.S., Ibers, J.A., Collman, J.P., Brauman, J.I. *et al.*, *J. Am. Chem. Soc.*, **1980**, 102, 9, 3224–3237, DOI: 10.1021/ja00529a055

significant role of the first and the second coordination spheres contribution to the formation and stabilization of such **(P)Fe-O$_2$** intermediates. In particular, the stabilization of the bound O$_2$ to the iron center is crucial to the function of the Hb and Mb as reversible O$_2$ carriers, as it prevents (i) the formation of μ-peroxo dimers and (ii) the heterolysis of the Fe-O bond to give Fe^{III}-OH$_2$ and free superoxide ($O_2^{\bullet -}$).[51]

1.1.2.2 Catching the Intermediates

In heme-containing enzymes, the role of the first and second coordination sphere expands further from the formation and stabilization of the **(P)Fe-O$_2$** adducts and has been proven as essential to the generation of the key intermediates in their catalytic cycle. Heme-oxygenases and heme-copper oxidases are ideal paradigms pointing out the differences of the first and second spheres contribution to the catalytic intermediates, even though the former activates and reduces molecular O$_2$ to oxygenate organic substrates, while the latter realizes the 4e$^-$/ 4H$^+$ reduction of O$_2$ to H$_2$O.

1.1.2.2.1 Cytochrome P$_{450}$ (Cyt-P$_{450}$)

Cyt-P$_{450}$ is among the most widespread superfamily of mono-oxygenases in Nature and their catalytic functions are by far the most well-investigated compared to other heme-containing enzymes. In mammals, they are involved in different metabolic pathways that span from the degradation of xenobiotics (e.g., caffeine) and drugs (e.g., theophylline) in the liver's tissues[52], to the biosynthesis of steroid hormones essential for the metabolism of glucose, the regulation of fluid volume retention within the body [53] or even for the determination of sexual characteristics (e.g., testosterone and estrogen) [54]. A broader scheme, including the diverse types of reactions catalyzed by Cyt-P$_{450,}$ is provided in Scheme 1-2.

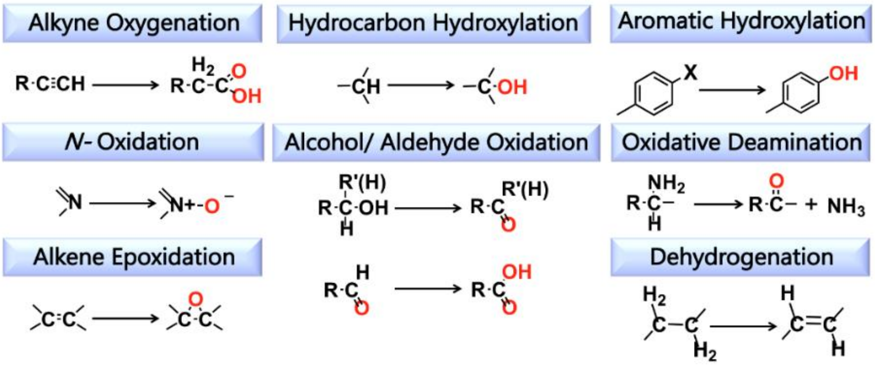

Scheme 1-2 Catalyzed reactions realized by Cyt-P$_{450}$ as proposed by Sono and co-workers [55].

This superfamily of heme-enzymes has a long history that places us back to 1958 when it was initially identified by Klingenberg [56] and later on the same year by Garfinkel [57]. It was described as a CO-binding pigment that exhibited an intense absorption band at

---

[51] Bonaventur, C., Henkens, R., Alayash, A.I., Banerjee. S., Crumbliss, A.L., *Antioxid. Redox Signal*, **2013**, 18, 17, 2298-2313, DOI: 10.1089/ars.2012.4947

[52] Shimada, T., Gillam, E.M.J., Sutter, T.R., Strickland, P.T., Guengerich, F.P., and Yamazaki, H., *Drug Metab. Dispos.*, **1997**, 25, 617–622, PMID: 9152602

[53] Bernhardt, R., **2014**, Mammalian and Bacterial Cytochromes P450 Involved in Steroid Hydroxylation : Regulation of Catalysis and Selectivity, and Potential Applications. In: Yamazaki, H. (eds) Fifty Years of Cytochrome P450 Research. Springer, Tokyo, Chapter 8, 135-151, DOI: 10.1007/978-4-431-54992-5_8 8

[54] Waxman, D.J., Chang, T.K.H., **2005**, Hormonal Regulation of Liver Cytochrome P450 Enzymes. In: Ortiz de Montellano, P.R. (eds) Cytochrome P450., , Springer, Boston, MA., Chapter 9, 347-376, DOI: 10.1007/0-387-27447-2_9

[55] Sono, M., Roach, M. R., Coulter, E.D., Dawson, J.H., *Chem. Rev.*, **1996**, 96, 7, 2841–2888, DOI: 10.1021/cr9500500

[56] Klingenberg, M., *Arch. Biochem. Biophys.*, **1958**, 75, 2, 376-386, DOI: 10.1016/0003-9861(58)90436-3

[57] Garfinkel, D., *Arch. Biochem. Biophys.*, **1958**, 77, 2, 493-509, DOI: 10.1016/0003-9861(58)90095-x

approximately 450 nm in the UV-Vis region, hence the given name of P_{450}. It was no more than a decade later that Omura and Sato [58] revealed that its solubilized form behaved like a typical heme protein with a maximum absorbance at 420 nm under anaerobic conditions. However, the precise structure of Cyt-P_{450} enzymes remained a mystery until the late 80s. In 1985, Poulos and co-workers [59] reported the first X-ray structure of a microbial Cyt-P_{450}cam, which was already known to catalyze the regio-stereospecific hydroxylation of camphor [60] (Fig. 1-5). Ever since, several other Cyt-P_{450} enzymes, including human's, have been characterized crystallographically, and some of the obtained X-ray structures are shown in Fig. 1-5, below. [61], [62]

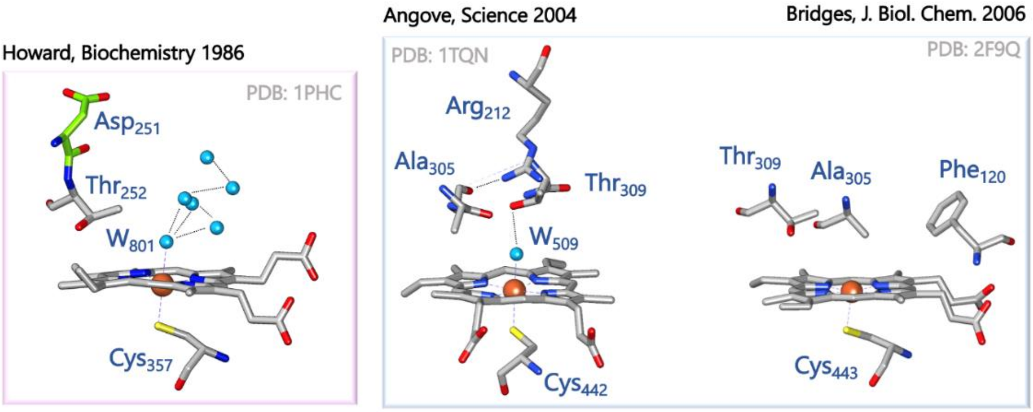

Fig. 1-5 Left: Crystal structure of Cyt-P_{450}cam, and right: Crystal structures of Cyt-P_{450} found in humans. The figures are redrawn using Chimera 1.16 software.

Catalytic Mechanism of Cyt-P_{450}

A general catalytic pathway of Cyt-P_{450} was already proposed in 1968[60] based on optical spectroscopic methods on the purified Cyt-P_{450}cam enzyme; however, it took several years to be commonly accepted. Spectroscopic and high-resolution cryo-crystallographic studies on both wild-type and mutagenized Cyt-P_{450} enzymes and model compounds led to the consensus catalytic cycle provided in Scheme 1-3.[63].

---

[58] Omura, T., Sato, R., *J. Biol. Chem.*, **1964**, 239, 2370-2378, DOI: 10.1016/S0021-9258(20)82244-3

[59] Poulos, T.L., Finzel, B.C., Gunsalus, I.C., Wagner, G.C., Kraut, J., *J. Biol. Chem.*, **1985**, 260, 30, 16122-16130, DOI: 10.1016/S0021-9258(17)36209-9

[60] Katagiri, M., Ganduli, B.N., Gunsalus, I.C., *J. Biol. Chem.*, **1968**, 243, 12, 3543-3546, DOI: 10.1016/S0021-9258(18)93343-0

[61] Williams, P.A., Cosme, J., Vinković, D.M., Ward, A., Angove, H.C., *Science*, **2004**, 305, 5684, 683-686, DOI: 10.1126/science.1099736

[62] Rowland, P., Blaney, F.E., Smyth, M.G., Jones, J.J., Leydon, V.R. *et al.*, *J. Biol. Chem*, **2006**, 281, 11, 7614 -7622, DOI: 10.1074/jbc.M511232200

[63] Makris, T.M., Denisov, I., Schlichting, I., Sligar, S.G., **2005**, Activation of Molecular Oxygen by Cytochrome P450. In: Ortiz de Montellano, P.R. (eds) Cytochrome P450. Springer, Boston, MA., Chapter 5, 149-181, DOI: 10.1007/0-387-27447-2_5

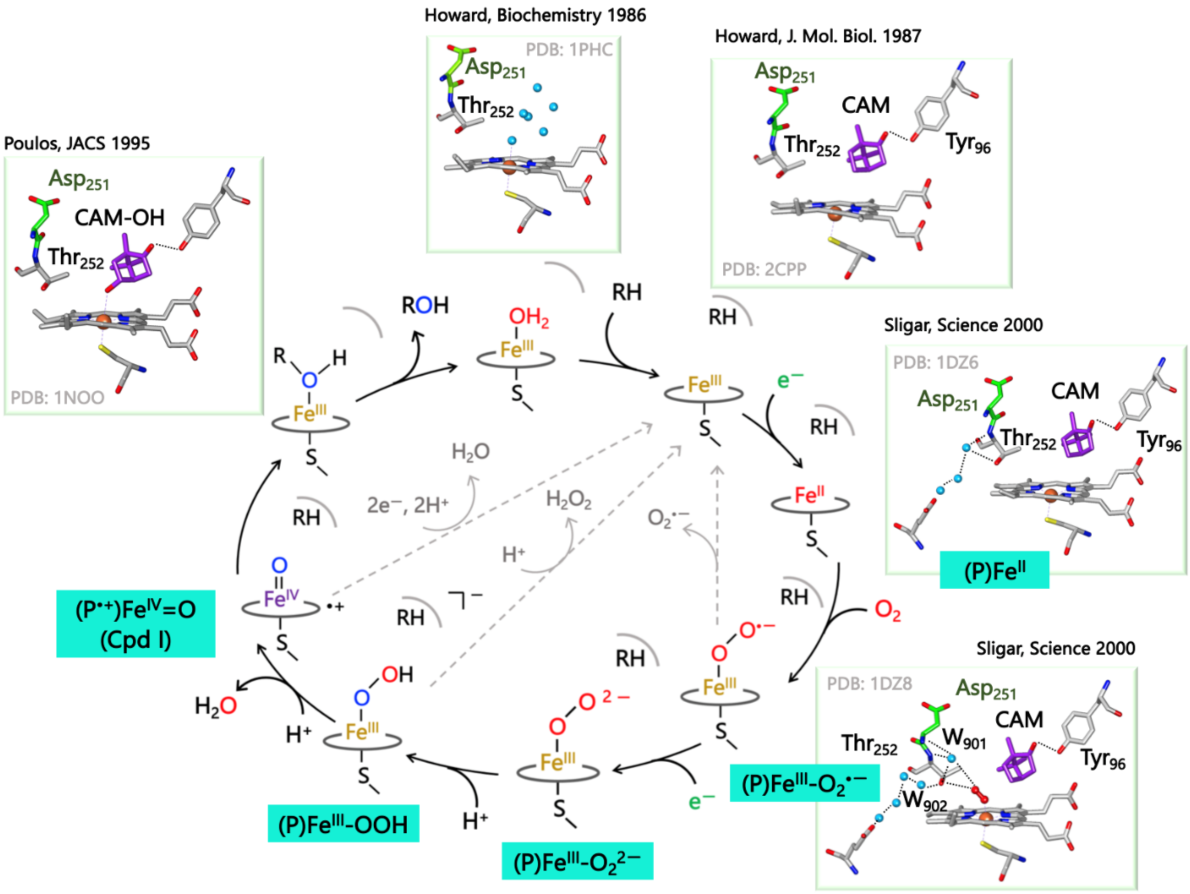

Scheme 1-3 Proposed catalytic mechanism of O_2 activation and reduction in Cyt-P_{450}. The X-ray structures are redrawn using Chimera 1.16 software.

The resting state of the catalytic site contains a low-spin [64] Fe^{III} center axially coordinated with a cysteine residue and a water molecule in a proximal and distal position, respectively [65]. The first step involves the substrate's insertion and stabilization into the enzyme's catalytic pocket via hydrogen-bonding interactions with a nearby Tyr_{96} residue. This spatial change causes the release of the bound water molecule, thus switching the spin state of the active site from a low-spin to a high-spin ferric heme and making the reduction of the Fe^{III} heme thermodynamically more favorable [66]. Upon one-electron reduction of **(P)Fe^{III}** by an associated reductase, molecular O_2 binds to the **(P)Fe^{II}** active site to yield a metastable **(P)Fe^{III}-O$_2^{\bullet-}$** intermediate analogous to the one observed in globin proteins. According to X-ray crystallography studies for Cyt-P_{450}cam by Sligar [67], O_2 binding to the Fe^{II} heme results in small yet pivotal conformation rearrangements within the distal pocket of the enzyme. The substrate, herein camphor, shifts towards the Tyr_{96} residue due to steric hindrance from the oxy-ligand, while the iron center moves inside the plane of the porphyrin core. At the same time, the Asp_{251} and Thr_{252} residues are now found hydrogen-bonded to two water molecules, W_{901} and W_{902}, respectively. These two new water molecules contribute to the stabilization of the oxy-heme adduct and induce the formation of a tight hydrogen-bonding water network that expands from Asp_{251} to Glu_{366}, thus preventing the release of free superoxide. Once the **(P)Fe^{III}-O$_2^{\bullet-}$**

---

[64] Sligar, G.S., *Biochemistry*, **1976**, 15, 24, 5399–5406, DOI: 10.1021/bi00669a029

[65] Poulos, T.L., Finzel, B.C., Howard, A.J., *Biochemistry*, **1986**, 25, 5314-5322, DOI: 10.1021/bi00366a049

[66] Poulos, T.L., Finzel, B.C., Howard, A.J., *J. Mol. Biol.*, **1987**, 195, 3, 687-700, DOI: 10.1016/0022-2836(87)90190-2

[67] Schlichting, I., Berendzen, J., Chu, Stock, A.M., Maves, S.A., Benson, D.E. *et al.*, *Science*, **2000**, 287, 5458, 1615-1622, DOI: 10.1126/science.287.5458.1615

species is formed, another one-electron reduction takes place, resulting in the **(P)Fe^{III}-O$_2$$^{2-}$** intermediate, which is subsequently protonated to **(P)Fe^{III}-OOH**. In the next catalytic step, two are the possible pathways, the protonation of either the proximal (highlighted in blue) or the distal oxygen atom (highlighted in red). Protonation of the proximal oxygen would result in the production and release of H_2O_2, while the enzyme would return to its inactivated form. However, this is not the case, and in Cyt-P$_{450,}$ the proton transfer is carried out on the distal oxygen atom. The reason lies in the axially coordinated thiolate ligand (Cys$_{357}$) that donates electron density to the metal center, strengthening the O-O bond, thus increasing the basicity of the distal oxygen atom and favoring its protonation. As such, further protonation of the **(P)Fe^{III}-OOH** adduct followed by the heterolytic O-O bond cleavage gives rise to the formation of a **(P$^{\bullet+}$)Fe^{IV}=O** intermediate, otherwise known as **Cpd I**. Sligar reported a putative X-ray structure of **Cpd I** derived from Cyt-P450cam enzyme in 2000; however, neither the identification of the oxidation state nor the electronic structure of the obtained intermediate was feasible [67]. After forming the high-valent iron oxo species, the substrate gets hydroxylated with the resulting product coordinating on the metal center as it was proven by Poulos in 1995 [68]. In the last and final step, the product escapes from the catalytic pocket, and the enzyme returns to its resting state, ready to start a new catalytic cycle.

1.1.2.2.2 Heme-Copper Oxidases (HCOs)

In contrast to oxygenases, heme-copper oxidases take things a little further and catalyze the 4e$^-$/4H$^+$ reduction of molecular O_2 to H_2O during cellular respiration. HCOs couple the ORR with the translocation of protons in and out of the protein-membrane to produce the essential proton motive force for the activation of ATP synthase, the very last enzyme of the oxidative phosphorylation pathway that generates ATP from ADP (Eq.1).

$$\mathbf{O_2} + \mathbf{8H^+_{in}} + \mathbf{4e^-} \rightarrow \mathbf{2H_2O} + \mathbf{4H^+_{out}} \qquad \text{Eq. 1}$$

Cytochrome *c* oxidase (C*c*O) and quinol oxidase (QO) are two of the most well-known subfamilies of HCOs. C*c*O is commonly found in eukaryotes and prokaryotes, while QO only in the latter and mainly in human pathogens[69]. Their crystallographic characterization was realized more than two decades ago when Yoshikawa[70] (1995) and Wilkström[71] (2000) determined the first X-ray structures of a C*c*O from a bovine heart and a QO from *E*.coli, respectively. Although derived from different organisms, their enzymatic architectures share similar structural and functional motifs.

C*c*O contains four redox-active metal centers: a dinuclear copper complex (**Cu$_A$**), a low-spin **heme a**, and a high-spin binuclear **heme a$_3$/ Cu$_B$** center that binds and reduces molecular O_2 to H_2O in its reduced state. The four electrons required for the ORR are transferred successively from cytochrome c, which is located on the P-side of the mitochondrial membrane, to the **Cu$_A$** and **heme a** cofactors and finally to the **heme a$_3$/ Cu$_B$** catalytic center. On the other hand, the four protons are abstracted from the mitochondrial matrix (N-side) and provided to the catalytic center via well-defined H$^+$ channels (Scheme 1-4).[70],[72]

---

[68]Li, H., Narasimhulu, S., Havran, L.M., Winkler, J.D., Poulos, T.L., *J. Am. Chem. Soc.*, **1995**, 117, 23, 6297–6299, DOI: 10.1021/ja00128a019

[69]Borisov, V.B., Gennis, R.B., Hemp, J., Verkhovsky, M.I., *Biochim. Biophys. Acta Bioenerg.*, **2011**, 1807, 11, 1398-1413, DOI: 10.1016/j.bbabio.2011.06.016

[70]Tsukihara, T., Aoyama, H., Yamashita, E., Tomizaki, T., Yamaguchi, H. *et al.*, *Science*, **1995**, 269, 5227, 1069-1074, DOI: 10.1126/science.7652554

[71]Abramson, J., Riistama, S., Larsson, G., Jasaitis, A., Svensson-Ek, M. *et al.*, *Nat. Struct. Biol.*, **2000**, 7, 910-917, DOI: 10.1038/82824

[72] Tsukihara T., Aoyama, H., Yamashita, E.,Tomizaki, T., Yamaguchi, H. *et al.*, *Science*, **1996**, 272, 5265, 1136-1144, DOI: 10.1126/science.272.5265.1136

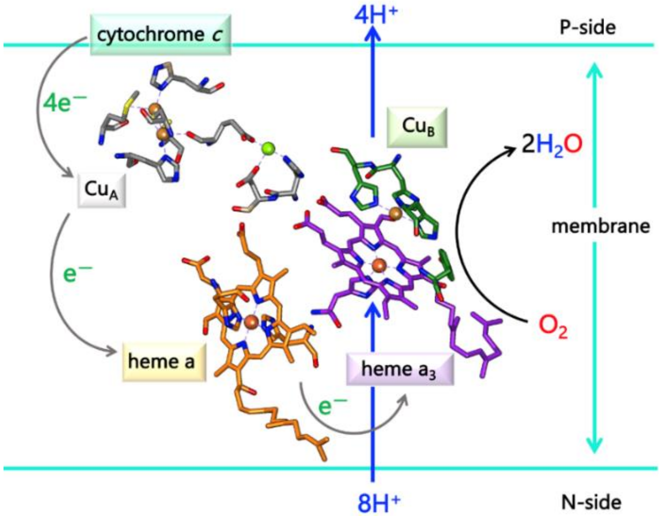

Scheme 1-4. Proposed electron and proton transfer pathways in bovine heart C*c*O (PDB: 1OCC).

As in the case of C*c*O, QO contains a low-spin **heme b** cofactor and a high-spin **heme o$_3$/ Cu$_B$** catalytic site; however, the dinuclear Cu$_A$ complex is absent. Therefore, the electrons are shuttled directly from the ubiquinol to the **heme b** and then to the **heme o$_3$/ Cu$_B$** center, while the protons are transferred from the N-side of the cytoplasmic membrane, as in C*c*O (Scheme 1-5).[71]

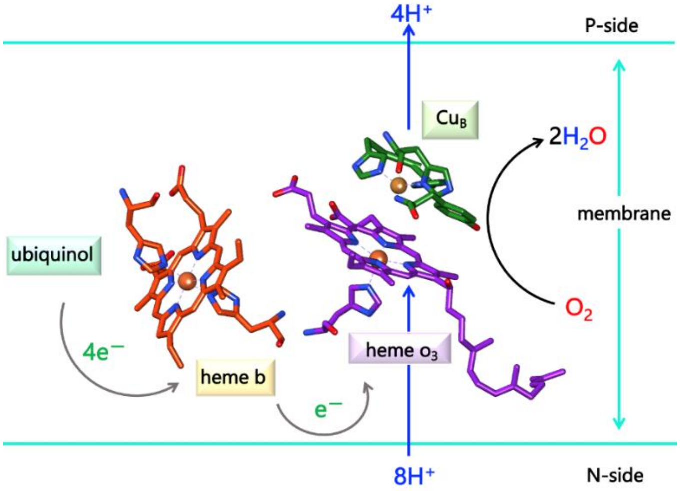

Scheme 1-5 Possible electron and proton transfer pathways in *E.*coli in QO (PDB: 1FFT).

Active Site and Proposed Catalytic ORR Mechanism

The catalytic site of C*c*O consists of a **heme a$_3$/ Cu$_B$** binuclear complex, as shown in Fig. 1-6. **Heme a$_3$** is axially coordinated with **His$_{376}$**, and the **Cu$_B$** metal center is ligated to two histidine residues, **His$_{290}$** and **His$_{291}$**, and an additional **His$_{240}$** which is covalently linked with **Tyr$_{244}$**. A similar structural motif is also present in QO isolated from *E.*coli; yet, the β-pyrrolic substitution on the heme is different (**heme o$_3$**).

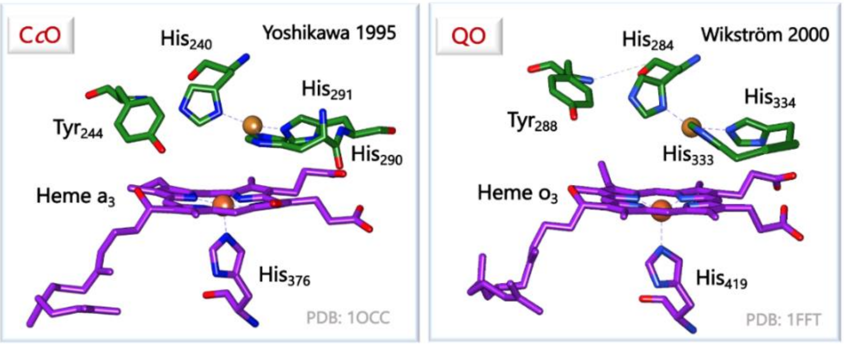

Fig. 1-6 X-ray structures of the catalytic ORR site in C*c*O and QO (redrawn using Chimera 1.16 software).

The overall catalytic cycle of ORR by C*c*O involves several oxidative and reductive steps, with the proposed intermediate species having been identified mainly through: (i) time-resolved spectroscopy studies, including laser flash photolysis, resonance Raman (*r*R), UV-vis absorption spectroscopy, (ii) EPR spectroscopy, and (iii) X-ray diffraction studies that have allowed the structural characterization of some of the intermediates.

A commonly accepted mechanism is provided in Scheme 1-6, and it has been extensively reviewed by Shimada (2015)[73], Karlin (2018)[74], and more recently by Lu (2021)[75].

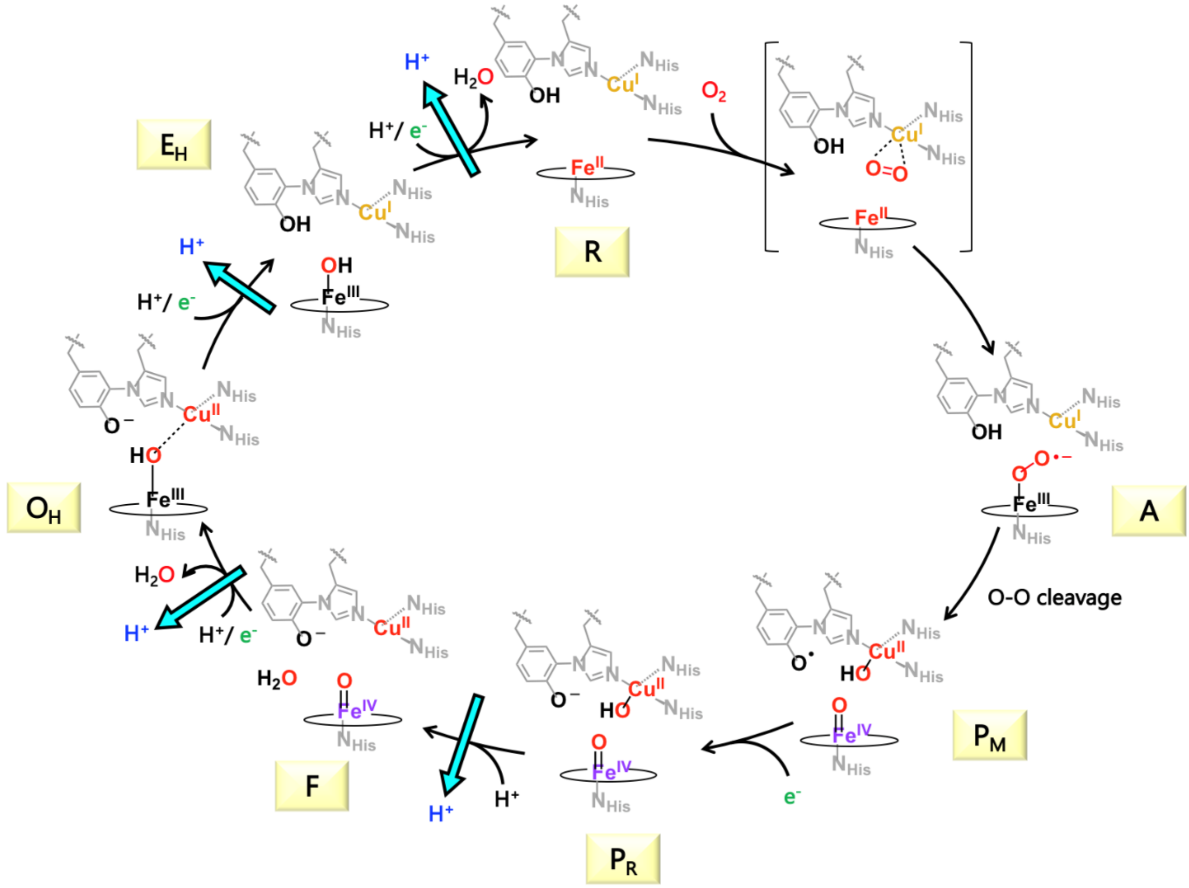

Scheme 1-6 Proposed catalytic mechanism of molecular O_2 activation and reduction to H_2O by C*c*O. Alternative O_2 activation and reduction steps involved in the transition from the R state to the F state.

---

[73]Yoshikawa, S., Shimada, A., *Chem. Rev.*, **2015**, 115, 4, 1936–1989, DOI: 10.1021/cr500266a

[74]Adam, S.M., Wijeratne, G.B., Rogler, P.J., Diaz, D.E., Quist, D.A. *et al.*, Chem. Rev., **2018**, 118, 22, 10840-11022, DOI: 10.1021/acs.chemrev.8b00074

[75]Reed, J.C., Lam, Q.N., Mirts, E.V., Lu, Y., *Chem. Soc. Rev.*, **2021**,50, 2486-2539, DOI: 10.1039/D0CS01297A

The subscripts M and P stand for the mixed-valence ($\mathbf{Cu^{II}_{A}}$, $\mathbf{Fe^{III}}$ heme **a**, $\mathbf{Fe^{II}}$ heme a_3, $\mathbf{Cu^{I}_{B}}$) and fully reduced ($\mathbf{Cu^{I}_{A}}$, $\mathbf{Fe^{II}}$ heme **a**, $\mathbf{Fe^{II}}$ heme a_3, $\mathbf{Cu^{I}_{B}}$) starting state of the entire enzyme.

As shown in Scheme 1-6, the catalytic cycle begins with the reduced state (**R** *state*) of the binuclear heme a_3/ Cu_B center, better designated as a $\mathbf{Fe^{II}}$ heme a_3, $\mathbf{Cu^{I}_{B}}$ **Tyr-OH** species[76]. It is proposed that O_2 is first trapped by the $\mathbf{Cu^{I}_{B}}$ metal site[77], and it is subsequently transferred to the $\mathbf{Fe^{II}}$ heme a_3 center[78], [79], [80], giving rise to a short-lived **heme** $\mathbf{a_3}$**-**$\mathbf{O_2}$ bound species (~20 µs) [81], [82]. Flash-flow spectroscopy studies have evidenced the formation of a $\mathbf{Fe^{II}}$ heme $\mathbf{a_3}$**-**$\mathbf{O_2}$ adduct, which rapidly evolves to a $\mathbf{Fe^{III}}$ heme $\mathbf{a_3}$ **-**$\mathbf{O_2^{\bullet -}}$ intermediate (**A** *state*) [83]. Once the $\mathbf{Fe^{II}}$ heme $\mathbf{a_3}$**-**$\mathbf{O_2}$ adduct is formed, the O-O bond cleaves rapidly to yield the EPR silent $\mathbf{P_M}$ *state*, in which the resulting $\mathbf{Fe^{IV}{=}O/\ Cu^{II}_{B}\text{-}OH}$ center [84], [85], [86] is antiferromagnetically coupled with a $\mathbf{Tyr\text{-}O^{\bullet}}$ radical[87], [88]. In the next step, $\mathbf{Tyr\text{-}O^{\bullet}}$ is singly reduced to tyrosinate ($\mathbf{Tyr\text{-}O^{-}}$), resulting in the formation of the $\mathbf{P_R}$ *state* ($\mathbf{Fe^{IV}{=}O/\ Cu^{II}_{B}\text{-}OH,\ Tyr\text{-}O^{-}}$) [89], [90]. A single proton transfer to the $\mathbf{P_R}$ intermediate gives the **F** *state* [91], which is then converted to the $\mathbf{O_H}$ species via a proton-coupled electron transfer (PCET) accompanied by the loss of a water molecule from the catalytic pocket [92]. The resulting $\mathbf{O_H}$ *state* is described as a $\mathbf{Fe^{III}\text{-}O(H)\cdots Cu^{II}_{B}}$, $\mathbf{Tyr\text{-}O^{-}}$ intermediate. Yet, two alternative structures: (i) $\mathbf{Fe^{III}\text{-}O(H)\cdots Cu^{I}_{B}}$, $\mathbf{Tyr\text{-}O^{\bullet}}$ and (ii) $\mathbf{Fe^{III}\text{-}O\text{-}Cu^{II}_{B}}$, **Tyr-OH** ($\mathbf{O_B}$), have also been proposed computationally [93]. A successive PCET to the $\mathbf{O_H}$ species yields the $\mathbf{E_H}$ *state*, possibly $\mathbf{Fe^{III}\text{-}OH}$, $\mathbf{Cu^{I}_{B}}$, **Tyr-OH** that is further protonated and reduced to generate the initial **R** *state* with the release of a second water molecule.[94]

Even though the above catalytic cycle is consensually recognized, recent crystallographic studies by Yoshikawa[95] offered a different perspective on the possible catalytic steps involved in the transition from the **R** to **F** *state* (Scheme 1-7). According to their findings, O_2 binding to $\mathbf{Fe^{II}}$ heme $\mathbf{a_3/Cu^{I}_{B}}$ results in the entrapment of a water molecule inside the catalytic pocket, hydrogen bonded to the distal **Tyr-OH** residue (*B*). Once the (*B*) intermediate is formed, the pending $\mathbf{Cu^{I}_{B}}$ metal center reduces the O_2 bound molecule to yield a bridged-peroxo complex

---

[76] Chance, B., Saronio, C., and Leigh Jr. J.S., **1975**, 72, 4, 1635-1640, DOI: 10.1073/pnas.72.4.1635

[77] Babcock, G., Wikström, M., *Nature*, **1992**, 356, 301–309, DOI: 10.1038/356301a0

[78] Han, S., Takahashi, S., Rousseau, D.L., *J. Biol. Chem.*, **2000**, 275, 3, 1910-1919, DOI: 10.1074/jbc.275.3.1910

[79] Muramoto, K., Ohta, K., Shinzawa-Itoh, K., Kanda, K., Taniguchi, M. *et al.*, *PNAS USA*, **2010**, 107, 17, 7740-7745, DOI: 10.1073/pnas.0910410107

[80] Nakashima, S., Ogura, T., Kitagawa, T., *Biochim. Biophys. Acta Bioenerg.*, **2015**, 1847, 1, 86-97, DOI: 10.1016/j.bbabio.2014.08.002

[81] Han, S.W., Ching, Y.C., Rousseau, D.L., *PNAS USA*, **1990**, 87, 7, 2491-2495, DOI: 10.1073/pnas.87.7.2491

[82] Varotsis, C., Woodruff, W.H., and Babcock, G.T., *J. Am. Chem. Soc.*, **1989**, 111, 16, 6439–6440 DOI: 10.1021/ja00198a075

[83] Verkhovsky, M.I., Morgan, J.E., Wikström, M., *Biochemistry*, **1994**, 33, 10, 3079–3086, DOI: 10.1021/bi00176a042

[84] Fabian, M., Wong, W.W., Gennis, R.B., Palmer, G., *PNAS USA*, **1999**, 96, 13114-13117, DOI: 10.1073/pnas.96.23.13114

[85] Cheesman, M.R., Watmough, N.J., Gennis, R.B., Greenwood, C., Thomson, A.J., *Eur. J. Biochem.*, **1994**, 219, 1-2, 595-602, DOI: 10.1111/j.1432-1033.1994.tb19975.x

[86] Ogura, T., Kitagawa, T., *Biochim. Biophys. Acta Bioenerg.*, **2004**, 1655, 290-297, DOI: 10.1016/j.bbabio.2003.10.013

[87] Blair, D.F., Witt, S.N., Chan, S.I., *J. Am. Chem. Soc.*, **1985**, 107, 25, 7389–7399, DOI:10.1021/ja00311a029

[88] Yu, M.A., Egawa, T., Shinzawa-Itoh, K., Yoshikawa, S., Guallar, V. *et al.*, *J. Am. Chem. Soc.*, **2012**, 134, 10, 4753–4761, DOI: 10.1021/ja210535w

[89] Karpefors, M., Ädelroth, P., Namslauer, A., Zhen, Y., Brzezinski, P., *Biochemistry*, **2000**, 39, 47, 14664–14669, DOI: 10.1021/bi0013748

[90] Brändén, M., Sigurdson, H., Namslauer, A., Gennis, R.B., Ädelroth, P., Brzezinski, P., *PNAS USA*, **2001**, 98, 9, 5013-5018, DOI: 10.1073/pnas.081088398

[91] Gorbikova, E.A., Wikström, M., Verkhovsky, M.I., *J. Biol. Chem.*, **2008**, 283, 34907-34912 DOI: 10.1074/jbc.M803511200

[92] Ogura, T., Takahashi, S., Hirota, S., Shinzawa-Itoh, K., Yoshikawa, S. *et al.*, *J. Am. Chem. Soc.*, **1993**, 115, 19, 8527-8536, DOI: 10.1021/ja00072a002

[93] Blomberg, M.R.A., *Biochemistry*, **2016**, 55, 3, 489-500, DOI: 10.1021/acs.biochem.5b01205

[94] Ruitenberg, M., Kannt, A., Bamberg, E., Fendler, K., Michel, H., *Nature*, **2002**, 417, 99-102, DOI: 10.1038/417099a

[95] Shimada, A., Etoh, Y.,Kitoh-Fujisawa, R., Sasaki, A., Shinzawa-Itoh, K. *et al.*, *J. Biol. Chem.*, **2020**, 295, 17, 5818-5833, DOI: 10.1074/jbc.RA119.009596

designated as **Fe^{III}-OO-Cu^{II}_{B}** (*C*). A similar peroxo intermediate prior to the cleavage of the O-O bond had already been proposed by Kitawaga (1993)[96] and Yoshikawa (1998[97], 2010[98]). In the next step, the hydrogen-bonded water molecule mediates a proton transfer from **Tyr-OH** to the distal oxygen atom of the peroxo ligand, giving rise to the intermediate species (*D*). The **Cu^{II}_{B}** center is then reduced from **Tyr-O⁻** (*E*), followed by a two-electron reduction and a proton transfer which leads to the cleavage O-O bond and the formation of a **Fe^{IV}=O···HO-Cu^{II}_{B}, Tyr-O• ··· H_2O** state (**P** *state*), analogous to the **P_M** *state* in Scheme X. A successive PCET to the **P** intermediate yields directly the **F** *state* (**Fe^{IV}=O···HO- Cu^{II}_{B}, Tyr-OH ···H_2O**. In other words, the previously proposed **P_R** *state* is not detectable, which supports Wikström's doubts about whether the **Fe^{IV}=O/ Cu^{II}_{B}-OH, Tyr-O⁻** species (**P_R** *state*) is a true catalytic intermediate[99].In 2021, the same group proposed two alternative intermediates for the O_H and E catalytic *states*.[100]

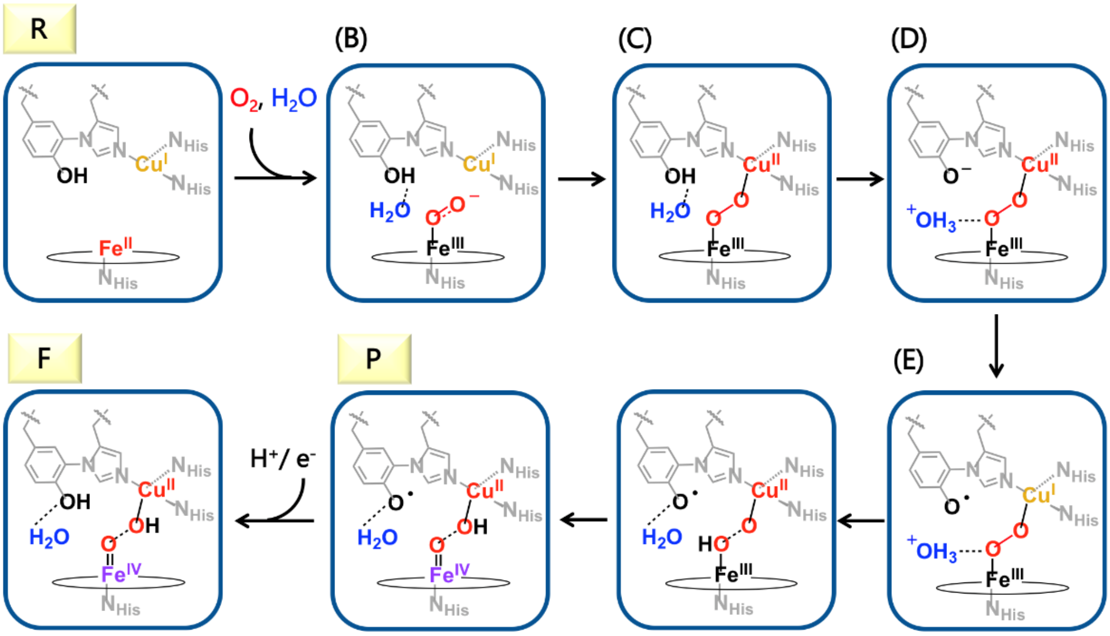

Scheme 1-7. Alternative O_2 activation and reduction steps involved in the transition from the R state to the F state.

Years of investigation into the enzymatic architectures and mechanisms of Cyt-P_{450} and HCOs have highlighted the necessity of a well-orchestrated first and second coordination sphere to gain control over the activation and reduction steps of O_2. The type of substitution on the porphine's macrocycle and the identity of the axial or/and proximal ligands have been found to modulate the redox properties and the spin state of the iron metal center both in the reduced and oxidized forms of the enzymes. In addition, redox-active metal centers, non-coordinated amino acid, and water residues in the binding pocket of the active site has been proven to hold a pivotal role as well in the ET, PT, or/and PCET steps involved in their catalytic cycle. Although these distal moieties do not bind to the metal center, they determine the

---

[96] Ogura, T., Takahashi, S., Hirota, S., Shinzawa-Itoh, K., Yoshikawa, S. *et al.*, *J. Am. Chem. Soc.*, **1993**, 115, 19, 8527–8536, DOI: 10.1021/ja00072a002

[97] Yoshikawa, S., Shinzawa-Itoh, K., Nakashima, R., Yaono, R., Yamashita, E. *et al.*, *Science*, **1998**, 280, 5370, 1723-1729, DOI: 10.1126/science.280.5370.1723

[98] Muramoto, M., Ohta, K., Shinzawa-Itoh, K., Kanda, K., Taniguchi, M. *et al.*, *PNAS USA*, **2010**, 107, 17, 7740-7745, DOI: 10.1073/pnas.0910410107

[99] Wikström M., *Biochim., Biophys. Acta Bioenerg.*, **2012**, 1817, 4, 468-475, DOI: 10.1016/j.bbabio.2011.10.010

[100] Shimada, A., Hara, F., Shinzawa-Itoh, K., Kanehisa, N., Yamashita, E. *et al.*, *J. Biol. Chem.*, **2021**, 297, 3, 100967, DOI: 10.1016/j.jbc.2021.100967

formation of key intermediates and their reactivity via long-range hydrogen-bonding and electrostatic interactions and, in a way, decide the fate of molecular O_2 within the cells.

In Cyt-P_{450}, for example, the electron-rich axial thiolate ligand of the iron center and the distal threonine work in synergy to yield high-valent Fe-oxo species which are indispensable for the oxygenation of (bio)molecules via the activation of their strong covalent bonds. On the other hand, in HCOs that realize the $4e^-/4H^+$ reduction of molecular O_2 to H_2O, the axial ligand of the heme is less basic (histidine), while the binding pocket considerably differs from that of Cyt-P_{450}. In particular, it contains a redox-active Cu center that stores and shuttles electrons and a tyrosine residue that serves as an electron and proton relay, with both of them being imperative for the enzyme's catalytic activity. The presence of water molecules has also been suggested to hold a key role in the activation of the O-O bond and subsequently its cleavage.

Indisputably, our understanding of how aerobic life leverages the high oxidizing power of molecular O_2 has tremendously advanced over the past decades; yet there are still many mechanistic aspects that remain to be unraveled, especially for HCOs. Shifting to less complicated synthetic models that adopt similar catalytic motifs could potentially add another facet to the role of the first and second sphere contributions in the enzymes that have not been yet well-considered. Parallelly, a bio-inspired approach might be a one way out when it comes to the design of efficient ORR molecular catalysts with a possible industrial interest, e.g., O_2-based fuel cells technologies. On that note, several synthetic compounds resembling the catalytic architectures in HCOs have been extensively investigated over the years. At the same time, considerable effort has been also put into the development of robust yet selective mononuclear iron porphyrins as simpler ORR electrocatalysts.

1.1.3 Bio-mimetic Models and Bio-Inspired ORR Electrocatalysts

When it comes to an HCOs bio-mimetic approach the aim is not to emulate exactly the enzymatic architectures, which is practically speaking impossible, but rather to gain insights into why Nature has chosen these precise catalytic motifs to realize the phenomenically simple, yet complicated selective reduction of molecular O_2 to H_2O. Hence, by understanding the structural and electronic dynamics that govern the ORR mechanisms, we can apply the obtained knowledge to design robust and efficient bio-inspired ORR (electro)catalysts.

Correlation between Molecular Design and Electrocatalytic Activity

1.1.3.1 Heme a_3/ Cu_B, Tyr_{244} Model Compounds

Recalling the catalytic site of HCOs, apart from the heme center, there are three additional and indispensable key players for the activation and reduction of molecular O_2 to H_2O: (i) an histidine residue axially ligated to the heme, (ii) a tris-histidyl Cu center, and (iii) a distal tyrosine amino acid covalently linked with one of the Cu histidines. Over the years, an intensive effort has been put into incorporating such structural motifs into the first and the second coordination spheres of iron porphyrins to resemble the binuclear catalytic site of HCOs and gain more insights into their role in ORR.

One of the first investigated synthetic models that imitate the heme a_3/ Cu_B dimetallic center of HCOs was reported in 1981 by Murray and co-workers.[101] In particular, they synthesized an iron porphyrin derivative appended with four pyridine moieties covalently linked to the phenyl groups of the macrocycle via amide bonds[102] and coordinated with a

---

[101] Gunter, M.J., Mander, L.N., Murray, K.S., *J. Chem. Soc., Chem. Commun.*, **1981**, 799-801, DOI:10.1039/C39810000799

[102] Buckingham, D.A., Gunter, M.J., Mander, L.N., *J. Am. Chem. Soc.*, **1978**, 100, 9, 2899-2901, DOI: 10.1021/ja00477a059

copper center (**Fe^{III}(P)/ Cu^{II}(N_4)**). Under ambient conditions and in the presence of an external base, O_2 reaction with the two-electron reduced bimetallic complex, **Fe^{II}P/ $Cu^{I}N_4$**, led to the final oxidized **(Fe^{III}P-OH/ $Cu^{II}N_4$)$^{+2}$** species, as shown in Fig. 1-7. Even though this model did not provide much information regarding the synergetic role of the Fe^{II} and Cu^{I} metal centers in the activation of molecular O_2, it touched off the design and study of several other HCOs bio-inspired systems.

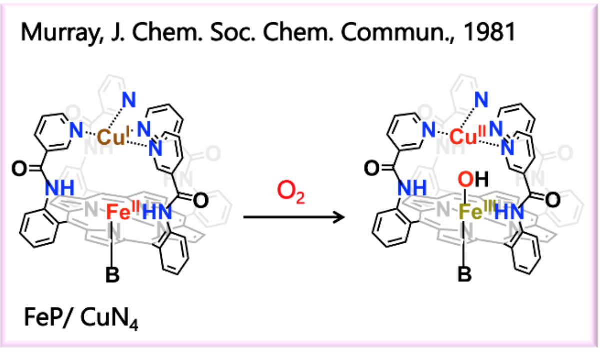

Fig. 1-7 Bio-mimetic heme a_3/ Cu model studied by Murray and co-workers in 1981 (B: base, Me_2SO or 1-methylimidazole).

Synthetically speaking, the design of such bio-mimetic complexes is mostly accomplished via: (i) the O_2-induced, or not, assembly between a **Fe^{II}** porphyrin and a pre-synthesized **Cu^{I}** complex, and (ii) the functionalization of the iron porphyrin macrocycle with proper pendant groups that can coordinate a copper atom on the distal plane. The first approach mostly aims to develop more flexible bio-inspired HCOs structures for investigating the chemistry between O_2 and the two metal centers. The second, on the other hand, targets mainly to electrocatalytic ORR studies accompanied by the detection and characterization of the involved intermediates.

The list of the documented bio-mimetic HCOs complexes in the literature is considerably long. Hence, only a couple of representative examples of each approach that highlight the importance of a well-orchestrated first and second coordination sphere on the activation and reduction of molecular O_2 will be provided below.

Iron Porphyrin/ Cu Assemblies

Since the early 90s, Karlin and co-workers have developed a series of non-covalently linked iron porphyrin/Cu derivatives to gain insights into the role of the distal Cu moiety and its second sphere contributions to the synergetic activation and reduction of molecular O_2 in HCOs. In their first studies, a tetradentate (**TMPA**) and a tridentate (**PY2**) ligands were chosen for the complexation of the Cu metal center, while the macrocycle framework was always kept the same (**FeF_8P**) (Fig. 1-8).[103], [104]

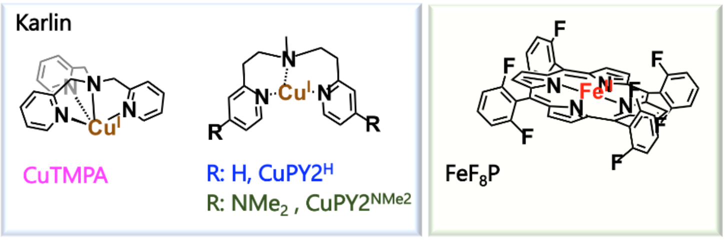

---

[103] Nanthakumar, A., Nasir, M.S., Karlin, K.D., Ravi, N., Hanh, H.B., *J. Am. Chem. Soc.*, **1992**, 114, 16, 6564–6566 DOI: 10.1021/ja00042a050

[104] del Río, D., Sarangi, R., Chufán, E.E., Karlin, K.D., Hedman, B. *et al.*, *J. Am. Chem. Soc.*, **2005**, 127, 34, 11969–11978, DOI: 10.1021/ja043374r

Fig. 1-8 Cu and Fe complexes synthesized and investigated by Karlin and co-workers (TMPA: :tris((2-pyridyl)methyl)amine), PY2: tris((2-pyridyl)methyl)amine)

O_2 reaction with an equimolar mixture of **Fe^{II}F$_8$P** with **Cu^{I}TMPA** at low temperatures gave rise to a transient **Fe^{III}F$_8$P-O$_2^{\bullet-}$** (~ 1 ms). The superoxide intermediate was rapidly reduced by the **Cu^{I}TMPA** complex to afford a **[Fe^{III}F$_8$P- (O$_2^{2-}$)- Cu^{II}TMPA]$^+$** species, for which, later studies suggested that the peroxo ligand coordinates to the two metal centers in a μ-η^2: η^1 manner. The **[Fe^{III}F$_8$P- (O$_2^{2-}$)- Cu^{II}TMPA]$^+$** intermediate was relatively stable, but it finally evolved to the corresponding oxidized μ-oxo binuclear dimer ($t_{1/2}$ ~ 17 min)· [105], [106] When similar studies were carried out using the **Cu^{I}PY2^{H}** complex the same O_2 activation and reduction steps were observed. However, the resulting bridged-peroxo intermediate was quite unstable even at low temperatures.[107] Functionalization of the pyridine groups with p-dimethylamino moieties (**Cu^{I}PY2^{Me2N}**) increased the stability of the **[Fe^{III}F$_8$P-(O$_2^{2-}$)- Cu^{II}PY2^{Me2N}]$^+$** species, whereby the coordination mode of the peroxide ligand was postulated to be μ-η^2: η^2 (Scheme 1-8).[108] According to these findings, it was concluded that O_2 binds preferably to the **Fe^{II}** instead of the **Cu^{I}** center and that the hydrolysis rate of the resulting bridged-peroxo intermediates depends on the O-O bond strength which is controlled by the coordination mode of O_2.

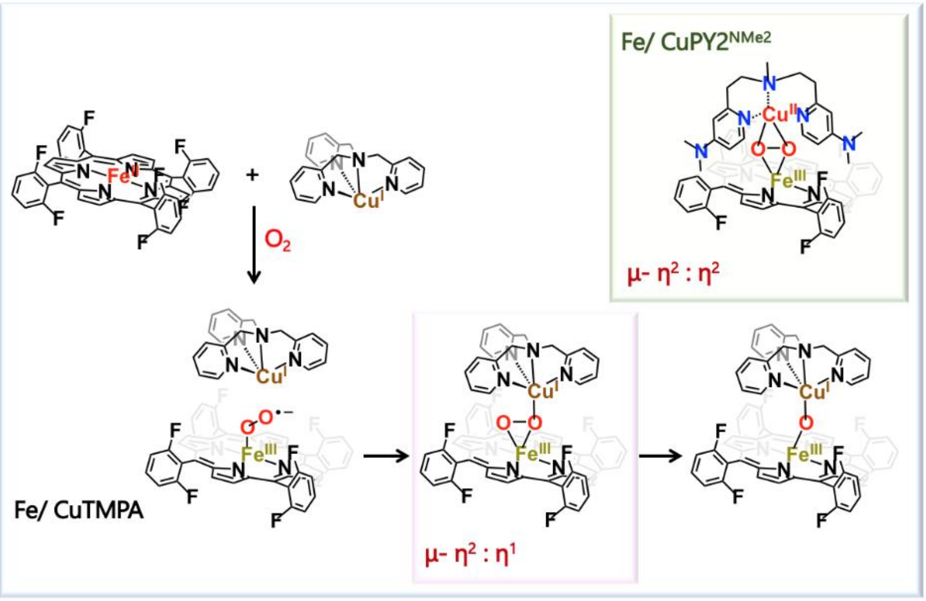

Scheme 1-8 O_2-bound species formed by the reaction of Fe^{II}F$_8$P with Cu^{I}TMPA and O_2. Boxes highlight the different coordination modes of the peroxo ligand between the two metal centers for the two studied Fe/CuTMPA and Fe/CuPY2^{NMe2} complexes.

Moving one step forward and wanting to investigate the second coordination sphere's contributions to the stabilization of the bridged-peroxo intermediates and the subsequent O-O cleavage, the **CuTMPA** complexes were functionalized with H-bonding groups or/and bulky substituents. It was shown that intramolecular H-bonding effects on the formed **[Fe^{III}F$_8$P- (O$_2^{2-}$)- Cu^{II}TMPA]$^+$** intermediates were strongly affected by the nature of the donor group. In particular, the incorporation of amine group(s) greatly enhanced the H-bonding contribution

---

[105] Nanthakumar, A., Fox, S., Murthy, N.N., Karlin, K.D., Ravi, N. *et al.*, *J. Am. Chem. Soc.*, **1993**, 115, 18, 8513–8514 DOI: 10.1021/ja00071a097

[106] Karlin, K.D., Nanthakumar, A., Fox, S., Murthy, N.N., Ravi, N. *et al.*, *J. Am. Chem. Soc.*, **1994**, 116, 11, 4753–4763, DOI: 10.1021/ja00090a023

[107] Kopf, M-A., Neuhold, Y-M., Zuberbühler, A.D., Karlin, K.D., *Inorg. Chem.*, **1999**, 38, 13, 3093–3102, DOI: 10.1021/ic981431

[108] Kim, E., Helton, M.E., Wasser, I.M., Karlin, K.D., Lu, S. *et al.*, *PNAS USA*, **2003**, 100, 7, 3623-3628, DOI:10.1073/pnas.0737180100

to the peroxo species, thus activating the O-O bond. However, this was not the case when amide derivatives were used instead, although they tend to form stronger hydrogen bonds than the amine groups. Herein, the presence of the bulky substituents prevented the H-bond formation with the corresponding bridged-peroxo intermediates due to steric repulsions (Fig. 1-9).[109]

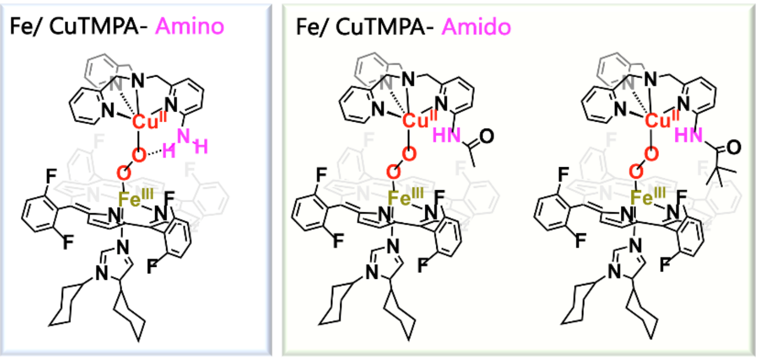

Fig. 1-9 Modified Fe/CuTMPA derivative with H-bonding groups by Karlin.

Later studies by Solomon[110] demonstrated that the spin state of the peroxo species is controlled by second sphere H-bonding interactions without the requirement for a strong axial base to the iron center (Scheme 1-9).

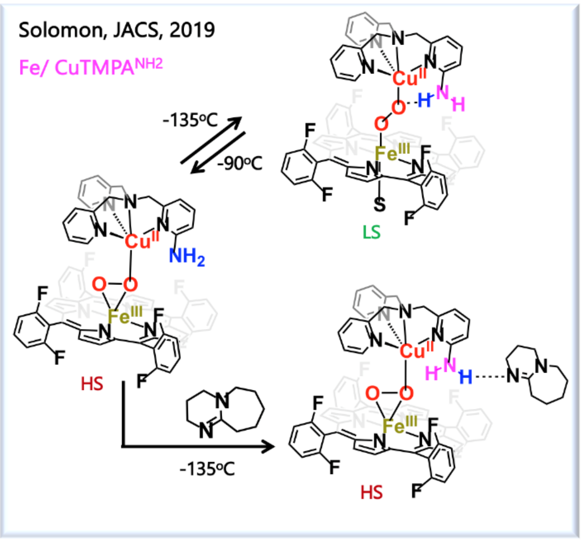

Scheme 1-9 Reversible thermally induced spin interconversion between a side-on and end-on peroxo Fe/Cu peroxo intermediate (S: solvent, MeTHF). Addition of an external base disrupts the H-bonding interaction with the intermediate and inhibits the SCO to take place.

As shown in Scheme 1-9, lowering the temperature from -90 °C to -135 °C resulted in the HS to LS state transition of the **$[Fe^{III}\text{-}(O_2^{2-})\text{-}Cu^{II}TMPA^{NH2}]^+$** which was described as $\mu\text{-}\eta^1\text{:}\ \eta^1$ intermediate with a relatively strong Fe^{III}-O and weakened O-O bonds. Moreover, the addition of an external base hindered the H-bond formation between the $-NH_2$ and the peroxo ligand, thus prevailing the thermal induced spin-crossover. As such, it was also shown that the

---

[109] Ehudin, M.A., Schaefer, A.W., Adam, S.M., Quist, D.A., Diaz, D.E. *et al.*, *Chem. Sci.*, **2019**, 10, 2893-2905 DOI: 10.1039/C8SC05165H

[110] Schaefer, W.A., Ehudin, M.A., Quist, D.A., Tang, J.A., Karlin, K.D., Solomon, E.I., *J. Am. Chem. Soc.*, **2019**, 141, 12, 4936-4951, DOI: 10.1021/jacs.9b00118

orientation of the H-bond donors with respect to the O_2 adducts is a crucial parameter that needs to be considered when investigating O-O bond activation.

On the other hand, recalling the proposed mechanism for *Cc*O, it has been suggested that water molecules trapped inside the catalytic pocket can facilitate the O-O bond cleavage in the Fe-O_2 adducts. Kano's group and their collaborators[111], in an effort to investigate such an O-O bond activation, synthesized a water-soluble supramolecular bis-cyclodextrin Fe/Cu complex (**Fe/Cu CD_2**), as shown in Fig. 1-10.

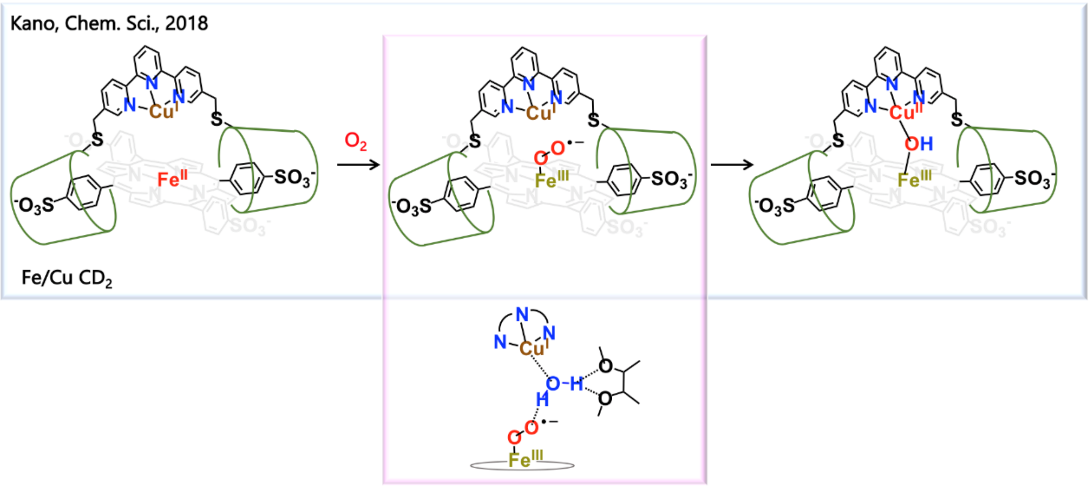

Fig. 1-10 O_2 reactivity studies on a water-soluble supermolecular Fe/Cu CD_2 model by Kano and co-workers.

O_2 binding to the reduced active state of the catalyst resulted in the formation of **Fe^{III}-$O_2^{\bullet-}$/Cu^I** adduct whose oxidation to the initial **Fe^{III}/Cu^{II}** species was pH dependent, with the faster rate being observed at less basic conditions. At neutral pH the **Fe^{III}-$O_2^{\bullet-}$/Cu^I** intermediate was converted to **Fe^{III}-OH-Cu^{II}** suggesting a proton-coupled O-O bond cleavage, mediated by a water molecule bound to the **Cu^I** distal center and hydrogen bonded between the cyclodextrin and the superoxide ligand. Electrochemical analysis of the O_2 activation and reduction showed that the **Cu^I** atom serves as an intramolecular electron donor to the **Fe^{III}-$O_2^{\bullet-}$/Cu^I** intermediate as in the case of *Cc*O.

While these studies did not aim to investigate the potential electrocatalytic ORR activity of the corresponding complexes, they pointed out the significance of H-bonding interactions and the implication of water molecules in the O-O bond activation.

Covalently Linked Iron Porphyrin/ Cu Complexes

In contrast to the assembly approach described above, the second established strategy to develop HCOs analogs concerns the proper modification of the porphyrin macrocycle with polydentate ligands or functional groups that serve as coordination points for the copper atom on the distal plane. On that note, several synthetic models have been reported in the literature mainly by the groups of Collman, Karlin, Boitrel, and Weiss over the last decades. The majority of these model compounds concerns properly functionalized arbor, picket fence, and capped iron porphyrins in which the iron center is most of the time axially ligated with an imidazolyl-like or a pyridine base, as a replica of the proximal histidine residue in *Cc*O and QO.

---

[111] Kitagishi, H., Shimoji, D., Ohta, T., Kamiya, R., Kudo, Y. *et al.*, *Chem. Sci.*, **2018**, 9, 1989–1995, DOI: 10.1039/c7sc04732k

As previously mentioned, Kano and co-workers showed that water molecules facilitate the O-O bond activation and its subsequent cleavage. Such an implication was also suggested by Naruta who investigated a binuclear Fe/Cu complex cross-linked with a phenol moiety (**$L^{OH}FeCu$**). However, in their case, oxygenation of a **$L^{OH}Fe^{II}/Cu^{I}$** solution at low temperatures yielded a **$L^{OH}Fe^{III}\text{-}(O_2)^{2-}\text{-}Cu^{II}$** species which unexpectedly evolved to a **$L^{OH}Fe^{III}\text{-}O_2^{\bullet-}Cu^{I}$** intermediate! Electrochemical characterization of the redox properties of **$L^{OH}FeCu$** under anaerobic conditions showed that the ferric center is harder to reduce compared to the Cu^{II} distal complex. As such, it was speculated that O_2 binds first to the Cu^{I} atom yielding a **$L^{OH}Fe^{III}Cu^{II}\text{-}\ O_2^{\bullet-}$** intermediate. Once the ferric center is singly reduced an intramolecular electron transfer from the Fe^{II} atom to the **$Cu^{II}\text{-}\ O_2^{\bullet-}$** distal complex takes place giving rise to the transient **$L^{OH}Fe^{III}\text{-}(O_2)^{2-}\text{-}Cu^{II}$** species. Now why the peroxo intermediate was converted to the corresponding **$L^{OH}Fe^{III}\text{-}O_2^{\bullet-}Cu^{I}$**, the authors proposed that both the axial imidazolyl base and a water molecule hydrogen bonded to the phenol group weaken the Cu-O bond, thus favoring the formation of **$L^{OH}Fe^{III}\text{-}O_2^{\bullet-}Cu^{I}$** (Scheme 1-10). [112]

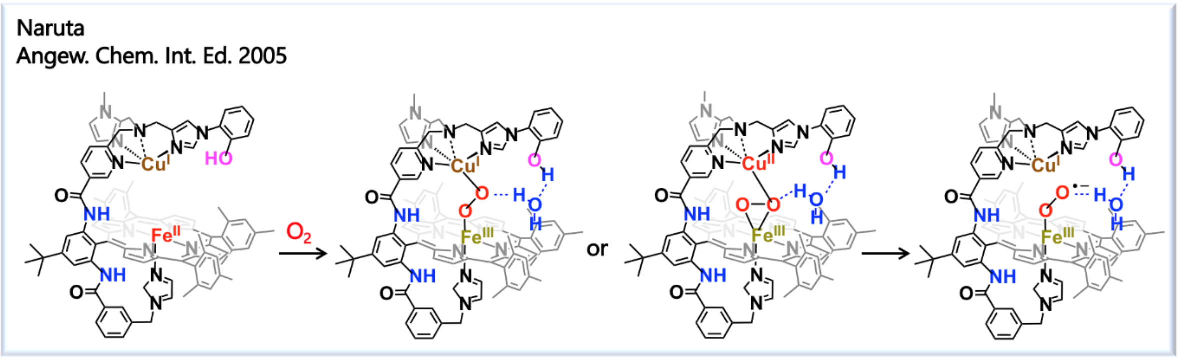

Scheme 1-10 O_2 reactivity studies by Naruta and co-workers for a heme a_3/ Cu_B, Tyr_{244} bio-mimetic model.

Although Naruta and co-workers did not examine the catalytic activity of their proposed model towards the reduction of molecular O_2, similar binuclear complexes have been investigated as potential ORR electrocatalysts by Collman, Boitrel, and Weiss, as shown in Fig. 1-11.

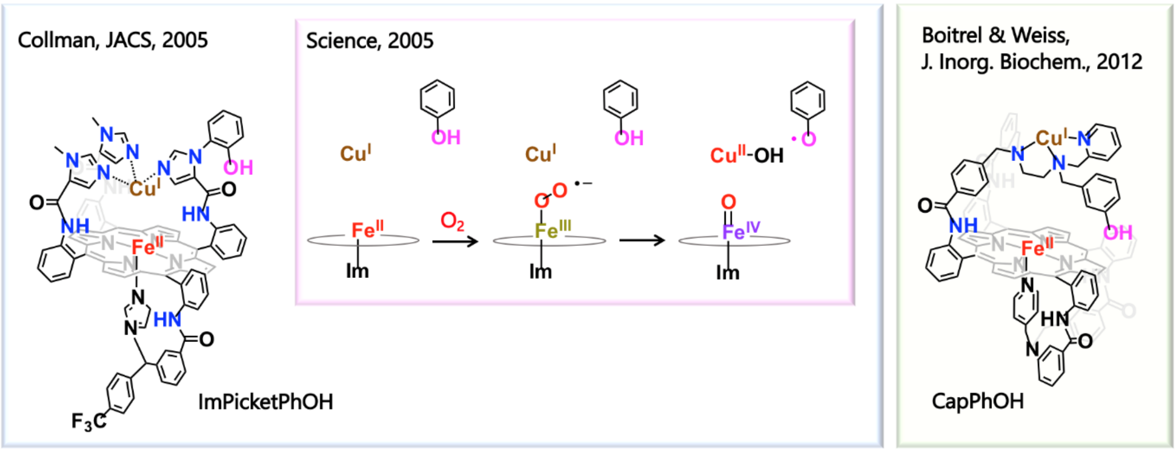

Fig. 1-11 Heme a_3/ Cu_B, Tyr_{244} bio-mimetic models developed by Collman and Boitrel/Weiss as ORR electrocatalysts.

---

[112] Liu, J-G., Naruta, Y., Tani, F., *Angew. Chem. Int. Ed.*, **2005**, 44, 12, 1836-1840, DOI: 10.1002/anie.200462582

According to the studies of Collman, O_2 reaction with the reduced state of **ImPicketPhOH** produced a **Fe^{III}-$O_2^{\bullet-}$$Cu^{I}$, PhOH** intermediate which upon increasing the temperature from -60 °C to -40 °C gradually evolved to **Fe^{IV}=O Cu^{I}-OH, $PhO^{\bullet}$** species (analogous to the P_M state in C*c*O) via an intramolecular three electron one proton transfer process. The two electrons were provided by the iron and copper centers, while the phOH moiety served both as a proton and electron donor for the activation of the O-O bond.[113] When **ImPicketPhOH** was grafted on the surface of an electrode at a distance that allowed a slow ET rate of 6.0 s^{-1}, similar to the one observed from cytochrome *c* to heme a_3/ Cu_B (4.0 s^{-1}), molecular O_2 was selectively reduced to H_2O, while only a 4% of H_2O_2 was detected. The authors suggested that its high selectivity was attributed to the ideal orientation and distance of the Cu and phOH moieties with the iron porphyrin that resembled well the corresponding ones in the catalytic site of C*c*O.[114]

On the contrary, when Boitrel and Weiss investigated **CapPhOH** under heterogeneous conditions, **CapPhOH** exhibited poor ORR activity and mostly realized the $2e^-/2H^+$ reduction of molecular O_2 to H_2O_2. A similar catalytic performance was also evaluated for the Cu-free derivative. A series of spectroscopic and electrochemical studies showed that the Cu atom was positioned far away from the iron center which strongly affected the O-O bond activation and its subsequent reduction.[115], [116]

However, the position of the Cu center is not the only parameter that decides the fate of molecular O_2, but also the relative first reduction potentials of the two assembled metal complexes which are controlled by their ligands environments. In the late 90s, Boitrel and Collman synthesized two arbor-like Fe porphyrins functionalized with tridentate (**TACN**) or tetradentate (**TBTren**) ligands units as coordination points to the copper center (Fig. 1-12).

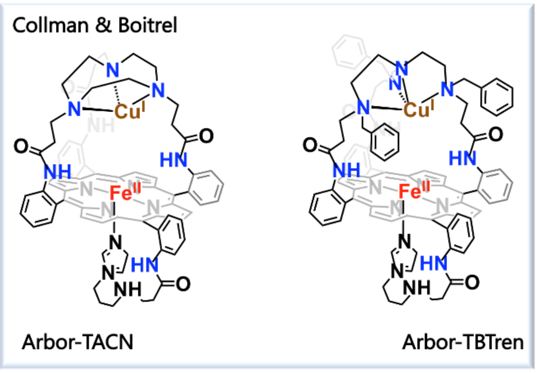

Fig. 1-12 Arbor-like Fe porphyrin -Cu derivatives investigated by Collman and Boitrel for ORR under heterogeneous conditions (TACN: 1,4,7 triazacyclononane, TBTren: N,N′,N′′-tribenzyltris(aminoethyl) amine).

Interestingly, electrocatalytic studies showed that only **Arbor-TBTren** could realize the complete reduction of molecular O_2 to H_2O. Electrochemical characterization of **Arbor-TBTren** under anaerobic conditions revealed that the Fe^{III} porphyrin was reduced prior to the distal Cu^{II}

---

[113] Collman, J.P., Decréau, R.A., Yan, Y., Yoon, J., Solomon, E.I., *J. Am. Chem. Soc.*, **2007**, 129, 5794-5795, DOI:10.1021/ja0690969

[114] Collman, J.P.,Devaraj, N.K., Decréau, R.A., Yang, Y., Yan, Y.-L. *et al.*, *Science*, **2007**, 315, 5818, 1565-1568, DOI: 10.1126/science.1135844

[115] Melin, F., Trivella, A., Lo, M., Ruzié, C., Hijazi, I. *et al.*, *J. Inorg. Biochem.*, **2012**, 108, 196-202, DOI: 10.1016/j.jinorgbio.2011.11.016

[116] Ruzié, C., Even-Hernandez, P., Boitrel, B., *Org. Lett.*, **2008**, 10, 13, 2673–2676, DOI: 10.1021/ol800731t

complex, while the opposite trend was observed for **Arbor-TACN**. [117], [118], [119] Hence, it was postulated that when the Fe^{III} center is reduced first, O_2 binds to the Fe^{II} center and it is further reduced to H_2O under catalytic conditions. On the contrary, for **Arbor-TACN** in which the reduction of the Cu^{II} complex is thermodynamically more favorable, O_2 is activated and reduced to H_2O_2 by Cu^{I}, presumably outside of the cavity.[120]

Recently, Weiss and co-workers provided a representative example of how subtle changes in the structural architecture of a binuclear Fe/Cu catalyst can affect its affinity for O_2 binding and its ORR performance. As shown in Fig. 1-13, two strapped iron porphyrins which mainly differ in (i) the basicity of the proximal ligand of the iron porphyrin, and (ii) the chain's length as well as the substitution of the pendant group as a potential third binding site for the Cu atom were synthesized.

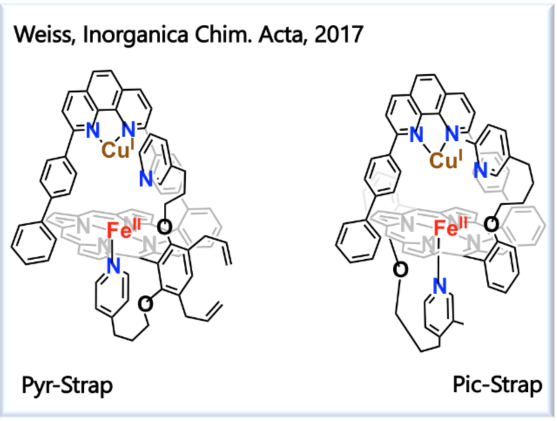

Fig. 1-13 Strapped Fe/ Cu complexes studied by Weiss *et. al*.

Both catalysts bound O_2 reversibly at room temperature; however, **Pic-Strap** with a more flexible distal pocket exhibited a higher affinity for O_2. The clarification of whether a **Fe^{III}-$(O_2)^{2-}$—Cu^{II}** species or a **Fe^{III}-$O_2^{\bullet}$—Cu^{I}** adduct was formed upon O_2 binding was not feasible for both catalysts. Yet, the authors suggested that the latter is a more likable scenario. The electrocatalytic performance of **Pyr-Strap** and **Pic-Strap** was evaluated heterogeneously in neutral aqueous solutions. **Pic-Strap** was a more selective catalyst compared to **Pyr-Strap** due to the stronger electron donation from the picolinyl base, and produced less H_2O_2 during ORR. However, this came with a detrimental cost on the overpotential of ORR. Hence, although **Pyr-Strap** was a poorer catalyst in terms of selectivity, it could activate and reduce O_2 at more positive potentials.[121]

Moving to less complicated catalytic architectures, Collman and co-workers synthesized two picket fence porphyrins with three pended imidazole ligands as the coordination point for the Cu atom. These models resemble the ones of Murray et. al. in 1981. In order to investigate also the influence of the Fe axial base in the electrocatalytic ORR, the binuclear complexes additionally bore an imidazolyl or a pyridine linked ligand, as shown in Fig. 1-14. Both catalysts exhibited high selectivity over the ORR in aqueous media (pH= 3.5-8.5), where the sole product of the reaction was H_2O. The different axial base did not affect the selectivity but it seemed to

---

[117] Collman, J. P., Fu, L., Herrmann, P.C., Zhang, X., *Science*, **1997**, 275, 949–951, DOI: 10.1126/science.275.5302.949

[118] Collman, J. P., Fu, L., Herrmann, P.C., Wang, Z., Rapta, M. *et al.*, *Angew. Chem. Int. Ed. Engl.*, **1998**, 37, 3397–3400, DOI: 10.1002/(SICI)1521-3773(19981231)37:24<3397::AID-ANIE3397>3.0.CO;2-N

[119] Collman, J. P., Schwenninger, R., Rapta, M., Bröring, M., Fu, L., *Chem. Commun.*, **1999**, 137–138, DOI: 10.1039/A807598K

[120] Collman, J. P., *Inorg. Chem.*, **1997**, 36, 5145–5155, DOI: 10.1021/ic971037w

[121] Vorburger, P., Lo, M., Choua, S., Bernard, M., Melin, F. *et al.*, *Inorganica Chim. Acta*, **2017**, 232-238, DOI: 10.1016/j.ica.2017.04.052

influence the overpotential of the reaction, with the imidazolyl derivative realizing the $4e^-$/ $4H^+$ reduction of O_2 at more positive potentials. [122]

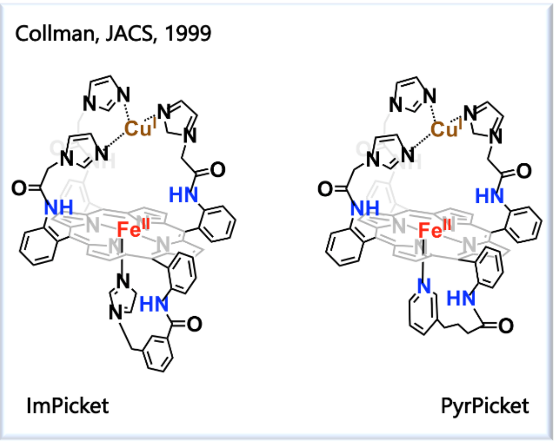

Fig. 1-14 Picket fence Fe/ Cu models investigated by Collman et. al. for ORR in a range of pH= 3.5-8.5 in aqueous media.

A couple of years later, Boitrel offered an alternative binuclear scaffold in which the porphyrin macrocycle was modified with quinolinyl groups, while the iron center was ligated either to an exogenous or endogenous base (Fig. 1-15). Unlike the previous studies by Collman *et al.*, both Fe/Cu derivatives were poor catalysts and reduced O_2 to H_2O_2 when physisorbed to the surface of an edge plane graphite (EPG) electrode at physiological pH. Surprisingly, the Cu-free analogs performed also the $4e^-$/ $4H^+$ reduction of O_2 to H_2O with the authors postulating that in the case of the Fe/Cu catalysts the Cu ion is released from the distal side of the iron porphyrin under electrocatalytic conditions and partially reduces O_2 to H_2O_2 in the solution. [123]

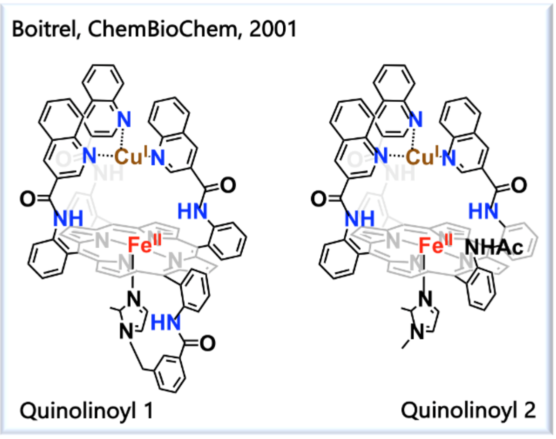

Fig. 1-15 Synthetic HCOs models by Boitrel et. al. used for electrocatalytic O_2 reaction at pH=7.

As previously mentioned Karlin in the 90s applied the O_2-induced assembly approach to elucidate the role of the Cu atom and chelation environment to the activation of O-O bond in the Fe-$(O_2)^{2-}$—Cu species. However, these complexes were quite unstable under electrocatalytic conditions, thus preventing their investigation as potential ORR electrocatalysts. Hence, Karlin

---

[122] Collman, J.P., Rapta, M., Bröring, M., Raptova, L., Schwenninger, R. *et al.*, *J. Am. Chem. Soc.*, **1999**, 121, 6, 1387–1388, DOI: 10.1021/ja983351a

[123] Ricard, D., Didier, A., L'Her, M., Boitrel, B., *ChemBioChem*, **2001**, 2, 2, 144-148, DOI: 10.1002/1439-7633(20010202)2:2<144::AID-CBIC144>3.0.CO;2-D

and co-workers established a different strategy which included the covalent attachment of the CuTMPA complex on the distal face of the FeF_8P, as shown in Scheme 1-11.

In 2011, Halime et al. evaluated the catalytic performance of **CapTMPA** under homogeneous conditions by using chemical reductants (Fc*) as the source of the electrons and trifluoroacetic acid (TFA) as the proton donor. Iodometric titrations of the resultant catalytic solution revealed no H_2O_2 reduction which along with the fact that $4e^-$ were required, viz. 4 eq. of Fc*, the authors concluded that **CapTMPA** reduced selectively O_2 to H_2O in a single-turnover.

The course of the catalytic reaction was followed by UV-Vis and other spectroscopies to detect and characterize the involved ORR intermediates. The obtained results proposed the following catalytic mechanism at room temperature (Scheme 1-11.).[124]

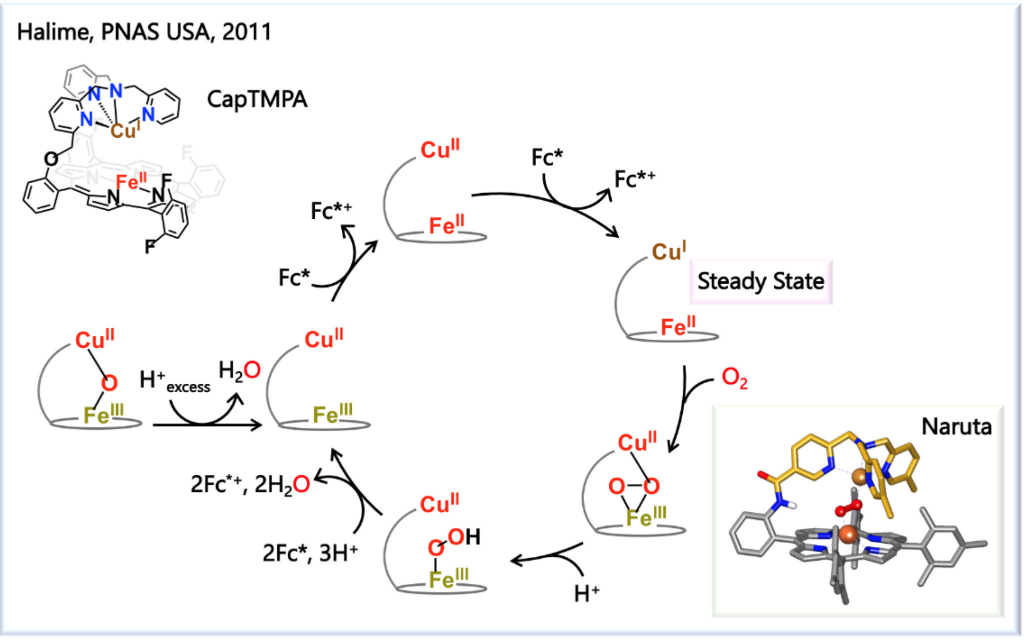

Scheme 1-11 Proposed mechanism for the ORR catalyzed by CapTMPA at room temperature in acetone under homogeneous conditions. Inset: X-ray structure of a peroxo Fe/Cu species reported by Naruta for a similar bio-mimetic complex. Data obtained from *www.ccdc.cam.ac.uk/structures* and redrawn using Chimera 1.16 software.

Starting from the **μ-oxo Fe^{III}/Cu^{II}** binuclear complex, protonation of the bridged oxygen atom leads to the release of an H_2O molecule, while the catalyst returns to its initial oxidized state. Two successive electron reductions of the metal centers generate the ascribed steady state **Fe^{II}/ Cu^I**, which reacts rapidly with O_2 to afford a **Fe^{III} μ-η^2 η^1- $O_2^{2-}$$Cu^{II}$** intermediate. The assignment of such side-on coordination fashion of the peroxo ligand was based on previous crystallographic data obtained by Naruta for a similar binuclear complex[125]. Once the peroxo species is formed, a subsequent proton transfer gives rise to the corresponding **Fe^{III}-OOH/ Cu^{II}** which is further protonated and reduced to yield two molecules of H_2O, while the catalyst returns to its fully oxidized state.

The ORR mechanism of the same binuclear catalyst, was examined also by Dey and co-workers in 2015 via Surface Enhanced Resonance Raman Spectroscopy (SERRS) coupled with

---

[124] Halime, Z., Kotani, H., Li, Y., Fukuzumi, S., Karlin, K.D., *PNAS USA*, **2011**, 108, 34, 13990-13994, DOI: 10.1073/pnas.1104698108

[125] Chishiro, T., Shimazaki, Y., Tani, F.,Tachi, Y., Naruta, Y. *et al.*, *Angew. Chem. Int. Ed.*, **2003**, 42, 2788 – 2791, DOI: 10.1002/anie.200351415

rotating disc voltammetry (RDV).[126] **CapTMPA** was physisorbed on an Edge Plane Pyrolytic graphite (EPG) electrode and its activity was evaluated in neutral aqueous conditions. Electrocatalytic studies indicated a $4e^-/4H^+$ reduction of molecular O_2, while only ~6% of H_2O_2 was detected. Based on the SERRS-RDE data, the authors suggested the below ORR steps at room temperature, in which the production of PROS was attributed to a possible coordination of O_2 in the proximal face of the iron porphyrin (Scheme 1-12).

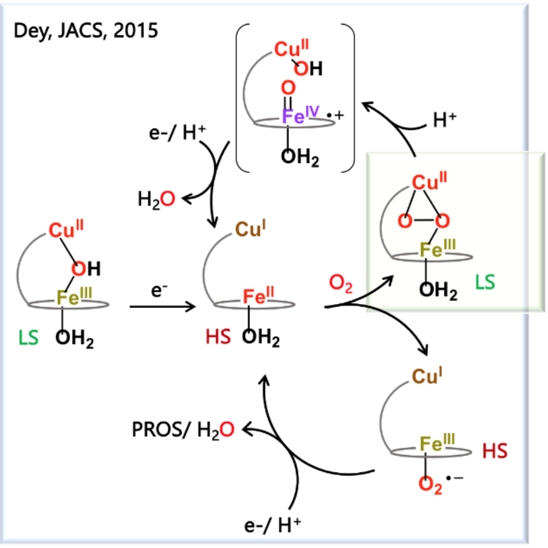

Scheme 1-12 Proposed mechanism for the ORR catalyzed by CapTMPA at room temperature in aqueous media (pH=7) under heterogeneous conditions during steady state.

In comparison with the previously reported mechanism by Halime *et al.*, ORR seems to proceed via different steady-state intermediates. However, in both organic and aqueous media, a peroxo intermediate was detected, for which two different coordination modes of the peroxo ligand were proposed.

It is evident that when it comes to efficient bio-mimetic ORR electrocatalysts, many different aspects concerning the first and second coordination spheres need to be considered carefully. Like in the case of HCOs, the identity of the axial ligand along with H-bonding interactions with the Fe-O_2 and peroxo intermediates hold a vital role in the stability of the superoxo species and the O-O bond activation and cleavage. Axial ligation on the iron center and H-bonds control the spin state of the iron porphyrin, which has been shown to affect the Fe-O and O-O bonds strength. These hydrogen bond interactions can be provided directly from appended H-donor groups or H_2O molecules trapped inside or near the binding O_2 pocket. However, for an efficient hydrogen bond formation, it is also essential for these distal residues to be well-oriented with respect to the O_2-bound species. On a similar note, the Cu center, which serves as an electron shuttler to the ORR intermediates, has to be also well-positioned inside the catalytic pocket. For example, in models where the Cu atom was positioned far away from the iron center, a considerable amount of H_2O_2 was produced. Moreover, we also need to remember that the Cu^I center can activate molecular O_2 and yield unstable Cu^{II}-$O_2^{\bullet-}$ species if its ligand environment is not appropriately functionalized. As such, free superoxide can be released and further disproportionate to H_2O_2 and O_2. At the same time, since both metal centers in their first reduced states can bind O_2, their first coordination sphere has to be designed as such, so the ferric center is thermodynamically

---

[126] Chatterjee, S., Sengupta, K., Hematian, S., Karlin, K.D., Dey, A., *J. Am. Chem. Soc.*, **2015**, 137, 40, 12897–12905, DOI: 10.1021/jacs.5b06513

more favorable to be reduced. However, as discussed above, less accurate HCOs models provided better ORR performance in terms of selectivity, thus pointing out that an iron porphyrin with a well-orchestrated second coordination sphere that does not include a second redox active metal center can equally realize the $4e^-/ 4H^+$ reduction of molecular O_2 to H_2O, as more elaborate bio-mimetic ORR electrocatalysts do.

1.3.1.2 Mononuclear Iron Porphyrin Compounds

Replicating the finesse of the catalytic center of HCOs in bio-mimetic systems is quite challenging. Yet, electrocatalytic ORR studies with binuclear Fe/Cu models have shown that even mononuclear iron porphyrins if designed tactfully can catalyze the selective $4e^-/4H^+$ reduction of molecular O_2 to H_2O. Indeed, years of investigation on bio-inspired iron porphyrins electrocatalysts have demonstrated that the incorporation of well-oriented pendant H-bonding groups, proton relays, redox-active groups, and non-Cu complexes, or even cationic moieties substantially improve their ORR performance.

The majority of such iron porphyrin complexes exhibit low solubility in water and are mostly soluble in organic media. Hence, their catalytic activity can be investigated both under heterogeneous and homogeneous conditions. In heterogeneous studies, the catalyst is physisorbed or covalently attached to the surface of an electrode, whereas in homogeneous ones, it is solubilized in a proper organic solvent. In both cases, the source of the electrons is the electrode, while the proton donor depends on the studied system, as will be discussed later. Before proceeding to the state-of-the-Art iron porphyrins as ORR electrocatalysts, it is helpful to introduce the ORR scheme for iron porphyrin that will help us to understand how a properly designed first and second coordination spheres can drastically enhance their catalytic activity.

As shown in Scheme 1-13, ORR catalyzed by iron porphyrin complexes involves multiple steps and quite resembles the proposed O_2 activation and reduction mechanism for Cyt-P_{450}.

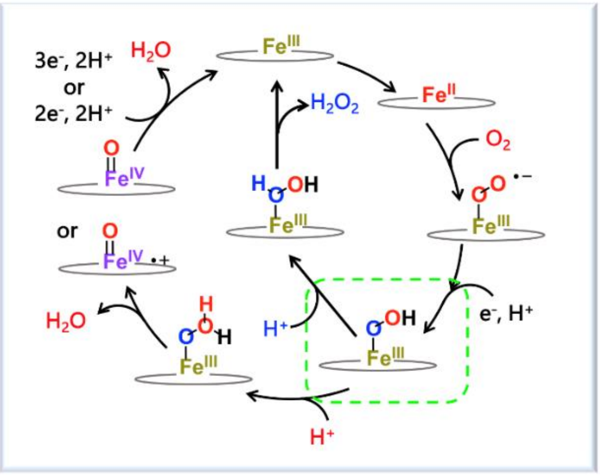

Scheme 1-13 Proposed ORR catalytic mechanism realized by iron porphyrin complexes.

Like in the case of natural enzymes and bio-mimetic HCOs models, the first step involves the one-electron reduction of the ferric porphyrin to the **Fe^{II}** oxidation state. O_2 binds to the ferrous center of the catalyst forming an **Fe-O_2** which is mostly designated as a **Fe^{III}-$O_2^{\bullet-}$**. Subsequent reduction and protonation of the superoxo species yields a hydroperoxo intermediate, **Fe^{III}-OOH**. The site of protonation of the **Fe^{III}-OOH** species has been shown to decide the fate of molecular O_2. As highlighted with different colors, the hydroperoxo ligand owns two different oxygen atoms, a proximal (**blue**) and a distal (**red**). The **Fe^{III}-OOH** can be further protonated on the proximal O atom or the distal one to yield H_2O_2 or H_2O upon O-O bond cleavage, respectively. In the next step, the high valent Fe-oxo species, **$(P^{\bullet+})Fe^{IV}=O$** or **$(P)Fe^{IV}=O$** are further reduced and protonated to release the second H_2O molecule, while the iron catalyst returns to its initial oxidized state, ready to start a new catalytic cycle. [127]

A series of spectroscopic studies under steady-state catalysis or single-turnover conditions have revealed that axial ligation effects and second coordination sphere H-bonding interactions can control the electron transfer and protonation steps, thus dictating whether a $2e^-/ 2H^+$ or $4e^-/ 4H^+$ pathway will be favored. For example, depending on the electron-donating strength of the axially coordinated ligand, different steps have been proposed after the formation of the **Fe^{III}-OOH** species, as summarized in Scheme 1-14.[128]

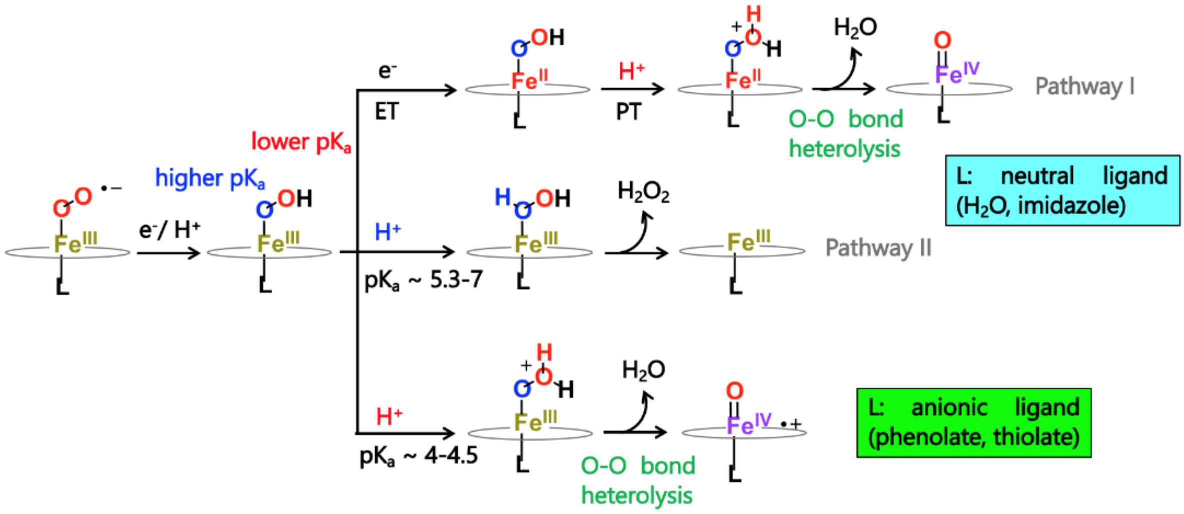

Scheme 1-14 Proposed electron and protonation steps on the Fe^{III}-OOH intermediate species and ORR products depending on the axial ligand of the iron porphyrin. ORR catalytic mechanism realized by iron porphyrin complexes.

For simple iron porphyrins bearing neutral axial ligands, two different pathways have been suggested under heterogeneous conditions (pH=7). In pathway I, the **Fe^{III}-OOH** species are initially reduced to their corresponding ferrous intermediates, thus increasing the basicity of the distal compared to the proximal oxygen atom; hence, the protonation of the distal oxygen is favored. In the next step, the scission of the O-O bond leads to the formation of **$(P)Fe^{IV}=O$** species which are further reduced and protonated to generate H_2O. On the other hand, in pathway II, when the electron transfer is rather limited, the proton transfer takes place in the proximal oxygen, since its pKa is lower than the distal O atom, resulting in the release of H_2O_2. Conversely, anionic axial ligands, due to the strong electron donation to the metal center, lower considerably the pKa of the O bound atom, and as such its protonation is very unlikely to occur at neutral pH. In that terms, the proton transfer to the **Fe^{III}-OOH** species is realized on the distal O and the resulting intermediate is converted upon O-O heterolytic cleavage to **$(P^{\bullet+})Fe^{IV}=O$** species that are subsequently reduced and protonated to yield H_2O.[129]

However, we should keep in mind that none of the aforementioned steps will take place if the initial **$Fe^{III}-O_2^{\bullet-}$** species are not stable enough. Although phenolate and thiolate axial ligands ensure the selective protonation of the distal O atom, they tend to destabilize the **Fe-**

---

[127] Brezny, A.C., Johnson, S.I., Raugei, S., Mayer, J.M., *J. Am. Chem. Soc.*, **2020**, 142, 4108−4113, DOI: 10.1021/jacs.9b13654
[128] Amanullah, Sk, Saha, P., Dey, A., *Chem. Commun.*, **2022**, 58, 5808–5828, DOI : 10.1039/d2cc00430e
[129] Amanullah, SK., Paramita, S., Dey, A., *Chem. Commun.*, **2022**, 58, 5808–5828, DOI: 10.1039/d2cc00430e

O_2. On the contrary, iron porphyrins bearing imidazolyl-like and H_2O ligands have a higher binding affinity for O_2 binding. The question that arises at this point is: how can a high affinity for O_2 binding and selectivity over the $4e^-/4H^+$ reduction of molecular O_2 to H_2O be accomplished? The answer lies in the proper modification of the second coordination sphere and some representative paradigms of such contributions in the stability of O_2 bound species and the rate and selectivity of ORR are provided below.

The first example highlighting the importance of well positioned H-bonding distal groups on the stabilization of Fe-O_2 adducts was provided by Collman in 1974 who solved the X-ray structure of a Fe-oxy picket fence porphyrin.[32] Ever since, several other iron porphyrin complexes have been functionalized with similar moieties and their Fe-O_2 species have been characterized via a variety of spectroscopic techniques, including NMR spectroscopy.[130]

Among the studied Fe-oxy species so far, the one that outstands in terms of stability was provided in 2003 by Naruta, who synthesized a "twin-coronet" iron porphyrin tethered with imidazole (**TC-FeP-Im**) or pyridine axial ligands (**TC-FeP-Pyr**), as shown in Fig. 1-16, below. The porphyrin macrocycle was functionalized with bulky and hydrophobic binaphthyl-bridged ligands that bore hydroxyl groups as H-bond donors to the **Fe^{III}-$O_2^{\bullet-}$** intermediates. In the Fe^{II} reduced state, O_2 bound rapidly and the resulting Fe-oxy species for both **TC-FeP** derivatives were extremely stable and exhibited a half-time of several days at room temperature![131] When the axial ligand was substituted by thiolate derivatives the stability substantially decreased and the **Fe^{III}-$O_2^{\bullet-}$** species were stable for a couple of hours and only at low temperature.[132]

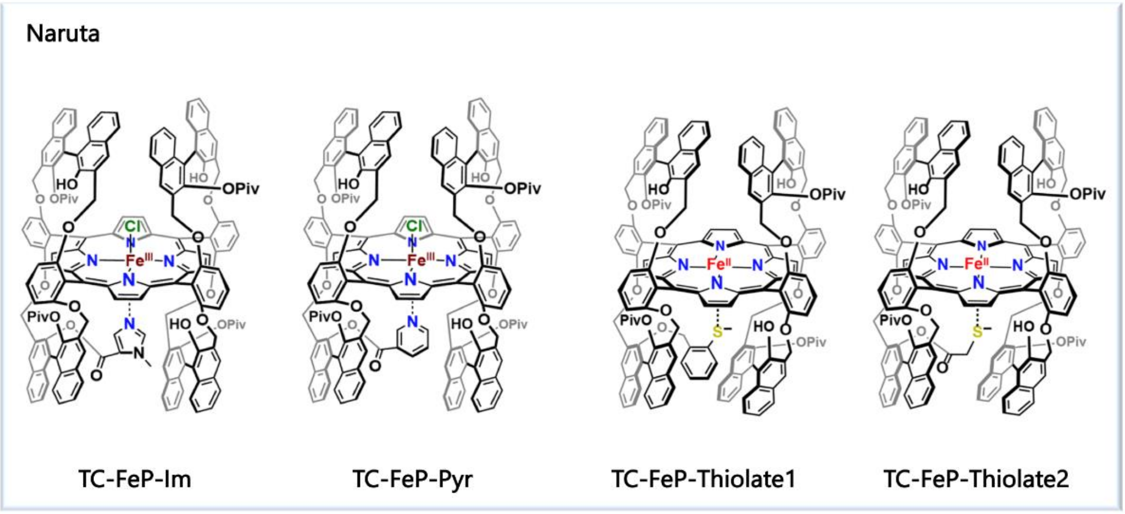

Fig. 1.16 "Twin-coronet" iron porphyrin derivatives synthesized by Naruta.

Moving on with a different porphyrin scaffold, in 2016, Naruta investigated an iron hangman porphyrin containing a carboxylic acid group on the distal plane and an imidazolyl axial ligand (**HGM-FeP-Im**) (Scheme 1-15). Reaction of **HGM-Fe^{II}P-Im** with molecular O_2 at cryogenic temperatures resulted in the formation of a superoxo intermediate which was stabilized via H-bonding with the distal carboxylic acid as shown in Scheme 1-15. Chemical reduction of **Fe^{III}-$O_2^{\bullet-}$** with cobaltocene ($CoCp_2$) yielded a **Fe^{III}-OOH** species in which the distal oxygen atom was found hydrogen-bonded to the acid residue. However, what is interesting

---

[130] Wuenschell, G.E., Tetreau, C., Lavalette, D., Reed, C.A., *J. Am. Chem. Soc.*, **1992**, 114, 9, 3346–3355, DOI: 10.1021/ja00035a028

[131] Tani, F., Matsura, M., Ariyama, K., Setoyama, T., Shimada, T. *et al.*, *Chem. Eur. J.*, **2003**, 9, 862−870, DOI: 10.1002/chem.200390096.

[132] Tani, F., Matsura, M., Nakayama, S., Ichimura, M., Nakamura, N. *et al.*, *J. Am. Chem. Soc.*, **2001**, 123, 1133−1142, DOI: 10.1021/ja003430y

about this study is that the same hydroperoxo species were also obtained in the absence of an electron and proton donor. The authors suggested that such an unexpected PCET process could be only rationalized if **HGM-Fe^{II}P-Im** was still present in the oxygenated solution. To verify this hypothesis, they realized a series of spectroscopic studies and theoretical calculations. According to their findings, it was proposed that unreacted **HGM-Fe^{II}P-Im** reduced the **Fe^{III}-O$_2$$^{\bullet-}$** intermediate and this electron transfer was coupled with a proton transfer from the carboxylic group of **HGM-Fe^{II}P-Im** to the bound O_2 species.[133]

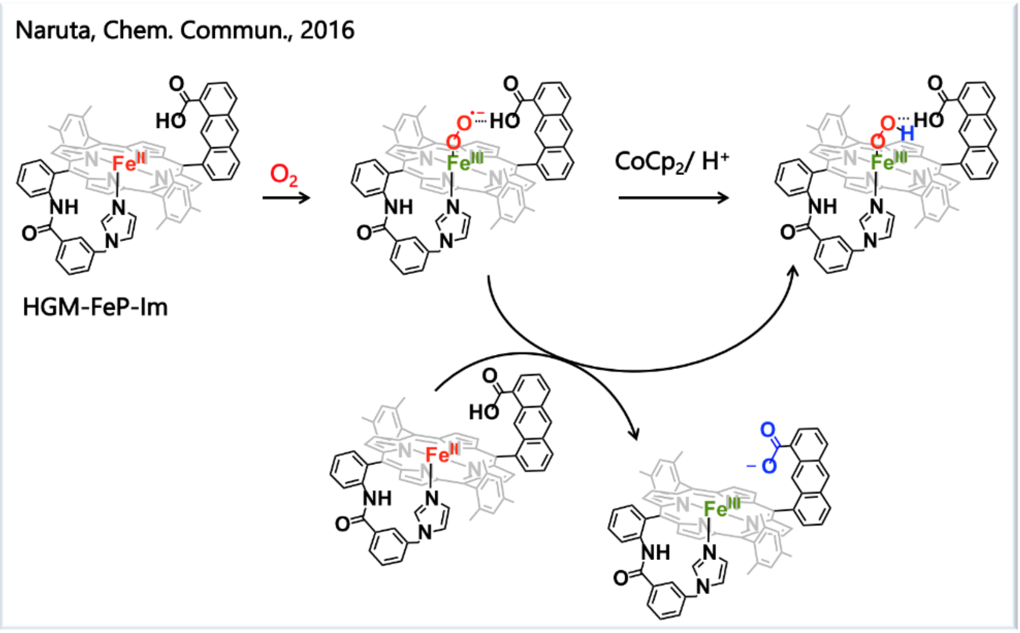

Scheme 1-15 Proposed O_2 reaction with a carboxyl-hangman porphyrin to yield a putative Fe^{III}-OOH intermediate hydrogen bonded to the distal carboxylic acid.

Another example of distal H-bonding contributions from carboxyl groups was reported by Mayer and co-workers a couple of years before (Fig. 1-17). However, their studies mostly focused on electrocatalytic ORR studies and not on the characterization of the intermediates. As shown in Fig. 1-17, two symmetric iron porphyrins were synthesized in which the phenyl groups were 2-or 4-substituted with carboxylic acids, **2-COOH-FeP,** and **4-COOH-FeP**, respectively.

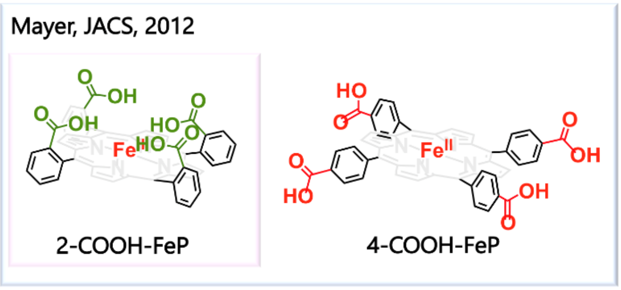

Fig. 1-17 Carboxy-Iron porphyrins synthesized and investigated by Mayer and co-workers as ORR electrocatalysts.

Their electrocatalytic activity was examined under homogeneous conditions in solution using [DMF-H$^+$](OTf$^-$) as a proton source. Both complexes catalyzed the reduction of molecular O_2 to H_2O, with **2-COOH-FeP** exhibiting higher selectivity. Bulk electrolysis

---

[133] Nagaraju, P., Ohta, T., Liu, J.-G.,Ogura, T., Naruta, Y., *Chem. Commun.*, **2016**, 52, 7213-7216, DOI : 10.1039/c6cc02162j

experiments and stability studies showed that the pendant carboxylic groups in **2-COOH-FeP** served as intramolecular proton relays to the distal O atom in the O_2 bound iron porphyrin intermediates, thus favoring the $4e^-/4H^+$ pathway to H_2O under the established experimental conditions. On the contrary, the carboxylic groups in **4-COOH-FeP** catalyst were positioned far away from the catalytic center and had zero control over the proximal *vs.* distal oxygen atom protonation.[134]

On a similar note, Mayer's group evaluated the electrocatalytic activity of two additional iron porphyrin salts as shown in Fig. 1-18. In acidic aqueous solutions, the pyridine groups were protonated, thus rendering the catalysts water-soluble.

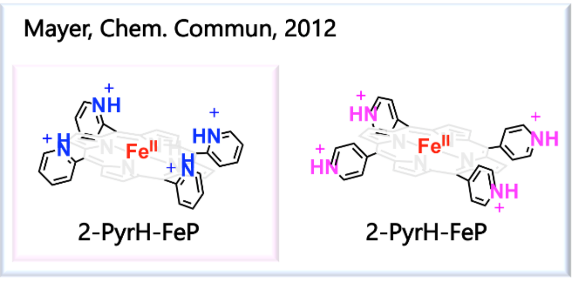

Fig. 1-18 Pyridine-Iron porphyrins synthesized and investigated by Mayer and co-workers as ORR electrocatalysts.

Both catalysts reduced O_2 to H_2O, with **2-PyrH-FeP** being more selective than **4-PyrH-FeP**. In particular, when the chloride salt of **2-PyrH-FeP** was investigated (**2-PyrH-FeP-Cl**), no H_2O_2 was detected, while the corresponding salt of **4-PyrH-FeP** generated ~ 15% of PROS. However, in the case of **2-PyrH-FeP-OTf**, the selectivity over H_2O decreased from 100% to 95%, whereas for **4-PyrH-FeP-OTf** it was slightly increased to 89%. In contrast to the **2-COOH-FeP** catalyst, the pyridyl groups of **2-PyrH-FeP** did not shuttle protons directly to the ORR catalytic species. Computational studies for a **Fe-O_2** intermediate suggested that for each protonated pyridine group a water molecule might be hydrogen bonded to the distal O atom and the proton of PyrH; hence, mediating the proton delivery.[135]

H_2O-mediated enhancement on the selectivity of ORR towards H_2O was also demonstrated by Collman and co-workers who developed two properly functionalized iron picket fence porphyrins, as shown in Fig. 1-19. In parallel studies, they also examined the catalytic activity of the non-modified FeTPP as a reference to investigate the effect of such pendant moieties on the product's selectivity. The electrocatalytic studies were realized heterogeneously at physiological pH and the catalysts were grafted on the surface of an azide-functionalized electrode via a click reaction between its $-N_3$ group and the alkyne of the axial imidazole ligand of the iron porphyrin. Electrocatalytic studies revealed that **PCF-Im** bound O_2 slower than **PCF-tBut** and parent **FeTPP**; however, it produced less amount of PROS. Infrared spectroscopy studies and titrations with H_2O showed that in the case of **PCF-Im**, a tight hydrogen-bond network of water molecules was formed between the three pendant triazole groups. Hence, the authors rationalized the higher selectivity of **PCF-Im**, although with a slow rate of O_2

---

[134] Carver, C.T., Matson, B.D., Mayer, J.M., *J. Am. Chem. Soc.*, **2012**, 134, 12, 5444–5447, DOI: 10.1021/ja211987f

[135] Matson, B.D., Carver, C.T., Von Ruden, A., Yang, J.Y., Raugei, S., Mayer, J.M., *Chem. Commun.*, **2012**, 48, 11100–11102, DOI: 10.1039/C2CC35576K

binding, to the presence of water molecules that stabilized the **Fe^{III}-OOH** adduct and served as a shield preventing their hydrolysis to produce H_2O_2.[136]

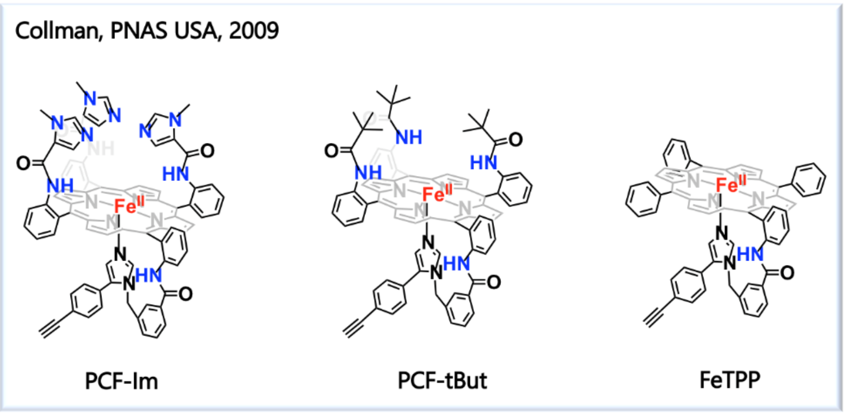

Fig. 1-19 Picket fence iron porphyrins synthesized and investigated by Collman and co-workers.

Quite recently, such an H_2O-directed protonation of the distal O atom was also demonstrated by Dey and co-workers. Their model concerned an iron porphyrin bearing two phenanthroline units, as shown in Scheme 1-16. Heterogeneous electrocatalytic studies in aqueous media (pH= 4-11) revealed that **Fe-bisPhen** exhibited more than 95% selectivity towards O_2 reduction to H_2O; however, a strong dependence of the catalytic rate on the pH of the solution was observed. In particular, compared to neutral aqueous media, the rate of ORR at higher pH was increased almost two orders of magnitude, while at lower pH it was enhanced by approximately 50 times. Based on X-ray crystallographic studies on its Zn analog and spectroscopic data obtained for **Fe-bisPhen** under catalytic conditions, the authors suggested that at pH<4, the phenanthroline units are protonated and stabilize directly the **Fe^{III}-OOH** species through hydrogen bonds. On the contrary, at neutral and basic conditions, a water molecule is locked by one of the phenanthroline groups and forms a hydrogen bond with the **Fe^{III}-OOH** intermediate, as shown in Fig. 1-16. In all ranges of pHs, the hydrogen-bonded oxygen atom is the distal one, however the activation of the O-O bond is governed by either only a "pull effect" from the distal protonated phenanthroline functions (low pH) or a "push-pull machinery" both from the axial ligand of the iron porphyrin and the water molecules (high pH). The latter considerably increased the pka of the distal oxygen atom in the putative **Fe^{III}-OOH** species, thus accelerating the O-O bond cleavage.[137]

---

[136] Collman, J.P., Decréau, R.A., Lin, H., Hosseini, A., Yang, Y., Dey, A., Eberspacher, T.A., *PNAS USA*, **2009**, 106, 18, DOI: 10.1073pnas.0902285106

[137] Mukherjee, S., Nayek, A., Bhunia, S., Ghosh Dey, S., Dey, A., *Inorg. Chem.*, **2020**, 59, 19, 14564–14576, DOI: 10.1021/acs.inorgchem.0c02408

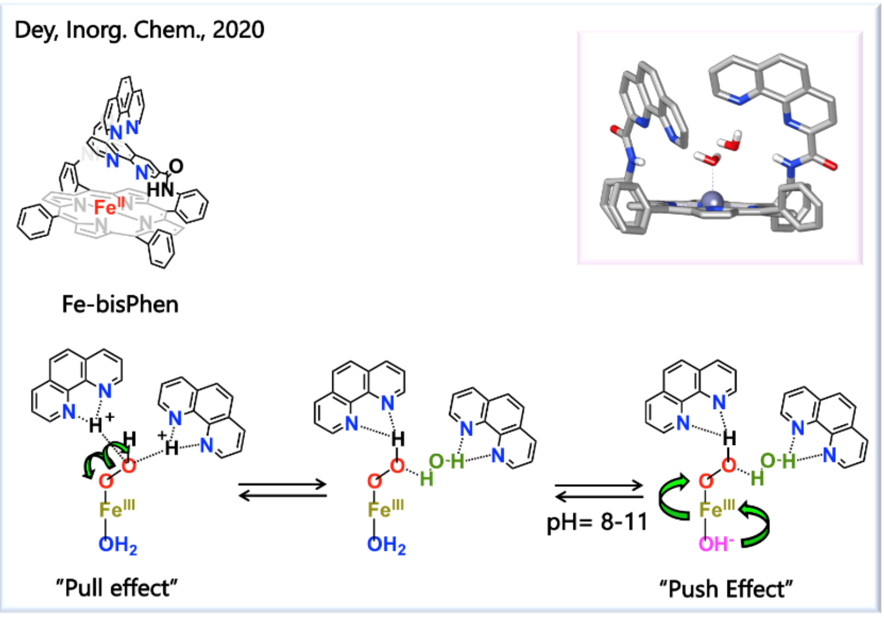

Scheme 1-16 Fe-bisPhen iron porphyrin investigated by Dey and the proposed push-pull effect that leads to the O-O activation.

Similarly, in an effort to elucidate how subtle changes in the second coordination sphere can influence the O-O bond activation, Dey's group, synthesized a series of iron picket fence porphyrins tethered with triazoles units bearing different substituents (Fig. 1-20). Previous X-ray crystallographic studies concerning a zinc analog of a similar complex revealed that a MeOH molecule bound to the metal center was stabilized via hydrogen bond interactions with a distal H_2O molecule trapped in between the triazole units. FTIR spectroscopic data of the iron porphyrin derivatives shown herein also confirmed this hydrogen-bond formation but this time with the O_2 bound species.

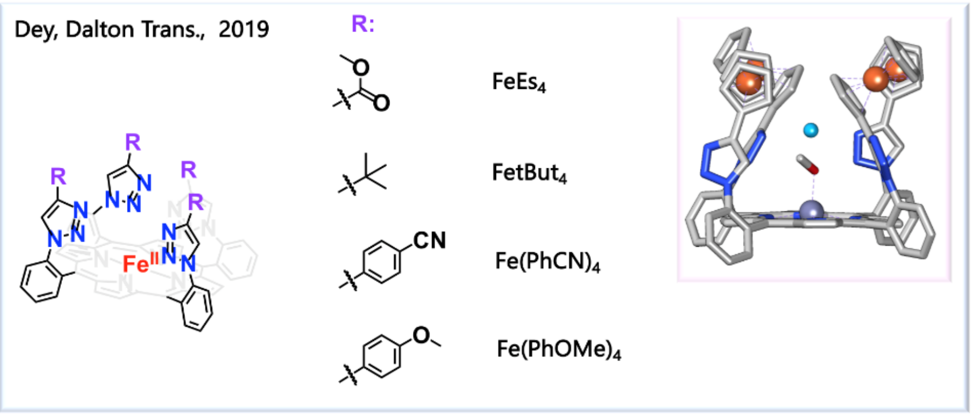

Fig. 1-20 Picket fence porphyrins investigated by Dey bearing electron-donating and electron-withdrawing groups.

According to O_2 reactivity studies, it was demonstrated that the type of substitution on the triazole rings strongly affected the stabilization of the **$Fe\text{-}O_2^{\bullet-}$** species by the water molecules. For example, in the Fe-O_2 adducts of **FetBut$_4$** and **Fe(PhOMe)$_4$** which bore electron-donating groups, the interaction with a water molecule was less strong, thus resulting in a weaker Fe-O bond. On the contrary, the opposite trend was observed for the picket fence porphyrins,

Fe(PhCN)₄ and **FeEs₄**, functionalized with electron-withdrawing groups in which the O-O bond strength was considerably lower. [138]

On the same note, Dey and co-workers examined also how the rate of electron transfer can influence the ORR performance of a catalyst. To do so, three iron porphyrin derivatives functionalized with distal basic residues were studied under heterogeneous and homogeneous conditions at different electrodes (Fig. 1-21). The chosen electrodes differ on their electron transfer (ET) rate to the catalyst, with EPG exhibiting the highest (~ 10^5 s^{-1}), while electrodes modified with self-assembled monolayers of thiols bearing short or long alkyl chains, SAM-HS-C_8, and SAM-HS-C_{16} displaying the lowest (~ 10^3 s^{-1} and ~ 6 s^{-1}). It is worth noting that the electron flux from SAM-HS-C_{16} is quite similar to the one observed in C*c*O from cytochrome *c* to the heme a_3/ Cu_B dinuclear catalytic site.

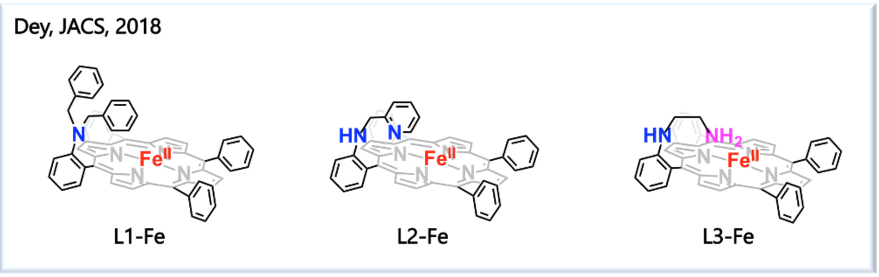

Fig. 1-21 Iron porphyrins tethered with pendant basic groups

When **L1-Fe**, **L2-Fe**, and **L3-Fe** were physisorbed on the surface of EPG they realized the $4e^-/4H^+$ reduction of molecular O_2 to H_2O, with a selectivity of >98 %. On the other hand, when **L2-Fe** and **L3-Fe** were studied using SAM-HS-C_8 and SAM-HS-C_{16}, the selectivity slightly decreased to ~ 95%. Interestingly, only the performance of **L1-Fe** was affected when electrodes with a slow ET rate were employed (SAM-HS) and **L1-Fe** produced 10% of PROS. This trend was attributed to the fact that at neutral pH the distal residues of **L2-Fe** and **L3-Fe** are protonated and as such the **Fe^{III}-$O_2^{\bullet-}$** and **Fe^{III}-OOH** intermediates were stabilized via H-bonding interactions independently of how fast the electrons are shuttled from the electrode. On the contrary, **L1-Fe** was not able to provide any of such H-bonding stabilization of the ORR intermediates and at slow ET rates, the O_2 bound species hydrolyzed before their further protonation proceeded. Similar behavior was also observed under homogeneous investigation, while DFT calculations highlighted the importance of the "pull effect" in the Fe^{III}-OOH intermediates species from the protonated residues in **L2-Fe** and **L3-Fe** electrocatalysts in which they elongated the O-O bond and thus enhancing the strength of the Fe-O bond. Hence, in **L2-Fe** and **L3-Fe** the O-O bond activation was more profound.[139]

In a more recent publication from the same group, the effect of the ET rate on the PROS production was also demonstrated; yet this time, the iron porphyrins were tethered with redox-active groups, as shown in Fig. 1-22.

---

[138] Singha, A., Mittra, K., Dey, A., *Dalton Trans.*, **2019**, 48, 7179–7186, DOI: 10.1039/c8dt03852j

[139] Bhunia, S., Rana, A., Roy, P., Martin, D.J., Pegis, M.L. *et al.*, *J. Am. Chem. Soc.*, **2018**, 140, 9444−9457 DOI: 10.1021/jacs.8b02983

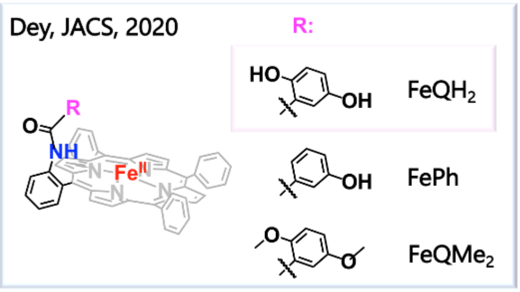

Fig. 1-22 Iron porphyrins modified with redox active groups.

Reactivity studies with O_2 revealed that in the case of **FeQH$_2$** the formed **Fe^{III}-O$_2^{\bullet-}$** species abstracted a proton from the distal hydroxyquinone to form a **Fe^{III}-OOH** intermediate followed by a second hydrogen atom transfer (HAT) to yield **Fe^{IV}=O** and an oxidized hydroxyquinone (**Scheme 1-17**). The high-valent metal oxo species gradually evolved to **Fe^{III}-OH**, as shown in **Scheme 1-17** Moving forwards with their studies, the electrocatalytic activity of the synthesized iron porphyrin complexes was also examined. Heterogeneous studies were initially conducted at pH=7 using EPG as the electrode (high ET rate) in which all of the synthesized catalysts selectively reduced O_2 to H_2O (>96%). When electrodes with slower ET rates were employed instead, the amount of PROS (~3%) produced by **FeQH$_2$** and **FePh** did not change compared to the EPG studies; however, this was not the case for the **FeQMe$_2$** catalyst whose selectivity dropped from ~98% to 94%. According to these findings, the authors suggested that when the reducing power from the quinol groups and the stabilization from the pending -OH units is missing, *viz.*, **FeQMe$_2$**, at slow ET from the electrode the **Fe^{III}-OOH** species hydrolyze to yield H_2O_2. On the contrary, for **FeQH$_2$** and **FePh** that bore two and one redox active groups, respectively, the slow flux from the electrode was compensated by the fast electron transfer from the quinol moieties. The proposed ORR mechanisms for these catalysts are summarized in Scheme 1-17. [140]

---

[140] Singha, A., Mondal, A., Nayek, A., Ghosh Dey, S., Dey, A., *J. Am. Chem. Soc.*, **2020**, 142, 21810−21828, DOI: 10.1021/jacs.0c10385

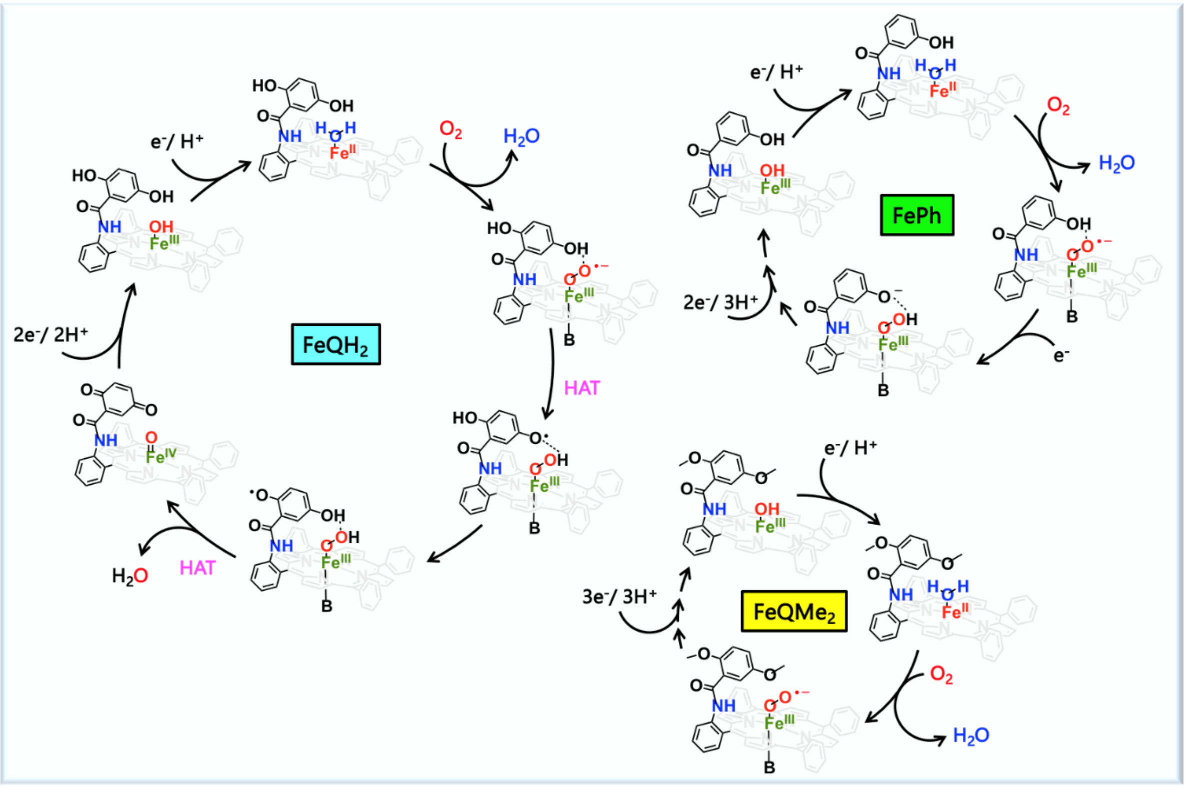

Scheme 1-17 Proposed ORR mechanism catalyzed by $FeQH_2$, FePh, and $FeQMe_2$; B: H_2O in aqueous media or MeOH in organic media.

1.2 Objectives and Scope

It is fascinating how almost effortlessly aerobic life activates and reduces molecular O_2 to realize diverse chemical transformations within the cells and translate the free energy released from the exergonic ORR into a proton motive force to drive cellular respiration. Although some pieces of the cellular O_2 biochemistry puzzle are still missing, our understanding of the enzymatic ORR fundamentals has been indisputably enhanced over the years.

The catalytic site of cytochrome *c* oxidase (C*c*O) contains a binuclear heme a_3-Cu_B with a distal tyrosine residue that catalyzes the complete reduction of molecular O_2 to H_2O under ambient conditions. Over the years, synthetic chemists have tried to incorporate similar structural motifs into less complicated bio-mimetic models to gain better insights into the synergistic role of these three functional units and develop ORR electrocatalysts with a potential industrial interest. While only a few bio-mimics are considered true structural and functional replicas of the heme a_3-Cu_B, TyrOH site, less elaborate C*c*O models and mononuclear iron porphyrins can equally perform the selective ORR to H_2O with a minimum or even zero production of PROS.

Mononuclear iron porphyrins can perform the seemingly simple yet challenging $4e^-$ $/4H^+$reduction of O_2 to H_2O, especially when its second coordination sphere is designed tactfully. Such a molecular functionalization mainly involves well-oriented pendant: (i) proton relays and redox-active residues that shuttle protons and electrons to the catalytic intermediates, and (ii) H-bonding groups that stabilize the Fe-O_2 bound species and direct the protonation in the Fe^{III}-OOH leading to the selective reduction of O_2 to H_2O.

Our research group [141] has previously shown that the introduction of urea units in the second coordination sphere of an iron porphyrin enhances the electrocatalytic reduction of CO_2 through an H-bonding stabilization of the Fe-CO_2 adduct compared to the parent FeTPP. In particular, two atropisomers of a bis-urea iron porphyrin were synthesized, Fe-αα-2Urea and Fe-αβ-2Urea, as shown in Fig. 1-23.

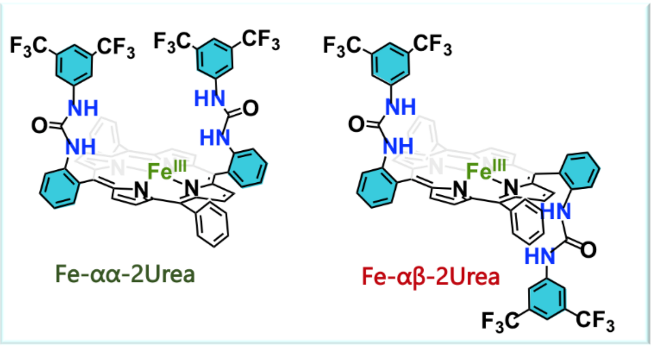

Fig. 1-23 Previously investigated Fe-αα-2Urea and Fe-αβ-2Urea porphyrins as CO_2 reduction electrocatalysts and proposed ORR electrocatalysts.

Both catalysts efficiently reduced CO_2 to CO; however, the topology of the urea units seemed to affect the CO_2 binding affinity on the iron center and the rate of the CO_2 reduction process. Although Fe-αα-2Urea exhibited almost 25 times higher affinity for CO_2, the rate of the overall CO_2 reduction reaction was approximately one order of magnitude lower than the Fe-αβ-2Urea atropisomer.[141] Taking leverage of the same structural motifs, this chapter aims at:

- investigating the topological effect of such urea tweezers on stabilizing the Fe-O2 adducts and forming the Fe-O_2^{2-} and Fe-OOH intermediates.
- gaining insights into the electronic states of Fe-O_2 and Fe-O_2^{2-} species and the coordination mode of the bound O_2 and peroxide ligand on the iron center for the two atropisomers.

It's been long known that urea units can stabilize H_2O_2 via H-bonding, with the first crystalline form of such moieties having been first characterized by X-ray and neutron diffraction studies in 1941[142] and 1981[143], respectively (**Fig. 1-24**). Several DFT studies have been conducted on their crystalline forms to investigate additional coordination modes of the urea units with several H_2O_2 molecules.[144]

In addition, in 2012, Nocera showed that a hexacarboxamide cryptand could reversibly bind a peroxide dianion (O_2^{2-}) in its cavity. Such an entrapment was confirmed by ^1H NMR spectroscopy and X-ray crystallographic studies, as shown in Fig. 1-24. Although this scaffold did not contain urea groups, the in-between distance of the -NH units of the cryptand that formed H-bonds with the same oxygen atom of O_2^{2-} was similar to the -NH_2 units of two urea molecules hydrogen bonded to one of the two oxygen atoms of H_2O_2. [145]

---

[141] Gotico, P., Roupnel, L., Guillot, R., Sircoglou, M., Dr. Leibl, W. et al., *Angew. Chem. Int. Ed.*, 2020, 59, 50, 22451-22455, DOI: 10.1002/anie.202010859

[142] Lu, C.-S., Hughes, E.W., Giguère, P.A., *J. Am. Chem. Soc.*, **1941**, 63, 6, 1507–1513, DOI: 10.1021/ja01851a007

[143] Fritchie Jr, C.J., McMullan, R.K., *Acta Cryst.*, **1981**, 37, 1086-1091, DOI: 10.1107/S0567740881005116

[144] Medvedev, A.G., Shishkina, A.V., Prikhodchenko, P.V., Lev, O., Vener, M.V., *RSC Adv.*, **2015**, 5, 29601–29608, DOI: 10.1039/c5ra02498f

[145] Lopez, N., Graham, D.J., McGuire, JR., R., Alliger, G.E., Shao-Horn, Y. *et al.*, *Science*, **2012**, 335, 6067, 450-453, DOI: 10.1126/science.1212678

Moreover, in 1992, Reed and co-workers synthesized a series of iron picket fence porphyrins as Hb-O_2 models to investigate how the different H-bonding groups on the distal plane of the macrocycle ring could affect the O_2 affinity of their iron center. The equilibrium constants (K_{O2} (M^{-1})) were determined via laser photolysis studies, while the corresponding picket fence Fe-oxy derivatives were characterized by ^{1}H-NMR spectroscopy. Among the investigated iron porphyrin complexes, the phenylurea analog exhibited one of the highest K_{O2} values (~0.035 M^{-1}). The authors attributed such an enhancement in O_2 binding to a well-oriented H-bond formation between the distal oxygen atom of the Fe-O_2 bound species and the distal urea function, as shown in Fig. 1-24. [146]

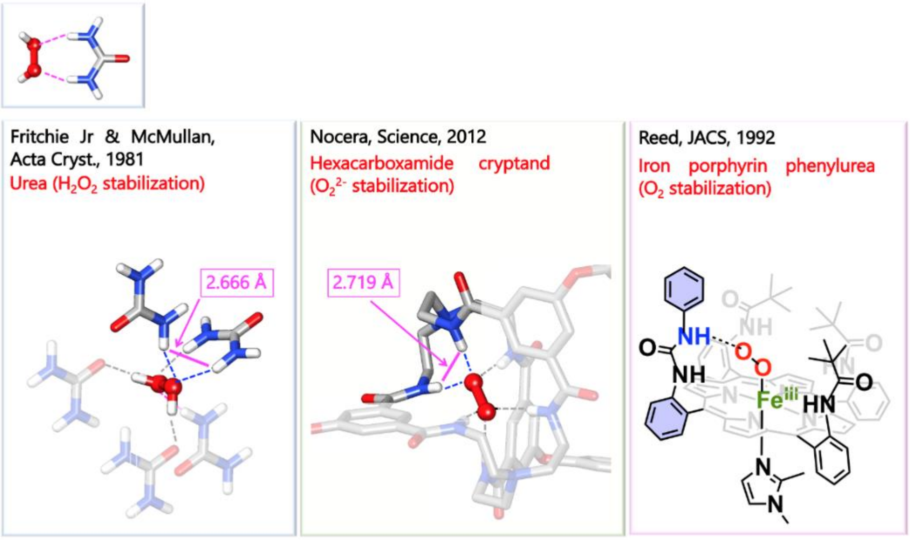
Fritchie Jr & McMullan, Acta Cryst., 1981
Urea (H_2O_2 stabilization)

Nocera, Science, 2012
Hexacarboxamide cryptand (O_2^{2-} stabilization)

Reed, JACS, 1992
Iron porphyrin phenylurea (O_2 stabilization)

Fig. 1-24 Stabilization of H_2O_2, O_2^{2-}, and Fe-O_2 adducts via urea, hexacarboxamide cryptand, and phenylurea, respectively.

---

[146] Wuenschell, G.E., Tetreau, C., Lavalette, D., Reed, C.A., *J. Am. Chem. Soc.*, **1992**, 114, 9, 3346–3355M DOI: 10.1021/ja00035a028

1.3 Synthetic approach and X-ray Crystallography Characterization

Fe-αα-2Urea and **Fe-αβ-2Urea** catalysts were synthesized following the synthetic steps[147] illustrated in Scheme 1-18. For brevity, the experimental details and the characterization of the synthesized intermediates and the final iron complexes are gathered in Annex I at the end of Chapter 1.

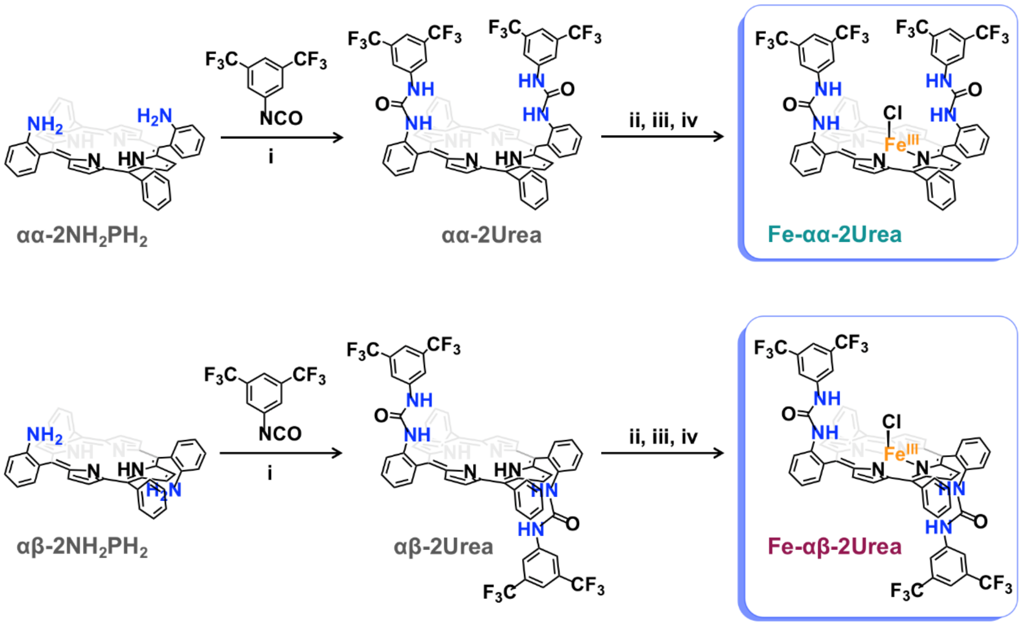

Scheme 1-18 General experimental approach for the synthesis of the **Fe-αα-2Urea** and **Fe-αβ-2Urea** catalysts. Experimental conditions: i) dry CH_2Cl_2, Ar atm, RT, 12h; ii) dry THF, $FeBr_2$, lutidine, RT, 16h; iii) 1M HCl iv) recrystallization from MeOH.

Suitable crystals for diffraction of **αα-Urea** (Fig. S1-1), **αβ-Urea** (Fig. S1-2), **Fe-αα-2Urea**, and **Fe-αβ-2Urea** porphyrin derivatives were obtained by the classical slow-evaporation method at ambient conditions. Rhomboid-shaped crystals of **Fe-αα-2Urea** were grown by slow evaporation of a saturated DMF solution and revealed a μ-oxo bridged dimer in solid-state as shown in Fig. 1-25. The formation of the dimer is probably attributed to the prolonged incubation time of the crystallization process since no formation of dimers was evident in solution from cyclic voltammetry studies, UV-Vis, and EPR spectroscopy investigation. The **Fe-αβ-2Urea** atropisomer, on the other hand, crystallized as a monomer, as was expected due to its αβ topology that prevents the dimerization. As shown in Fig. 1-25, two X-ray structures were attained that differentiate in the nature of the axial ligand, although the same solvent (DMF) was used in the crystallization process. As such, **Fe-αβ-2Urea** was obtained as a chloro-porphyrinato Fe^{III} and hydroxo-porphyrinato Fe^{III} complex. In the latter X-ray structure, a water molecule was found trapped and hydrogen-bonded to the -OH axial ligand, which resembles the last ORR catalytic intermediate and points out the potential role of the urea functions in the stabilization of the O_2 reduction intermediates as it will extensively discuss in the following sections.

---

[147] Gotico, P., Roupnel, L., Guillot, R., Sircoglou, M., Leibl, W., *et al.*, *Angew. Chem. Int. Ed.*, **2020**, 59, 50, 22451-22455, DOI: 10.1002/anie.202010859

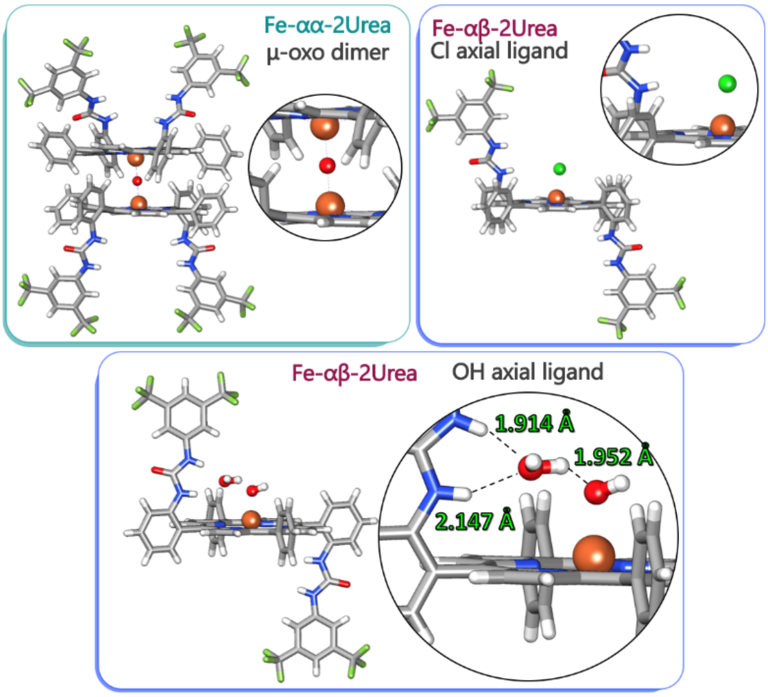

Fig. 1-25 Capped sticks representation of the X-ray crystal structures of **Fe-αα-2Urea** and **Fe-αβ-2Urea**.

1.4 Electrochemical Characterization

1.4.1 Anaerobic conditions

In an Ar-degassed DMF solution, **Fe-αα-2Urea** and **Fe-αβ-2Urea** exhibited three successive reversible redox waves attributed to the **$Fe^{III/II}$** and the formal **$Fe^{II/I}$** and **$Fe^{I/0}$** couples (Fig. 1-26). Compared to the parent FeTPP, for both catalysts, these three redox processes took place at more positive potentials due to the presence of the electron-withdrawing amido functions and the -CF_3 groups. [141],[148]

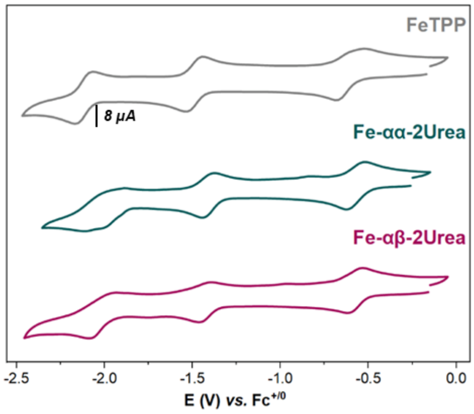

Catalyst	$E_{1/2}$ (V) vs. $Fc^{+/0}$		
	$Fe^{III/II}$	$Fe^{II/I}$	$Fe^{I/0}$
FeTPP	-0.625	-1.489	-2.119
Fe-αα-2Urea	-0.569	-1.413	-1.961
Fe-αβ-2Urea	-0.554	-1.434	-2.018

Fig. 1-26 Left: CVs of 1 mM of **Fe-αα-2Urea**, **Fe-αβ-2Urea**, and **FeTPP** porphyrin recorded in Ar-degassed DMF/$TBAPF_6$ (0.1 M) solution at a scan rate of 100 mV/s. Right: Table summarizing the redox potentials (*vs.* $Fc^{+/0}$) of the investigated iron porphyrins.

While in our previous studies with the **Fe-αα-2Urea** and **Fe-αβ-2Urea** derivatives concerning the reduction of CO_2 to CO at the formal Fe^0 state[141], herein we will focus on the

---

[148] Steven A. Holmes and T. Darrah Thomas *J. Am. Chem. Soc.*, **1975**, 97, 9, 2337–2341 10.1021/ja00842a004

first reduced state of the catalysts, *viz.*, the iron(II) oxidation state where O_2 activation and reduction take place.

1.4.2 Aerobic and non-acidic conditions

Saturation of the electrolytic **Fe-αα-2Urea** and **Fe-αβ-2Urea** solutions with O_2 resulted in two major changes in their CVs footprints. First, like in the case of the non-functionalized **FeTPP** catalyst, their redox **Fe$^{III/II}$** couple became irreversible and shifted approximately 20 mV to more positive potentials, while the current intensity slightly increased. Such a CV response is indicative of O_2 activation by the Fe^{II} reduced state of the catalysts resulting in the formation of Fe^{III}-($O_2^{\bullet-}$), as has been previously reported for other iron porphyrin catalysts[149]. Second and more importantly, the CVs of **Fe-αα-2Urea** and **Fe-αβ-2Urea** catalysts displayed a new cathodic wave with an E_p of -0.887 V *vs.* Fc$^{+/0}$, which was absent for the parent **FeTPP** (Fig. 1-27.).

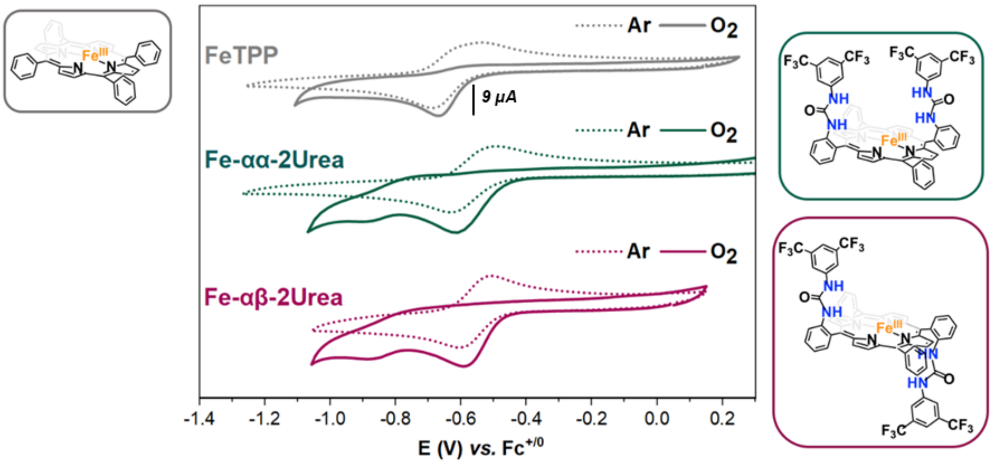

Fig. 1-27 CVs of 1 mM of **Fe-αα-2Urea** and **Fe-αβ-2Urea** DMF/TBAPF$_6$ (0.1 M) solution, compared to the parent **FeTPP** porphyrin under Ar (dash-dotted lines) and in the presence of 1 atm O_2 (solid lines); 100 mV/s scan rate.

This additional reduction wave cannot be assigned to the reversible one-electron reduction of O_2 at the surface of the electrode since its redox couple is located at more negative potentials ($E(O_2/O_2^{\bullet-})$ = -1.30 V *vs.* Fc$^{+/0}$, Fig. S1-5). Therefore, our experimental results suggest that the new reduction wave with an E_p of -0.887 V *vs.* Fc$^{+/0}$ might be related to a further one-electron reduction of the **Fe^{III}-($O_2^{\bullet-}$)** to **Fe^{III}-(O_2^{2-})** species (otherwise noted as ***(S)*** and ***(P)***, respectively) as has also been reported for Fe^{III}(F_{20}TPP) by Anxolabéhère-Mallart (E_p = −0.95 V *vs.* Fc$^{+/0}$) [149]. Moreover, Naruta's **HGM-Fe^{II}P-Im** cytochrome P_{450} heme mimic, described earlier in paragraph 1.1.3.2, bearing both an imidazole as an axial base and an appended carboxylic acid as H-(bond) donor [150]., the determination of the reduction potential of ***(S)*** was not feasible experimentally, but it was instead calculated by density functional theory (DFT) studies. The obtained reduction potential of the Fe^{III}-$O_2^{\bullet-}$ species was -1.36 V *vs.* Fc$^{+/0}$ which is considerably more negative than the reduction potential determined electrochemically by Anxolabéhère-Mallart [149]. Recently, Karlin and co-workers[151] reported the reduction potential for the [(F_8)Fe^{III}-($O_2^{\bullet-}$)] / [(F_8)Fe^{III}-(O_2^{2-})] couple which was calculated

---

[149] Oliveira, R. Zouari, W., Herrero, C., Banse, F., Schöllhorn, B. *et al.*, *Inorg. Chem.*, **2016**, 55, 12204−12210, DOI: 10.1021/acs.inorgchem.6b01804

[150] Nagaraju, P., Ohta, T., Liu, J-G., Ogurac, T., Naruta, Y., *Chem. Commun.*, **2016**, 52, 7213-7216, DOI: 10.1039/c6cc02162j

[151] Kim, H., Rogler, P.J., Sharma, S.K., Schaefer, A.W., Solomon, E.I., Karlin, K.D., *J. Am. Chem. Soc.*, **2020**, 142, 6, 3104–3116, DOI: 10.1021/jacs.9b12571

to be −1.17 V *vs.* $Fc^{+/0}$. However, in their case, the determination of the redox couple's potential was realized by generating the corresponding ferric-**(*S*)** and ferric-**(*P*)** intermediates chemically and calculating it via the equilibrium constants from the Nernst equation. On a similar note, the group of Karlin also reported the **(*S*)**/**(*P*)** redox potential for a ferric-heme synthetic compound, which was appended with an internal axial ligand (imidazolyl). The calculated $[(PIm)Fe^{III}\text{-}(O_2^{\bullet -})]$ / $[(PIm)Fe^{III}\text{-}(O_2^{2-})]$ couple was located at more negative potentials (−1.33 V *vs.* $Fc^{+/0}$) than the non-ligated analog (−1.17 V *vs.* $Fc^{+/0}$) due to the electron donation from the axial base[152].

The questions that arise at this point for **Fe-αα-2Urea** and **Fe-αβ-2Urea** are: (i) *What is the coordination mode of O_2 on the metal center; Is it an end-on or a side-on peroxo species?(* **Scheme 1-19***)* and (ii) *Is it possible to extract any information about the electronic structure of the peroxo intermediates by their cyclic voltammograms?*

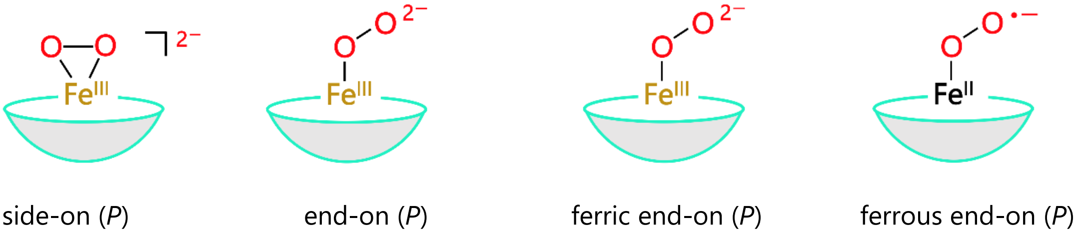

Scheme 1-19 Possible coordination modes of the peroxo ligand and electronic structures of an iron (*P*) porphyrin intermediate.

To answer the first question, we initially investigated the reversibility of the **(*S*)**/**(*P*)** redox couple at 100 mV/sec. As shown in **Fig. 1-20**, the reduction of the **Fe-αα-2Urea (*S*)** (pathway B) species seemed a quasi-reversible process, while for the **Fe-αβ-2Urea** atropisomer, the **(*S*)**/**(*P*)** redox couple was irreversible (pathway B and C). Indeed, the **Fe-αβ-2Urea (*S*)** species was reduced at Ep= -0.887 V *vs.* $Fc^{+/0}$, while a new anodic wave at -0.095 V *vs.* $Fc^{+/0}$ was observed.

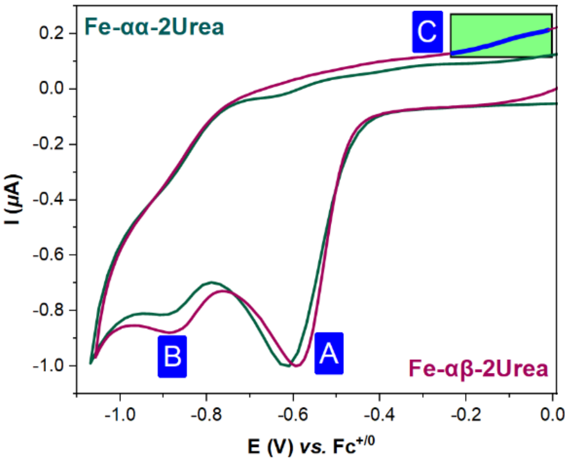

Fig. 1-20 CVs comparison of 1 mM of **Fe-αα-2Urea** and **Fe-αβ-2Urea** DMF/$TBAPF_6$ (0.1 M) solution under 1 atm O_2; scan rate= 100 mV/s.

A similar irreversible reduction wave (E_p= -0.950 V *vs.* $Fc^{+/0}$) prior to the one-electron reduction of O_2 at the surface of the electrode has also been documented by Anxolabéhère-Mallart and co-workers who investigated a series of iron porphyrins as catalysts for the

---

[152] Kim, H., Rogler, P.J., Sharma, S.K., Schaefer, A.W., Solomon, E.I., Karlin, K.D., *Angew. Chem. Int. Ed.*, **2021**, 60, 5907 – 5912, DOI : 10.1002/anie.202013791

activation and reduction of O_2 via cyclic voltammetry[149] and Scanning ElectroChemical Microscopy (SECM)[153]. According to their studies, the irreversibility of the cathodic wave was attributed to the reduction of the ***(S)*** species to the corresponding side-on ***(P)*** intermediate, which was oxidized at considerably more positive potentials (+0.05 V *vs.* $Fc^{+/0}$). Spectroelectrochemistry studies proposed that the side-on $\boldsymbol{(P)}_{ox}$ species were converted to their initial Fe^{III} porphyrin derivatives probably upon O_2 release. [151]

Henceforth, the irreversibility of the **Fe-αβ-2Urea (*S*)/(*P*)** redox couple, along with the appearance of the anodic wave at -0.095 V *vs.* $Fc^{+/0}$ (Fig. 1-20, solid line), might as well suggest the formulation of a side-on ***(P)*** intermediate (Scheme 1-20, pathway B). On the contrary, since the **Fe-αα-2Urea (*S*)/(*P*)** redox couple seemed quasi-reversible and no anodic wave was observed at around -0.095 V *vs.* $Fc^{+/0}$ (Fig. 1-20), we can postulate that the **Fe-αα-2Urea (*S*)** species is reduced to an end-on ***(P)*** intermediate, as depicted in Scheme 1-20.

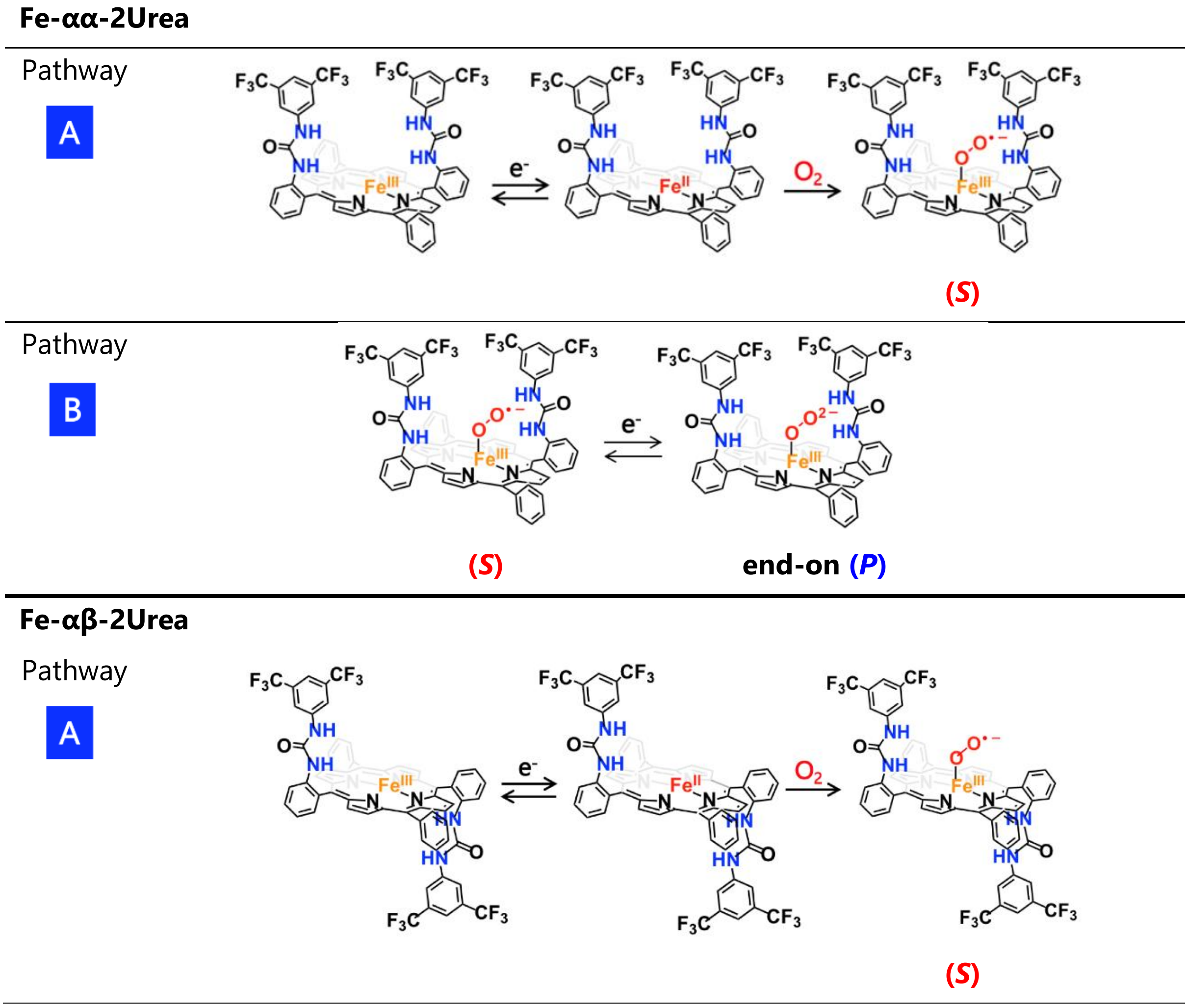

---

[153] Noël, J-M., Kostopoulos, N., Achaibou, C., Fave, C., Kanoufi, F. *et al.*, *Angew. Chem. Int. Ed.*, **2020**, 132, 38, 16518 – 16522, DOI: 10.1002/ange.202004977

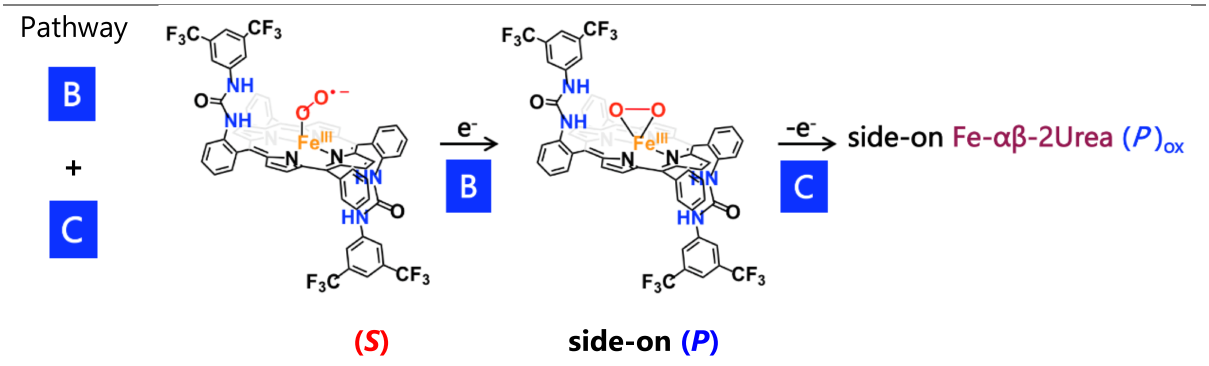

Scheme 1-20 Synopsis of the possible O_2 reduction intermediates of **Fe-αα-2Urea** and **Fe-αβ-2Urea** formed at each electro(chemical) step.

These electrochemical studies demonstrated that the incorporation of the urea groups on the second-coordination sphere of the iron catalysts greatly enhanced the stability of the **(*S*)** intermediates compared to the parent **FeTPP**, and shifted the **(*S*)**/ **(*P*)** redox couple to more positive potentials, allowing us to detect it via cyclic voltammetry experiments. The redox couple of this quasi-reversible process was not only located at more positive potentials (E= -0.796 V *vs.* Fc$^{+/0}$) compared to the previously reported heme **(*S*)**/ **(*P*)** redox couples, but it is also the first to be determined by cyclic voltammetry. In addition, the topology of the urea functions appeared to also affect the coordination mode of the bound peroxo (**O_2^{2-}**) ligands, with the **Fe-αα-2Urea (*P*)** seeming to adopt an end-on configuration, while the **Fe-αβ-2Urea (*P*)** species a side-on.

Interestingly, at lower scan rates (5 mV/sec), both **Fe-αα-2Urea** and **Fe-αβ-2Urea** displayed a quasi-reversible **(*S*)**/**(*P*)** redox couple with the same E= -0.796 V *vs.* Fc$^{+/0}$. However, upon increasing the scan rate from 5 to 10 mV/sec only the **Fe-αα-2Urea (*S*)**/**(*P*)** redox couple remained quasi-reversible (Fig. 1-21). To rationalize this trend we performed a series of experiments as described below.

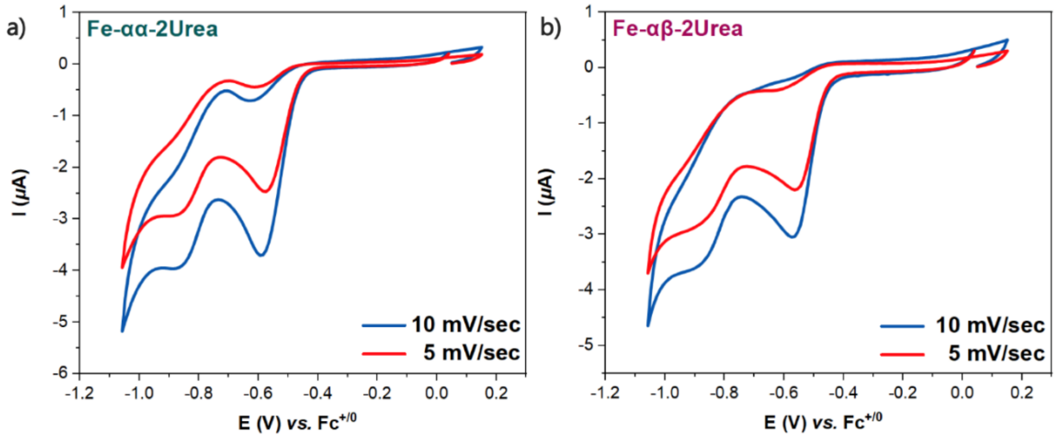

Fig. 1-21 CVs of 1.0 mM of **Fe-αα-2Urea** and **Fe-αβ-2Urea** DMF/$TBAPF_6$ (0.1 M) solution, under O_2 recorded at 5 and 10 mV/sec.

1.4.3 Quasi-reversible Fe-αα-2Urea **(*S*)**/ **(*P*)** redox couple at low scan rates

At lower scan rates, one would expect that the side-on peroxo species would be dominant due to the longer time course of the experiment that would allow the electronic reshuffling in the end-on **(*P*)** intermediates (EC mechanism) and thus favoring the sole formation of side-on peroxo intermediates. For non-heme systems, it is proposed that a side-on peroxo species is thermodynamically more stable than its end-on analogs, with representative examples of mononuclear and dinuclear manganese or copper complexes by the group of Jackson and Anxolabéhère-Mallart [154], Zuberbühler [155], and Kovacs [156] However, this was not the case (Fig. S1-6) and made us consider another parameter that was initially neglected: the presence of H_2O. Although the experiments were carried out in extra dry DMF, we couldn't exclude the possibility of traces of H_2O present in the electrolytic solution since DMF is quite hygroscopic[157]. With that in mind, we performed another set of experiments in which the DMF solution of 0.5 mM **Fe-αα-2Urea** contained 0.33 % of H_2O and examined the reversibility of the ***(S)***/ ***(P)*** redox couple at a range of different scan rates.

As shown in Fig. 1-22, when the electrolytic solution contained 0.33% of H_2O, the wave corresponding to the ***(S)***/ ***(P)*** redox couple became more reversible even at faster scan rates (5 *vs*. 25 mV/sec), while its potential shifted approximately 36 mV to more negative values (E= -0.833 V *vs.* $Fc^{+/0}$). However, upon increasing the scan rate from 25 to 300 mV/sec, the same CVs response was observed as in the absence of H_2O, *viz*. the loss of reversibility for the ***(S)***/ ***(P)*** redox couple (Fig. S1-7).

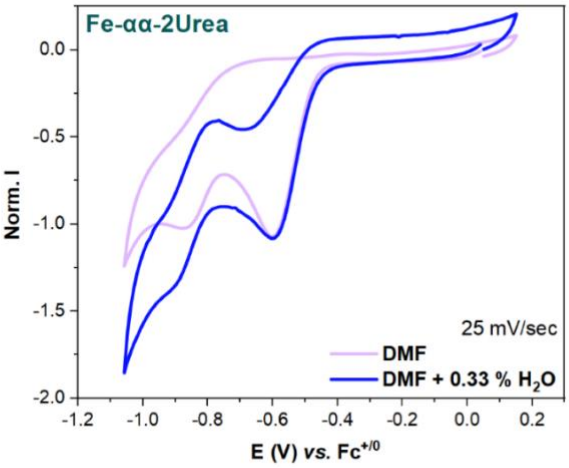

Fig. 1-22 CVs of 1 mM of **Fe-αα-2Urea** in DMF/$TBAPF_6$ (0.1 M) (purple line) and in DMF + 0.33 % H_2O /$TBAPF_6$ (0.1 M) under 1 atm of O_2; scan rate= 25 mV/s.

It is evident that the presence of H_2O might also hold a role in the stabilization of the ORR intermediates as has been also shown from the obtained X-ray structure for the hydroxo-porphyrinato **Fe-αβ-2Urea** (Fig. 1-25). In addition, the fact that the quasi-reversibility of the ***(S)***/***(P)*** redox couple was restored at scan rates less than 10 mV/sec in the absence and 25 mV/sec in the presence of H_2O compared to higher scan rates, may suggest the formation of a tight hydrogen-bonding network locked by the urea arm(s) as it has been also shown from our previous DFT calculations; yet for a Fe-CO_2 adduct[141]. As such, we could postulate that a well-oriented water molecule network with respect to the Fe-[O_2] intermediates could potentially also control the coordination mode of O_2 in the ***(P)*** species. In other words, favor an end-on ***(P)*** over side-on ***(P)*** species formation upon reduction of the ***(S)*** intermediates. However, these obtained results require further investigation before reaching conclusive remarks.

---

[154] Geiger, R.A., Leto, D.F, Chattopadhyay, S., Dorlet, P., Anxolabéhère-Mallart, E., Jackson, T.A., *Inorg. Chem.* **2011**, 50, 10190–10203, DOI: 10.1021/ic201168j

[155] Jung, B., Karlin, K.D., Zuberbühler, A.D., *J. Am. Chem. Soc.*, **1996**, 118, 3763-3764, DOI: 10.1021/ja954157g

[156] Poon, P.C.Y., Dedushko, M.A., Sun, X., Yang, G., Toledo, S. *et al.*, *J. Am. Chem. Soc.*, **2019**, 141, 15046−15057, DOI: 10.1021/jacs.9b04729

[157] Brezny, A.C., Johnson, S.I., Raugei, S., Mayer, J.M, *J. Am. Chem. Soc.*, **2020**, 142, 9, 4108–4113, DOI: 10.1021/jacs.9b13654

1.5 Chemical Generation and Characterization of the Superoxo (*S*), Peroxo (*P*), and Hydroperoxo (*HP*) Intermediates

To further investigate the intermediates involved in the ORR and potentially corroborate our electrochemical studies, we moved forward with the chemical preparation and characterization of the superoxo **(*S*)**, peroxo **(*P*)**, and hydroperoxo **(*HP*)** **Fe-αα-2Urea** and **Fe-αβ-2Urea** species via UV-Vis, EPR and *r*Raman spectroscopy.

1.5.1. Superoxo (S) species

Fe^{III}-αα-2Urea and **Fe^{III}-αβ-2Urea** were chemically reduced to their corresponding **Fe^{II}** complexes with Zn amalgam in dry THF inside an N_2-filled glovebox. The UV-Vis spectra of the reduced **Fe^{II}-αα-2Urea** and **Fe^{II}-αβ-2Urea** complexes were recorded at -80 °C and exhibited considerably different features compared to their corresponding **Fe^{III}** species. As shown in Fig.1-23., the UV-Vis spectrum of **Fe^{II}-αα-2Urea** displayed a sharp Soret band at 427 nm while the Q bands were blue-shifted to 533 and 546 nm. Similar changes in the UV-Vis features were also observed for **Fe^{II}-αβ-2Urea** with the maximum absorbance of the Soret and Q bands located at 426 and 536, 550 nm, respectively.

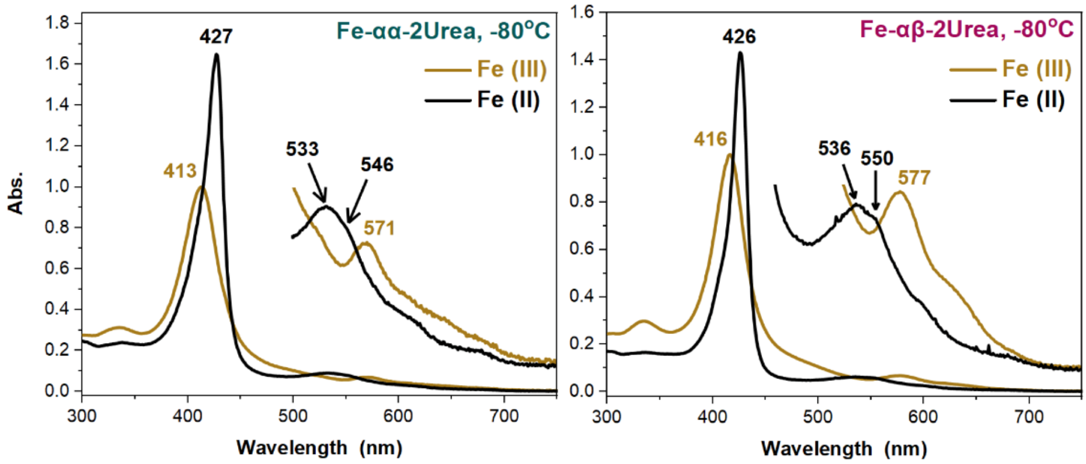

Fig. 1-23 UV Vis spectra of the **Fe^{III}-αα-2Urea** and **Fe^{III}-αβ-2Urea** in THF at -80 °C (yellow line) and their corresponding one-electron reduced **Fe^{II}** species (black line) The inset shows the magnified Q-band region.

Saturation of the **Fe^{II}-αα-2Urea** and **Fe^{II}-αβ-2Urea** solution with O_2 resulted in an immediate change in their spectra footprints, suggesting the formation of new species. For both atropisomers, the Soret band shifted to lower wavelengths, while its absorbance was considerably decreased. The newly formed species from **Fe-αα-2Urea** and **Fe-αβ-2Urea** exhibited UV-Vis features at λ_{max}= 417, 542, 581, and 623 nm, and λ_{max}= 418, 543, 578, and 620 nm, respectively (Fig. 1-24). These UV-Vis changes are in good accord with the formulation of 6-coordinated end-on superoxo species, as has been previously reported by Karlin[158] or 5-coordinated end-on superoxo complexes by Mayer[159], who also chemically prepared analogous superoxo heme complexes in weakly coordinated solvents.

---

[158] Ghiladi, R.A., Kretzer, R.M., Guzei, I., Rheingold, A.L., Neuhold, Y-M. *et al.*, *Inorg. Chem.*, **2001**, 40, 5754-5767, DOI: 10.1021/ic0105866

[159] Pegis, L.P., Martin, D.J., Wise, C.F., Brezny, A.C., Johnson, S.I. *et al.*, *J. Am. Chem. Soc.*, **2019**, 141, 20, 8315–8326, DOI: 10.1021/jacs.9b02640

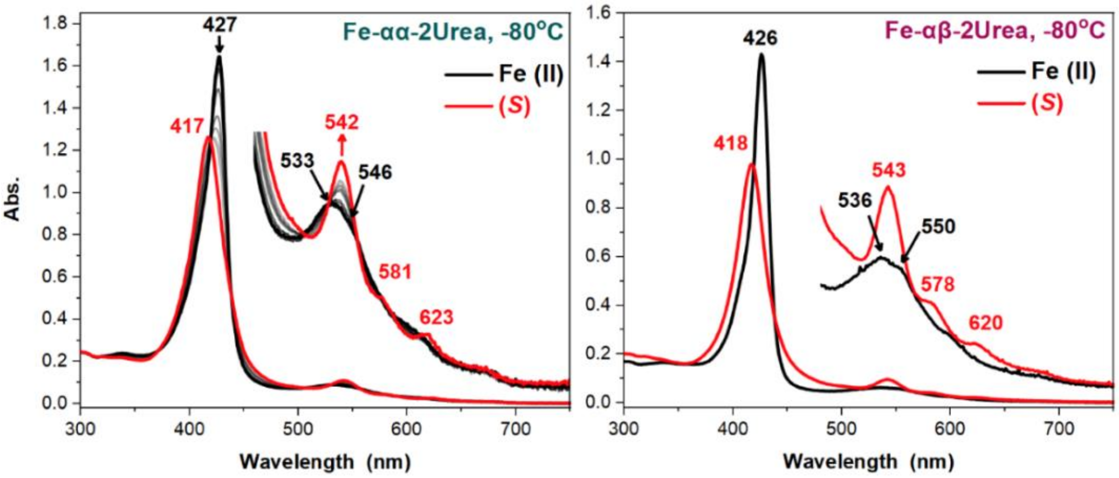

Fig. 1-24 UV Vis spectra of the **Fe^{II}** species in THF at -80 °C (black line) under N_2 atmosphere and the resulting UV-Vis features upon oxygenation of the solution to afford the **(*S*)** intermediates (red line) **Fe-αα-2Urea** and **Fe-αβ-2Urea**. The inset shows the magnified Q-band region.

1.5.1.1 Reversible O₂ binding

To investigate the reversible O_2 binding to the **Fe^{II}-αα-2Urea** and **Fe^{II}-αβ-2Urea** reduced complexes, **Fe-αα-2Urea (*S*)** and **Fe-αβ-2Urea (*S*)** solutions were purged with Ar at -80 °C. However, no UV-Vis changes indicating the formation of **Fe^{II}-αα-2Urea** and **Fe^{II}-αβ-2Urea** species were observed. Interestingly, when the solution of **Fe-αα-2Urea (*S*)** was purged with Ar at 5 °C, the UV-Vis spectra gradually evolved to the one corresponding to the **Fe^{II}-αα-2Urea** species (Fig. 1-25a). The addition of O_2 to the generated **Fe^{II}-αα-2Urea** solution gave back the **Fe-αα-2Urea (*S*)** species, according to the UV-Vis spectra of Fig. 1-25b, and showed no thermal degradation of the **Fe-αα-2Urea (*S*)** to the Fe^{III}-OH porphyrin complex. Therefore, although purging Ar through the solution of the **Fe-αα-2Urea (*S*)** was not able to reverse the O_2 binding at low temperatures, it was possible at 5°C for a couple of oxygenation and de-oxygenation cycles.

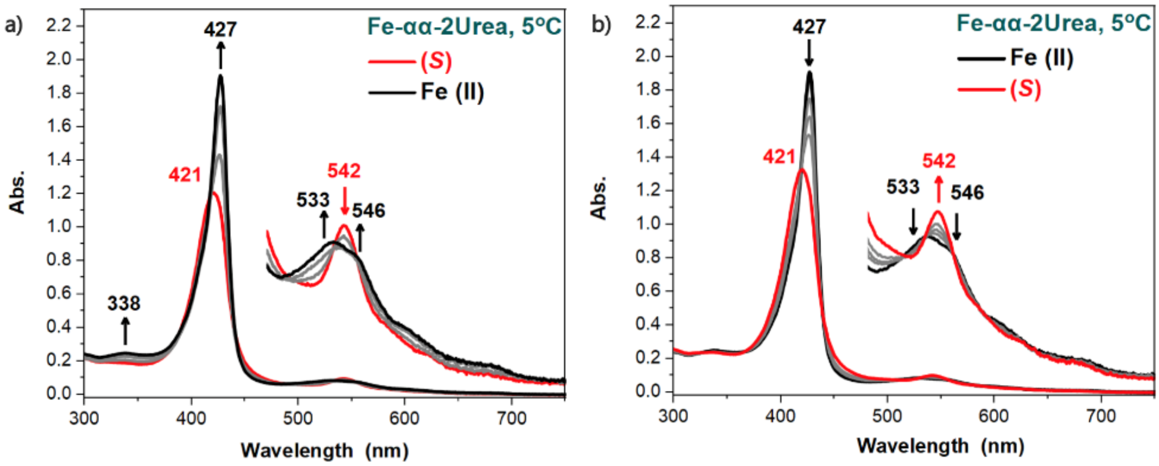

Fig. 1-25 a) Evolution of the **Fe-αα-2Urea (*S*)** UV-Vis spectra generated at 5°C (red line) upon deaerating gently the THF solution with Ar to afford the **Fe^{II}-αα-2Urea** complex (black line), b) Oxygenation of the generated **Fe^{II}-αα-2Urea** THF solution (black line) to yield back the **Fe-αα-2Urea (*S*)** (red line).

1.5.1.2 Stability of Superoxo (S) species

To examine the stability of the **Fe-αα-2Urea (*S*)** and **Fe-αβ-2Urea (*S*)** species, a series of temperature-related stability studies were performed and compared to the corresponding superoxo species of the non-functionalized **FeTPP**. The Fe-O_2 adducts of **Fe-αα-2Urea**, **Fe-αβ-2Urea,** and **FeTPP** were generated and the evolution of their UV-Vis spectra was monitored over 30 min under stirring conditions at – 20 °C. As shown in Fig. 1-27., the UV-Vis spectra of **Fe-αα-2Urea (*S*)** (Fig. 1-26a) and **Fe-αβ-2Urea (*S*)** (Fig. 1-26b) species at -20 °C displayed minor changes over the time course of 30 min. However, this was not the case for the **FeTPP (*S*)** species, which immediately evolved to new species exhibiting UV-Vis features with λ_{max}= 350, 415, 501, and 570 nm (Fig. 1-27c). These changes, especially in the Q region, match well the UV-Vis spectra of previously reported **$[Fe^{III}TPP]_2O$** μ-oxo dimers[160].

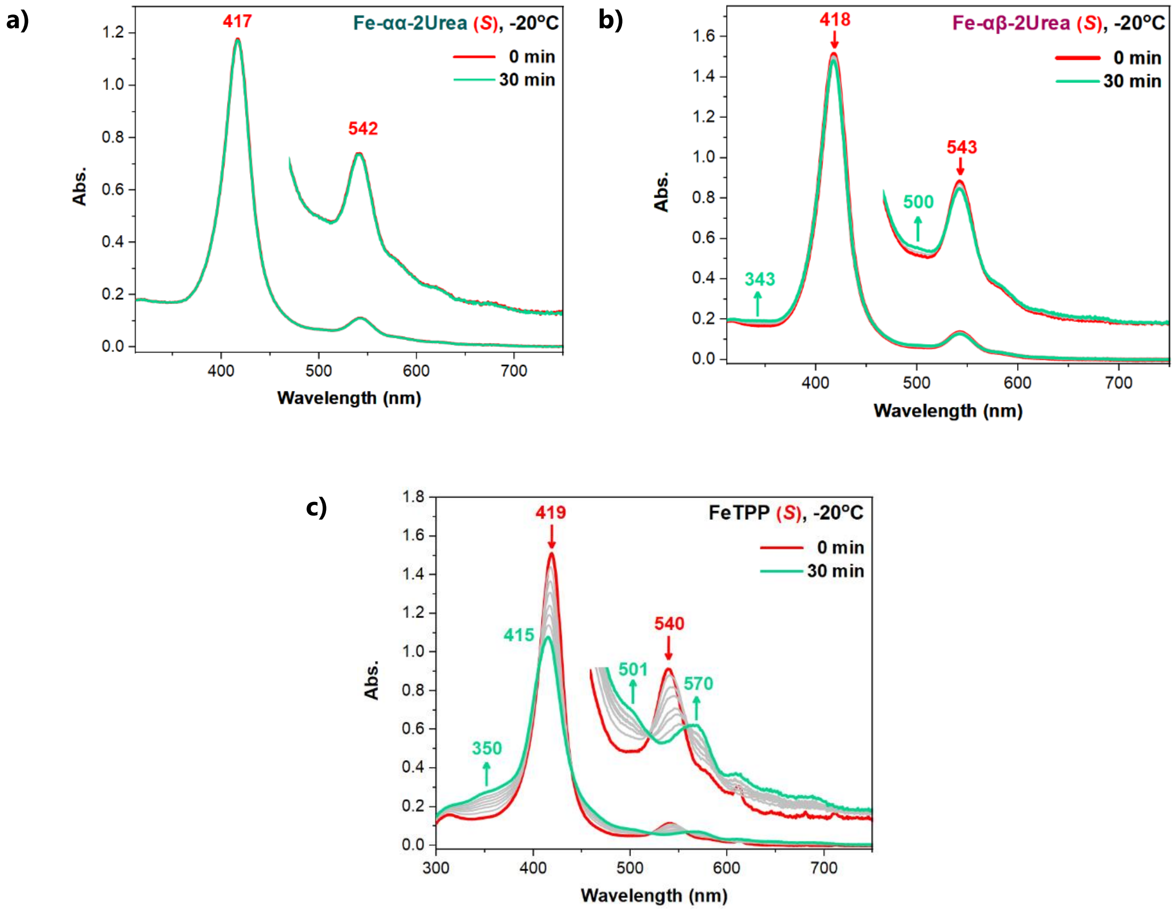

Fig. 1-26 UV Vis evolution spectra of the generated (S) species at -20 °C in dry THF of a) **Fe-αα-2Urea,** b) **Fe-αβ-2Urea,** and c) **FeTPP**. The inset shows the magnified Q-band region.

A better comparison of the **Fe-αα-2Urea (*S*)**, **Fe-αβ-2Urea (*S*),** and **FeTPP (*S*)** stability at -20 °C is provided in Fig. 1-27 by plotting the maximum absorbance of the Soret band as a function of time.

---

[160] Sacramento, J. J. D., Goldberg, D. P., *Chem. Commun.*, **2020**, 56, 3089-3092, DOI: 10.1039/c9cc10019a

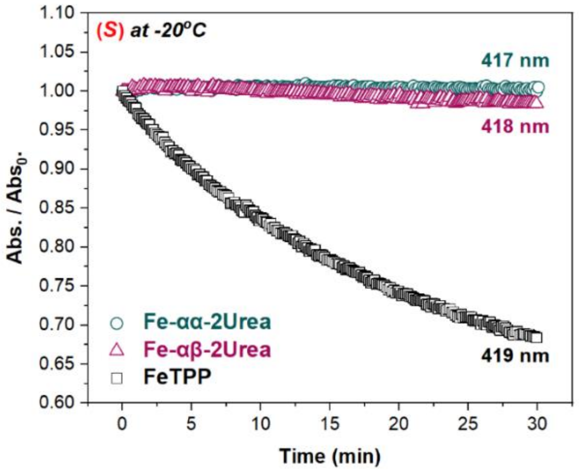

Fig. 1-27 Comparison of the evolution of the maxima absorption (Soret band) at -20 °C in dry THF of **Fe-αα-2Urea (*S*)** (green circles) the **Fe-αβ-2Urea (*S*)** (burgundy triangles) and **FeTPP (*S*)** (black squares) species over time.

The stability of the **Fe-2Urea** atropisomers and **FeTPP** was also investigated in a range of temperatures as shown in (Fig. S1-11-13). Among the iron porphyrin complexes, **Fe-αα-2Urea (*S*)** exhibited the greatest stability of all, followed by the **Fe-αβ-2Urea (*S*)** and **FeTPP (*S*)** species. These findings corroborate our previous electrochemistry studies that the incorporation of urea arms in the second coordination sphere greatly enhances the stability of the Fe-O_2 adducts. In addition, the topology of the urea functions also influences the stability of the superoxo species, with **Fe-αα-2Urea (*S*)** displaying slightly higher stability than the **Fe-αβ-2Urea (*S*)** species. These results further justified our initial suggestions that two urea groups on the same side with respect to the porphyrin plane stabilize more efficiently the superoxo intermediates.

1.5.1.3 Stoichiometric O_2 binding

The 1:1 O_2 binding to the **Fe^{II}-αα-2Urea** and **Fe^{II}-αβ-2Urea** complexes was also investigated by titrating the corresponding **Fe^{II}** porphyrin solution at -60 °C with sub-stoichiometric aliquots of THF solution saturated with O_2 (8.62 mM [O_2][161]) (Fig. 1-28). As shown in Fig. 1-28a, upon titration of the stirring **Fe^{II}-αα-2Urea** solution with O_2, the absorbance of the Q band at 542 nm gradually increased, whereas two additional absorption bands at 581 and 622 nm also emerged. These new UV-Vis features fit well with the formation of solely **Fe-αα-2Urea (*S*)**. Slightly more than 1 eq. of O_2 (1.08 eq) was required to reach maximum absorbance, while no UV-Vis changes were observed when more than 1.08 eq. of O_2 was introduced to the reaction mixture. When monitoring the evolution of the Q band at 542 nm over the time course of the experiment after each O_2 addition, a minor decrease was observed in the absorbance, and it was attributed to the thermal equilibration of the system (Fig. 1-28b).

---

[161] Quaranta, M., Murkovic, M., Klimant, I., *Analyst*, **2013**, 138, 6243–6245, DOI: 10.1039/c3an36782g

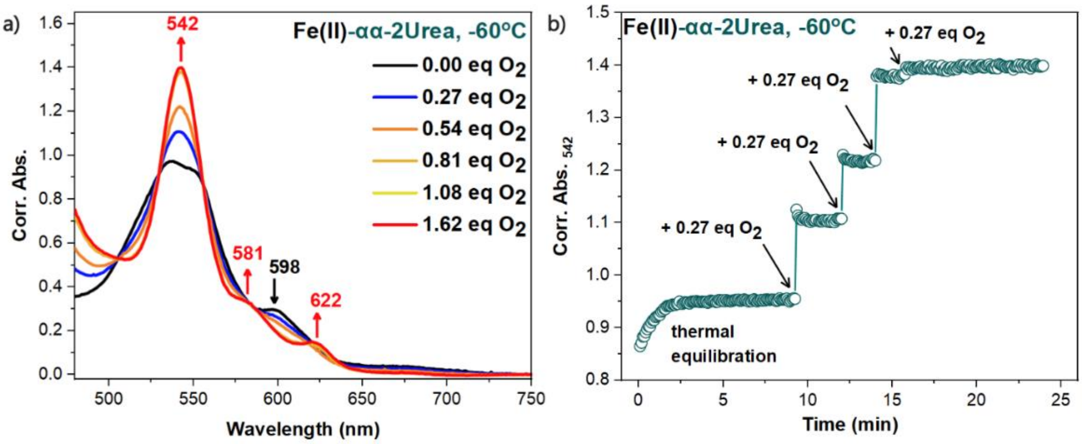

Fig. 1-28 a) UV Vis evolution spectra of **Fe^{II}-αα-2Urea** upon titration with aliquots of an O_2 saturated THF solution at -60 °C; b) Monitoring of the absorption peak at 542 nm upon addition of n eq. of O_2 over time. The absorbance was corrected to compensate for dilution upon addition of O_2 saturated THF solution .

The fact that after each sub-stoichiometric addition of O_2, the UV-Vis spectra remained unchanged, along with the requirement of only 1 eq. of O_2 to reach the end-point of the titration, provides strong proof of a 1:1 O_2 binding. In addition, it also suggests that O_2 prefers to bind on the **Fe^{II}** metal center by the site of the urea tweezers, since if O_2 bound on the other side of the macrocycle plane, it would possibly give rise to the formation of μ-peroxo dimers that would evolve to μ-oxo species, like in the case of FeTPP, as it will be discussed later on. Similar UV-Vis responses were also observed upon sub-stoichiometric addition of O_2 to a **Fe^{II}-αβ-2Urea** THF solution (Fig. S1-14).

On the contrary, when the **Fe^{II}TPP** THF solution was titrated with O_2 aliquots at -60 °C and was left to thermally equilibrate after each addition of O_2, the UV-Vis spectra rapidly changed and gave rise to the unknown absorbances at the Q region, as illustrated in Fig. 1-29a and Fig. 1-29b, corresponding probably to the decomposition of the **FeTPP (*S*)** intermediate.

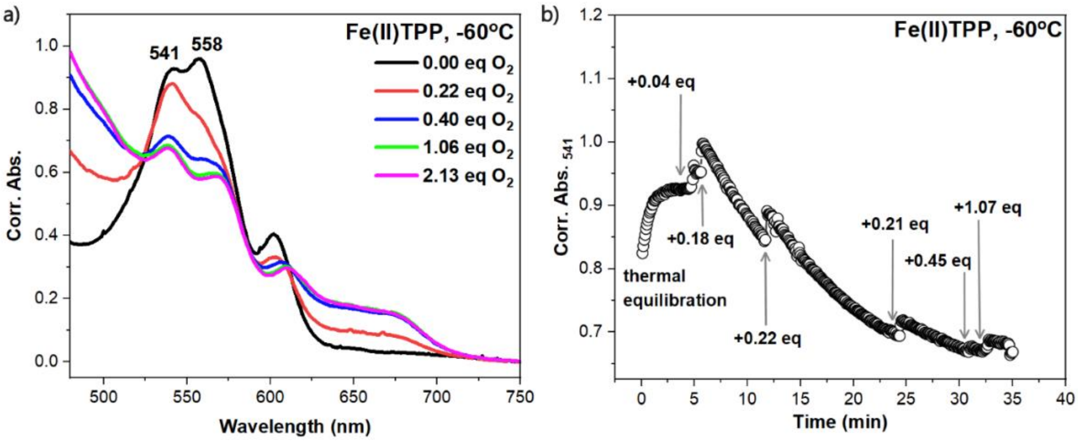

Fig. 1-29 a) UV Vis evolution spectra of **Fe^{II}TPP** upon titration with aliquots of an O_2 saturated solution at -60 °C; b) Monitoring of the absorption peak at 541 nm upon addition of eq. of O_2 over time. The absorbance was corrected due to dilution.

We speculate that the obtained UV-Vis spectra, after each addition of O_2, correspond to a mixture of species in the resulting solution. These species can be **FeTPP (*S*)**, peroxo-bridged Fe^{III}TPP dimers (Fe^{III}TPP-OO-Fe^{III}TPP) as well its decomposition products, μ-oxo [Fe^{III}TPP]$_2$O complexes, as it is established for ferrous porphyrins that lack a well-orchestrated second coordination sphere.[162] Our stoichiometric studies for FeTPP, raise doubts about whether Fe^{II}TPP can bind O_2 equimolarly as has been previously proposed.[157]

Based on these findings, it is apparent that the functionalization of the second coordination sphere of iron porphyrins with multi-point hydrogen bonding groups is essential to facilitate the stoichiometric O_2 binding to the reduced **Fe^{II}** metal center. In addition, according to the method reported by Mayer[159], the equilibrium constant of O_2 binding to the Fe^{II}-αα-2Urea was calculated at 298 K and the obtained value was $K_{O2} = 6.62\ M^{-1}$, which is higher than the corresponding one for the parent FeTPP ($KO_2 = 5.09\ M^{-1}$) [156]. However, as is discussed in Annex I, considerable concerns are raised about Mayer's K_{O2} determination method.

1.5.1.4 EPR studies

The successful chemical reduction of **Fe^{III}-αα-2Urea** to **Fe^{II}-αα-2Urea** and the formation of the corresponding end-on **(*S*)** species is further supported by EPR spectroscopy studies. As shown in Fig. 1-30, the EPR spectra of a **Fe^{III}-αα-2Urea** THF solution recorded at 10 K displayed a g tensor values of 5.9 and 2.0, which are typical for high-spin (S= 5/2) chloro-porphyrinato **Fe^{III}** complexes[163]. Upon reduction with Zn amalgam, the resultant solution exhibited an EPR silent spectrum, suggesting the formation of **Fe^{II}** (d^6) species that can be either diamagnetic (S=0) or paramagnetic (S=1, S=2) which due to the high zero-field splitting parameter (D) are EPR silent[164].

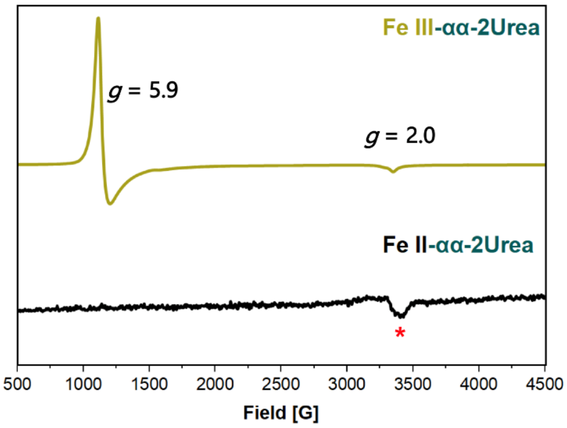

Fig. 1-30 X-band EPR spectra of **Fe^{III}-αα-2Urea** (yellow line) and **Fe^{II}-αα-2Urea** (black line) recorded at 10 K in THF.

Oxygenation of the **Fe^{II}-αα-2Urea** THF solution at -90 °C resulted in no changes in the EPR spectrum, although the reaction products exhibited completely different UV-Vis features compared to the **Fe^{II}-αα-2Urea** precursor. These observations are consistent with the formation of low-spin **Fe^{III}** metal center antiferromagnetically coupled with the unpaired electron of the bound superoxide (Fig. 1-31) as has been previously proposed for [(P^{Py}) **Fe^{III}-($O_2^{\bullet-}$)**] porphyrin intermediates[165],[166]. **Fe-αβ-2Urea (*S*)** also exhibited an EPR silent spectrum (Fig. S1-21).

---

[162] Chin, D-H., La Mar, G.N., Balch, A.L., *J. Am. Chem. Soc.*, **1980**, 102, 13, 4344–4350, DOI: 10.1021/ja00533a009

[163] Shankar, S., Peters, M., Steinborn, K., Krahwinkel, B. *et al.*, *Nat. Commun.* **2018**, 9, 4750, DOI: 10.1038/s41467-018-07023-1

[164] Walker, F. A., Simonis, U., "Iron Porphyrin Chemistry-A Ten-Year Update," In Encyclopedia of Inorganic Chemistry, Ed. 2, King, R. B., Wiley & Sons, Ltd.: Chichester, **2005**, 2390-2521, ISBN: 0-470-86078-2

[165] Li, Y., Sharma, S.K., Karlin, K.D., *Polyhedron*, **2013**, 58, 190-196, DOI: 10.1016/j.poly.2012.11.011

[166] Sharma, S.K., Rogler, P.J., Karlin, K.D., *J. Porphyr. Phthalocyanines*, **2015**, 19, 1-3, 352-360, DOI :10.1142/S108842461550025X

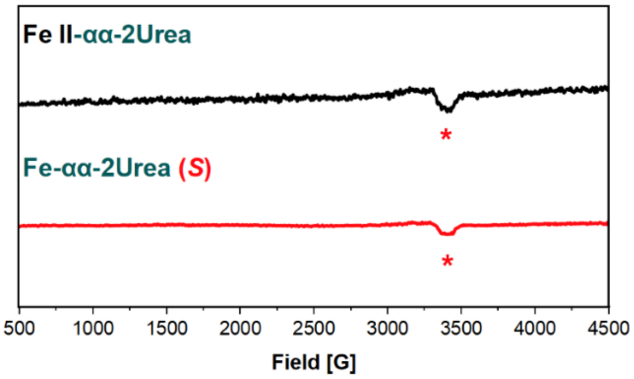

Fig. 1-31 X-band EPR spectra of **Fe^{II}-αα-2Urea** (black line) and **Fe^{II}-αβ-2Urea** (black line) recorded at 10 K in THF. Possible spin states and corresponding d orbital configuration for Fe^{III} and Fe^{II} porphyrins.

1.5.1.5 Preliminary resonance Raman (*r*Raman) studies

The electronic properties of **Fe^{II}**-αα-2Urea and **Fe^{II}**-αβ-2Urea and their $^{16}O_2$ reaction products, **Fe-αα-2Urea (*S*)** and **Fe-αβ-2Urea (*S*)**, respectively, were further investigated by *r*Raman spectroscopy. The high-frequency *r*Raman spectra for the reduced (**Fe^{II}**) and corresponding Fe-O_2 adducts were obtained with excitation at 441.6 nm.

The *r*Raman spectra of **Fe^{II}-αα-2Urea** exhibited oxidation marker bands (ν$_4$) at 1345 cm^{-1} and a spin-state marker band (ν$_2$) at 1539 cm^{-1} which are characteristic of a high-spin (S=2) 5-coordinated heme-Fe^{II} complex[167]. Similar vibrations frequencies were also obtained for **Fe^{II}-αβ-2Urea,** as indicated in Fig. 1-32.

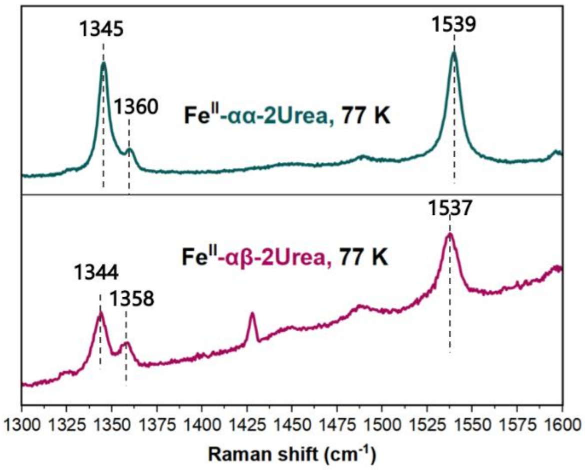

Fig. 1-32 Comparison of rRaman spectra of **Fe^{II}-αα-2Urea** (top) and **Fe^{II}-αβ-2Urea** (bottom) in MeTHF at 77 K. Spectra were collected with Q band excitation at 441.6 nm.

Oxygenation of a MeTHF solution containing the **Fe^{II}**-αα-2Urea and **Fe^{II}**-αβ-2Urea complexes resulted in *r*Raman spectra changes which suggest the formation of new species, presumably their corresponding Fe-O_2 adducts. As shown in Fig. 1-33, the *r*Raman spectrum of the **Fe^{II}**-αα-2Urea $^{16}O_2$ solution displayed two major sets of ν$_4$ and ν$_2$ marker bands at 1364 and 1555 cm^{-1}, which are indicative of high-spin **Fe^{III}** heme-species, while no *r*Raman vibration frequencies that could suggest the formation of low-spin **Fe^{III}-αα-2Urea (*S*)** were detected. According to *r*Raman spectroscopy studies, 5-coordinated low-spin (S=1/2) **porphyrin-Fe^{III}-($O_2^{\bullet-}$)** end-on **(*S*)** species exhibit a set of ν$_4$ and ν$_2$ marker bands between 1365-1369 cm^{-1} and

---

[167] Linard, J.E., Shriver, D.F., Basolo, F., *PNAS USA*, **1980**, 77, 4, 1741-1744, DOI: 10.1073/pnas.77.4.1741

1562-1569 cm^{-1}, respectively[168]. Additionally, 6-coordinated low-spin (S= 1/2) **Fe^{III}**-($O_2^{\bullet-}$) derivatives display ν_4 and ν_2 vibration frequencies in between 1374-1376 cm^{-1} and 1584-1588 cm^{-1} [169].

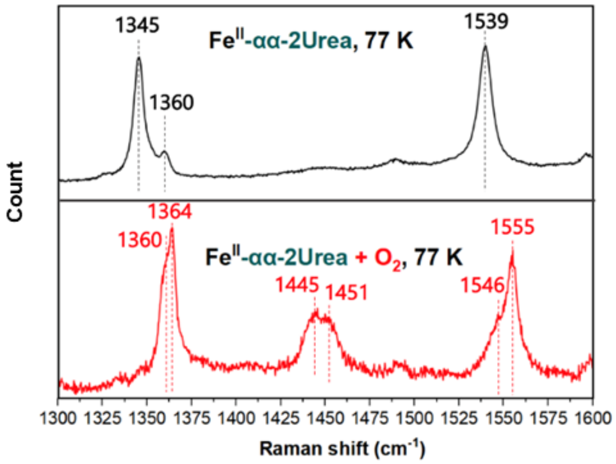

Fig. 1-33 rRaman spectra of **Fe^{II}-αα-2Urea** (top) and **Fe^{II}-αα-2Urea + $^{16}O_2$** (bottom) in MeTHF at 77 K. Spectra were collected with Q band excitation at 441.6 nm.

Similar *r*Raman features were also observed in the case of the oxygenated **Fe^{II}**-αβ-2Urea solution, with the only exception that an additional ν_4 marker band at 1565 cm^{-1} was observed, suggesting a minor fraction of **Fe^{III}**-αβ-2Urea ***(S)*** species[170], as shown in Fig.1-34.

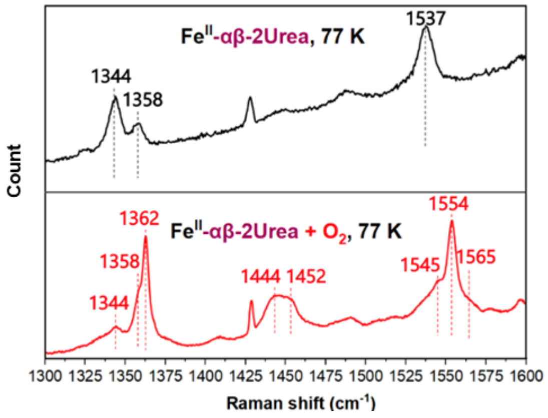

Fig. 1-34 *r*Raman spectra of **Fe^{II}-αβ-2Urea** (top) and **Fe^{II}-αβ-2Urea + $^{16}O_2$** (bottom) in MeTHF at 77 K. Spectra were collected with Q band excitation at 441.6 nm.

Temperature annealing of the **Fe^{II}-αα-2Urea** aerobic solution from 77 K (-196 °C) to 223 K (-50 °C) gave rise to a new set of ν_4 and ν_2 marker bands at 1367 and 1565 cm^{-1} that fit well with previously well-characterized low-spin **Fe^{III}**-($O_2^{\bullet-}$) ***(S)*** species, as indicated in Fig.1-35.

---

[168] Mittra, K., Chatterjee, S., Samanta, S., Sengupta, K., Bhattacharjee, H., Dey, A., *Chem. Commun.*, **2012**, 48, 10535–10537, DOI: 10.1039/c2cc35162e

[169] Seal, M., Mukherjee, S., and Ghosh Dey, S., *Metallomics*, **2016**, 8, 12, 1266-1272, DOI: 10.1039/c6mt00214e

[170] Sengupta, K., Chatterjee, S., Samanta, S., Dey, A., *PNAS USA*, **2013**, 110, 21 | 8431–8436 843, DOI: 10.1073/pnas.1300808110

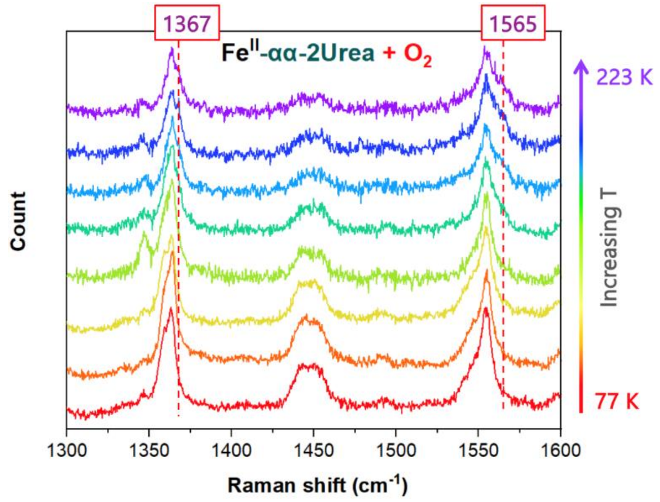

Fig. 1-35 *r*Raman spectra evolution of **Fe^{II}-αα-2Urea** + **$^{16}O_2$** upon increasing the temperature from 77 K to 223 K.

On the other hand, the temperature increase of the **Fe^{III}-αβ-2Urea (*S*)** species solution from 77 (-196 °C) to 223 K (-50 °C) resulted in the generation of **Fe^{II}-αβ-2Urea** species with v_4 and v_2 marker bands at 1347 and 1545 cm^{-1} (Fig. 1-36).

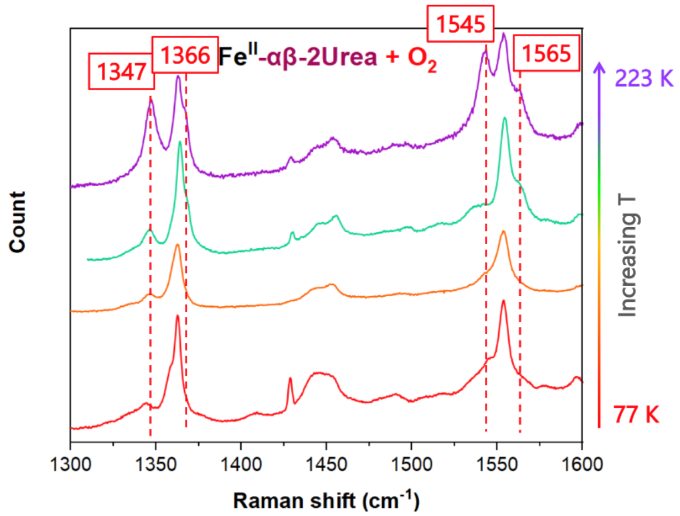

Fig. 1-36 rRaman spectra evolution of **Fe^{II}-αβ-2Urea** + **$^{16}O_2$** upon increasing the temperature from 77 K to 223 K.

The formation of the **Fe^{II}** reduced species at 223 K suggests a weaker Fe-O$_2$ stabilization, presumably due to the presence of only one urea function in the second-coordination sphere of the **Fe-αβ-2Urea**, rendering the **Fe^{III}**-αβ-2Urea **(*S*)** species more prompt to photolysis.

As such, the *r*Raman studies at 223 K further support our low-temperature UV-Vis findings that the **Fe-αα-2Urea** catalyst with two multi-point hydrogen bonding groups at the same plane of the porphyrin stabilizes more efficiently the **Fe^{III}**-($O_2^{\bullet-}$) **(*S*)** intermediates. Currently, the temperature-dependent partial conversion of the high-spin **Fe^{III}** heme-species to low-spin **Fe^{III}**-αβ-2Urea **(*S*)** species is under investigation.

1.5.2. Formation of the Peroxo (P) species

The one-electron reduction of the **Fe-αα-2Urea (*S*)** or **Fe-αβ-2Urea (*S*)** was realized at -80 °C by adding cobaltocene ($CoCp_2$, E=-1.33 V *vs.* $Fc^{+/0}$) to their Ar-degassed solutions. The addition of 3 eq. of $CoCp_2$ brought forth a new species which exhibited red-shifted Soret and Q bands compared to their corresponding Fe-O_2 precursors as shown in Fig. 1-37. The UV-Vis spectra of the resultant **Fe-αα-2Urea (*S*)** reduced solution displayed absorption maxima at 436, 547, 564, and 610 nm (Fig. 1-37a), whereas the newly formed species upon reduction of **Fe-αβ-2Urea (*S*)** had a UV-Vis fingerprint with λ_{max}= 434, 556 (br), and 610 nm (Fig. 1-37b).

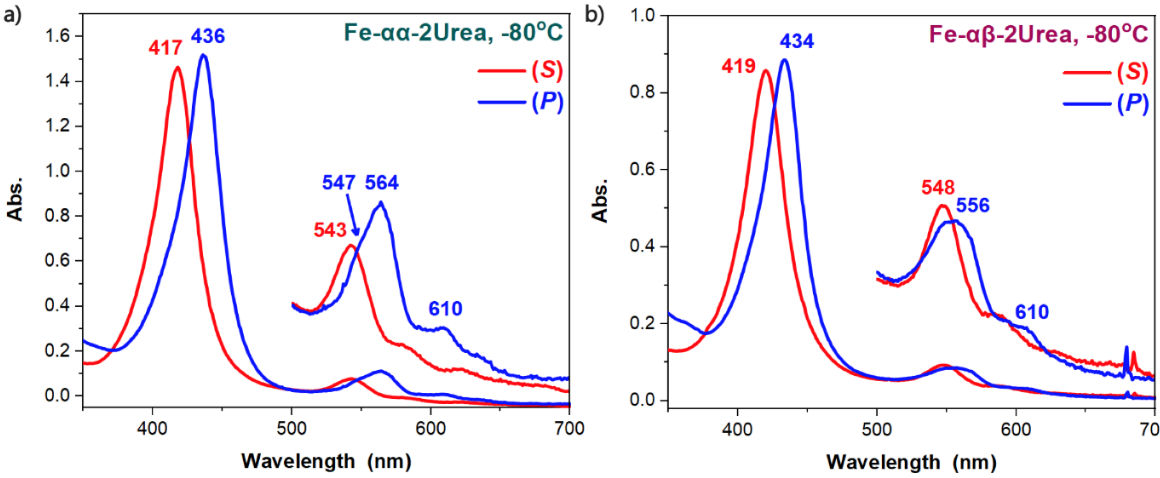

Fig. 1-37 UV-Vis spectra of the **(*S*)** species in THF/Butyronitrile 1:1 at -80 °C (red line) and its reaction with 3 eq of $CoCp_2$ to afford the one-electron reduced **(*P*)** intermediate (blue line); a) for **Fe-αα-2Urea** and b) **Fe-αβ-2Urea**. The inset shows the magnified Q-band region.

The electronic absorption spectra obtained for the reduced **Fe-αα-2Urea (*S*)** and **Fe-αβ-2Urea (*S*)** species exhibited similar λ_{max} values with other side-on ferric porphyrin peroxide intermediates reported in the literature [171], [172], suggesting the formation of side-on **Fe^{III}-αα-2Urea (*P*)** and **Fe^{III}-αβ-2Urea (*P*)**, respectively.

The same UV-Vis absorption features were also obtained when the **Fe-αα-2Urea (*S*)** species were chemically reduced with a weaker reductant, Cr(η-C_6H_6)$_2$ (-1.15 V *vs.* $Fc^{+/0}$) (Fig. S1-20), further supporting the potential value of the Fe^{III}-($O_2^{\bullet -}$)**(*S*)**/ Fe^{III}-(O_2^{2-})] **(*P*)** redox couple (E= -0.796 V *vs.* $Fc^{+/0}$) observed by cyclic voltammetry experiments (Fig 1-20).

1.5.2.1 EPR studies

To further investigate the formation of side-on peroxo species, EPR spectroscopy studies for the chemically generated **Fe-αα-2Urea (*P*)** and **Fe-αβ-2Urea (*P*)** were carried out at 8.6 K. As shown in Fig. 1-38, the EPR spectra of **Fe-αα-2Urea (*P*)** and **Fe-αβ-2Urea (*P*)** species displayed both a g tensor value of 4.28, which is typical for high-spin Fe^{III} complexes (S= 5/2) and is indicative of side-on **(*P*)** heme intermediates[152].

---

[171] Liu, J-G., Ohta, T., Yamaguchi, S., Ogura, T., Sakamoto, S., Maeda, Y., Naruta, Y., *Angew. Chem. Int. Ed.*, **2009**, 48, 9262-9267, DOI: 10.1002/anie.200904572

[172] Selke, M., Sisemore, M.F., Valentine, J.S., *J. Am. Chem. Soc.*, **1996**, 118, 8, 2008-2012, DOI: 10.1021/ja953694y

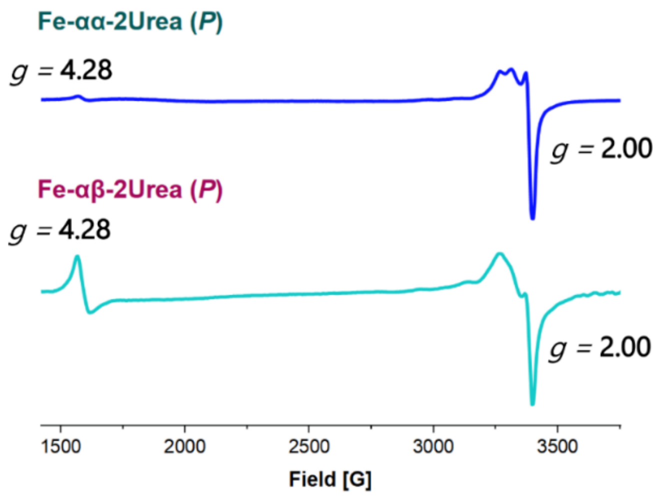

Fig. 1-38 X-band EPR spectra of **Fe-αα-2Urea (*P*)** (blue line) and **Fe-αβ-2Urea (*P*)** (light blue line) recorded at 10 K.

However, additional g signals were also observed at higher field. The EPR spectra of the Fe-αα-2Urea **(*P*)** showed signals of g=2.27, 2.18, 2.07, and 2.04 (Fig. 1-39a) whereas, for the Fe-αα-2Urea **(*P*),** the extra set of signals was at g=2.3, 2.16, 2.07, and 2.05 (Fig. 1-39b).

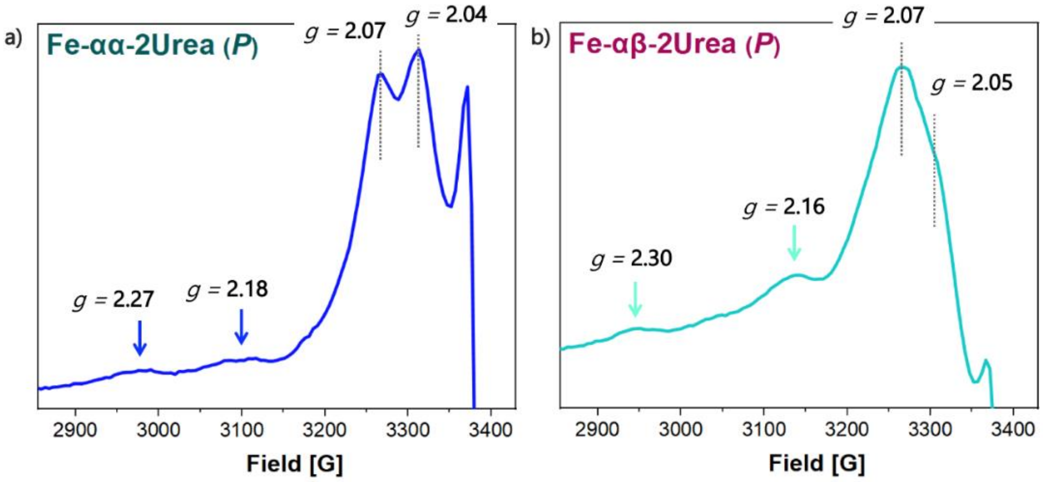

Fig. 1-39 Magnified X-band EPR spectra of a) **Fe-αα-2Urea (*P*)** and b) **Fe-αβ-2Urea (*P*)** at the high field region recorded at 10 K.

The presence of such signals may indicate a mixture of (i) low-spin end-on ferric **(*P*)**, (ii) ferrous **(*P*)** species, or even (iii) hydroperoxo **(*HP*)**. End-on ferric **(*P*)** intermediates (**Fe^{III}-(O_2^{2-})**) and ferrous **(*P*)** species (**Fe^{II}-($O_2^{\bullet-}$)**) are electronic tautomers that differ in the localization of the electrons. In the case of the **Fe^{III}-(O_2^{2-})**, the electron density is localized on the O_2 frontier orbitals, whereas for **Fe^{III}-(O_2^{2-})** on the iron metal center. As such, these two species exhibit different EPR spectra. Heme end-on **Fe^{III}-(O_2^{2-}) (*P*)** intermediates, for example, display a set of g-tensor components of 2.24, 2.14, 1.96 [173],[174], while the EPR spectra of cryo-generated or chemically produced **Fe^{II}-($O_2^{\bullet-}$) (*P*)** species show a signal with g values of

---

[173] Leibl, W., Nitschke, W., Huttermann, *J. Biochim. Biophys. Acta*, **1986**, 870, 20-30, DOI: 10.1016/0167-4838(86)90004-X .

[174] Sligar, S.G., Makris, T.M., Denisov, I.G., *Biochem. Biophys. Res. Commun.*, **2005**, 338, 1, 346-354, DOI: 10.1016/j.bbrc.2005.08.094

2.10[175] and 2.09-2.10[176],[177], respectively. In addition, EPR studies on heme **Fe^{III}-(O_2^{2-})** **(*P*)** and **Fe^{II}-($O_2^{\bullet -}$)** **(*P*)** at low temperatures (4K-77K) have shown that upon annealing the temperature of the experiment (i.e., 173K), the corresponding **(*P*)** intermediates are evolving to their hydroperoxo **(*HP*)**. ***HP*** species displaying a set of g values of 2.30, 2.17, and 1.95[178]. We cannot exclude the possibility, though, that the g= 2.3, 2.16 for **Fe-αβ-2Urea (*P*)** might correspond to their protonated products. The formation of the **Fe-αβ-2Urea (*HP*)** species could be explained by the presence of traces of water in the samples, possibly upon their transfer into the EPR spectrometer (absorption of moisture).

At present, the assignment of the additional g tensor components to any of the species discussed above would be misleading, and simulations on the EPR spectra for the **Fe-αα-2Urea (*P*)** and **Fe-αβ-2Urea (*P*)** are required to interpret the additional signals.

1.5.2.2 Interconvertibility of the Superoxo and Peroxo Intermediates

As shown in Fig. 1-40, the addition of an oxidant (ferrocenium, Fc^+) to the solution of the **Fe-αα-2Urea (*P*)** and **Fe-αβ-2Urea (*P*)** at -80 °C resulted in the appearance of the UV-Vis features that corresponded to the **Fe-αα-2Urea (*S*)** and **Fe-αβ-2Urea (*S*)** species, respectively.

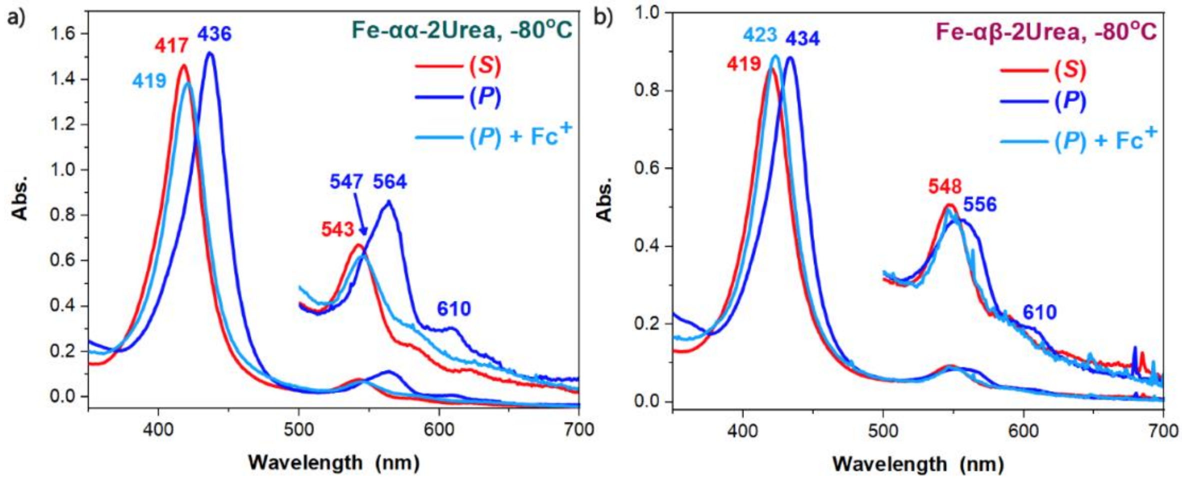

Fig. 1-40 UV Vis spectra of the **(*S*)** species in THF/butyronitrile 1:1 at -80 °C (red line) and its reaction with 3 eq of $CoCp_2$ to afford the one-electron reduced **(*P*)** intermediate (blue line). Addition of 3 eq of Fc^+ yielded back the **(*S*)** species (light blue line); a) for **Fe-αα-2Urea** and b) **Fe-αβ-2Urea**. The inset shows the magnified Q-band region.

The interconvertibility between the chemically produced **(*P*)** and **(*S*)** intermediates of **Fe-αα-2Urea** and **Fe-αβ-2Urea** further corroborated our initial electrochemistry findings that the reduction of the **(*S*)** to the **(*P*)** species is a reversible process.

1.5.3. Formation of the Hydroperoxo (*HP*) species

Moving one step forward, the addition of methanol (MeOH, 1.55 mM) as a proton source to a solution of **Fe-αα-2Urea (*P*)** and **Fe-αβ-2Urea (*P*)** at -80 °C afforded their corresponding **Fe-αα-2Urea (*HP*)** and **Fe-αβ-2Urea (*HP*)** species. **Fe-αα-2Urea (*HP*)** exhibited UV-Vis absorption maxima at 426, 544, 561, and 614 nm (Fig. 1-41a), while **Fe-αβ-2Urea (*HP*)**

---

[175] Ohta, T., Liu, J-G., Nagaraju, P., Ogura T., Naruta, Y., *Chem. Commun.*, **2015**, 51, 12407-12410, DOI: 10.1039/c5cc03520a

[176] Duerr, K., Olah, J., Davydov, R., Kleimann, M., Li, J., *et al.*, *Dalton Trans.*, **2010**, 39, 2049-2056, DOI: 10.1039/b920237d

[177] Duerr, K., Troeppner, O., Olah, J., Li, J., Zahl, A. *et al.*, *Dalton Trans.*, **2012**, 41, 546–557, DOI: 10.1039/c1dt11521a

[178] Davydov, R., Makris, T.M., Kofman, V., Werst, D.E., Sligar, S.G., Hoffman, B.M., *J. Am. Chem. Soc.*, **2001**, 123, 1403-1415, DOI: 10.1021/ja003583l

displayed absorptions at 428, 551, and 589 nm (Fig. 1-41b). These UV-Vis characteristics matched well with previously reported low-spin **(*HP*)** heme complexes by Naruta *et al.*[171]

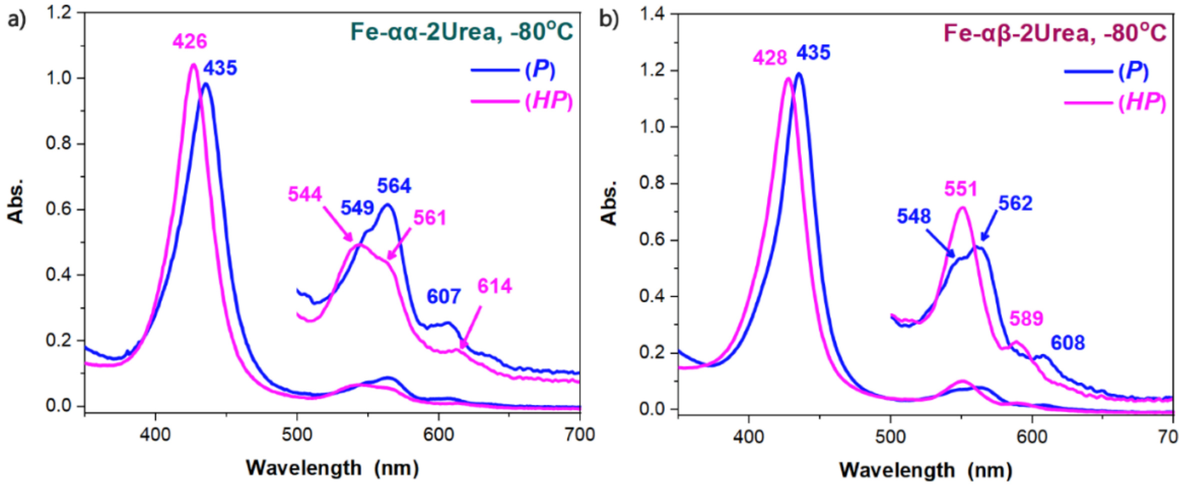

Fig. 1-41 UV Vis spectra of the **(*P*)** species in THF/Butyronitrile 1:1 at -80ºC (blue line) and its reaction with 250 eq of MeOH to afford the **(*HP*)** (magenta line); a) for **Fe-αα-2Urea** and b) **Fe-αβ-2Urea**. The inset shows the magnified Q-band region.

The fact that a weak acid could protonate the side-on **(*P*)** species and give their stable **(*HP*)** complexes adds another facet to Naruta's findings[171] where the authors demonstrated that the presence of a strong axial ligand (e.g., imidazolyl) is essential to generate the **(*HP*)** species under similar conditions. As such, our experimental results suggest that the generation and stabilization of ferric-**(*HP*)** intermediates are possible to be finetuned by the proper modification of the second-coordination sphere of a catalyst with suitable H-bonding donors, without the need for a strong axial base ("push" effect).

1.6 Conclusions and Perspectives

In conclusion, we have synthesized two atropisomers of an iron porphyrin functionalized with urea units in their second coordination sphere as multi-point hydrogen-bonding groups. Both iron complexes, **Fe-αα-2Urea** and **Fe-αβ-2Urea**, and their free base analogs were fully characterized and their X-ray diffraction structures resolved. Fe-αα-2Urea crystallized as a *μ*-oxo dimer, whereas **Fe-αβ-2Urea** as a monomer. In particular, the latter was obtained as a chloro-porphyrinato Fe^{III} and hydroxo-porphyrinato Fe^{III} complex in which a water molecule is hydrogen bonded to the urea unit and the -OH axial ligand, highlighting the potential role of the urea function(s) in the stabilization of the O_2 reduction catalytic intermediates.

The electrochemical properties of **Fe-αα-2Urea** and **Fe-αβ-2Urea** were investigated by cyclic voltammetry in solution under anaerobic and aerobic conditions in the absence of a proton source. Under an Argon atmosphere, both iron porphyrin derivatives exhibited three successive reversible redox waves upon scanning in the negative potential window, that were attributed to the Fe$^{III/II}$ and the formal Fe$^{II/I}$ and Fe$^{I/0}$ couples. We also noted a positive shift in the potentials when compared to the parent FeTPP due to the urea functions holding the electron-withdrawing -CF_3 groups. When the electrolytic solution was saturated with O_2, the Fe$^{III/II}$ redox couple became irreversible, with a slight gain in the current intensity. Such a response is indicative of O_2 binding to the ferrous iron center followed by a simultaneous electron transfer from the metal to the bound O_2 molecule to yield a Fe^{III}-$O_2^{\bullet-}$ noted as superoxo (*S*) intermediate. The CVs of Fe-αα-2Urea and Fe-αβ-2Urea displayed a new cathodic wave prior to the Fe$^{II/I}$ redox couple, and the reduction of O_2 at the surface of the GC electrode.

This redox process seemed quasi-reversible, and it was absent in the non-modified FeTPP. This additional wave was assigned to the further reduction of the **Fe-αα-2Urea (*S*)** and **Fe-αβ-2Urea (*S*)** species to their corresponding **Fe^{III}-O_2^{2-} (*P*)** intermediates, as has been previously reported by Anxolabéhère-Mallart and co-workers.

Our iron porphyrins models point out the essential role of the urea units on the second coordination sphere to stabilize the (S) intermediates and make the reduction of the **(*S*)** to **(*P*)** species thermodynamically more favorable. Interestingly, at a scan rate of 5 mV/sec, the reduction of the **(*S*)** to **(*P*)** species becomes a quasi-reversible process for both **Fe-αα-2Urea** and **Fe-αβ-2Urea** porphyrins. Hence, we determined the redox potential of the (*S*)/(*P*) couple at E= -0.796 V vs. $Fc^{+/0}$, which was the same for both atropisomers. It is worth noting that this is the first example of an iron porphyrin **(*S*)**/**(*P*)** redox couple determined via cyclic voltammetry. In addition, this redox process was realized at considerably more positive potential than other iron porphyrins derivatives documented in the literature.

Moreover, to rationalize the reversibility of the **(*S*)**/**(*P*)** redox couple upon decreasing the scan rate, we performed a series of cyclic voltammetry studies in which the electrolytic solution contained 0.33% of H_2O. Our findings suggest that H_2O might also hold an important role in stabilizing the ORR intermediates, as shown from the obtained X-ray structure for the hydroxo-porphyrinato **Fe^{III}αβ-2Urea** atropisomer. In the presence of H_2O, the quasi-reversibility of the **(*S*)**/**(*P*)** redox couple was restored even at 25 mV/sec, compared to ≤ 10 mV/sec in dry solvents. At this moment, this H_2O scan rate-dependent reversibility of the **(*S*)**/**(*P*)** redox process is under further investigation before reaching any conclusive remarks.

To further characterize the first intermediates involved in the activation and reduction of molecular O_2, we also generated the **(*S*)**, **(*P*)**, and **(*HP*)** species of **Fe-αα-2Urea** and **Fe-αβ-2Urea** chemically at low temperatures. The **(S)** intermediates exhibited a remarkable stability at -20°C for over 30 min for the **Fe-αα-2Urea (*S*)** when compared to the corresponding Fe-αβ-2Urea species. Yet, both were substantially more stable than the parent **FeTPP (*S*)**. These results further corroborate our initial cyclic voltammetry findings that incorporating urea arms in the second coordination sphere greatly enhances the stability of the Fe-O_2 adducts. In addition, the topology of the urea functions also influences the stability of the superoxo species indicating that the superoxo intermediates are better stabilized when both of the urea groups are on the same porphyrin plane. Moreover, **Fe^{II}-αα-2Urea** and **Fe^{II}-αβ-2Urea** bound O_2 stoichiometrically. However, this was not the case for **Fe^{II}TPP**. The EPR spectra of both the **Fe-αα-2Urea (*S*)** and **Fe-αβ-2Urea (*S*)** were silent, suggesting the formation of diamagnetic species.

To gain more insights into such intermediates' electronic structures, we performed *r*Raman spectroscopy studies at 77K. The *r*Raman spectrum of a **Fe^{II}-αα-2Urea** frozen solution saturated in $^{16}O_2$ displayed two major sets of v_4 and v_2 marker bands at 1364 and 1555 cm^{-1}, indicative of high Fe^{III} porphyrins. This is in contrast with known iron porphyrin **(S)** intermediates, which are typically low-spin. Similar *r*Raman features were also observed for **Fe-αβ-2Urea**. However, a low-intensity v_4 marker band at 1565 cm^{-1} suggests a minor fraction of **Fe^{III}-αβ-2Urea (S)** species. More importantly, upon increasing the temperature from 77K to 223K, the high-spin **Fe^{III}-αα-2Urea** species evolved to a low-spin **Fe^{III}-αα-2Urea (*S*)** intermediate with v_4 and v_2 marker bands at 1367 and 1565 cm^{-1} that are in good agreement with previously reported iron porphyrins superoxo intermediates. When similar studies were carried out for the Fe-αβ-2Urea atropisomer, the obtained *r*Raman signatures at 223K suggested the formation of mainly **Fe^{II}-αβ-2Urea**, probably due to the weaker stabilization of the **Fe-oxy** intermediate to the **Fe-αα-2Urea**. Unfortunately, due to low-resolution signals for the Fe-O and O-O vibration frequencies region, we could not obtain any information concerning the coordination mode of the O_2 molecule on the iron center. At this moment, optimization of the *r*Raman conditions and studies with $^{16}O_2$ and $^{18}O_2$ are ongoing to elucidate this aspect. Furthermore, the determination of the pK_a of the superoxo intermediates is also under examination.

Moving one step forward, after the successful formation of the **Fe-αα-2Urea (*S*)** and **Fe-αβ-2Urea (*S*)** species, we chemically reduced them to their corresponding **(*P*)** intermediates at -80 °C. Their UV-Vis spectra exhibited characteristic absorption bands of side-on peroxo species. In addition, the conversion of the **(*S*)** to **(*P*)** species was a reversible process, as our initial electrochemistry studies also indicated it at low scan rates. The EPR spectra of **Fe-αα-2Urea (*P*)** and **Fe-αβ-2Urea (*P*)** at 10 K further corroborate the UV-Vis findings concerning the formation of high-spin side-on peroxo species. However, additional signals were also present that might be attributed to low-spin **end-on ferric (*P*)** or/and **ferrous (*P*)** species. EPR simulation studies are currently underway to investigate the possible different coordination fashions of the peroxo ligand.

Finally, the **Fe-αα-2Urea (*HP*)** and **Fe-αβ-2Urea (*HP*)** species were generated via the addition of a strong or a weak acid to a solution of the corresponding **(*P*)** intermediates and characterized by UV-Vis spectroscopy studies at low-temperature. The fact that a weak acid could protonate the **(*P*)** species demonstrates that generating and stabilizing **ferric-(*HP*)** intermediates is possible by appropriately modifying the second-coordination sphere with suitable H-bonding donors urea functions without the need for a strong axial base. Here too, EPR and *r*Raman studies are ongoing.

At this point, it would be interesting to investigate whether a tethered axial base would affect the formation and the stability of the **(*S*)**, **(*P*)**, and **(*HP*)** species Currently, the ORR electrocatalytic activity of the **Fe-2Urea** atropisomers is under investigation in homogeneous conditions On a different note, the **Mn-αα-2Urea** and **Mn-αβ-2Urea** have been synthesized and preliminary ORR studies for the **Mn-αα-2Urea** are quite promising.

Annex I

Synthetic Procedure

Synthesis of αα-2Urea

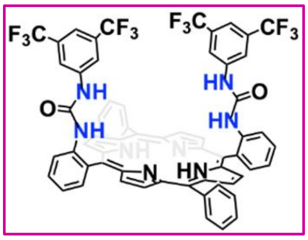

To a dry CH_2Cl_2 (20 mL) solution of αα-2NH_2PH_2 (95 mg, 147 µmol), 3,5-Bis(trifluoromethyl)phenyl isocyanate (100 µL, 0.590 mmol) was added and the resultant reaction mixture was left stirring at room temperature under anaerobic conditions for 12h and in the absence of light. Upon reaction completion, the crude solid was purified via column chromatography (SiO_2, CH_2Cl_2/Cyclohexane 1%) providing αα-2Urea as a purple solid. Finally, αα-2Urea was further purified by recrystallization from MeOH (156 mg, 92%). Single crystals were obtained by slow evaporation of an **αα-2Urea** saturated solution in CH_2Cl_2 (Fig.S1-1).

^{1}H NMR (360 MHz, Acetone-*d$_6$*): δ 8.88 (bs s, 8H), 8.52 (d, J = 7.8 Hz, 2H), 8.21 (d, J = 6.3 Hz, 2H), 8.12 (d, J = 7.8 Hz, 2H), 8.04 (dd, J_1 = 7.5 Hz, J_2 = 1.2 Hz, 2H), 7.88-7.78 (m, 10H), 7.58 (m, 6H), 7.38 (s, 2H), 7.32 (s, 2H), -2.74 (s, 2H) ppm.

ESI-HRMS: calculated m/z = 1155.2999 $[M+H^+]^+$ for $C_{62}H_{39}F_{12}N_8O_2$, found 1155.2940; calculated m/z = 1177.2818 $[M+Na^+]^+$ for $C_{62}H_{38}F_{12}N_8NaO_2$, found 1177.2761.

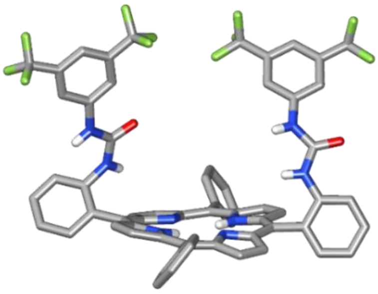

Fig. S1-1 Capped sticks representation of the X-ray crystal structures of **αα-2Urea**.

Synthesis of αβ-2Urea

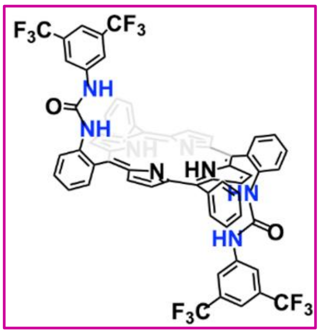

For the synthesis of αβ-2Urea, the same experimental procedure was followed as in the case of αα-2Urea with the only exception being the purification of the crude reaction mixture via column chromatography that was performed on SiO_2 with CH_2Cl_2/Hexane 25% as the eluent (103 mg, 89%). Suitable single crystals for X-ray diffraction were obtained by slow evaporation of an **αβ-2Urea** saturated solution in CH_2Cl_2/$CHCl_3$.

^{1}H NMR (360 MHz, Acetone-*d$_6$*): δ 8.91 (bs s, 8H), 8.73 (d, J = 8.1 Hz, 2H), 8.19 (m, 4H), 8.01 (dd, J_1 = 7.5 Hz, J_2 = 1.5 Hz, 4H), 7.93-7.78 (m, 10H), 7.59-7.52 (m, 6H), 7.39 (s, 2H), 7.36 (s, 2H), -2.76 (s, 2H) ppm.

ESI-HRMS: calculated m/z = 1155.2999 [M+H+] + for $C_{62}H_{39}F_{12}N_8O$, found 1155.2944; calculated m/z = 1177.2818 $[M+Na^+]^+$ for $C_{62}H_{38}F_{12}N_8NaO_2$, found 1177.2763.

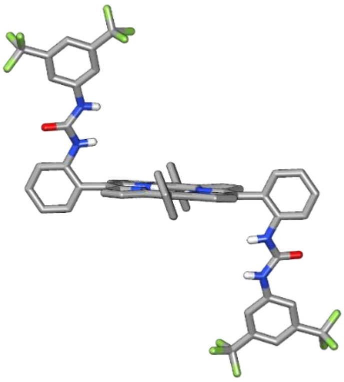

Fig. S1-2 Capped sticks representation of the X-ray crystal structures of **αβ-2Urea**.

Synthesis of Fe-αα-2Urea

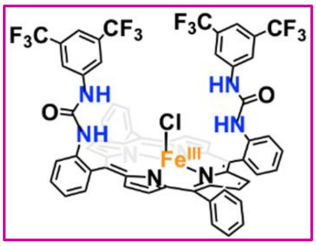

In an N_2-filled glovebox, αα-2Urea (100 mg, 87 µmol) was dissolved in dry THF (8 mL) and 20 eq. of lutidine (200 µL, 1.73 mmol) was slowly added under stirring. Once lutidine was added, $FeBr_2$ (152 mg, 0.705 mmol) was transferred to the resultant solution and the reaction mixture was left stirring in the absence of light. The progress of the reaction was monitored by thin-layer chromatography (TLC) and UV-Vis spectroscopy. Once the reaction reached completion, approximately after 16h, the solution was exposed to ambient conditions, and the solvent was evaporated under vacuum. The obtained solid was dissolved in CH_2Cl_2 (50 mL), washed with 1M HCl aqueous solution (2 x 200 mL), dried over Na_2SO_4, filtered, and evaporated in vacuo. The crude residue was purified via column chromatography (SiO_2, $CHCl_3$/MeOH 0.5%) providing **Fe-αα-2Urea** as a purple-orange solid (92.6 mg, 86%). Solid NaCl was introduced to the chromatographic column so at to ensure that the axial ligand of the Fe^{III} would remain the Cl^{-} anion. Single crystals for diffraction were obtained by slow evaporation of a saturated **Fe-αα-2Urea** DMF solution.

ESI-HRMS: calculated m/z = 1208.2115 $[M-Cl^{-}]^{+}$ for $C_{62}H_{36}F_{12}FeN_8O_2$, found 1208.2062.

Synthesis of Fe-αβ-2Urea

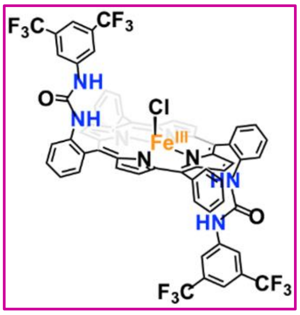

For the synthesis of Fe-αβ-2Urea, the same experimental procedure was followed as in the case of Fe-αα-2Urea, with the only difference that the purification via column chromatography was carried out on SiO_2 and a mixture of CH_2Cl_2/MeOH 2% as the eluent (60 mg, 79%). Single crystals for diffraction were obtained by slow evaporation of a saturated **Fe-αα-2Urea** DMF solution.

ESI-HRMS: calculated m/z = 1208.2115 $[M-Cl^{-}]^{+}$ for $C_{62}H_{36}F_{12}FeN_8O_2$, found 1208.2068; calculated m/z = 1262.2201 $[M-Cl^{-+}MeONa]^{+}$ for $C_{81}H_{47}F_{24}FeN_{12}NaO_5$, found 1262.2133.

Electrochemical Characterization

Cyclic Voltammetry Experiments

The electrochemical characterization of the studied compounds was realized in an electrochemical cell with a conventional three-electrode system. A glassy carbon electrode with a 3 mm diameter was used as the working electrode, a saturated KCl aqueous standard calomel electrode (SCE) as the reference, and a platinum wire as the counter electrode. Extra-dry dimethylformamide (DMF) was used as the solvent while recrystallized tertbutylammonium hexafluorophosphate ($TBAPF_6$) as the supporting electrolyte. The concentration of the studied compounds was 1 mM, otherwise noted, while $TBAPF_6$ was at 0.1 M concentration. At the end of each experiment, ferrocenium was added to the electrolytic solution as an internal standard. Before recording any cyclic voltammogram, the working electrode was carefully polished with a 6 μm diamond paste, washed successively with ethanol (EtOH) and acetone, and dried.

Anaerobic Conditions

Calculation of the Diffusion coefficient

The diffusion coefficients of **Fe-αα-2Urea** and **Fe-αβ-2Urea** catalysts were calculated by plotting the peak current of the **$Fe^{III/II}$** redox couple *vs*. the square root of the scan rate (Fig.S1-3 and Fig. S1-4, respectively), employing the Randles-Sevcik equation:

$$i_p = 0.4463\, nFAC \left(\frac{nFvD}{RT}\right)^{1/2}$$

where,

$n: number\ of\ electrons\ transferred, n = 1$

$F: Faraday\ constant, F = 96485\ Cmol^{-1}$

$A: surface\ of\ the\ electrode, A = 0.07065\ cm^2$

$v: scan\ rate, Vs^{-1}$

$D: diffusion\ coefficient, cm^2s^{-1}$

$R: gas\ constant, R = 8.314\ JK^{-1}mol^{-1}$

$T: temperature, \quad T = 278\ K$

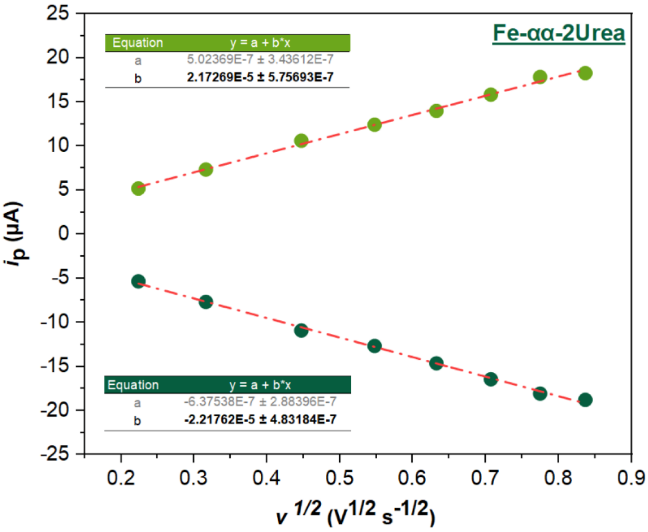

Fig. S1-3 Diffusion current peak (**$Fe^{III/II}$**) as a function of square root of scan rate for **Fe-αα-2Urea**. Conditions: 1 mM of catalyst in Ar-saturated DMF/$TBAPF_6$ (0.1 M) solution.

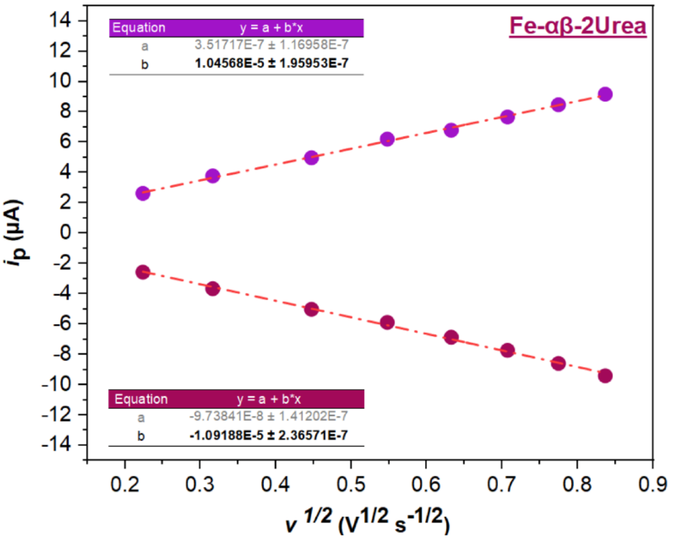

Fig. S1-4 Diffusion current peak (**$Fe^{III/II}$**) as a function of square root of scan rate for **Fe-αβ-2Urea**. Conditions: 0.45 mM of catalyst in Ar-saturated DMF/$TBAPF_6$ (0.1 M) solution.

Table S1-1. Average diffusion coefficients calculated from the **$Fe^{III/II}$** redox couple for the studied iron porphyrin catalysts.

Catalyst	$D\ (cm^2 s^{-1})$
Fe-αα-2Urea	$1.34\ x\ 10^{-6}$
Fe-αβ-2Urea	$1.53\ x\ 10^{-6}$

Under 1 atm of O_2 – non-catalytic Conditions

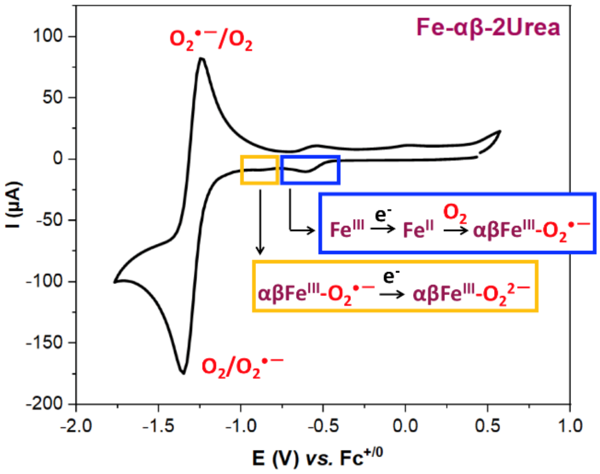

Fig. S1-5 CVs of 1 mM **Fe-αβ-2Urea** DMF/$TBAPF_6$ (0.1 M) solution in the presence of 1 atm O_2; scan rate= 100 mV/s.

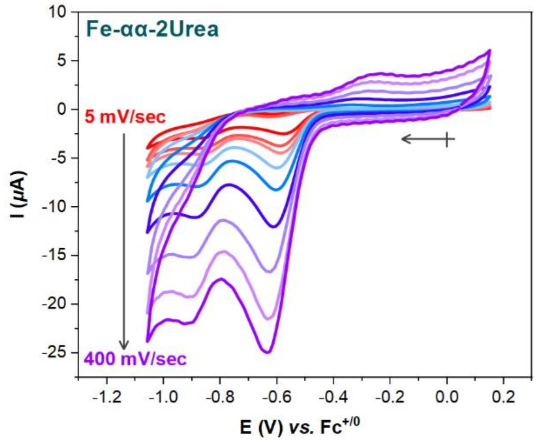

Fig. S1-6 CVs of 1 mM **Fe-αα-2Urea** DMF/TBAPF$_6$ (0.1 M) recorded at different scan rates under aerobic 1 atm of O_2.

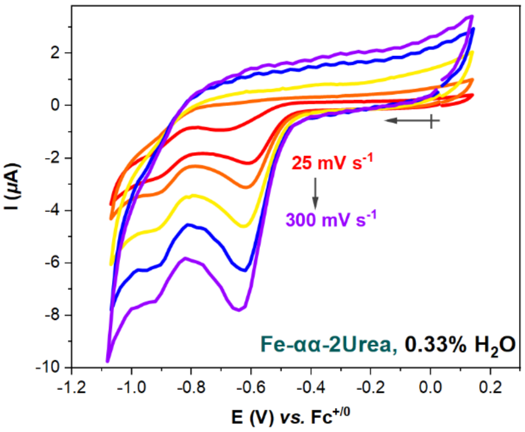

Fig. S1-7 CVs of 1 mM **Fe-αα-2Urea** DMF/TBAPF$_6$ (0.1 M) containing 0.33% of H_2O recorded at different scan rates in the presence of 1 atm O_2.

UV-Vis Spectroscopy Studies

Generation of Fe-αα-2Urea (*S*) and Fe-αβ-2Urea (*S*) species

Fe^{III}- αα-2Urea was chemically reduced to **Fe^{II}- αα-2Urea** with Zn amalgam in extra dry THF, in an N_2 atmosphere glovebox. A solution of the **Fe^{II}** species was then transferred to a 10 mm pathlength quartz cuvette and sealed carefully with a septum. The cuvette was placed out of the glovebox and cooled down in the cryostat chamber at -80 °C. The solution was allowed to thermally equilibrate for approximately 15 min. Thermal equilibration was controlled via UV-Vis spectrometry by following the maximum absorption increase of the Soret band. Once no UV-Vis changes were observed (λ_{max}= 427, 533, 546 nm) dioxygen was bubbled gently into the corresponding cryogenic **Fe^{II}** solution yielding the Fe-αα-2Urea **(*S*)** species (λ_{max}= 417, 542, 581, 623 nm). **Fe^{II}**-αβ-2Urea (λ_{max}= 426, 536, 550 nm) and Fe-αβ-2Urea **(*S*)** (λ_{max}= 418, 543, 578, 620 nm) species were chemically prepared and characterized via UV-Vis spectroscopy following the same experimental procedure.

UV-Vis spectra of **Fe^{II}**-αα-2Urea and Fe-αβ-2Urea **(*S*)** species upon temperature increase

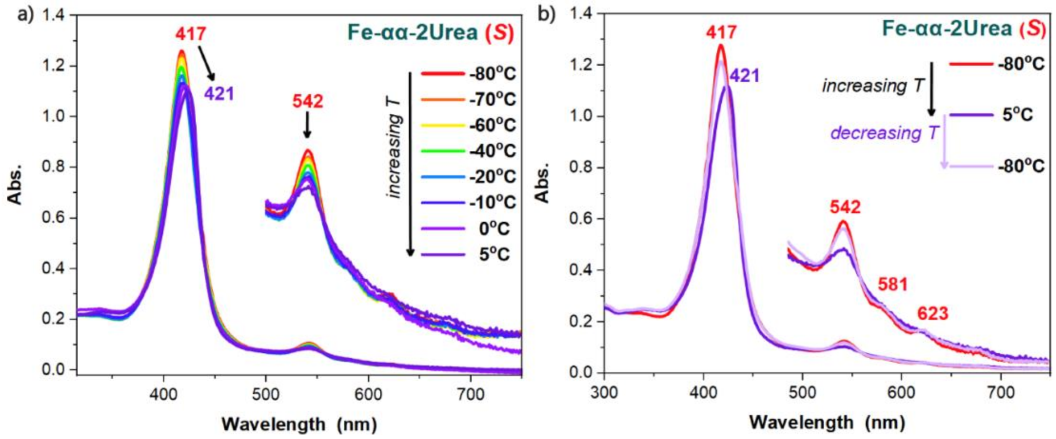

Fig. S1-8 a) Evolution of the **Fe-αα-2Urea (*S*)** UV-Vis spectra in THF upon gradually increasing the temperature from -80 °C to 5 °C b) Comparison of the UV-Vis spectra obtained initially at -80 °C (red line), when increasing the temperature at 5°C (purple line) and when decreasing the temperature at -80°C (light purple line).

Upon gradually increasing the temperature from -80 °C to 5 °C, the Soret band of the **Fe-αα-2Urea (*S*)** species shifted from 417 to 421 nm while the Q band at 542 nm became broader with its intensity being considerably lower (Fig. S1-8a). Subsequent re-cooling of the solution to -80 °C yielded an identical UV-Vis spectrum to the one initially recorded at -80 °C, as shown in Fig. S1-8b. Similar UV-Vis changes were also obtained for the **Fe-αβ-2Urea (*S*)** species (Fig. S1-9). The shift of the Soret band upon warming up and cooling down the solution of the **Fe-αα-2Urea (*S*)** and **Fe-αβ-2Urea (*S*)** species might suggest a reversible O_2 binding to the **Fe^{II}** metal center. It is worth noting that the decrease in the absorption intensity of the Soret and Q bands was also observed for their **Fe^{II}** analogs upon increasing the temperature of the solution; however, no shift was observed (Fig. S1-10).

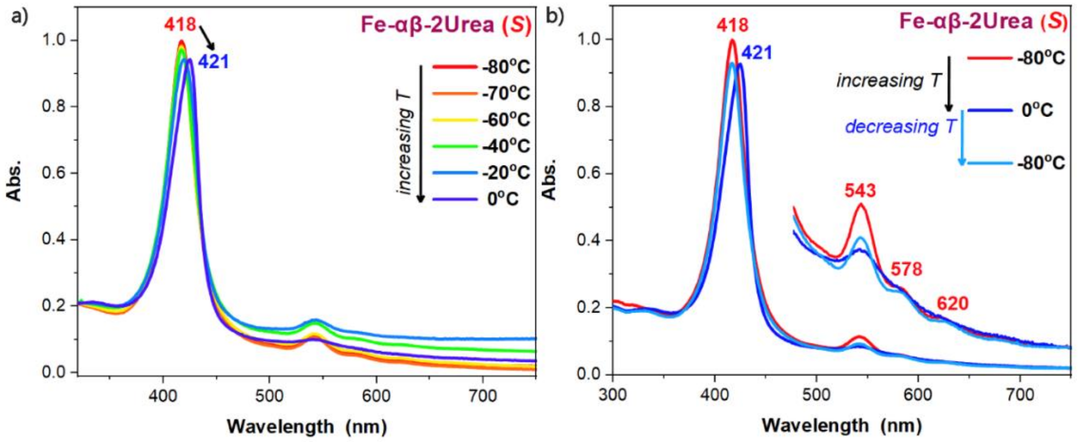

Fig. S1-9 a) Evolution of the **Fe-αβ-2Urea (*S*)** UV-Vis spectra in THF upon gradually increasing the temperature from -80 °C to 0 °C b) Comparison of the UV-Vis spectra obtained initially at -80 °C (red line), when increasing the temperature at 0 °C (blue line) and when decreasing the temperature at -80 °C (light blue line).

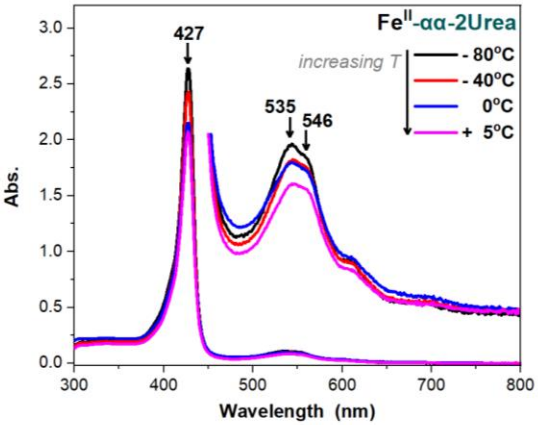

Fig. S1-10 Evolution of the **Fe^{II}-αα-2Urea** UV-Vis spectra in THF upon gradually increasing the temperature from -80 °C (black line) to +5 °C (magenta line).

Reversible O_2 binding at 5 °C

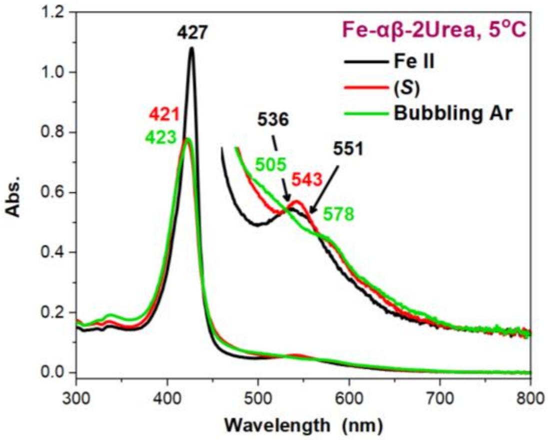

Fig. S1-11 Fe^{II}-αβ-2Urea UV-Vis spectra recorded at 5 °C (black line), upon oxygenation of the **Fe^{II}-**αβ-2Urea THF solution to afford the **Fe-αβ-2Urea (*S*)** (red line), upon deaerating gently the THF solution with Ar (green line). Concentration of **Fe^{II}-**αβ-2Urea was 6 μM.

Stability of Superoxo (S) species over time at different Temperatures

Fe-αα-2Urea ***(S)***

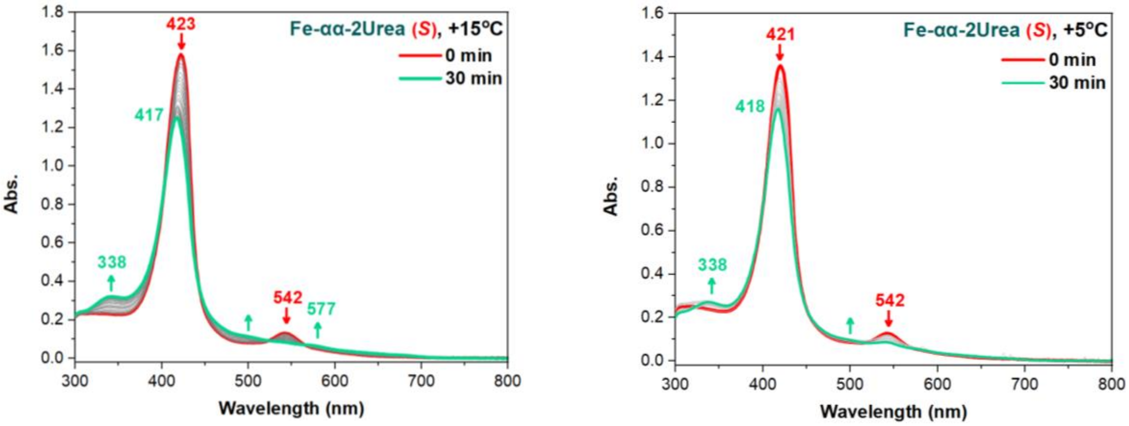

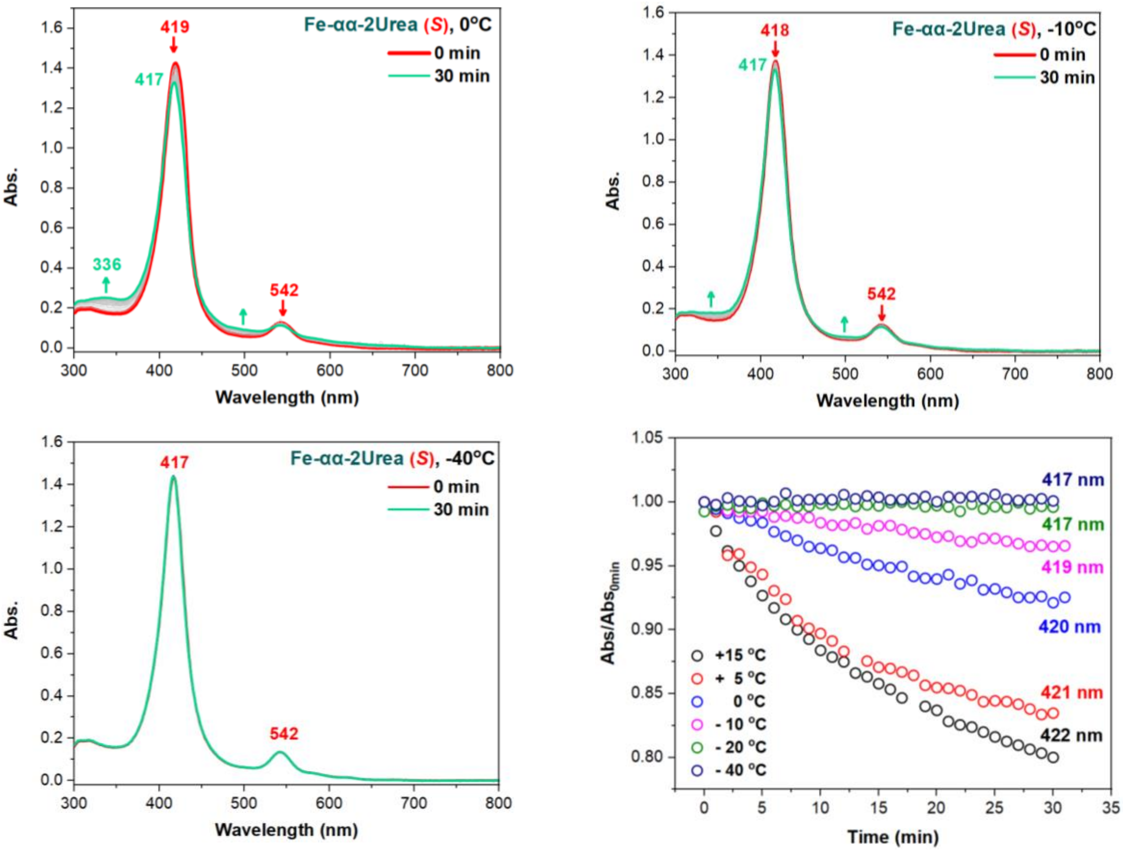

Fig. S1-12 UV-Vis evolution spectra of the Fe-αα-2Urea ***(S)*** species at different temperatures in dry THF over a period of 30 min. Comparison of the evolution of the maxima absorption (Soret band) at +15 ºC (black), +5 ºC (red), 0 ºC (blue), -10 ºC (magenta), -20 ºC (green), and -40 ºC (navy blue).

Fe-αβ-2Urea ***(S)***

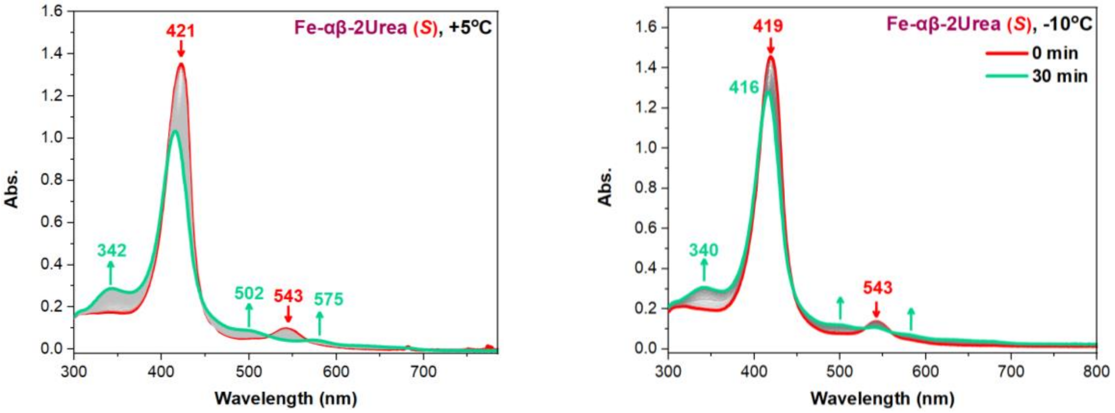

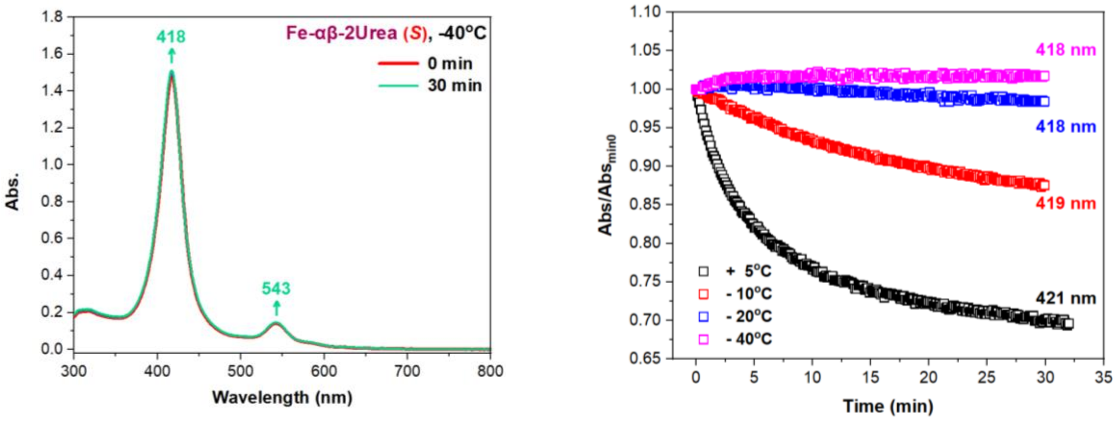

Fig. S1-13 UV-Vis evolution spectra of the Fe-αβ-2Urea ***(S)*** species at different temperatures in dry THF over a period of 30 min. Comparison of the evolution of the maxima absorption (Soret band) at + 5°C (black), -10 °C (red), -20 °C (blue), and -40 °C (magenta).

FeTPP ***(S)***

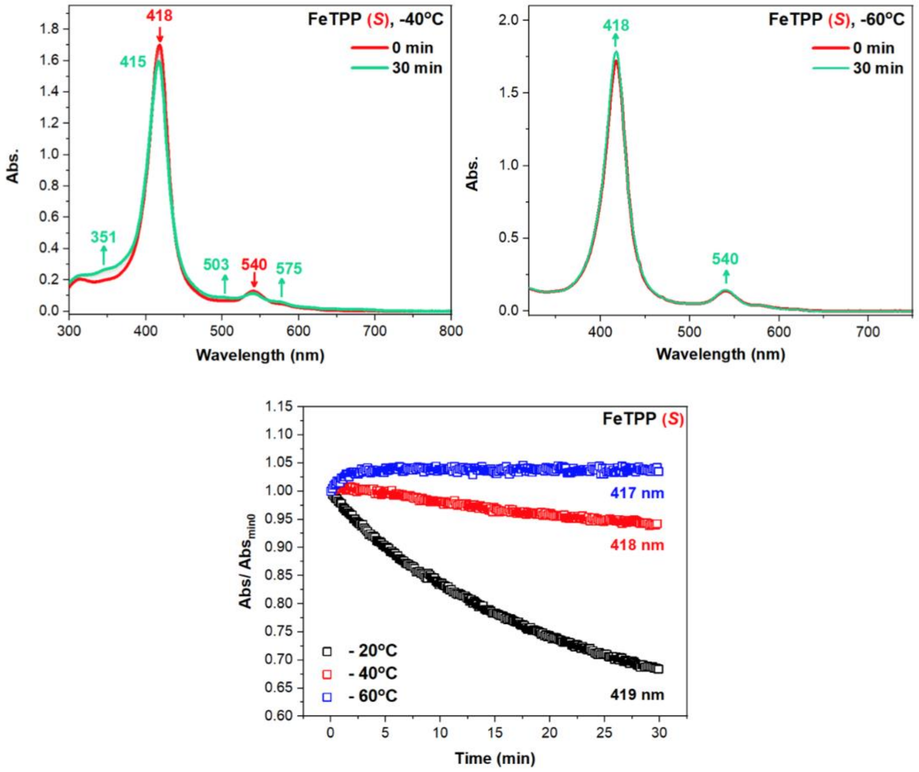

Fig. S1-14 UV-Vis evolution spectra of the FeTPP ***(S)*** species at different temperatures in dry THF over a period of 30 min. Comparison of the evolution of the maxima absorption (Soret band) at -20°C (black), -40°C (red) and -60°C (blue).

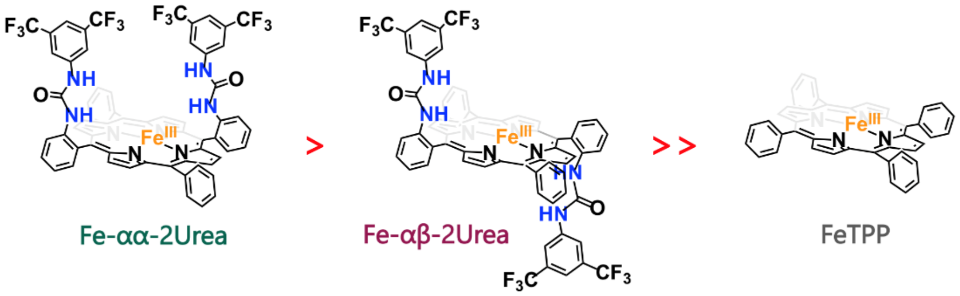

Scheme S1-1 Comparison of the ***(S)*** stability species for the **Fe-αα-2Urea**, **Fe-αβ-2Urea** and non-functionalized **FeTPP** porphyrin.

Stoichiometric O_2 binding

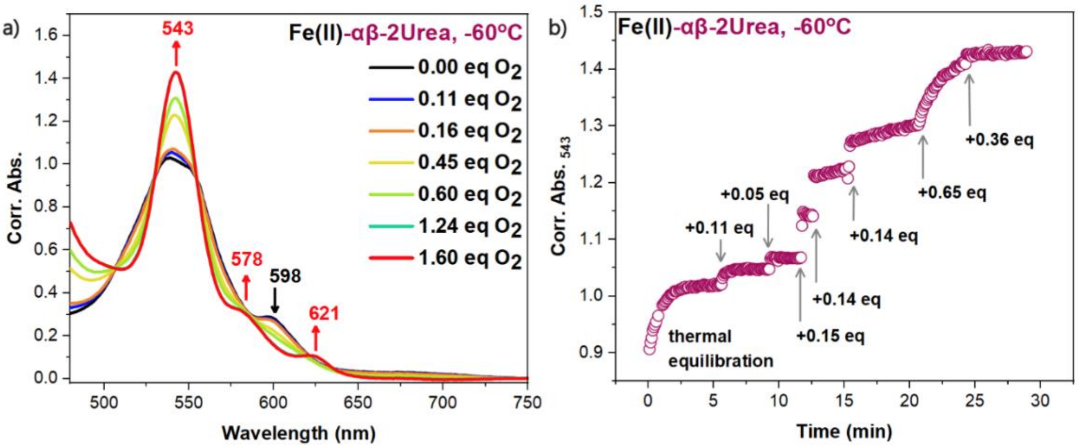

Fig. S1-15 a) UV Vis evolution spectra of **Fe^{II}-αβ-2Urea** upon titration with aliquots of an O_2 saturated THF solution at -60ºC; b) Monitor of the absorption peak at 543 nm upon addition of eq. of O_2 over time. The absorbance was corrected due to dilution.

Calculation of the equilibrium KO_2 constant for Fe-αα-2Urea

A THF solution of Fe^{II}-αα-2Urea (76 µM) was prepared in an N_2 atmosphere glovebox as previously described and transferred in a quartz cuvette which was sealed with a rubber septum. The cuvette was placed out of the glovebox and cooled down in the cryostat chamber of the UV-Vis spectrometer at -60 ºC. After reaching -60 ºC, the Fe^{II}-αα-2Urea solution was left to thermally equilibrate for a couple of minutes, before an initial spectrum was recorded. Addition of 1.2 eq of O_2 resulted in the formation of the Fe-αα-2Urea (*S*) species and the resulting solution was then gradually heated up to -30 ºC. Every time the temperature was increased by 5 ºC, the solution was left to thermally equilibrate and then a spectrum was collected. As shown in Fig. S1-16, annealing of temperature from -60 ºC to -30 ºC resulted in the decrease of the absorbance of the Q bands.

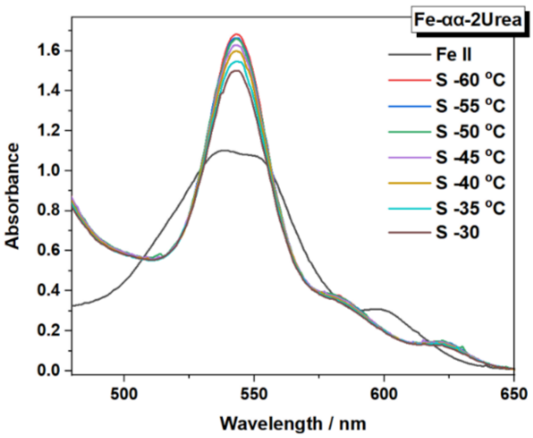

Fig. S1-16 UV Vis evolution spectra of **Fe-αα-2Urea (*S*)** upon increasing the temperature from -60 °C to -30 °C.

Although our UV-Vis studies showed that O_2 binds irreversibly to Fe^{II}-αα-2Urea at low temperatures, we cannot exclude the possibility that a small percentage of O_2 decoordinates from the iron center and such reversible O_2 binding behavior can be followed by UV-Vis spectroscopy only at high concentrations of the ferrous porphyrin. Hence, the decrease of absorption at the Q region observed herein could suggest a reversible O_2 binding. Prompted by the results of Mayer and co-workers concerning O_2 binding reversibility studies for the non-functionalized FeTPP, we decided to calculate the K_{O2} (M^{-1}) constant for Fe-αα-2Urea according to their method.[156] To do so, we simulated the UV-Vis absorption spectra of the Fe-αα-2Urea (*S*) species for each temperature by using the following equation and minimizing their differences.

$$A_{542} = \varepsilon_{542,\ Fe-aa-2Urea\,(S)} + \varepsilon_{542,\,Fe^{II}-\alpha\alpha-2Urea}$$

where,A_{542}: Absorbance at 542 nm, and ε_{542}: molar extinction coefficient at 542 nm at -60 °C

Fe^{II}-αα-2Urea

UV-Vis (THF, -60 °C): λmax/nm (10^3 ε. M^{-1} cm^{-1}) : 427, 536 (12.8), 550 sh (12.1), 597 (4.0)

Fe-αα-2Urea (*S*)

UV-Vis (THF, -60 °C): λmax/nm (10^3 ε. M^{-1} cm^{-1}) : 417, 542 (18.4), 578 sh (4.4), 621 (2.1)

As such, we were able to estimate the percentage of Fe^{II}-αα-2Urea formed upon a possible O_2 de-coordination when increasing the temperature of the solution. Some of the comparative experimental and simulated spectra are provided below.

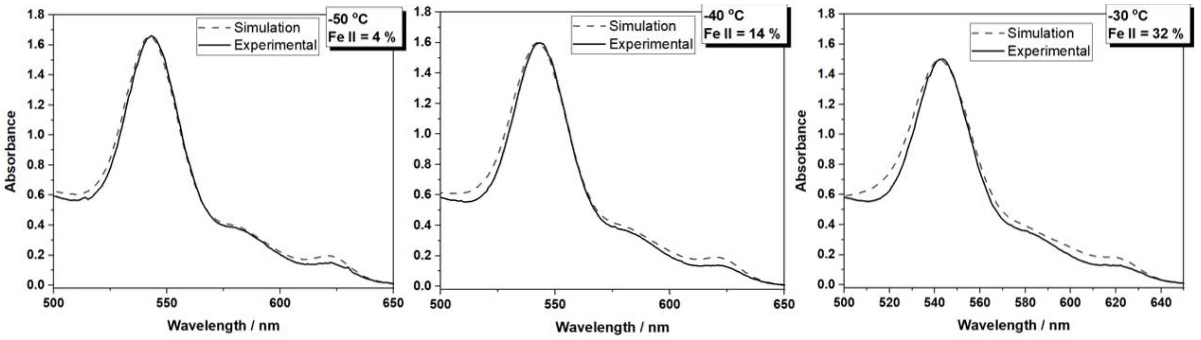

Fig. S1-17 UV Vis simulated and experimental spectra of Fe-αα-2Urea (*S*) formed upon increasing the temperature from -60 °C to -30 °C in an oxygenated THF solution.

By applying the equation below and using the concentration of the Fe^{II}-αα-2Urea species obtained by the simulated UV-Vis, we determined the K_{O2} (M^{-1}) for each temperature. Finally, in order to extrapolate the K_{O2} (M^{-1}) at room temperature, we plot the ln(K_{O2}) (M^{-1}) *vs.* 1/T (K^{-1}). The van't Hoff analysis gave a linear relationship, y= a+bx, where a = ΔS°/R and b = -ΔH°/RT. From the obtained values the K_{O2} (M^{-1}) at 25 °C was calculated to be 6.62 M^{-1}.

$$K_{O_2}\,(M^{-1}) = \frac{[Fe-\alpha\alpha-2Urea\,(S)]}{[Fe^{II}-aa-2Urea]\,[O_2]_{free}}$$

$$\boxed{ln(K_{O2}) = \underbrace{-\frac{\Delta H^o}{RT}}_{\text{Slope}} + \underbrace{\frac{\Delta S^o}{R}}_{\text{Intercept}}, R = 1.987\ cal\ x\ K^{-1}\ x\ mol^{-1}}$$

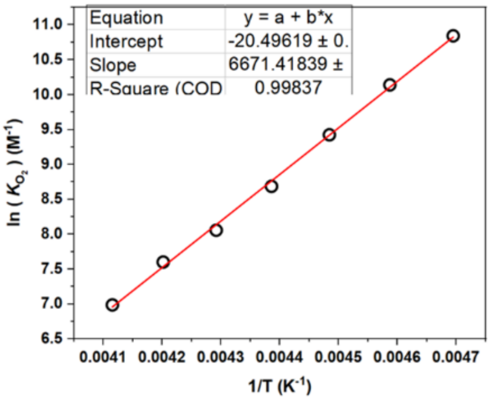

Equation	y = a + b*x
Intercept	-20.49619 ± 0.
Slope	6671.41839 ±
R-Square (COD	0.99837

Fig. S1-18 Van't Hoff plot.

To evaluate whether the UV-Vis changes observed upon temperature increase were attributed to the reversible O_2 binding on the ferrous center, we lowered the temperature of the oxygenated Fe-αα-2Urea solution from -15 °C to -60 °C. Interestingly, no UV-Vis changes were observed. In the beginning, we speculated that the irreversibility was attributed to the low concentration of O_2 (86 μM); as such we purged O_2 inside the solution but still, no increase in the absorption band at 542 nm was detected (Fig. S1-19).

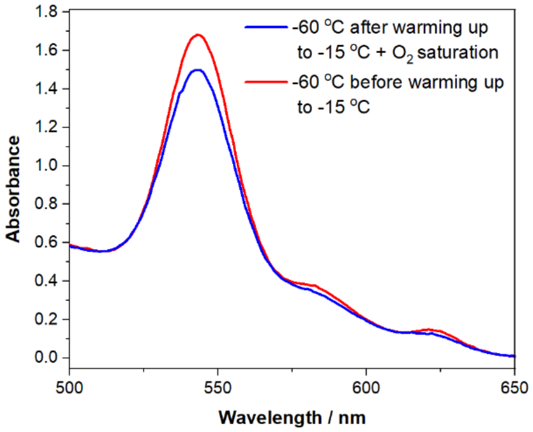

Fig. S1-19 Comparison of the UV-Vis spectra before and after warming up the solution to -15 °C of Fe-αα-2Urea (*S*) recorded at -60 °C.

These findings made us question Mayer's method for the calculation of the K_{O2}. In addition to that, the stoichiometric O_2 binding studies showed that FeTPP does not bind O_2 equimolarly, and probably μ-(per)oxo iron dimers are formed. Therefore, it was surprising to us how the K_{O2} for FeTPP was determined by Mayer and co-workers. Based on that, the determination of the K_{O2} via laser flash photolysis studies are undergoing.

Generation of Fe-αα-2Urea ***(P)*** and Fe-αβ-2Urea ***(P)*** species

Fe-αα-2Urea ***(P)*** and Fe-αβ-2Urea ***(P)*** species were generated by one-electron reduction of their corresponding ***(S)*** species in an extra dry THF/Butyronitrile 1:1 stirring solution by using $CoCp_2$ as a reductant at -80°C. Butyronitrile was used as a solvent due to the low solubility of $CoCp_2$ in THF. More specifically, 3 eq. of a butyronitrile solution of $CoCp_2$ were transferred via a gastight syringe to the deaerated ***(S)*** solution at -80 °C, while Ar was purged inside the solution. $CoCp_2$ light sensitive and extremely sensitive to air and gets readily oxidized to form $(Cp_2Co^{II})_2O_2$ dimers that exhibit an absorption at 363 nm[179]. UV-Vis: Fe-αα-2Urea ***(P)*** λ_{max}= 436, 547, 564, 610 nm and Fe-αβ-2Urea ***(P)*** λ_{max}= 435, 548, 562, 608 nm. Fe-αα-2Urea ***(P)*** species were also prepared in pure THF at -80 °C by $Cr(\eta-C_6H_6)_2$, λ_{max}= 435, 547, 564, 610 nm (Fig. S1-20).

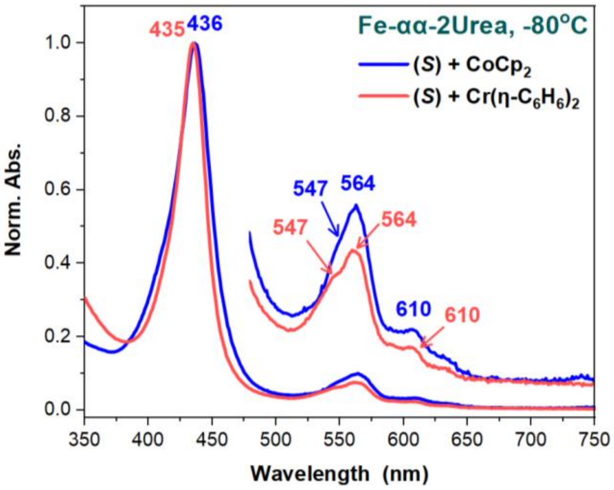

Fig. S1-20 Normalized UV-Vis spectra of the Fe-αα-2Urea ***(P)*** species prepared by the one-electron reduction of Fe-αα-2Urea ***(S)*** with 3 eq. of $CoCp_2$ (dry THF: Butyronitrile 1:1) (blue line) and with 3 eq. of $Cr(\eta-C_6H_6)_2$ (dry THF) (salmon line) at -80 °C.

EPR Studies

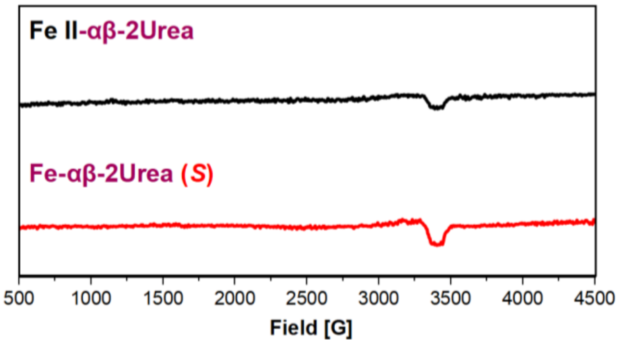

Fig. S1-21 X-band EPR spectra of **Fe^{II}-αβ-2Urea (*P*)** (black line) and **Fe-αβ-2Urea (*S*)** (red line).

---

[179] Qian, Z., Li, X., Sun, B., Du, L., Wang, Y. *et al.*, *J. Phys. Chem. Lett.*, **2020**, 11, 17, 7028–7034, DOI: 10.1021/acs.jpclett.0c01921

Generation of Fe-αα-2Urea ***(HP)*** and Fe-αβ-2Urea ***(HP)*** species

After generating the Fe-αα-2Urea ***(P)*** and Fe-αβ-2Urea ***(P)*** intermediates following the above experimental procedure, aliquots of MeOH were added as a proton source via an airtight syringe yielding their corresponding ***(HP)*** species. Fe-αα-2Urea ***(HP)***: λ_{max}= 426, 544, 561, 614 nm and Fe-αβ-2Urea ***(HP)***: λ_{max}= 428, 551, 589 nm

*r*Raman Studies for Fe-αα-2Urea upon decreasing the temperature from 223 K to 77 K

Interestingly, when the solution was cooled down again to 77 K, the vibration frequencies at 1367 and 1565 cm^{-1} seemed to decrease, and the *r*Raman spectrum displayed additional ν_4 and ν_2 marker bands at 1347 and 1541 cm^{-1}, respectively, which are indicative of high-spin heme-**Fe^{II}** species, suggesting partial decoordination of the O_2 ligand from the iron metal center (Fig. S1-23), probably attributed to photolysis due to extended irradiation time.

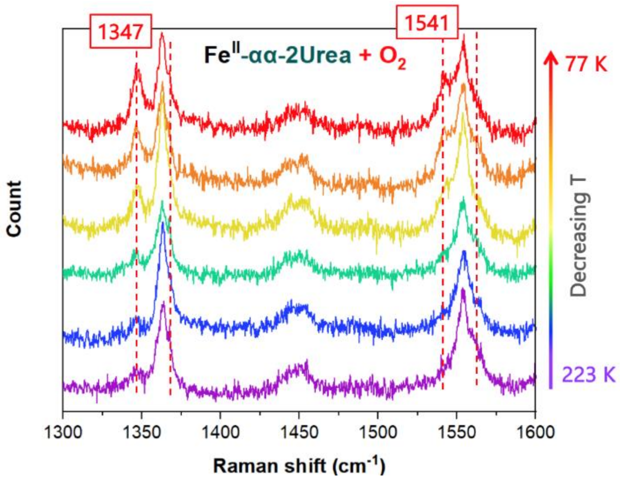

Fig. S1-22. *r*Raman spectra evolution of **Fe^{II}**-αα-2Urea **+ $^{16}O_2$** upon decreasing the temperature from 223 K to 77 K.

Chapter II

CO_2 Reduction in the Presence of O_2

2.1 Introduction

2.1.1 Climate Fluctuations in a Nutshell

Just as human life revolves around repeating patterns, the climate of Earth has been subjected to recurring fluctuations as well ever since its formation approximately 4.5 billion years ago. Only in the previous 450 000 years, for instance, the average temperature of Earth and the levels of greenhouse gases (GHGs) have varied multiple times. During the last five glacial-interglacial cycles, the sea's surface temperature had risen and fallen by about 4 °C, while the levels of GHGs such as carbon dioxide (CO_2) and methane (CH_4) have hovered between 180-280 ppm and 0.2-0.6 ppm, respectively (Fig. 2-1).[1],[2]

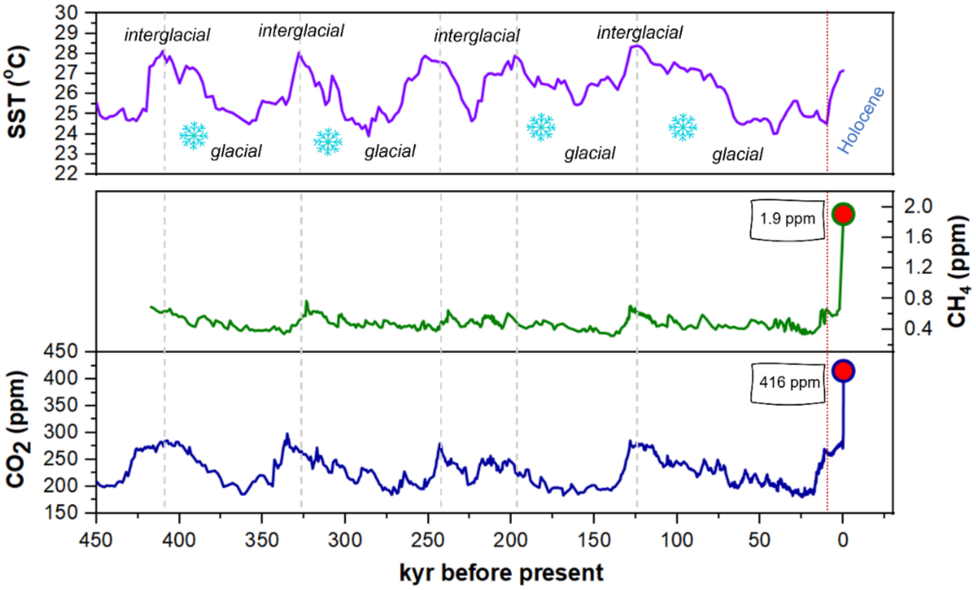

Fig. 2-1 Estimated Sea Surface Temperature (SST) based on alkenone paleotemperature determinations (top, purple line).[3] Atmospheric CH_4 (center, green line) and CO_2 (bottom, blue line) measured from the Vostok ice core.[4] Dot grey lines indicate the interglacial peaks, while the red dot line indicates the beginning of the interglacial period that are currently elapsing (Holocene Era).

These variations were primarily driven by slight changes in the orbit of Earth that affected the solar energy distribution over the surface combined with the continuous alterations of the geosphere and ocean basins.[5] Before the end of the last glacial period, almost 12 000 years ago, the CO_2 level in the atmosphere reached the lowest level ever been documented in Earth's history. CO_2 concentration in the atmosphere was barely 180 ppm approaching the lowest CO_2 level at which most photosynthetic organisms stay functional.[6] Contingently, a further decrease could have imposed life-threatening consequences.

The end of the last Ice Age marked the beginning of the interglacial period that are currently elapsing. For almost half a million year, the interglacial CO_2 level remained relatively stable and fluctuated between 260 and 280 ppm. This tendency was disrupted abruptly during the Industrial Revolution, dating back to the 18th and 19th centuries. This era was marked by rapid changes and reformations both at techno-economic and social levels that led to the

---

[1] Herbert, T.D., Cleaveland Peterson, L., Lawrence, K.T., Liu, Z., *Science*, **2010**, 328 (5985), 1530-1534, DOI: 10.1126/science.1185435

[2] Petit, J., Jouzel, J., Raynaud, D. *et al.*, *Nature*, **1999**, 399, 429–436, DOI: 10.1038/20859

[3] Raw data obtained from: Fedorov, A., Brierley, C., Lawrence, K. *et al.*, *Nature*, **2013**, 496, 43–49, DOI: 10.1038/nature12003

[4] Raw data obtained from the registered database of National Centers for Environmental Information (NCEI)

[5] Paillard, D., *Rev. Geoph.*, **2001**, 39 (3), 325-346, DOI: 10.1029/2000RG000091

[6] Ward, J.K., Harris, J., M., Cerling, T., *et al.*, *PNAS*, **2005**, 102 (3), 690-694, DOI: 10.1073/pnas.0408315102

emergence of an "industrialized" society. The industrialization of the Modern Era triggered the exploitation of natural resources so that modern societies could meet their ever-increasing demands on energy. Ever since, emissions rates and the concentration of GHGs in the atmosphere have increased exponentially, to levels that are unprecedented over at least the last half-million year.[7]

2.1.2 A Planet in Crisis

Since the mid-18th century, approximately 2.3 teratonnes (Tt) of CO_2 have been released into the atmosphere, with the most significant percentage attributed to coal, petroleum, and natural gas combustion. The rate of the annual CO_2 emissions, over the decades, is increasing at alarmingly high rates and exceeds the rate at which Nature can assimilate CO_2. In 2021, CO_2 global emissions were approximately 38 Gt, while the atmospheric concentration of CO_2 and CH_4 reached 416 and 1.9 ppm, respectively.

The 6th Assessment Report of the Intergovernmental Panel on Climate Change (AR6-IPCC) underlines that the weather and climate extremes our planet is encountering are entwined with the exceptionally high atmospheric concentration of GHGs. Liable for the unprecedented accumulation of GHGs is indisputably human activity. The consequences of climate change are just but deteriorating over the past decades, with the IPCC declaring code red for the planet's sustainability. Since the 80s, each decade has become noticeably warmer than the previous one, with the average temperature of Earth being increased by almost 1°C degree and indeed at fast rates. IPCC forewarns that global warming of more than 4°C is ahead of us if no drastic measures concerning the global GHGs emissions are taken both at an individual and intergovernmental level (Fig. 2-2).[8],[9]

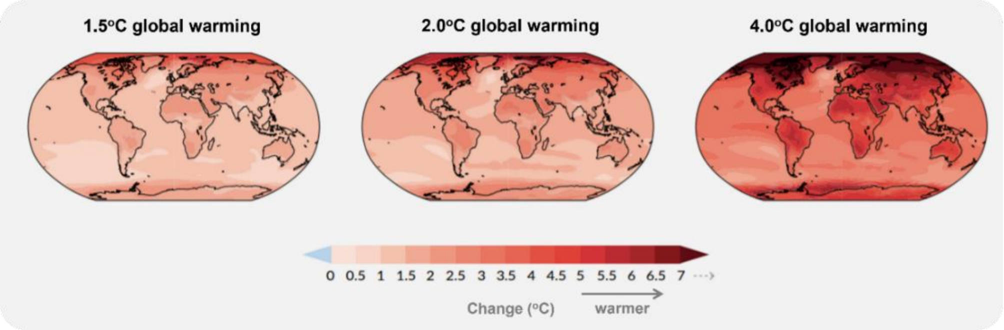

Fig. 2-2 Simulations of annual mean temperature changes (°C) relative to 1850-1900 for three possible scenarios of global warming: 1.5 °C (left), 2.0 °C (middle) and 4.0 °C (right).[9]

An intensification of climate change will bring about a chain of catastrophic impacts on the environment and humanity. On top of that, it could, unfortunately, increase the risk of future warfare and reshape the map of the present nations. To avoid the consequences of such an unpleasant scenario, we need to re-evaluate the already established climate policies and follow key guidelines that will lead society to the solution of the two interconnected energy-related problems that plague the modern world. The depletion of fossil fuels that raises the national

---

[7] Doney, S.C., Schimel, D.S., *Annu. Rev. Environ. Resour.*, **2007**, 32, 31-66, DOI: 10.1146/annurev.energy.32.041706.124700

[8] IPCC, **2021**: Summary for Policymakers. In: *Climate Change 2021: The Physical Science Basis. Contribution of Working Group I to the Sixth Assessment Report of the Intergovernmental Panel on Climate Change* [Masson-Delmotte, V., P. Zhai, A. Pirani, S.L. Connors, C. Péan, S. Berger, N. Caud, Y. Chen, L. Goldfarb, M.I. Gomis, M. Huang, K. Leitzell, E. Lonnoy, J.B.R. Matthews, T.K. Maycock, T. Waterfield, O. Yelekçi, R. Yu, and B. Zhou (eds.)]. In Press.

[9] Kramer, R. J., He, H., Soden, B. J., Oreopoulos, L., *et al., Geophys. Res. Lett.*, **2021**, 48, e2020GL091585, DOI: 10.1029/2020GL091585

economic and political competitiveness and the ever-increasing GHGs emissions that are held accountable for global warming.

2.1.3 Mitigation of Climate Change

To limit global warming and meet the primary goals of the Paris Agreement, the world economy has to employ carbon-neutral and net-zero strategies.[10] The first step towards a carbon-neutral world is to meticulously evaluate the anthropogenic CO_2 emissions by sector. According to the data obtained in 2016, the Energy sector is responsible for the highest percentage of the emitted CO_2 (73.2 %), followed by the sectors of Agriculture, Forest & Land Use (18.4 %), and Industry (5.2 %).[11] Estimating the CO_2 footprint enables each country and their organizations (*e.g.,* EU) to plan their strategies conscientiously towards climate change mitigation. These strategies include well-thought-out actions such as i) decarbonization of energy production by substitution of fossil fuel by nuclear and renewable energy, ii) reduction of energy consumption and elimination of CO_2 emissions, especially in sectors like agriculture and industry, iii) increase of natural and artificial carbon sinks and iv) CO_2 capture, storage, and its direct utilization or/and assimilation.

Carbon capture and utilization (CCU) refers to a series of sophisticated technologies that capture and separate CO_2 either from the atmosphere or directly from industrial sites that emit vast quantities of GHGs via the combustion of carbon-based fuels. Once CO_2 is captured, it can be further utilized to enhance, for example, oil recovery and fertilizers production, or it can be converted into valuable chemicals, fuels such as methanol and methane, and building materials.[12] The capture and conversion of CO_2 into liquid fuels and value-added chemicals provides a sustainable pathway towards a circular CO_2 economy. However, it is a challenging process that requires attentive design.

2.1.4 The nature of CO_2

From a chemical perspective, one of the preeminent reasons CO_2 valorization systems have not lived up to their expectations is the high stability of the CO_2 molecule. The inert nature of CO_2 is strongly reflected in its high activation barrier (1.9 eV), which could be rationalized by molecular orbital theory. CO_2 is a diamagnetic molecule with sixteen valence electrons populating four non-bonding and four bonding σ and π molecular orbitals. The so-called "activation" of CO_2 involves the one-electron transfer to the lowest unoccupied molecular orbital (LUMO), a σ* antibonding orbital, which mainly localizes on the carbon atom. The single-electron transfer to the carbon atom decreases the bond order of the two C-O bonds, thus changing the molecule's geometry from linear to bent Fig. 2-3.[13],[14] This geometrical rearrangement, however, is associated with a high energy input as it is indicated by the large negative one-electron reduction potential of CO_2 to $CO_2^{\bullet -}$ (-1.90 V *vs*. SHE, pH=7, Table 2-1 Eq.1).

---

[10] *Paris Agreement to the United Nations Framework Convention on Climate Change (UNFCCC)*, Adopted Dec. 12, **2015**, T.I.A.S. No. 16-1104; entered into force Nov. 4, **2016**.

[11] Ritchie, H., and Roser, M., "*CO_2 and Greenhouse Gas Emissions*"., **2020**, Published online at OurWorldInData.org. https://ourworldindata.org/co2-and-other-greenhouse-gas-emissions

[12] International Energy Agency (IEA), *About CCUS*, **2021**, Paris, https://www.iea.org/reports/about-ccus

[13] Frese, K. W., Jr. In Electrochemical and Electrocatalytic Reactions of Carbon Dioxide, Sullivan, B. P., Krist, K., Guard, H. E., *Eds. Elsevier : New York*, **1993**, Chapter 1 & 6, ISBN : 978-0-444-88316-2

[14] Schröder, D., Schalley, C.A., Harvey, J.N., Schwarz, H., *Int. J. Mass Spectrom.*, **1999**, 185-187, 25-35, DOI: 10.1016/S1387-3806(98)14042-3

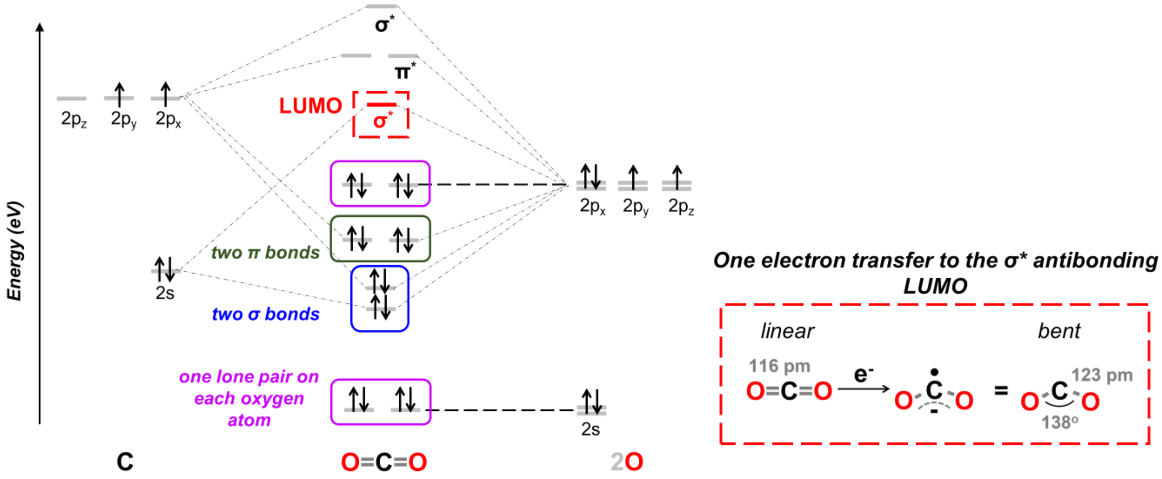

Fig. 2-3. Molecular Orbital (MO) diagram of CO_2. CO_2 is activated by a one-electron transfer to its LUMO, a σ^* antibonding MO, resulting in change of the molecule geometry from linear to bent.

A less energy-demanding alternative to overcome the high energy barrier of CO_2 activation is the "proton-assisted even-number of electrons" transfer (Table 2-1, Eq. (2-7)). Following this favorable energy pathway, CO_2 is reduced to thermodynamically more stable C_1 or even C_2 products such as carbon monoxide (CO), formate ($HCOO^-$), methanol (MeOH), and methane (CH_4) as well as ethylene (C_2H_4), and ethane (C_2H_6), respectively.

Table 2-1. Standard electrochemical potentials of CO_2 reduction reactions

Reduction Process	E^0 (V) *vs* SHE	
$CO_{2(aq)} + e^- \rightarrow CO_2^{\bullet -}{}_{(aq)}$	-1.90	(1)
$CO_{2(g)} + 2e^- + 2H^+ \rightarrow CO_{(g)} + H_2O$	-0.52	(2)
$CO_{2(g)} + 2e^- + H^+ \rightarrow HCO_2^-{}_{(aq)}$	-0.43	(3)
$CO_{2(g)} + 4e^- + 4H^+ \rightarrow CH_2O_{(aq)} + H_2O$	-0.51	(4)
$CO_{2(g)} + 6e^- + 6H^+ \rightarrow CH_3OH_{(aq)} + H_2O$	-0.38	(5)
$CO_{2(g)} + 8e^- + 8H^+ \rightarrow CH_{4(g)}$	-0.24	(6)
$2CO_{2(g)} + 12e^- + 12H^+ \rightarrow C_2H_{4(g)} + 4H_2O$	-0.35	(7)

Thermodynamically speaking, according to the Gibbs free energy equation 8, it would be reasonable to assume that the less negative the electron reduction potential (E^0) is, the more favorable the reaction process would be.

$$\Delta G^0 = -nFE^0 \qquad (Eq.8)$$

$$n = number\ of\ electrons\ and\ F = faradaic\ constant$$

However, this is not the case, and the conversion of CO_2 into products such as MeOH and CH_4 is not favored. The reason lies in the sluggish kinetics of these reactions that mainly depend on the protons' availability and the competitive H^+ reduction to H_2 (H^+/H_2, E^0 = 0.0 V *vs.* SHE). Hence, when it comes to the efficient CO_2 reduction into valuable chemicals, both the thermodynamic and kinetic barriers need to be considered and overcome. [15]

---

[15] Appel, A.M., Bercaw, J.E., Bocarsly, A.B., Dobbek, H., DuBois, D.L., *et al.*, *Chem. Rev.*, **2013**, 113, 8, 6621–6658, DOI: 10.1021/cr300463y

2.1.5 CO_2 fixation in Nature

Cellular life is an excellent paradigm for getting insights into how to gain thermodynamic and kinetic control over CO_2 fixation into biomass. Archaea, bacteria, and eukaryotes assimilate atmospheric CO_2 via six main pathways summarized in Table 2-2. They employ several CO_2 fixation enzymes, strong reducing and oxidizing agents, and high energy carriers to incorporate inorganic carbon into vital precursors for the biosynthesis of fatty acids, carbohydrates, and amino acids.

Table 2-2. Summary of the six biological carbon fixation pathways[16]

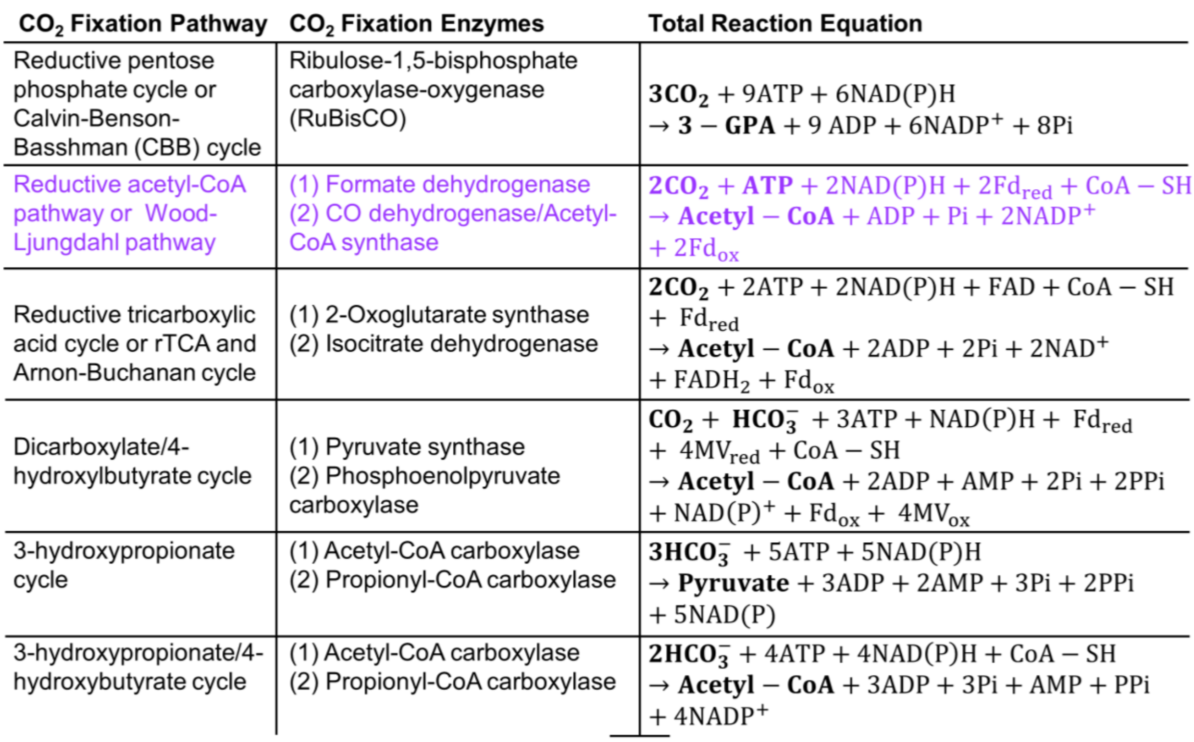

CO_2 Fixation Pathway	CO_2 Fixation Enzymes	Total Reaction Equation
Reductive pentose phosphate cycle or Calvin-Benson-Bassham (CBB) cycle	Ribulose-1,5-bisphosphate carboxylase-oxygenase (RuBisCO)	$\mathbf{3CO_2} + 9ATP + 6NAD(P)H \rightarrow \mathbf{3-GPA} + 9\ ADP + 6NADP^+ + 8Pi$
Reductive acetyl-CoA pathway or Wood-Ljungdahl pathway	(1) Formate dehydrogenase (2) CO dehydrogenase/Acetyl-CoA synthase	$\mathbf{2CO_2} + \mathbf{ATP} + 2NAD(P)H + 2Fd_{red} + CoA-SH \rightarrow \mathbf{Acetyl-CoA} + ADP + Pi + 2NADP^+ + 2Fd_{ox}$
Reductive tricarboxylic acid cycle or rTCA and Arnon-Buchanan cycle	(1) 2-Oxoglutarate synthase (2) Isocitrate dehydrogenase	$\mathbf{2CO_2} + 2ATP + 2NAD(P)H + FAD + CoA-SH + Fd_{red} \rightarrow \mathbf{Acetyl-CoA} + 2ADP + 2Pi + 2NAD^+ + FADH_2 + Fd_{ox}$
Dicarboxylate/4-hydroxylbutyrate cycle	(1) Pyruvate synthase (2) Phosphoenolpyruvate carboxylase	$\mathbf{CO_2} + \mathbf{HCO_3^-} + 3ATP + NAD(P)H + Fd_{red} + 4MV_{red} + CoA-SH \rightarrow \mathbf{Acetyl-CoA} + 2ADP + AMP + 2Pi + 2PPi + NAD(P)^+ + Fd_{ox} + 4MV_{ox}$
3-hydroxypropionate cycle	(1) Acetyl-CoA carboxylase (2) Propionyl-CoA carboxylase	$\mathbf{3HCO_3^-} + 5ATP + 5NAD(P)H \rightarrow \mathbf{Pyruvate} + 3ADP + 2AMP + 3Pi + 2PPi + 5NAD(P)$
3-hydroxypropionate/4-hydroxybutyrate cycle	(1) Acetyl-CoA carboxylase (2) Propionyl-CoA carboxylase	$\mathbf{2HCO_3^-} + 4ATP + 4NAD(P)H + CoA-SH \rightarrow \mathbf{Acetyl-CoA} + 3ADP + 3Pi + AMP + PPi + 4NADP^+$

Although cellular life has evolved a diversity of CO_2 fixation pathways over billion years, CO_2 enters the cellular metabolism only via two main routes i) carboxylation by which CO_2 is fixated directly onto a metabolite or ii) reduction by initially converting CO_2 into CO or formate and further coupling them to a metabolite.[17] The second route is not so common, and it is only followed by the Wood-Ljungdahl (WL) pathway highlighted in purple in Table 2.

This pathway is employed by several acetogenic microbes, which mostly use CO_2 and H_2 for their growth. These bacteria prefer to feed their metabolism by a CO_2 reduction strategy over carboxylation because the former is a less energy-demanding process. Indeed, by comparing the net reactions between the WL pathway and any other fixation pathway of Table 2, fewer ATP molecules are invested for the CO_2 fixation in the WL pathway. This energy conservation enables these microbes to produce more biomass (except the rTCA cycle) as the reducing power from NAD(P)H is mainly used to drive the CO_2 fixation instead of ATP synthesis.[18] Shedding light on the WL pathway should provide us with a better understanding of how nature activates and reduces CO_2 into added-valuable products.

---

[16] Gong, F., Cai, Z., Li, Y., *Sci. China Life Sci.*, **2016**, 59**,** 1106–1114, DOI: 10.1007/s11427-016-0304-2

[17] Cotton, C.AR., Edlich-Muth, C., Bar-Even, A., *Curr. Opin. Biotechnol.*, **2018**, 49, 49-56, DOI: 10.1016/j.copbio.2017.07.014

2.1.6 Biological CO_2 activation

Acetogens and methanogens activate and reduce CO_2 to formate by using the WL pathway,[18],[19] via two-electron two-proton discrete steps before incorporating it into cellular metabolites. As their names imply, acetogens generate acetate while methanogens produce CH_4 as by-products of their metabolism.

CO_2 reduction to CO and HCOOH

The Wood-Ljungdahl pathway (WL pathway) in acetogenesis

In acetogenesis, the WL pathway consists of two joined methyl and carbonyl branches. Within the methyl branch, one molecule of CO_2 is initially reduced to HCOOH, which is further fixated into a methyl-H_4folate molecule via two successive two-electron two-proton transfers. The methyl group is then transferred to a Co-Fe-S protein (CoFeSP) via a methyltransferase (Metr). Concurrently, a second CO_2 molecule is reduced to CO in the carbonyl branch, which is condensed with the methyl group of CoFeSP and coenzyme A (CoA-SH) to produce acetyl-CoA that is later reduced to acetate (Scheme 2-1).[20],[21]

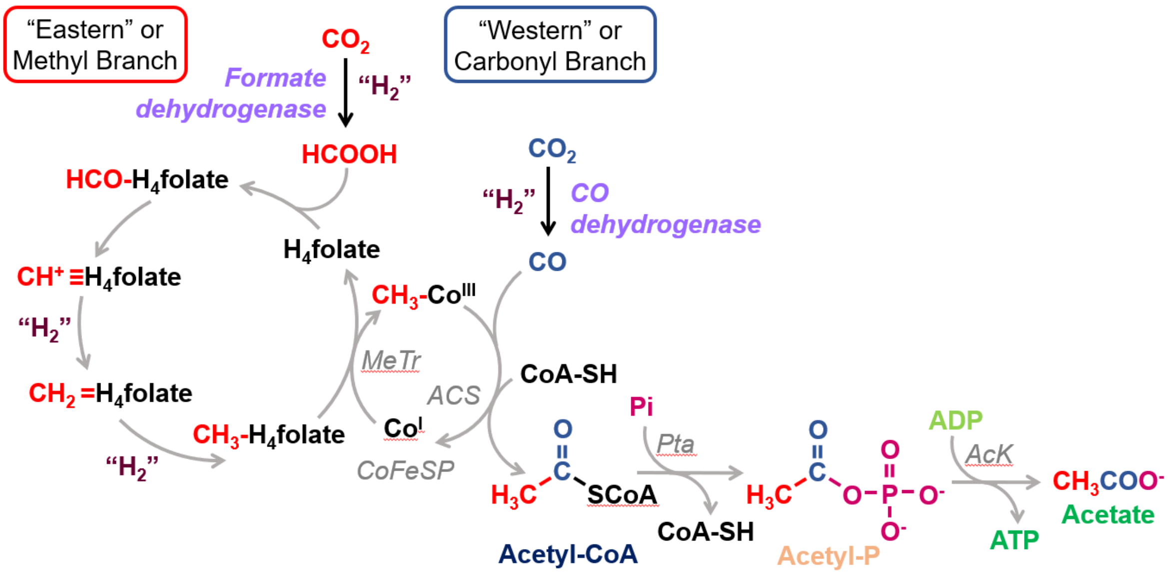

Scheme 2-1. Schematic representation of the Wood-Ljungdahl (WL) pathway. "H_2", $2e^-$/ $2H^+$ transfer; Metr, methyltransferase; ACS, acetyl-CoA synthase; CoFeSP, corrinoid iron-sulfur protein; CoA-SH, coenzyme A; Pi, inorganic phosphate; Pta, phosphotransferase; Acetyl-P, acetyl phosphate; ADP, adenosine diphosphate; AcK, acetate kinase; ATP, adenosine triphosphate.[22]

Two key enzymes catalyze the initial two-electron reduction of the two CO_2 molecules within the WL pathway: i) a CO dehydrogenase (CODH) that reduces CO_2 to CO in the carbonyl branch, and ii) a formate-dehydrogenase (FDH) that converts CO_2 into HCOOH in the methyl branch. Although CO and HCOOH are not as high-density energy fuels as MeOH and CH_4, they still find enormous industrial interest as C1 source. CO, for instance, is used in Fischer-Tropsch

---

[18] Katsyv, A., Müller V., *Front. Bioeng. Biotechnol.*, **2020**, 8, 621166, DOI: 10.3389/fbioe.2020.621166

[19] Evans, P.N., Boyd, J.A., Leu, A.O. *et al.*, *Nat. Rev. Microbiol.*, **2019**, 17, 219–232, DOI: 10.1038/s41579-018-0136-7

[20] Ragsdale, S.W., *Biofactors*, **1997**, 6, 1, 3-11, DOI: 10.1002/biof.5520060102

[21] Schuchmann, K., Müller, V., *Nat. Rev. Microbiol.*, **2014**, 12, 809–821, DOI: 10.1038/nrmicro3365

[22] Ragsdale, S.W., Pierce, E., *Biochim Biophys Acta.*, **2008**, 1784, 12, 1873-1898 DOI:10.1016/j.bbapap.2008.08.012

technologies to produce liquid hydrocarbons like gasoline and diesel fuels[23], while HCOOH is widely used as a preservative and antibacterial agent[24], as well as a H_2 carrier25 Elucidating the mechanistic aspects of CODHs and FDHs would enable us to gain more insights into how to design robust and efficient artificial CO_2 valorization systems.

2.1.6.1 CO Dehydrogenases

CO dehydrogenases (CODHs) are found in anaerobic and aerobic microorganisms such as *Moorella thermoacetica* and *Oligotropha carboxidovorans*, respectively. They are classified into two types i) [NiFe]CODHs, and ii) [MoSCu]CODHs[26]. [NiFe]CODHs reduce CO_2 to CO reversibly, whereas [MoSCu]CODHs can only oxidize CO to CO_2.

[NiFe]CO Dehydrogenases

Crystallographic studies of [NiFe]CODHs isolated from *Moorella thermoacetica* bacteria have shown that their active site consists of a [Fe_3-S_4-Ni] cluster bridged with one Fe^{II} center. The Ni center is coordinated with two of the four sulfur atoms of the Fe_3S_4 cluster and one cysteine (Cys_{526}) residue. The high spin Fe^{II} center is tetracoordinated and binds one μ_3-sulfido ligand of the [Fe_3-S_4-Ni] cluster as well as one histidine (His_{261}) and one cysteine (Cys_{295}) amino acid. [27], [28] The fourth ligand is speculated to be either a -OH or a water molecule, possibly interacting with the Ni atom.[29] In 2001, another structure of [NiFe]CODH isolated this time from *Carboxydothermus hydrogenoformans* was reported by Dobbek[30], in which the two metal centers, Ni and Fe, were bridged by an extra μ_2-sulfido ligand as depicted in Fig. 2-4.

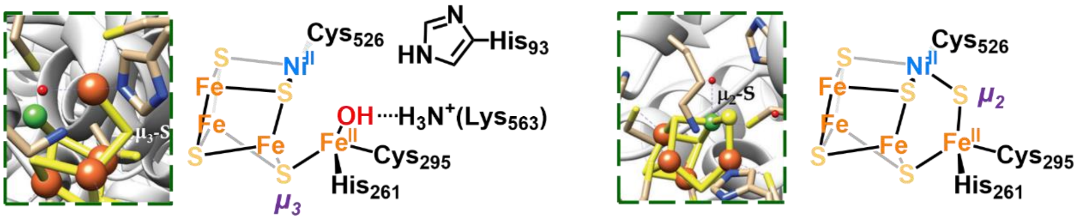

Fig. 2-4. X-ray structures[31] of [NiFe]CODHs (resting state) isolated from *Moorella thermoacetica* (left) and *Carboxydothermus hydrogenoformans* (right); ChemDraw of the reduced states were drawn for clarity.

The X-ray structures of [NiFe]CODHs, along with the results of numerous spectroscopic studies with different substrates and inhibitors, have led to the proposal of the following mechanism[27] (Scheme 2-2). The catalytic cycle starts with the $2e^-$ reduction of the enzyme's

---

[23] Baredar, P., Khare, V., Nema, S., *Design and Optimization of Biogas Energy Systems*, **2020**, Chapter 6, 231-266, DOI: 10.1016/B978-0-12-822718-3.00006-X

[24] lvarez, A.A., Bansode, A., Urakawa, A., Bavykina, A.V., Wezendonk, T.A., *et al.*, *Chem. Rev.*, **2017**, 117, 9804–9838, DOI: 10.1021/acs.chemrev.6b00816

[25] Mellmann, D., Sponholz, P., Junge, H., Beller, M., *Chem. Soc. Rev.*, **2016**,45, 3954-3988, DOI: 10.1039/C5CS00618J

[26] Holger Dobbek, H., Gremer, L., Kiefersauer R., Huber, R., Meyer, O., *Proc. Natl. Acad. Sci. U.S.A.*, **2002**, 99, 25, 15971-15976, DOI: 10.1073/pnas.212640899

[27] Dernault, C., Volbeda, A., Jin Kim, E., Legrand, P., *et al.*, *Nat. Struct. Biol.*, **2003**, 10, 4, 271-279, DOI: 10.1038/nsb912

[28] Jeoung, JH., Dobbek, H., *Science*, **2007**, 318, 1461-1464, DOI: 10.1126/science.1148481

[29] Kung, Y., Doukov, T., I., Seravalli, J., Ragsdale, S., W., Drennan, C., L., Biochemistry, **2009**, 48, 31, 7432-7440, DOI: 10.1021/bi900574h

[30] Dobbek, H., Svetlitchny, V., Gremer, L., Huber, R., Meyer, O., *Science*, **2001**, 293, 5533, 1281-1285, DOI: 10.1126/science.1061500

[31] Amanullah, Sk., Saha, P., Nayek, A., Ahmed, Md, E., Dey, A., *Chem. Soc. Rev.*, **2021**, 50, 3755-3823, DOI: 10.1039/D0CS01405B

active site by a reduced ferredoxin. CO_2 binds to the formal Ni^0 via the C atom, changing the geometry of the Ni center from a T-shaped conformation to a square-planar. At the same time, the Fe^{II} center releases its axial ligand and coordinates with one of the two oxygen atoms of the bound CO_2 (O_α). The two metal centers act as a Frustrated Lewis Pair (FLP), with the soft Ni^0 metal as the Lewis base and the hard ferrous center as the Lewis acid. Because of their FLP character, CO_2 can be activated through a "push-pull" effect.[32] Ni^0 "pushes" the electron density towards CO_2, whereas Fe^{II} "pulls" the electron density so that the Ni center can efficiently activate CO_2. The activated CO_2 is stabilized on the Ni and Fe centers by second sphere electrostatic and H-bonding interactions from two positively charged amino acids residues. One lysine (Lys$_{563}$) residue is hydrogen-bonded to O_α, and one protonated histidine (His$_{93}$) is hydrogen-bonded to O_β. The minor change from a distorted T-shaped to a square-planar geometry results in low reorganization energy that synergistically with the second sphere contributions from the peptide residues promote the heterolytic C-O bond cleavage in the following step of the catalytic cycle, in which the Ni-CO adduct is formed. CO is released from the active site, with the enzyme returning to its initial oxidized state closing the catalytic cycle.

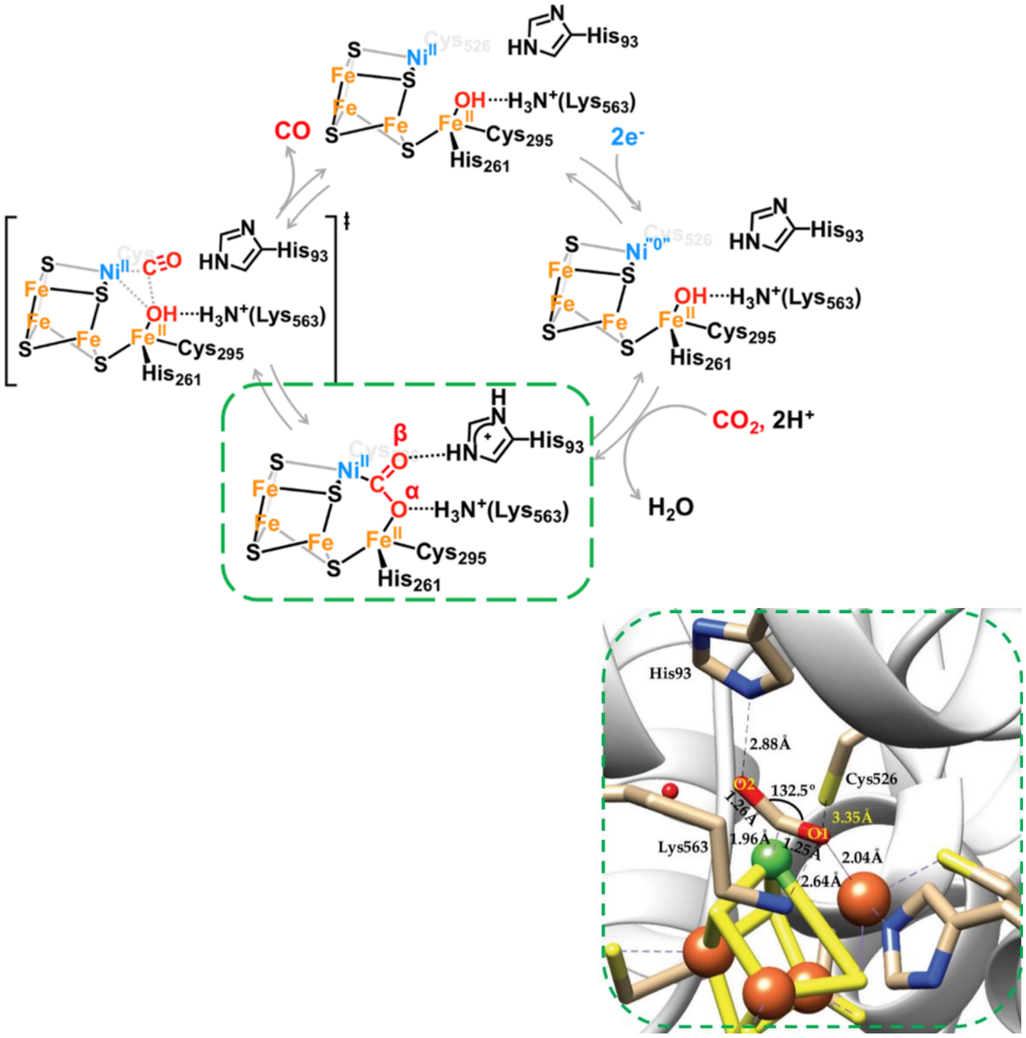

---

[32] Mondal, B., Song, J., Neese, F., Ye, S., *Curr. Opin. Chem. Biol.*, **2015**, 25, 103–109. DOI: 10.1016/j.cbpa.2014.12.022

Scheme 2-2. Structure-based proposed mechanism of the catalytic reverse reduction of CO_2 to CO by [NiFe]CODH. Inset[30]: X-ray structure of the reduced state of [NiFe]CODH with CO_2 (-600 mV + CO_2) obtained from *Carboxydothermus hydrogenoformans* (CODHIICh).

2.1.6.2 Mo- and W- Formate Dehydrogenases

Metal-dependent formate dehydrogenases (FDHs) are the second class of enzymes involved in the initial steps of the WL pathway. They catalyze the two-electron two-proton reduction of CO_2 to formate, possibly via a hydride atom transfer pathway. Their catalytic site contains either a molybdenum (Mo^{VI}) or tungsten (W^{IV}) metal atom coordinated to two electron-rich bidentate pterin cofactors. X-ray structures of the oxidized state of these enzymes have revealed that the metal center is also coordinated to a sulfur atom of a nearby cysteine residue or to a selenium atom of selenocysteine (SeC_{140}). The sixth vacant coordination site of the metal is possibly occupied either by an additional sulfur atom or by a water molecule with the metal cation adopting a distorted trigonal prismatic conformation. Two amino acids, one positively charged arginine (Arg_{333}) and one histidine (His_{141}), have also been found near the single metal active centers, holding a key role in the hydride atom transfer (Fig. 2-5).[33],[34]

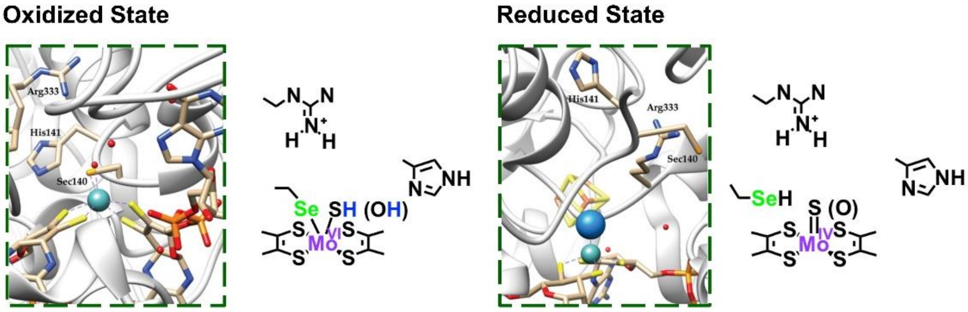

Fig. 2-5. X-ray structure[30] of the active site of a Mo- FDH isolated from *Escherichia coli*; left the oxidized state, and right the reduced state.

According to the proposed mechanism (Scheme 2-3), the catalytic cycle involves, initially, the two-electron reduction of the active site with the Mo^{VI} being reduced to Mo^{IV}. At the same time, the selenocysteine ligand decoordinates from the metallic center, which eventually adopts a square pyramidal geometry. The following steps involve the protonation of the nearby histidine residue and the binding of CO_2 on the metal center. Unlike the [NiFe]CODHs, CO_2 binds on the Mo^{IV} via one of its carboxylate oxygens instead of the carbon atom. The non-bounded carboxylate oxygen is H-bonded to an arginine residue, placing the CO_2 adduct close to the protonated histidine. The small distance between the CO_2 and the histidine allows the hydride atom transfer to the carboxylate C atom leading to the formation of a C-H bond. Once the "formate" adduct is formed, formate is released from the active site, and the enzyme returns to its oxidized form, ready to start a new catalytic cycle.[35],[36]

---

[33] Boyington, J., C., Gladyshev, V., N., Khangulov, S., V., Stadtman T., C., Sun, P., D., *Science*, **1997**, 275, 5304, 1305–1308, DOI: 10.1126/science.275.5304.1305

[34] Raaijmakers, H., C., A., Romão, M. J., *J. Biol. Inorg. Chem.*, **2006**, 11, 7, 849–854, DOI: 10.1007/s00775-006-0129-2

[35] Mota, C., S., Rivas, M., G., Brondino, C., D., Moura, I., *et al.*, *J. Biol. Inorg. Chem.*, **2011**, 16, 1255–1268, DOI: 10.1007/s00775-011-0813-8

[36] Dobbek, H., *Coord. Chem. Rev.*, **2011**, 255, 1104–1116, DOI: 10.1016/j.ccr.2010.11.017

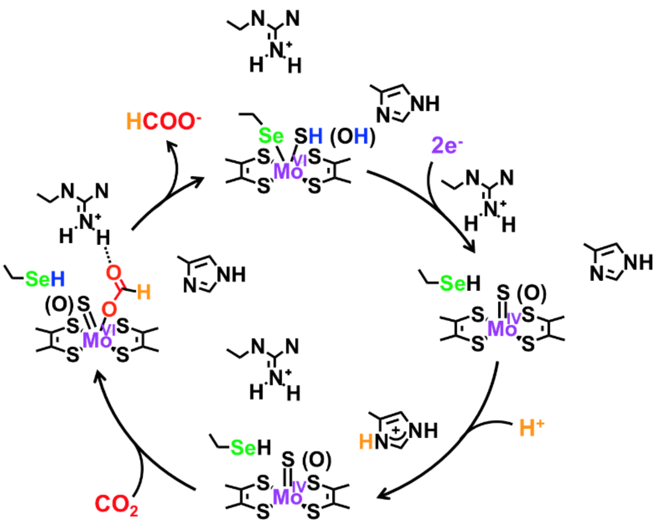

Scheme 2-3. Structure-based proposed mechanism of catalytic CO_2 reduction to formate by Mo-FDHs

CO_2 Reduction to CH_4

Compared to the previously discussed reduction pathways of CO_2 to CO and HCOOH, the biological conversion of CO_2 to CH_4 by methanogens involves several enzymes, coenzymes, and cofactors. In the late 80s, Wolfe and Rouvière described a possible methanogenesis cycle in which CO_2 was reduced to CH_4 via a seven-step pathway (Scheme 2-4).[37],[38]

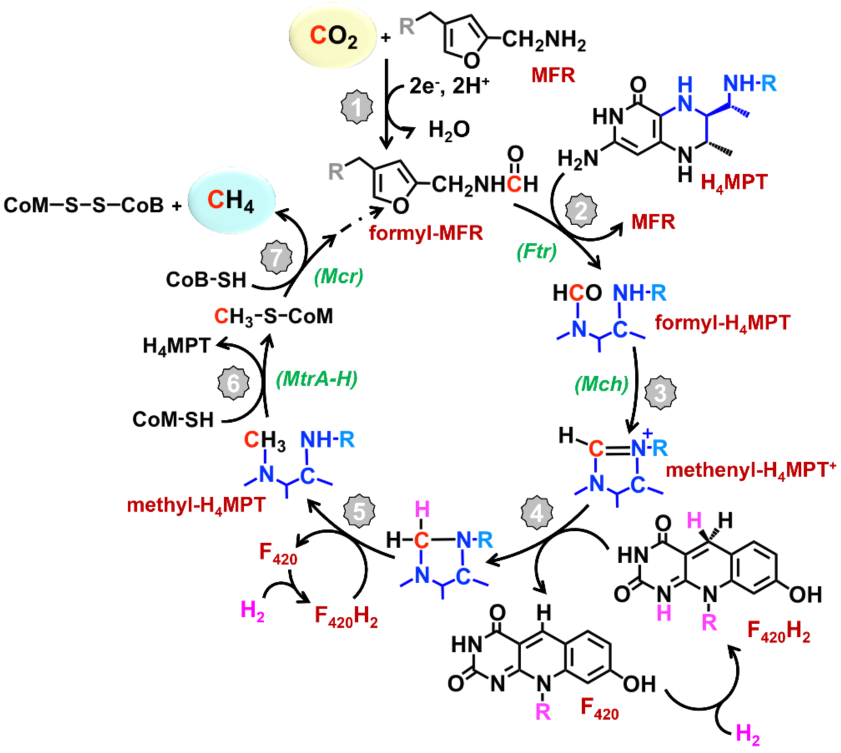

---

[37] Rouviere P.E., Wolfe, R.S., *J. Biol. Chem.*, **1988**, 263, 17, 7913-7916

[38] Thauer, R.K., *Proc. Natl. Acad. Sci. U.S.A.*, **2012**, 109, 38, 15084-15085, DOI: 10.1073/pnas.1213193109

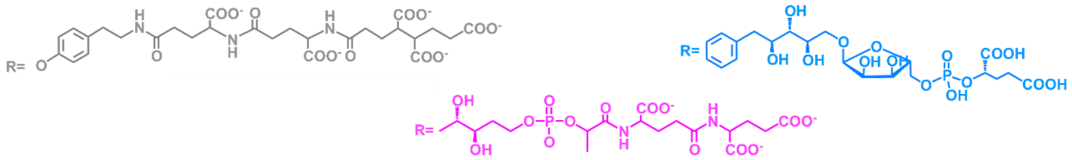

Scheme 2-4. Structure-based proposed hydrogenotrophic methanogenesis cycle by Wolfe and Rouvière (Wolfe Cycle). Abbreviations: MFR, methanofuran; H_4MPT, tetrahydromethanopterin; Ftr, formyltransferase; Mch, methenyl-H_4MPT cyclohydrolase; $F_{420}H_2$, reduced coenzyme F_{420}; $F_{420,}$ coenzyme F_{420}; CoM-SH, coenzyme M; MtrA-H, coenzyme M methyltransferase; CoB-SH, coenzyme B; Mcr, methyl–coenzyme M reductase.

As depicted in Scheme 2-4, CO_2 is initially reduced and fixated into a formyl group, bound to a methanofuran (**MFR**) coenzyme. The formyl group is subsequently transferred to a tetrahydromethanopterin (**H_4MPT**) via a formyltransferase (**Ftr**), generating the formyl-H_4MPT intermediate. The formyl group is then converted to methenyl (=CH) via a condensation reaction catalyzed by methenyl-H_4MPT cyclohydrolase (**Mch**). In the next steps, the double bond of the methenyl-H_4MPT^+ is reduced by two successive hydride abstractions, affording methyl-H_4MPT. The last two catalytic steps involve two enzymes: i) coenzyme M methyltransferase (**MtrA−H**) that catalyzes the transfer of the methyl group to coenzyme CoM-SH and ii) Methyl–coenzyme M reductase (**Mcr**) that utilizes coenzyme CoB-SH as a reductant to catalyze the reduction of CH_3-CoM-SH to CoM-S-S-CoB and CH_4.

Although CO_2 reduction to CH_4 by methanogens is quite complex, a couple of focal points in their fixation pathways are worth investigating; i) *How CO_2 enters their cellular metabolism* and ii) *how CO_2 is fixated into a formyl group bound to the MFR coenzyme*.

Formylmethanofuran Dehydrogenases

In the early 90s, Thauer proposed that the enzyme catalyzing the reduction and fixation of CO_2 into a formyl group was a formylmethanofuran dehydrogenase that could exist in two isoforms: a molybdenum-containing (Fmd)[39],[40] and a tungsten-containing (Fwd)[41],[42] enzyme. However, its exact structure remained unknown until almost 30 years later. In 2016, Wagner and his group solved the first X-ray structure of a formylmethanofuran dehydrogenase isolated from *Methanothermobacter wolfeii*.[43] X-ray analysis of the obtained crystals revealed an 800 kDa tetramer (Fwd(ABCDFG)$_4$) with 46 [4Fe-4S] clusters arranged in a "string-like distribution." Each monomer consists of six subunits, with the FwdBD and FwdA subunits realizing the reductive CO_2 fixation. FwdBD subunits reduce CO_2 into formate while the FwdA catalyzes the condensation reaction between formate and the -NH_2 group of the MFR coenzyme (Fig. 2-6)

---

[39] Börner, G., Karrasch, M.,Thauer, R.K., *FEBS Lett.,* **1989**, 244, 1, 21-25

[40] Börner, G., Karrasch, M.,Thauer, R.K., *FEBS Lett.,* **1991**, 290, 1-2, 31-34

[41] Schmitz, R. A., Richter, M., Linder, D., Thauer, R. K., *Eur. J. Biochem.*, **1992**, 207, 559-565

[42] Bertram, P., A., Schmitz, R., A., Linder, D., Thauer, R.K., *Arch. MIcrobiol.*, **1994**, 161, 220-228

[43] Wagner, T., Ermler, U., Shima, S., *Science*, **2016**, 354, 6308, 114-117, DOI: 10.1126/science.aaf9284

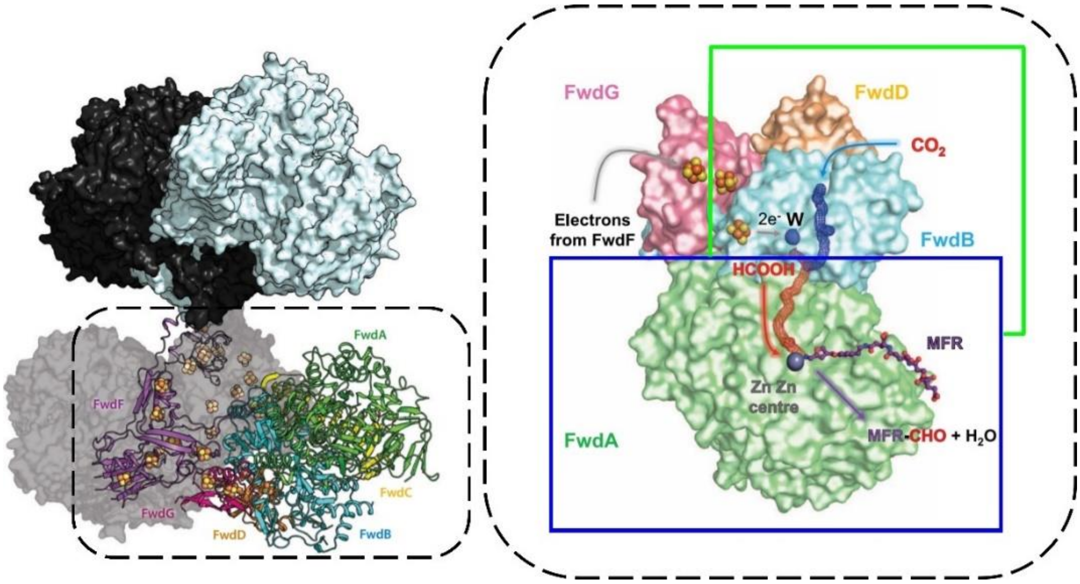

Fig. 2-6. Left: X-ray structure of the tetrameric Fwd (Fwd(ABCDFG)$_4$) isolated from *Methanothermobacter wolfeii*. One of the four monomers is shown as a ribbon diagram, while the others are indicated in different colors.[44] Right: Catalytic mechanism of CO_2 reduction to formyl-MFR by the Fwd(ABCDFG) complex. Green square, CO_2 reduction to formate or formic acid; Blue square, formate condensation with MFR to produce formyl-MFR. W, tungstenpterin dependent formylmethanofuran dehydrogenase; MFR is shown in balls and sticks. [42]

The CO_2 reduction into formate is catalyzed by a W-FDH that holds a [4Fe-4S] cluster and a W-active center. Electrons are provided to the catalytic site by the FwdF subunit, first to the [4Fe-4S] cluster and finally to the W^{VI} metal center. Tungsten is coordinated to four sulfur of two pterin cofactors, a thiolate from a cysteine amino acid (Cys$_{118}$), and an additional sulfur atom. It is speculated that the mechanism of CO_2 reduction into formate is the same as in the case of acetogenic bacteria, as described above for a Mo-FDH. Once formate is formed, it migrates to the second catalytic site via a hydrophilic channel that connects the two FwdBD and FwdA subunits (Fig. 2-6). FwdA subunit contains a dimetallic zinc (Zn) active site with each of the two Zn^{II} centers coordinated to two histidine cofactors. The two Zn^{II} centers are bridged by a lysine (Carboxy-lysine$_{178}$), while one of the two metals is also coordinated with one aspartic acid residue (D$_{358}$) (Fig. 2-7).

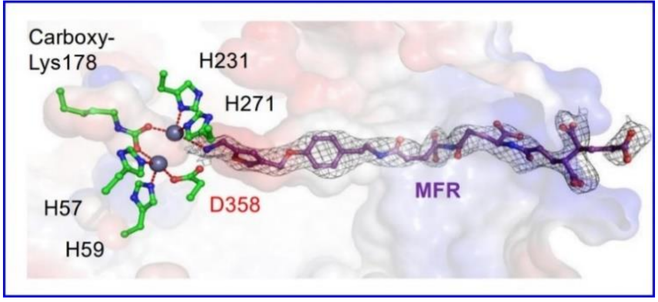

Fig. 2-7. The active site of FwdA bound to MFR.

According to the mechanism proposed by Wagner, two components are the key elements in the fixation of formate into formyl-MFR; i) the dimetallic Zn^{II} center with a dual role, and ii) the aspartic acid. The dimetallic Zn^{II} center serves as a *syn*-*syn* bidentate bridging site that

---

[44] Shima, S., Huang, G., Wagner, T., Ermler, U., *Annu. Rev. Microbiol.*, **2020**, 74, 1, 713-733, DOI: 10.1146/annurev-micro-011720-122807

stabilizes formate and directs it close to the MFR coenzyme. On the other hand, D_{358} enhances the electrophilicity of the C atom of formate through the Zn center, thus promoting the nucleophilic attack by the $-NH_2$ group of MFR. The obtained transition state is stabilized by the two Zn^{II} cations as depicted in Scheme 2-5.

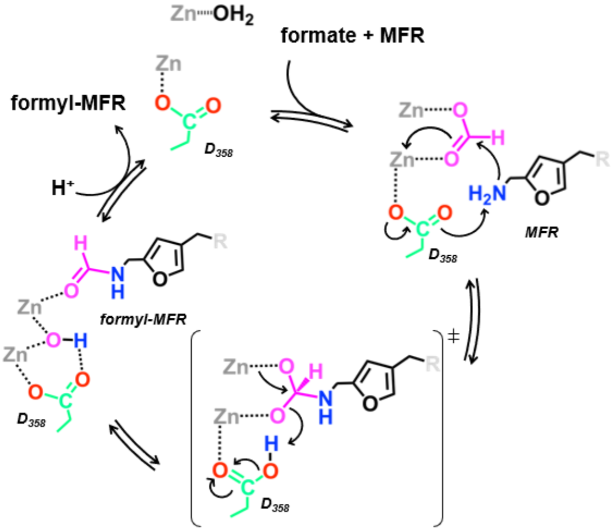

Scheme 2-5. Proposed catalytic mechanism of the condensation reaction between formate and MFR coenzyme.

It is more than evident that cellular life uses complex yet well-orchestrated enzymatic pathways to incorporate inorganic carbon into high or medium-density energy products. Enzymes are the key players that outline the vital role of the first, second, and outer coordination spheres of a catalyst in enhancing its catalytic activity and selectivity. Shedding light on the CO_2 fixation enzymes' architectures and mechanisms has always been challenging; however, enzymes can provide a few fundamental principles that can be adopted in CO_2 valorization systems.

Enzymes use 2nd or 3rd-row transition metals to activate and reduce CO_2. These metals are typically positioned in a trigonal or square-planar ligand field that results in low-spin catalytic sites. Low-spin transition metals are essential for CO_2 activation, since the metal's occupied d_{z^2} and $d_{xz/yz}$ orbitals provide the most efficient overlapping with the σ* LUMO and π* LUMO + 1 antibonding orbitals of CO_2, respectively.[30] However, in some cases, just one metal center may not be efficient enough for CO_2 activation, and a Lewis acid on the second coordination sphere is required. This kind of assisted activation is typical for [NiFe]CODHs that bind CO_2 via a "push-pull" mechanism with the low-spin $Ni^{"0"}$ center as the Lewis base and binding site, and the Fe^{II} metal as the Lewis acid. Biological systems are elegant examples showing how a well-structured second and outer coordination sphere regulates and optimizes the reactivity of the catalytic centers.

Like in the case of Fwd, the outer coordination spheres contain well-defined channels that modulate the access of substrates (*e.g.*, CO_2, CO_2 derivatives, protons, and electrons) to the catalytic sites. The second coordination sphere consists of precisely positioned functional groups that guide CO_2 and/or its derivatives on the binding centers. These functional groups are mainly amino acid residues that stabilize the transition states of the enzymes via electrostatic and/or H-bonding interactions. Since the reduction of CO_2 is a multi-electron multi-proton reaction, enzymes host close to the catalytic center strong reducing agents such as Fd_{red} or NAD(P)H that fuel the metal center with high-energy electrons. The electron transfer is mediated by the first coordination sphere, where the metal is coordinated with electron-rich ligands that serve as electron reservoirs. In contrast, the protons are provided mainly from the outer sphere, and their transfer is facilitated by the second coordination sphere, mainly from the amino acid residues that act as proton relays.

2.1.7 Artificial CO_2 Reduction Approaches

Any conversion of CO_2 into higher added value reagents and valuable fuels requires an input of energy in the form of high-energy-electrons, or highly reducing agents. Under this context, artificial approaches that integrate catalytic systems with renewable energy sources could lay the foundations for a carbon-neutral and sustainable future. These approaches commonly harness and convert solar energy into an (electro)chemical potential to drive the CO_2 reduction reaction (CO_2RR). Among the already established systems, photovoltaic-electrocatalytic (PV-EC) schemes have afforded the most promising results for potential industrial applications.[45] A PV-EC scheme could be better described as a two-compartment apparatus in which electrons and holes are provided from the photovoltaic to the electrochemical cell where the CO_2RR takes place (cathode) along with water-splitting (anode).[46] The long-term sustainability of such devices relies on chemically-stable CO_2-reduction electrocatalysts based on low-cost metals that can operate at low overpotentials and exhibit optimal stability and selectivity towards the CO_2 reduction products. Understanding catalytic reaction mechanisms is a primary pre-requisite to meeting these requirements. Molecular catalysts are an excellent platform for investigating the CO_2RR dynamics at the atomic level, with complementary computational modeling studies that can provide valuable guidelines to optimize their catalytic activities.

2.1.7.1 Bio-inspired Electrocatalytic CO_2 Reduction

Incorporating the second coordination sphere principles of enzymatic CO_2 fixation into synthetic CO_2 electrocatalysts is a promising approach for tuning and enhancing their reactivities. Such a bio-inspired approach can be successfully attained by electrocatalysts with a versatile building framework so that a well-designed second coordination sphere can be integrated. In this perspective, a plethora of metalloporphyrin derivatives has been designed over the years[47],[48] and modified with well-positioned H-bonding groups, cationic moieties, and pendent proton relays[49],[50] as a means to achieve faster kinetics and low overpotentials, enhanced stability, and higher product selectivity. Before proceeding to the state-of-the-art iron and copper porphyrins as CO_2 reduction electrocatalysts, it is helpful to introduce some of the main performance markers that will help us compare their catalytic activity.

Benchmarking catalysts performance

In electrocatalytic CO_2RR systems, three main indicators are used to describe their performances: turnover frequency (TOF / s^{-1}), overpotential (η / V), and Faraday efficiency (FE %).[51] TOF refers to the catalytic rate of the reaction. It is defined as the number of a specified product molecules produced in a given interval of time divided by the number of the active

---

[45] He, J., Janáky, C., *ACS Energy Lett.*, **2020**, 5, 6, 1996–2014, DOI: 10.1021/acsenergylett.0c00645

[46] Kim, J., Jeong, S., Beak, M., Park, J., Kwon, K., *Chem. Eng. J.*, **2021**, 428, 11-12, 130259, DOI: 10.1016/j.cej.2021.130259

[47] Gotico, P., Halime, Z., Aukauloo, A., *Dalton Trans.*, **2020**, 49, 2381-2396, DOI: 10.1039/C9DT04709C

[48] Saha, P., Amanullah, S., Dey, A., *Acc. Chem. Res.*, **2022**, 55, 134–144, DOI: 10.1021/acs.accounts.1c00678

[49] Margarit, C.G., Schnedermann, C., Asimow, N.G., Nocera. D.G, *Organometallics*, **2019**, 38, 6, 1219-1223, DOI: 10.1021/acs.organomet.8b00334

[50] Amanullah, S., Saha, P., Dey, A., *J. Am. Chem. Soc.*, **2021**, 143, 34, 13579-13592, DOI: 10.1021/jacs.1c04392

[51] Costentin, C., Savéant, J-M., *Nat. Rev. Chem.*, **2017**, 1, 0087, DOI: 10.1038/s41570-017-0087

catalyst molecules. Overpotential (η), on the other hand, describes the additional kinetic energy beyond the thermodynamic requirement that has to be supplied to the catalytic system to drive a specific redox electrochemical reaction. Lastly, Faraday efficiency denotes the ratio of the charge required to produce a specific product to the total charge flow during electrolysis. Ideally, a catalyst should be able to realize the CO_2RR at low overpotentials (close to the thermodynamic potential) with high TOFs (fast) and FE % (higher selectivity).

2.1.7.1.1 Iron Porphyrins

Iron porphyrins stimulated research interest already since the early 80s, and they were profoundly investigated by Savéant and co-workers as potential electrocatalysts for CO_2RR.[52] Ever since, numerous electrocatalytic and spectro-electrochemical studies have been conducted, shedding light on CO_2 reduction mechanism. As illustrated in Scheme 2-6, iron porphyrins undergo three successive reversible reductions, with the last two being ligand-centered.[53] Three-electron reduction of the catalyst generates the $[Fe^{II}(TPP^{\bullet\bullet})]^{2-}$ state that activates and binds CO_2 by an electron transfer to the σ* LUMO orbital of CO_2, affording the $[Fe^{II}(TPP^{\bullet})CO_2]^{-}$ intermediate.[54] The $[Fe^{II}(TPP^{\bullet})CO_2]^{-}$ species are highly unstable, and the presence of weak Brønsted or Lewis acids is essential not only to stabilize the Fe-CO_2 adduct but also to facilitate the C-O bond cleavage. Once Fe^{II}-CO intermediate is formed, it is further reduced by one-electron transfer, with CO being released and the catalyst returning to its doubly reduced state.

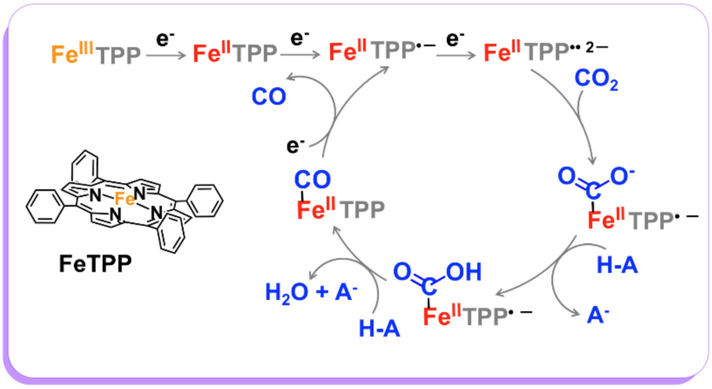

Scheme 2-6. Proposed catalytic mechanism of the reduction of CO_2 to CO by iron porphyrins in the presence of a Brønsted acid (H-A).

H-Bonding Interactions

Recalling the role of amino acid residues in [NiFe]CODHs and FDHs, several research teams have investigated a series of iron porphyrins appended with H-bonding groups in their second coordination sphere.

Chang and co-workers[55] in 2018 synthesized four isomers of an iron porphyrin bearing a pendent amide group and investigated the dependence of the electrocatalyst's performance on the position of the amide (Fig. 2-8). The ***o*-2-amide** isomer exhibited the best performance with an enhanced catalytic rate ($\log TOF_{max}$) and high faradaic efficiency (FE) for CO formation among the studied iron porphyrins. To exclude an intermolecular interaction of the amide groups, they studied the catalytic activity of the parent FeTPP porphyrin in the presence of an

---

[52] Hammouche, H., Lexa, D., Savéant, J.M., *J. Electroanal. Chem.*, **1988**, 249, 1-2, 347-351, DOI: 10.1016/0022-0728(88)80372-3

[53] Römelt, C., Ye, S., Bill, E., Weyhermüller, T., van Gastel, M., Neese, F., *Inorg. Chem.*, **2018**, 57, 4, 2141–2148, DOI: 10.1021/acs.inorgchem.7b03018

[54] Mondal, B., Rana, A., Sen, P., Dey, A., *J. Am. Chem. Soc.*, **2015**, 137, 35, 11214–11217, DOI: 10.1021/jacs.5b05992

[55] Nichols, E.M., Derrick, J.S., Nistanaki, S.K, Smith, P.T., Chang, C.J., *Chem. Sci.*, **2018**, 9, 2952-2960, DOI: 10.1039/C7SC04682K

external aryl amide. The obtained results revealed a considerably lower logTOF$_{max}$ indicating that the high logTOF$_{max}$ observed for the functionalized ***o*-2-amide** derivative derived from the covalent attachment of the amide on the macrocycle's framework. The abovementioned results pointed out the essential role of ortho and distal H-bond fragments in a catalyst's second coordination sphere for the efficient stabilization of the CO$_2$ reduction intermediates through H-bonding interactions (*e.g.*, CO$_2^{\bullet-}$, carboxylate intermediate).

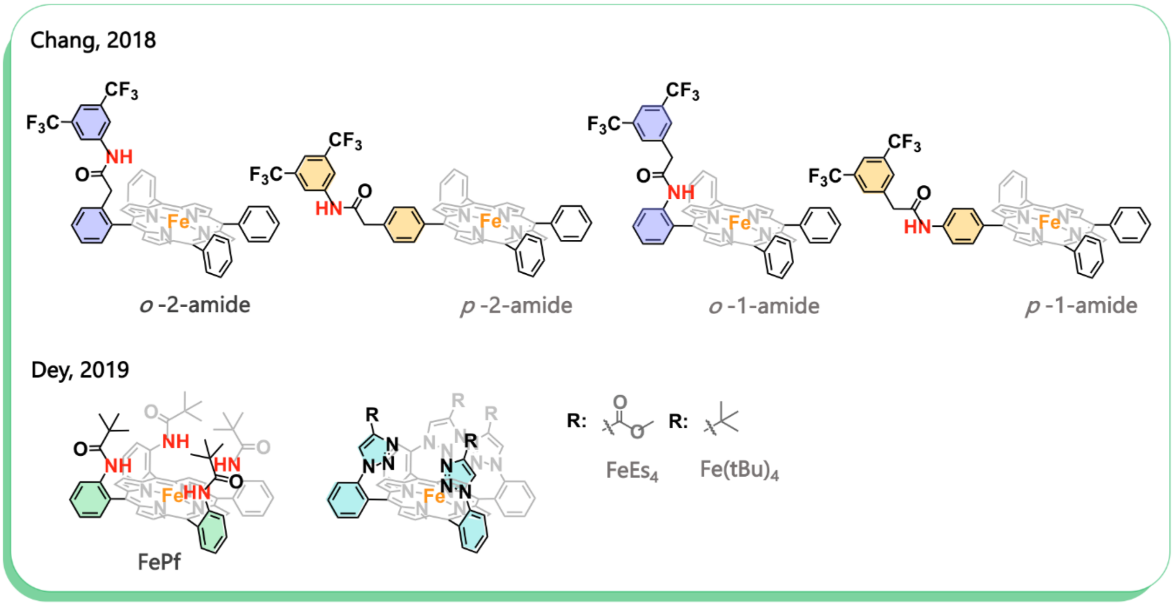

Fig. 2-8. Introduction of hydrogen bond donors on the second coordination sphere of iron porphyrin catalysts.

On a similar note, the group of Dey [56] functionalized three iron porphyrin complexes with either four pendent αααα-amide groups (**FePf**) or triazole moieties (**FeEs$_4$ and Fe(tBu)$_4$**), as depicted in Fig. 2-8. The three main pillars of this study involved the investigation of whether i) the incorporation of more than one hydrogen bonding site on the same plane of the porphyrin could contribute to a higher CO$_2$ binding rate, ii) a hydrophobic or hydrophilic catalytic environment could affect the CO$_2$ reduction rate and iii) the strength of the hydrogen-bond donor could affect the reaction rate. Electrocatalytic studies in the presence of an external proton source (PhOH) showed that the amide derivative displayed at least three orders of magnitude faster catalytic rate compared to the two triazole iron porphyrins. To further rationalize the experimental findings, geometry-optimized DFT calculations were performed to investigate the nature of the Fe-CO$_2$ intermediates. It was found that the amide groups of the **FePf** porphyrin do not stabilize the [Fe^{II} (TPP$^{\bullet}$) CO$_2$]$^-$ adduct via hydrogen bonding but instead via electrostatic interactions due to their dipole character. Interestingly, these findings were opposite to what was reported previously by Chang on a similar amide derivative which stabilized the primary intermediate via weak hydrogen bonds. This difference in CO$_2$ activation was attributed to the sterically hindered environment caused by the bulky tert-butyl groups (tBut). On the other hand, the DFT studies on the **FeEs$_4$** and **Fe(tBu)$_4$** triazole porphyrins revealed a much lower CO$_2$ activation than the **FePf** porphyrin justifying the experimental results. As it was expected but further confirmed by FTIR studies, the triazole moieties are H-bond acceptors that can entrap water molecules inside the catalytic vicinity.

---

[56] Sen, P., Mondal, B., Saha, D., Rana, A., Dey, A., *Dalton Trans.*, **2019**, 48, 5965-5977, DOI: 10.1039/c8dt03850c

Although the **$FeEs_4$** and **$Fe(tBu)_4$** offered different distal cavities in terms of hydrophilicity and hydrophobicity, they exhibited comparable CO_2 reduction rates. The fact that all the electrocatalytic studies were conducted in the presence of the same proton source indicated that the catalytic rates depend on the p*K*a values of the hydrogen bond donors. Indeed, the Brønsted catalysis equation afforded a linear relationship between the logarithmic relative catalysis rate and the p*K*a of the hydrogen bond donors. The obtained small negative slope suggested that the rate-determining step (*RDS*) involves a proton transfer. According to Dey and co-workers, this proton transfer is likely realized on the Fe^{I}-COOH intermediate.

A different approach was employed by our group [57] which proposed two αβαβ iron porphyrin atropisomers functionalized with urea (**FeTPP-Ur**) or amide (**FeTPP-Am**) groups as multi-point hydrogen bonding sites towards the stabilization of the catalytic intermediates (Fig. 2-9). The introduction of these pendent groups resulted in a higher log TOF_{max} when using H_2O as the proton source and significantly lowered the overpotential of the CO_2 reduction to CO, compared to the parent FeTPP analogue. DFT calculations on **FeTPP-Ur** and **FeTPP-Am** catalysts revealed that these catalysts could stabilize the $[Fe^{II}\ (TPP^{\bullet})\ CO_2\ ]^{-}$ primary intermediates via hydrogen bonds from the N-H fragments. The **FeTPP-Ur** catalyst offered a more robust hydrogen bonding framework than the **FeTPP-Am** since each urea arm served as a two-point hydrogen bonding site. Indeed, **FeTPP-Ur** appeared to have shorter (N)H···O(C) four hydrogen bond distances of 2.738, 2.804, 2 x 2.832 Å for each urea arm, comparable with those of the (His)H···O(C)O···H($_3N^+$Lys) in the natural [NiFe]CODH enzyme (inset Scheme 2-2). The stronger H-bonding interactions with the carboxylate intermediate were also reflected in the higher CO_2 binding affinity with the **FeTPP-Ur**, displaying almost ten times higher CO_2 binding rate constant than the **FeTPP-Am** catalyst. Crystallographic data obtained for the **FeTPP-Ur** derivative revealed a well-defined water molecule network inside the catalytic cavity, suggesting that water molecules may stabilize not only the catalytic intermediates but also mediate the proton transfer to the intermediate carboxylate species. Geometry-optimized DFT calculations and kinetic isotope effect (KIE) studies also supported this hypothesis and further rationalized the 300 mV and the 200 mV drop of the overpotential compared to the nonfunctionalized **FeTPP** and the **FeTPP-Am**, respectively.

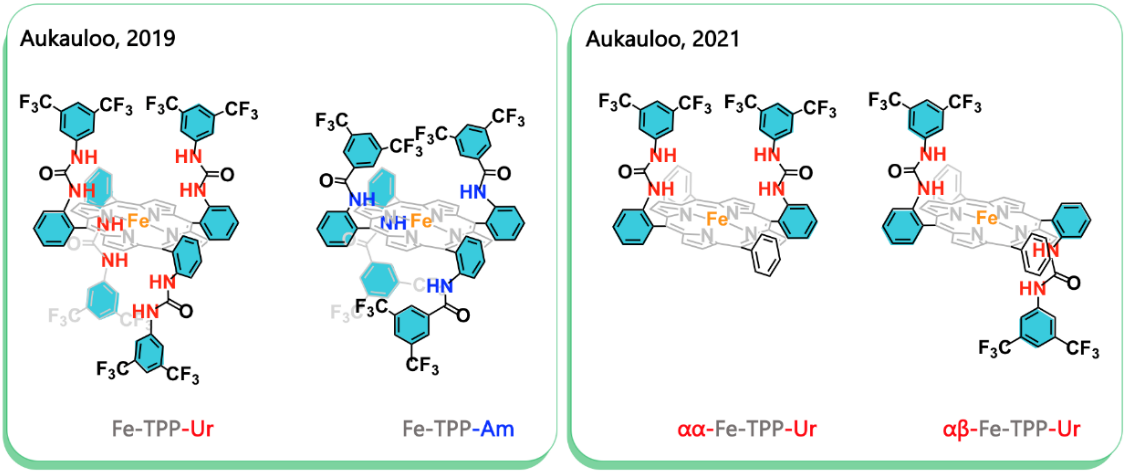

Fig. 2-9. Incorporation of multiple hydrogen bonding sites on the second coordination sphere of iron porphyrin catalysts.

---

[57] Gotico, P., Boitrel, B., Guillot, R., Sircoglou, M., Quaranta, A., Halime, Z. *et al., Angew. Chem. Int. Ed.*, **2019**, 58, 14, 4504-4509, DOI: 10.1002/anie.201814339

Moving one step forward, our team[58] also synthesized two additional derivatives, **αα-FeTPP-Ur**, and **αβ-FeTPP-Ur**, to elucidate how the topological isomerism of the urea groups could affect the binding affinity of CO_2 on the metal center and, by extension, the electrocatalytic rate of the CO_2 reduction (Fig. 2-9). Surprisingly the **αα-FeTPP-Ur** atropisomer was a much poorer catalyst (k_{cat}= 9.25 × 10^3 s^{-1}) than the **αβ-FeTPP-Ur** (k_{cat}= 7.75 × 10^4 s^{-1}) although exhibiting an almost 25 times higher CO_2 binding rate constant (k_{CO2} = 90.6 $M^{-1}s^{-1}$ *vs.* k_{CO2} = 3.9 $M^{-1}s^{-1}$). H/D kinetic isotopic studies for both isomers revealed that the *RDS* of the CO_2 reduction reaction involves a proton transfer to the carboxylate intermediate, contradicting the findings of Dey's group mentioned above. The **αα-FeTPP-Ur** atropisomer displayed a much stronger KIE of 5.6 compared to **αβ-FeTPP-Ur** (KIE= 1.5), suggesting a tight hydrogen-bonding network between the carboxylate intermediate and the two face-to-face urea arms could hinder the proton transfer in the *RDS*. On the contrary, the **αβ-FeTPP-Ur** isomer could provide a more accessible proton transfer to the carboxylate intermediate. In addition, **αβ-FeTPP-Ur** exhibited almost one order of magnitude higher overall reaction rate than the **αα-FeTPP-Ur** isomer indicating that a more "open" catalytic environment results in a much faster proton transfer in the *RDS*.

Cationic Interactions

Inspired by the positively charged amino acids in the second sphere of catalytic centre of the CO_2 fixation enzymes, cationic moieties have also been incorporated in the second coordination sphere of a series of synthetic metalloporphyrins. The introduction of positive charges in the periphery of the metalloporphyrin macrocycle has been shown to considerably improve the CO_2 reduction reaction catalytic rates.

As reported by the group of Savéant[59], the functionalization of the porphyrin's phenyl groups with trimethyl-ammonium substituents on the para (**Fe-*p*-TMA**) or ortho (**Fe-*o*-TMA**) position resulted in a significantly higher catalytic reactivity in DMF/PhOH/H_2O, compared to the unsubstituted **FeTPP** (Fig. 2-10). Both isomers could stabilize the primary $[Fe^{II}(TPP^{\bullet})CO_2]^-$ intermediate via through-space coulombic interactions, with **Fe-*o*-TMA** exhibiting a stronger stabilization due to a more optimal orientation of the quaternary ammonium groups. This effect was reflected in the very low overpotential (220 mV) and the exceptionally high catalytic rate (TOF = 10^6 s^{-1}). More importantly, since the cationic groups rendered the catalysts soluble in aqueous solutions, preparative-scale electrolysis was also performed in water. **Fe-p-TMA** displayed a great selectivity over CO_2 reduction to CO in neutral pH, with an average FE_{CO} of 90% and a FE for H_2 of only 7%. Interestingly, traces of C_2 reduction products such as acetate and oxalate were also detected.[60]

Using a more sophisticated structural approach, Aukauloo and co-workers[61],[62] introduced ionic liquid-like functionalities on the macrocyclic ring and explored how these positively charged units could affect the electronics and the reactivity of the CO_2 reduction electrocatalyst. A series of iron porphyrins derivatives was investigated bearing a different number of methyl-imidazolium units as depicted in Fig. 2-10. Electrocatalytic studies in

---

[58] Gotico, P., Roupnel, L., Guillot, R., Sircoglou, M., Leibl, W. *et al., Angew. Chem. Int. Ed.*, **2020**, 59, 50, 22451-22455, DOI: 10.1002/anie.202010859

[59] Azcarate, I., Costentin, C., Robert, M., Savéant, JM., *J. Am. Chem. Soc.*, **2016**, 138, 51, 16639–16644, DOI: 10.1021/jacs.6b07014

[60] Costentin, C., Robert, M., Savéant, JM., Tatin. A., *PNAS USA*, **2015**, 112, 22, 6882-6886, DOI: 10.1073/pnas.1507063112.

[61] Khadhraoui, A., Gotico, P., Boitrel, B., Leibl, W. *et al., Chem. Commun.*, **2018**, 54,11630-11633, DOI: 10.1039/C8CC06475J

[62] Khadhraoui, A., Gotico, P., Leibl, W., Halime, Z., Aukauloo, A., *ChemSusChem*, **2021**, 14, 5, 1308-1315, DOI: 10.1002/cssc.202002718

DMF/H_2O revealed that the insertion of the methyl-imidazolium group(s) considerably enhanced the reactivity of the catalysts, with the **1-Im-Fe** derivative exhibiting an unprecedently high TOF of 2×10^8 s^{-1}. Although the **1-Im-Fe** was the most efficient catalyst, it displayed the highest CO_2 to CO overpotential. The higher overpotential was attributed to the lack of a cumulative positive charge that could stabilize through-space the $[Fe^{II}(TPP^{\bullet})CO_2]^{-}$ state and as such, prevent a more thermodynamically favorable transfer of electrons to the metal center. To rationalize this trend between kinetics and thermodynamics, H/D KIE studies were performed suggesting that a different *RDS* might be involved in the catalytic mechanisms between the **1-Im-Fe** and **4-Im-Fe** catalyst. **4-Im-Fe**, as a water-soluble electrocatalyst, was also investigated for its CO_2 reduction activity in aqueous solutions. In contrast to the electrocatalytic experiments in DMF/H_2O, bulk electrolysis studies in pure water revealed a significantly higher catalytic rate at lower overpotentials, with CO as the sole reduction product.

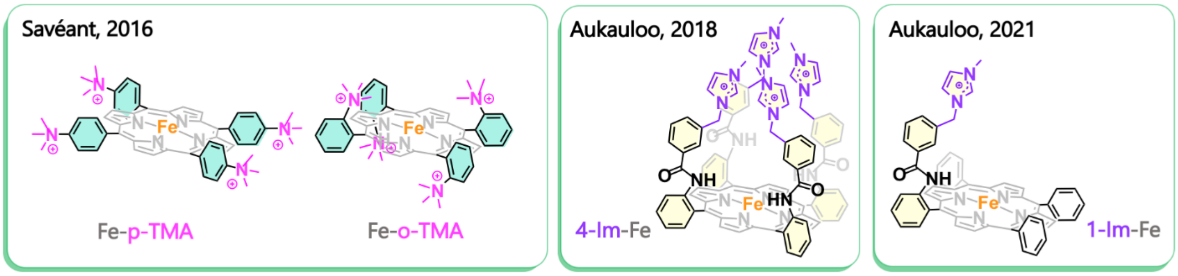

Fig. 2-10. Insertion of cationic moieties in the periphery or the second coordination sphere of iron porphyrin catalysts.

2.1.7.1.2 Copper Complexes

Copper-based molecular complexes have drawn considerably less attention in electrocatalytic CO_2 reduction systems than the thoroughly investigated iron porphyrins; however, they can be promising catalysts if their thoughtful design is considered. Copper is the only pure metal that catalyzes the reduction of CO_2 into C_2 and C_3 products such as C_2H_4, ethanol (EtOH), and propanol (PrOH) with substantial FEs![63] In literature, the number of reports on molecular copper catalysts for homogeneous CO_2 reduction is limited, and some of the most common catalysts are depicted in Fig. 2-11.

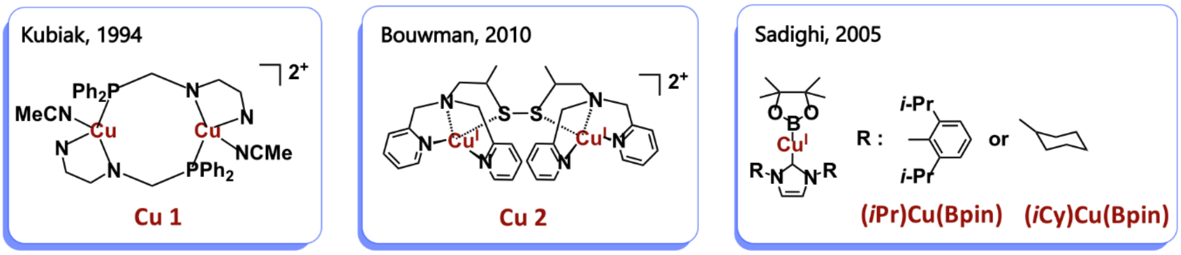

Fig. 2-11. Copper-based dinuclear and mononuclear complexes studied as catalysts for CO_2 reduction.

Almost three decades ago, Kubiak [64] reported a bis-copper μ-phosphinobipyridyl complex (**Cu 1**) that could catalyze the two-electron reduction of CO_2 to CO at moderate onset

---

[63] Hori, Y., Wakebe, H., Tsukamoto, T., Koga, O., *Electrochim. Acta*, **1994**, 39, 11-12, 1833-1839, DOI: 10.1016/0013-4686(94)85172-7

[64] Haines, R.J., Wittrig. R.E., Kubiak, C.P., *Inorg. Chem.*, **1994**, 33, 4723-4728, DOI: 10.1021/ic00099a024

potentials, with the bipyridyl ligands serving as a four-electron reservoir to the copper metals (Fig. 2-11). Infrared spectro-electrochemical measurements demonstrated that during electrocatalysis, carbonate was also formed, suggesting a CO_2 dimerization prior to the release of CO and carbonate. This possible disproportionation of two CO_2 molecules could rationalize the reduction of CO_2 in the absence of a proton source.

Bouwman and co-workers[65] on the contrary, investigated a dinuclear copper (I) complex (**Cu 2**) that converted CO_2 into oxalate (Fig. 2-11). This novel catalyst captured rapidly, atmospheric CO_2 yielding a thermodynamically stable copper (II) oxalate tetramer, which was further reduced chemically to regenerate the bis-copper (I) catalyst. An X-ray structure of an oxalate bis-copper complex has been reported by Farrugia *et al.* in 2001.[66] On a similar note, Sadighi's group [67] synthesized two carbene-copper (I) boryl complexes that activated CO_2 through their copper (I) metal center while the boryl group abstracted one of the two carbonyl oxygen atoms, thus producing an oxo-bridged pinB-O-Bpin dimer and releasing CO as a by-product (Fig. 2-11). The rate of the CO_2 conversion to CO was fine-tuned by varying the temperature of the catalytic reaction with the **(IPr)Cu(Bpin)** exhibiting 1000 TON after 20h at 100 °C and **(ICy)Cu(Bpin)** 100 TON after only 1h at 0 °C.

Moving to more rigid and versatile organic ligands, Masaoka[68] reported quite recently a highly-active copper porphyrin bearing strong-electron withdrawing fluoro groups (**CuTPFP**) (Fig. 2-12). This catalyst could catalyze the two-electron reduction of CO_2 to CO with 1 M of trifluoroethanol as proton source, having a peculiar TOF_{CO} of more than 1.4×10^6 s^{-1}, outperforming a series of previously reported iron porphyrin and copper-based homogeneous catalysts, albeit at higher overpotentials.

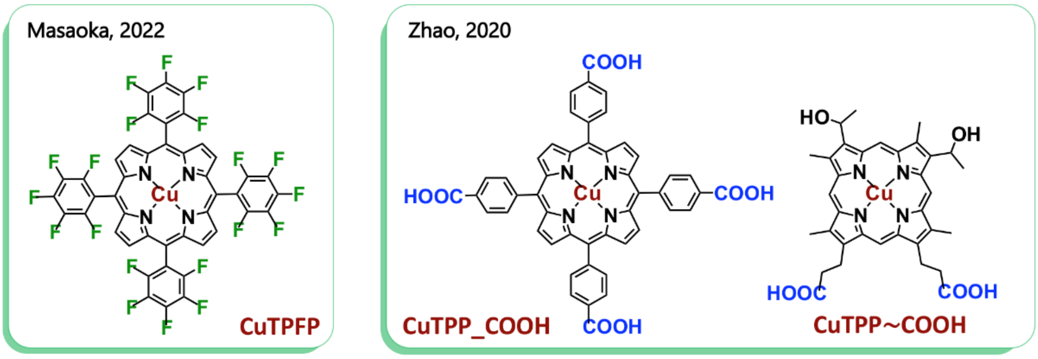

Fig. 2-12. Copper porphyrins modified with electron-withdrawing groups and local proton sources as catalysts studied for CO_2RR in homogeneous electrocatalytic systems.

Meanwhile, Zhao[69] inspired by the pioneering work of Nocera,[70],[71] and Savéant,[72] who functionalized a series of iron porphyrins with pendent proton relay, introduced carboxyl groups on two copper porphyrins as depicted in Fig. 2-12. Both *para-phenyl* (**CuTPP_COOH**) and *β*-substituted (**CuTPP ~ COOH**) copper porphyrins displayed good catalytic activity

---

[65] Angamuthu, R., Byers, P., Lutz, M., Spek, A.L., Bouwman, E., *Science*, **2010**, 327, 5963, 313-315, DOI: 10.1126/science.1177981

[66] Farrugia, L.J., Lopinski, S., Lovatt, P.A., Peacock, R.D., *Inorg. Chem.* **2001**, 40, 558-559, DOI: 10.1021/ic000418y

[67] Laitar, D.S., Müller, P., Sadighi, J.P., *J. Am. Chem. Soc.*, **2005**, 127, 17196-17197, DOI: 10.1021/ja0566679

[68] Kosugi, K., Kashima, H., Kondo, M., Masaoka, S., *Chem. Commun.*, **2022**, 58, 2975–2978, DOI: 10.1039/d1cc05880k

[69] Zhou, Y., Xiao, Y., Zhao, J., *New J. Chem.*, **2020**, 44, 16062-16068, DOI: 10.1039/d0nj02900a

[70] Margarit, C.G., Schnedermann, C., Asimow, N.G., Nocera, D.G., *Organometallics*, **2019**, 38, 6, 1219–1223, DOI: 10.1021/acs.organomet.8b00334

[71] Margarit, C.G., Asimow, N.G., Gonzalez, M.I., Nocera, D.G., *Phys. Chem. Lett.*, **2020**, 11, 5, 1890–1895, DOI: 10.1021/acs.jpclett.9b03897

[72] Costentin, C., Drouet, S., Robert, M., Savéant, J-M., *Science*, **2012**, 338, 90–94, DOI: 10.1126/science.1224581

towards CO_2 conversion to CO, with **CuTPP ~ COOH** being significantly more efficient catalyst. β-COOH groups could intermolecularly deliver protons to the catalytic site even in the absence of a proton source, while aromatic -COOH groups could act as intramolecular proton relays only in the presence of Brønsted acids. Although **CuTPP_COOH** was a less efficient catalyst, it displayed almost five times higher FE_{co} than its iron analogue. However, this was not the case for **CuTPP ~ COOH** and **FeTPP ~ COOH,** which exhibited comparable FE_{co} of approximately 55%.

Indubitably, a considerable effort has been devoted to the diligent design of iron porphyrin electrocatalysts. Following the enzymes' fine-tuned strategies to reduce CO_2, the porphyrin platform has been functionalized with several H-bonding and cationic units to gain both thermodynamic and kinetic control over the CO_2RR. The incorporation of such moieties on the second coordination sphere significantly improved the reactivity of the catalysts, as reflected not only in the enhanced catalytic rates and selectivity but also in the considerably lower overpotentials. On the other hand, copper porphyrins are less commonly studied. Only recently, a couple of examples have been reported in the literature for homogeneous catalysis, with **CuTPFP** as the sole example with a promising catalytic rate (Fig. 2-13).

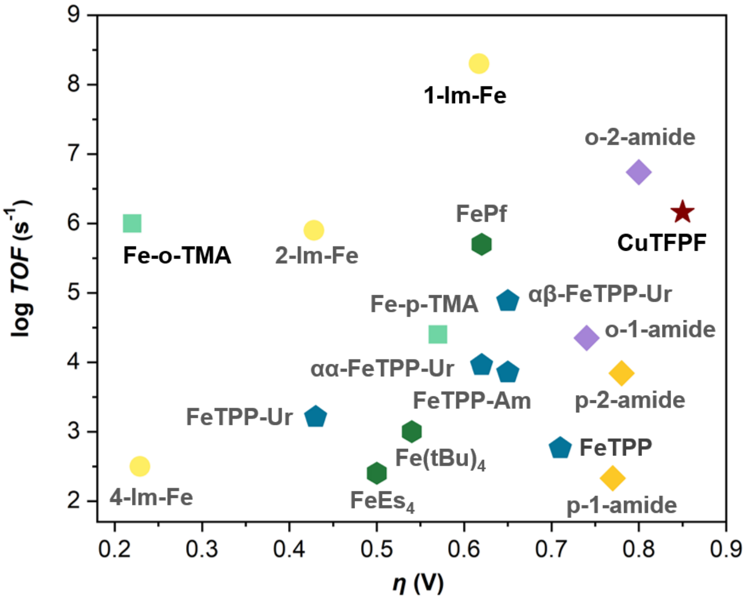

Fig. 2-13. Summary of the catalytic performances of the above-mentioned iron and copper porphyrins modified with; cationic moieties: squares-circles, multipoint hydrogen bonding groups: pentagon, hydrogen-bonding groups: hexagon-rhombus. A rough comparison is presented given the differences in experimental conditions (solvent, proton source).

From an industrial perspective, however, the implementation of these catalysts faces some considerable challenges. The presence of oxygen, especially in iron-based electrocatalytic systems, can considerably diminish or even hinder the reduction of CO_2, thus losing their potential industrial value.

2.1.7.2 CO_2 Reduction in the presence of O_2

Although the prevailing logic in the industrial CO_2 valorization is utilizing a pure CO_2 gas source, the separation of CO_2 from ambient air comes with substantial energy and economical cost. On this note, direct utilization of concentrated CO_2 sources such as flue gas streams would be a sustainable way out. The combustion of fossil fuels generates a gas mixture of CO_2

and O_2 with an O_2 to CO_2 ratio of approximately 35%.[73] In this context, the design of O_2-tolerant catalysts for CO_2 reduction is highly desirable. In molecular catalysis, however, CO_2 reduction in the presence of O_2 is a field still in its infancy, and only a couple of paradigms concerning iron-porphyrins catalysts have been reported in the literature.

In 2019, Dey and co-workers[74] set the first example of a ferrocene-appended iron porphyrin (**FeFc$_4$**) that was able to efficiently catalyze the reduction of CO_2 in the presence of O_2 (Scheme 2-7).

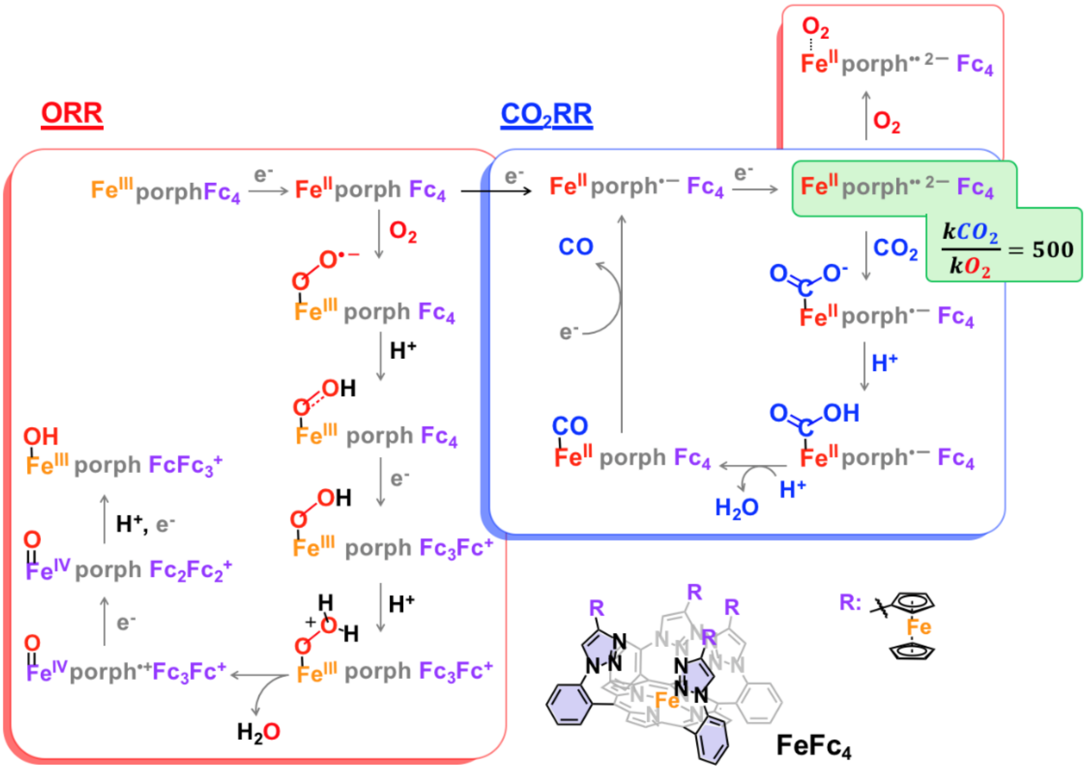

Scheme 2-7. General ORR and CO_2RR pathway followed by the O_2-tolerant FeFc$_4$ catalyst.

FeFc$_4$ was already known to realize the $4e^-/4H^+$reduction of O_2 to H_2O both under homogeneous conditions in the presence of a strong acid and under heterogeneous conditions with water as the proton source. O_2 was activated by the Fe^{II} oxidation state of the catalyst, and it was selectively reduced to H_2O with the four electrons provided from the three ferrocene groups and the reduced metal center.[75],[76] **FeFc$_4$** also displayed great catalytic activity towards the reduction of CO_2 to CO and formate in aprotic polar media, with PhOH as the external proton source, exhibiting a FEco of more than 92%. Interestingly, when up to 20 % of O_2 was introduced into the CO_2 electrochemical cell, the CO_2 catalytic efficiency of **FeFc$_4$** remained almost intact, while O_2 was reduced to water with only 5 % of PROS being produced. This high tolerance of the **FeFc$_4$** catalyst to reduce CO_2 even in the presence of oxygen was attributed to the 500 times faster reaction rate of its formal Fe^0 state with CO_2 compared to O_2, even though DFT calculations proved the latter to be thermodynamically more favorable by approximately 23 kcal/mol.

---

[73] Song, C. Pan, W., Srimat, S.T., Zheng, J. *et al.*, *Stud. Surf. Sci. Catal.*, **2004**, 153, 315-322, DOI: 10.1016/S0167-2991(04)80270-2

[74] Mondal, B., Sen, P., Rana, A., Saha, D., Das, P., Dey, A., *ACS Catal.*, **2019**, 9, 3895−3899 DOI: 10.1021/acscatal.9b00529

[75] Mittra, K., Chatterjee, S., Samanta, S., Dey, A., *Inorg. Chem.*, **2013**, 52, 14317−14325, DOI: 10.1021/ic402297f

[76] Samanta, S., Mittra, K., Sengupta, K., Chatterjee, S., Dey, A., *Inorg. Chem.*, **2013**, 52, 3, 1443–1453, DOI: 10.1021/ic3021782

Although **FeFc₄** is the only example of an iron porphyrin that can catalyze the reduction of CO_2 under aerobic conditions, there are several paradigms of O_2-tolerant catalysts reported for hydrogen evolution (HER) and hydrogen oxidation (HOR) reactions.[77],[78] Adopting similar concepts can offer a promising route towards robust and highly efficient CO_2 electrocatalysts with high aerobic stability.

O_2-tolerant Catalyst's Design in HER and HOR catalytic systems

There are two common strategies established in HER and HOR electrocatalytic schemes for making a catalyst O_2-tolerant. The catalyst can be tactfully modified to realize the HER reaction selectively, or it can be incorporated into an oxygen-reducing matrix. The latter approach is mainly employed in hydrogenase enzymes[79] to prevent the binding of O_2 to the HOR catalytic site, which is extremely sensitive to oxidative stress responsible for its deactivation.

In 2014, Reisner and Wakerley[80] investigated a series of O_2-tolerant cobaloxime catalysts through electrochemical molecular catalyst screening (EMoCS) to elucidate how the axial ligand's substituents affect the catalytic activity of these catalysts. More than 20 axial ligands were investigated; however, for brevity, only a couple of examples are depicted in Scheme 2-8. Controlled potential electrolysis (CPE) experiments under anaerobic conditions revealed that catalysts with more electron-donating axial ligands exhibited higher catalytic activity, which they could maintain even in the presence of O_2. The preference of proton over O_2 reduction was attributed to the formation of a more basic Co^{II}-H intermediate species that accelerated the rate of HER catalysis compared to the O_2 reduction on the electrode, thus rendering catalysts with a more electron-rich metal center more O_2-tolerant.

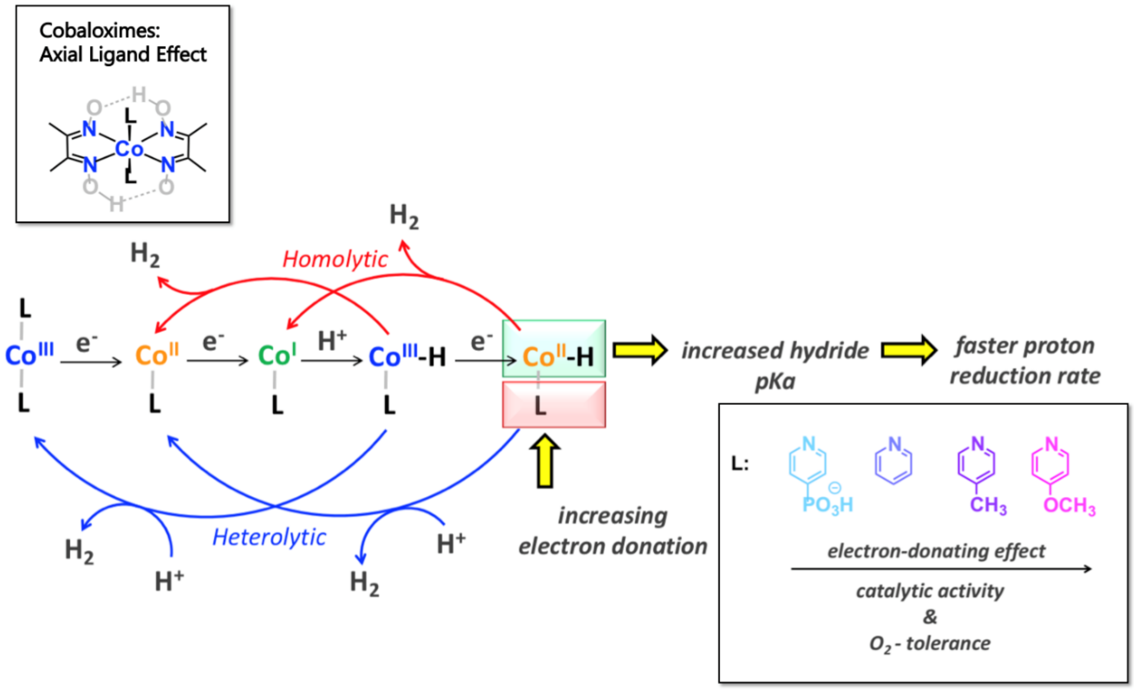

Scheme 2-8. A proposed mechanistic overview of H_2 evolution realized by cobaloximes pointing out the effect of the axial ligand on HER catalytic rate and subsequently on the O_2 insensitivity of the catalyst.

---

[77] Wakerley, D. W., Reisner, E., *Energy Environ. Sci.*, **2015**, 8, 2283−2295, DOI: 10.1039/C5EE01167A
[78] Mondal, B., Dey, A., *Chem. Commun.*, **2017**, 53, 7707−7715, DOI: 10.1039/C7CC02941A
[79] Lubitz, W., Ogata, H., Rüdiger, O., Reijerse, E., *Chem. Rev.*, **2014**, 114, 8, 4081–4148, DOI: 10.1021/cr4005814
[80] Wakerley, D.W., Reisner, E., *Phys. Chem. Chem. Phys.*, **2014**, 16, 5739-5746, DOI: 10.1039/c4cp00453a

Meanwhile, Dey and co-workers[81] demonstrated that a *β*-fluoro-substituted cobalt corrole (**CoF$_8$**) could catalyze the reduction of protons to H_2 with a good faraday yield (FY = 52 %) also under ambient atmosphere (Scheme 2-9). Cobalt corroles are known to activate and reduce O_2 in their Co^{II} oxidation state, while they are excellent catalysts for reducing protons to H_2 in their Co^{I} active form. The insertion of strong σ-electron-withdrawing groups to the pyrroles of the macrocyclic ring shifted the $Co^{III/II}$ and $Co^{II/I}$ redox couples to more positive potentials, thus thermodynamically easing the reduction of the metal center compared to the non-*β*-substituted analog. **CoF$_8$** was physisorbed on an edge plane graphite (EPG) electrode, and rotating ring disc experiments at pH 0 revealed that **CoF$_8$** could reduce protons to H_2 even under aerobic conditions. In contrast with the **CoBr$_8$** derivative[82], a considerable amount of H_2O_2 was produced. The lower selectivity over the complete reduction of O_2 to H_2O could be rationalized by the fact that fluorine atoms exhibit a stronger π-electron-donating effect to the Co^{II} active center via the aromatic system of the corrole that localizes the electron density closer to the metal center. A more electron-rich Co^{II} reducing state decreases the affinity for O_2 binding and renders less favorable the reduction of the ORR intermediates due to higher thermodynamic and kinetic barriers.[83]

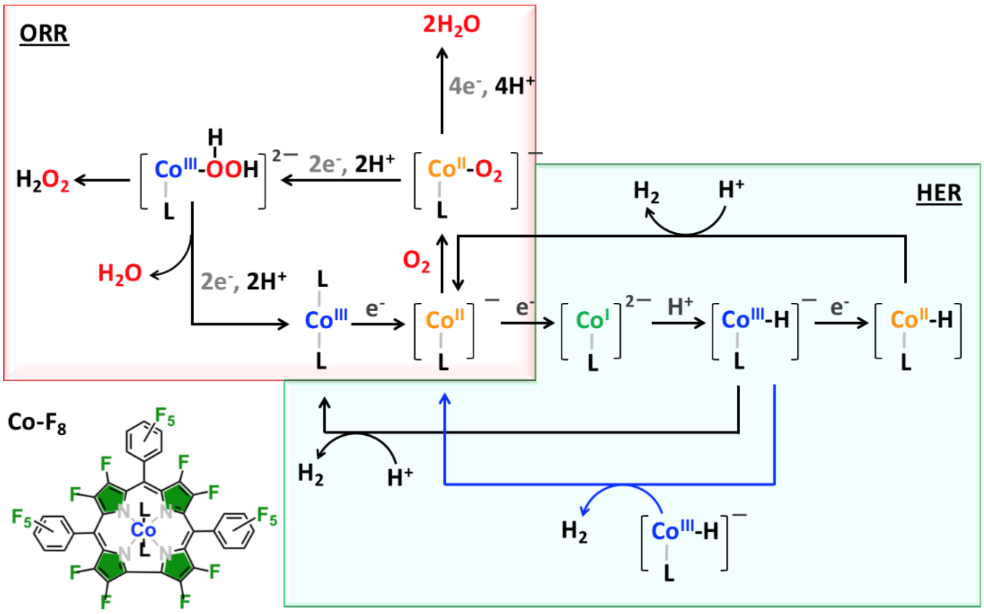

Scheme 2-9. Proposed ORR and HER pathway followed by cobalt corroles.

A more promising strategy to tackle the high O_2 intolerance of a catalyst was introduced by Plumeré and co-workers[84] who incorporated a [NiFe] hydrogenase into a specifically designed viologen matrix to shield the active site of the enzyme from oxidative

---

[81] Mondal, B., Sengupta, K., Rana, A., Mahammed, A., Botoshansky, A. *et al.*, *Inorg. Chem.*, **2013**, 52, 3381−3387, DOI: 10.1021/ic4000473

[82] Schechter, A., Stanevsky, M., Mahammed, A., Gross, Z., *Inorg. Chem.*, **2012**, 51, 1, 22–24, DOI: 10.1021/ic202139f

[83] Levy, N., Shpilman, J.S., Honig, H.C., Major, D.T., Elbaz, L., *Chem. Commun.*, **2017**, 53, 12942-12945, DOI: 10.1039/c7cc06920k

[84] Plumeré, N., Rüdiger, O., Oughli, A., Williams. R., Vivekananthan, J. *et al.*, *Nature Chem.*, **2014**, 6, 822–827, DOI: 10.1038/nchem.2022

inactivation.[85],[86] The one-electron-reduced viologen species are known to react rapidly with molecular oxygen and reduce it to H_2O_2 and OH^- in acidic media and polar aprotic solvents.[87],[88] Exploiting this intriguing O_2–reducing activity of viologen molecules, a highly stable hydrogenase-viologen polymer film was synthesized, and it was later immobilized on the anode of an H_2/O_2 biofuel cell (Scheme 2-9). Hydrogenase exhibited the same electrocatalytic activity both in an H_2 and H_2/O_2 mixed feed, pointing out the crucial contribution of viologen moieties to protect the enzyme's active site from oxidative stress. H_2 oxidation by the enzyme in the intermediate film layer resulted in the reduction of the nearby viologen (V^{2+}) moieties to $V^{\bullet+}$. Electrons were transferred from the intermediate to the outer layer of the hydrogel film, where the ORR took place by the single electron reduced viologen species. O_2 was initially reduced to H_2O_2 and further to H_2O either by a viologen-catalyzed reaction or via an H_2O_2 disproportionation pathway. In addition, the cross-linked viologen chains regulated the potential applied to the catalyst by serving as electron shuttles between the active site and the electrode, thus protecting the catalyst from high potential damage imposed by the electrode and subsequently increasing the lifetime of the biofuel cell.

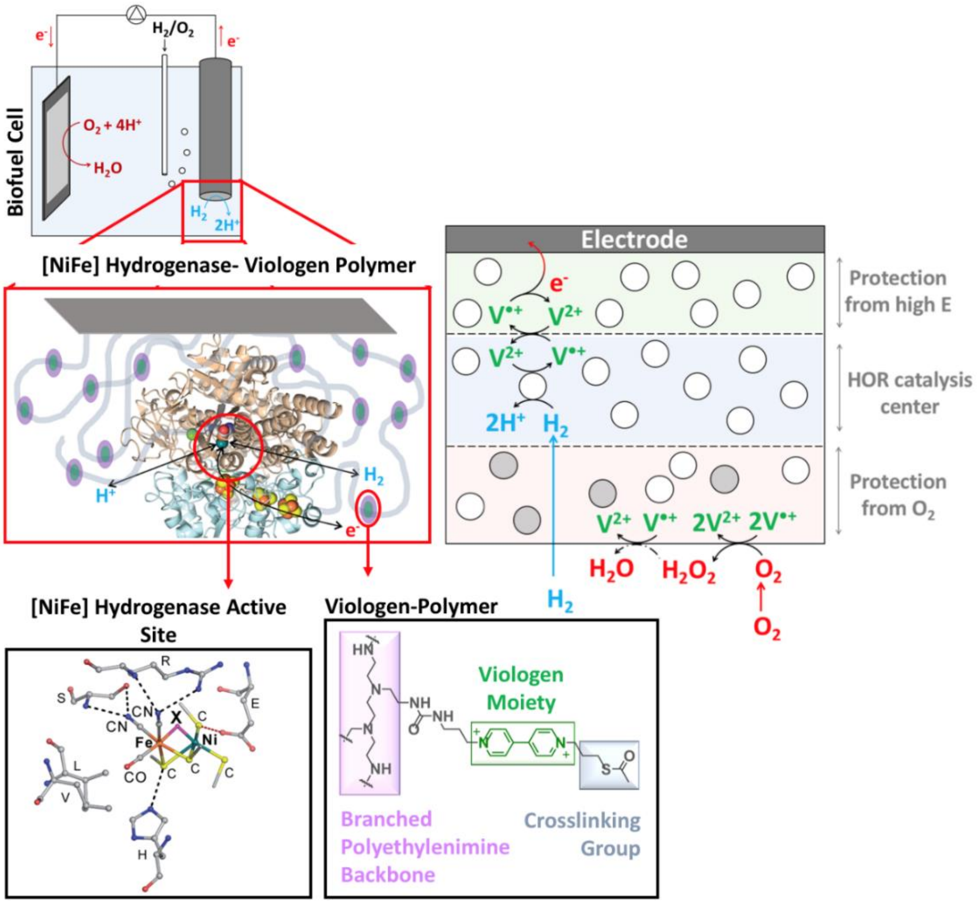

Scheme 2-9. H_2/O_2 biofuel cell constructed by Plumeré and co-workers with a [NiFe] hydrogenase-viologen polymer-modified cathode. [NiFe] hydrogenase oxidizes H_2 in the interlayer of the polymer

---

[85] Fourmond, V., Stapf, S., Li, H., Buesen, D. *et al., J. Am. Chem. Soc.,* **2015**, 137, 5494–5505, DOI: 10.1021/jacs.5b01194

[86] Li, H., Münchberg, U., Oughli, A.A., Buesen, D., Lubitz, W., *et al., Nat. Commun.*, **2020**, 11, 920, DOI: 10.1038/s41467-020-14673-7

[87] Andrieux, C.P., Hapiot. P., Savéant, J.M., *Electroanal. Chem.*, **1985**, 189, 121-133, DOI: 10.1016/0368-1874(85)85630-6

[88] Lin, Q., Li, Q., Batchelor-McAuley, C., Compton, R.G., *J. Electrochem. Sci. Technol.*, **2013**, 4, 2, 71-80, DOI: 10.5229/JECST.2013.4.2.71

film (HOR catalysis center) and generates electrons which reduce the viologen moieties in the outer layer. There the reduced viologen species reduce O_2 to H_2O_2 and/or H_2O inhibiting the penetration of O_2 to the HOR catalysis center. Meanwhile, the generated electrons from HOR are transferred to the electrode via the viologen species in the inner film.

Unlike the studies of Plumeré to confront the O_2 sensitivity of a catalytic system by the integration of the catalyst into an O_2–reducing hydrogel, Compton proposed a more versatile concept of how viologen moieties can be grafted on the surface of an electrode to realize the ORR catalysis in a more general application framework. His team studied the ORR activity of a modified glassy carbon electrode with methyl-viologen (MV^{2+}) doped Nafion particles. The hybrid electrode exhibited enhanced activity towards the reduction of O_2 to H_2O_2 in aqueous media and at low overpotentials. Such a strategy is quite promising for CO_2 and HOR/HER electrocatalytic systems whose efficiency is inhibited by the competitive ORR.[89]

Viologens: A Versatile Electron Mediator in Catalysis

Viologens are a sub-family of quaternary pyridiniums salts (QDSs) conjugated with one or more pyridyl groups with multifunctional features in a variety of applications as has been extensively reviewed by Baumgartner,[90] Zhang,[91] and more recently by Stephan[92]. As mentioned previously, viologens serve as pool for electrons to activate and reduce small molecules such as molecular oxygen or as electron mediators in energy conversion catalytic schemes. They can undergo up to two reversible reductions to form stable cationic radicals and neutral species,[93] while their spectro-electrochemical properties can be fine-tuned by the proper substitution of their nitrogen atoms with a diversity of functional groups.[86]

Intense research focused on efficient photosensitization of metal complexes in natural enzymes for CO_2 and O_2 reduction has offered quite representative paradigms on photo-induced electron transfer mediated by well-designed viologen derivatives. Recently, Amao and Miyaji[94] introduced amino and carbamoyl groups to a bipyridinium salt (**ACBP**) as an electron mediator between a water-soluble photosensitizer (**ZnTPPS**) and a *Candida boidinii* formate dehydrogenase (**CbFDH**) (Scheme 2-10). Docking simulations for the intermolecular interactions between the ground state of **ZnTPPS** and the viologen species revealed that **ACBP** was oriented near the porphyrin center due to electrostatic interaction of the pyridinium positive charge with the p-sulfonate porphyrin's groups. On the contrary, **ACBP** in its reduced state was hydrogen-bonded to the amino residues of the CbFDH enzyme in a similar manner as co-enzyme NAD^+. Upon visible-light irradiation, **ACBP** was reduced to **ACBP**$^{\bullet+}$ by the excited state of the zinc porphyrin, followed by a fast electron transfer from **ACBP**$^{\bullet+}$ to the catalytic site of the enzyme. **CbFDH** reduced CO_2 to HCOOH with good TOF attributed to the high affinity of **ACBP** radical with **CbFDH**.

---

[89] Chen, L., Lin, C., Compton, G.R., *Phys. Chem. Chem. Phys.*, **2018**, 20, 15795-15806, DOI: 10.1039/C8CP02311E

[90] Striepe, L., Baumgartner, T., *Chem. Eur. J.*, **2017**, 23, 67, 16924-16940, DOI: 10.1002/chem.201703348

[91] Ding, J., Zheng, C., Wang, L., Lu, C., Zhang, B. *et al.*, *J. Mater. Chem. A*, **2019**, 7, 23337-23360, DOI: 10.1039/C9TA01724K

[92] Kathiresan, M., Ambrose, B., Angulakshmi, N., Mathew, D.E., Sujatha, D., Stephan, A.R., *J. Mater. Chem. A*, **2021**, 9, 27215-27233, DOI: 10.1039/D1TA07201C

[93] Berville, M., Richard, J., Stolar, M., Choua, S., Le Breton, N. *et al.*, *Org. Lett.*, **2018**, 20, 24, 8004–8008, DOI: 10.1021/acs.orglett.8b03579

[94] Miyajia, A., Amao, Y., *New J. Chem.*, **2021**, 45, 13, 5780-5790, DOI: 10.1039/d1nj00889g

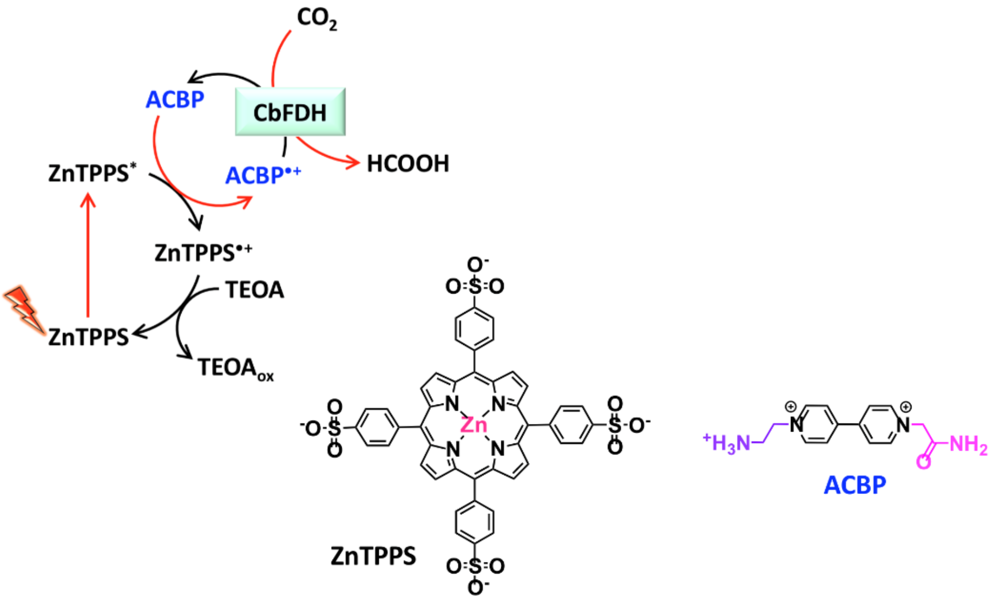

Scheme 2-10. Visible-light-driven CO_2 reduction to formate.

A similar approach was also followed by Leibl and co-workers[95], who employed a much simpler viologen derivative, methyl viologen, as an electron relay in a laccase photocatalytic O_2 reduction system. Methyl viologen (**MV^{2+}**) sufficiently mediated the electron transfer from the photoexcited chromophore to the laccase, thus hindering both the undesirable back electron transfer and the energy transfer from the quenching of the photosensitizer's excited state. Meanwhile, the methyl viologen radical reduces molecular oxygen to $O_2^{•-}$ serving as a one-electron reduced substrate for the enzyme and/or directly transfer electrons to the enzyme to realize the reduction of O_2 to H_2O, as schematically depicted in Scheme 2-11.

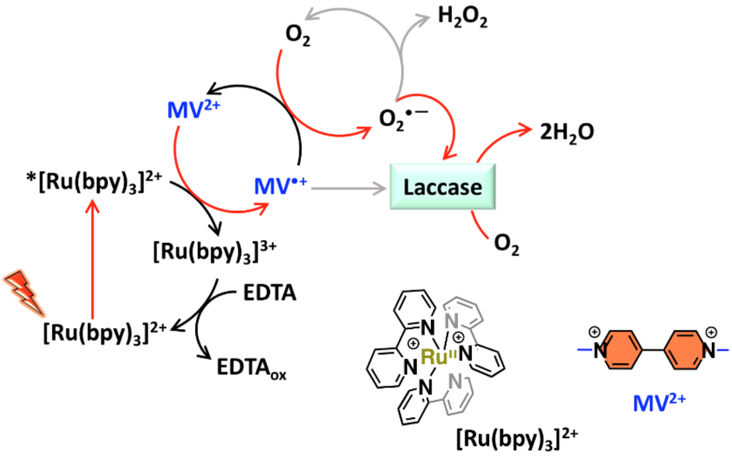

Scheme 2-11. ORR pathway in the absence (H_2O_2 evolution) and the presence (H_2O formation) of laccase, with the grey arrows indicating the less dominant reaction routes.

Another strategy to increase the lifetime of the charge separation state between the photo-excited chromophore and the electron mediator is their covalent coupling. Some typical examples of (metallo)porphyrins covalently linked with viologen moieties are illustrated in Fig.

---

[95] Farran, R., Mekmouche, Y., Vo, T.N., Herrero, C., Quaranta, A. *et al.*, *iScience*, **2021**, 24, 102378, DOI: 10.1016/ j.isci.2021.102378

2-12. The insertion of viologen moieties in the second coordination sphere of the photosensitizer has been shown to considerably impede the back electron transfer from the reduced viologen species to the chromophore.

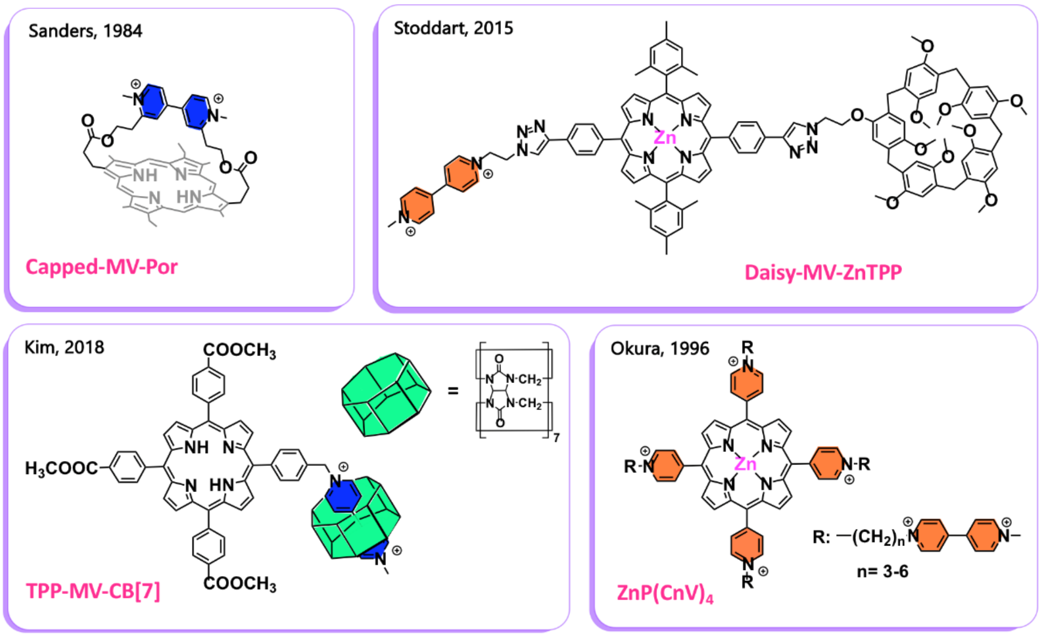

Fig. 2-12. Typical examples of covalently linked porphyrin with viologen moieties: Capped-MV-Por,[96] Daisy-MV-ZnTPP,[97] TPP-MV-CB[7],[98] and ZnP(CnV)$_4$.[99]

2.2 Objectives and Scope

Mitigating climate change based on a CO_2 circular economy can pave the way toward a sustainable future. Although challenging, reducing atmospheric CO_2 into high-density energy fuels is feasible if molecular catalysts are tactfully designed to gain thermodynamic and kinetic control over the CO_2RR. Inspired by the structural motifs employed by Nature's CO_2 fixation catalysts, metalloporphyrins, especially iron porphyrins, have been modified with H-bonding groups, and cationic moieties in their second coordination sphere substantially enhanced their catalytic efficiency. On the other hand, copper porphyrins have not been extensively studied, as is reflected in the trivial amount of CO_2RR electrocatalytic studies reported in the literature. However, industrial implementation is not highly considered for iron and copper porphyrin catalysts since they can only achieve exceptional CO_2 reduction performances when operating under an exclusive CO_2 atmosphere. As such, it is vital as chemists to address our interest in designing robust and efficient catalysts that can maintain their high catalytic activity even in the presence of O_2. CO_2 reduction under aerobic conditions is a field still in its infancy. However, substantial advancements have been realized in HOR and HER catalytic systems that can tackle the competitive ORR by introducing oxygen reduction catalysts such as viologen moieties mainly in their outer coordination sphere.

Taking leverage of similar catalytic motifs, the second topic of this Ph.D. thesis focuses on the electrocatalytic CO_2 reduction in the presence of O_2 realized by a copper porphyrin

---

[96] Leighton, P., Sander, K.M.J., *J. Chem. Soc., Chem. Commun.*, **1984**, 13, 856-857, DOI: 10.1039/C39840000856

[97] Fathalla, M., Strutt, N.L., Sampath, S., Katsiev, K., Hartlie, K.J., *Chem. Commun.*, **2015**, 51, 10455-10458, DOI: 10.1039/C5CC03717D

[98] Lee, M.J., Kim, M.K., Shee, N.K., Lee, J., Yoon, M., Kim, H-J., *Chemistry Select*, **2018**, 3, 256–261, DOI: 10.1002/slct.201702638

[99] Amao, Y., Kamachi, T., Okura, I., *J. Photochem. Photobiol. A.*, **1996**, 98, 59-64, DOI: 10.1016/1010-6030(96)04353-5

functionalized with pendent viologen groups as illustrated in Fig. 2-15. More specifically, Chapter II aims to:

- Synthesize and characterize viologen-appended copper porphyrins (**Cu-*o*-VP**, **Cu-*o*-MVP**), and their corresponding zinc derivatives (**Zn-*o*-VP**, **Zn-*o*-MVP**).
- Investigate the electrocatalytic CO_2RR performance of **Cu-*o*-VP** and **Cu-*o*-MVP** under anaerobic conditions, and compare it with control analogs **CuTPP**, **Zn-*o*-VP**, and **Zn-*o*-MVP**.
- Investigate the electrocatalytic ORR performance of **Cu-*o*-VP** and **Cu-*o*-MVP**.
- Investigate the electrocatalytic CO_2RR performance of **Cu-*o*-VP** and **Cu-*o*-MVP** under aerobic conditions.

2.3 Synthesis and X-Ray Crystallography Characterization

Viologen-appended copper porphyrins, non-methylated **Cu-*o*-VP** and methylated **Cu-*o*-MVP**, and their corresponding zinc derivatives **Zn-*o*-VP** and **Zn-*o*-MVP** were synthesized according to the multi-step synthetic approach in Fig. 2-13. Following Lindsey's method[100], an acid-catalyzed condensation reaction between pyrrole, benzaldehyde, and *ortho*-nitrobenzaldehyde afforded *o*-NO_2PH_2, which was further reduced to yield the amino porphyrin intermediate, *o*-NH_2PH_2. This was then coupled with the activated Zincke-salt of viologen, leading to the formation of the free-base viologen porphyrin *o*-VPH_2. Metallation of *o*-VPH_2 with zinc or copper afforded the corresponding metallated compounds, **Zn-*o*-VP** and **Cu-*o*-VP**. In the next and final step, the pyridyl group of **Zn-o-VP** and **Cu-o-VP** was methylatedto obtain **Zn-o-MVP** and **Cu-o-MVP** compounds. All experimental details and the characterization of the synthesized intermediates and final products are gathered in Annex II at the end of Chapter 2.

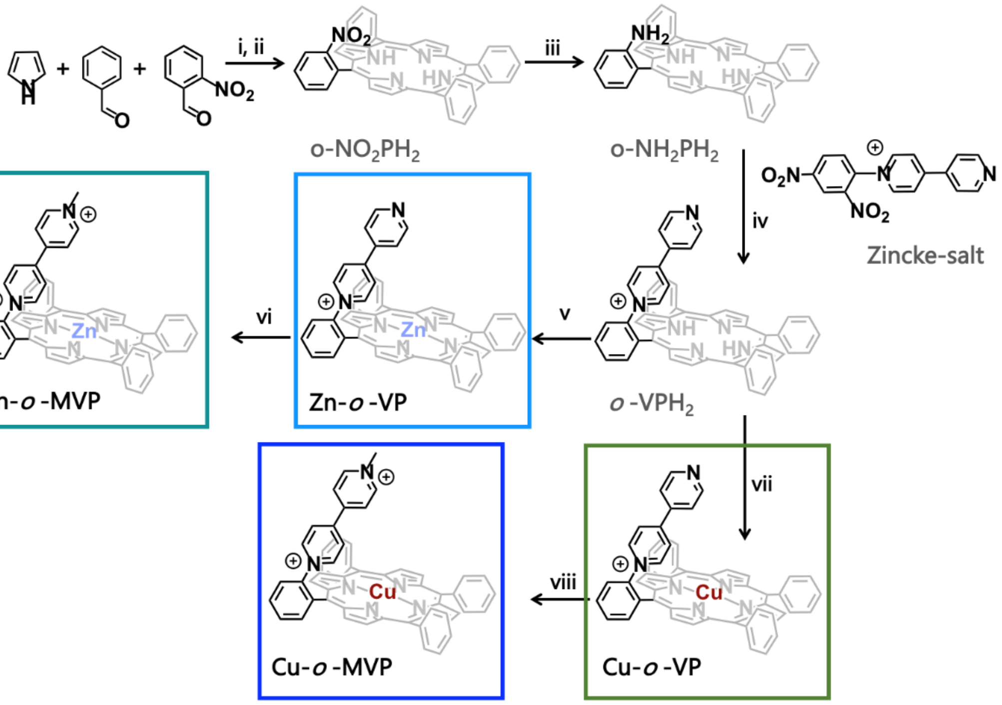

Fig. 2-13 General experimental approach for the syntheses of the **Cu-*o*-MVP** and **Cu-*o*-VP** complexes and the corresponding reference complexes **Zn-*o*-MVP** and **Zn-*o*-VP** . Experimental conditions: i) $CHCl_3$/EtOH (99:1), BF_3OEt_2, RT, 3h; ii) DDQ, RT, 1h; iii) CH_2Cl_2, $SnCl_2$, HCl, RT, 72h; iv) $CHCl_3$/EtOH (1:1),

---

[100] Lindsey, J. S., Schreiman, I. C., Hsu, H. C., Kearney, P.C., Marguerettaz, A. M., *J. Org. Chem.*, **1987**, 52, 5, 827-836 DOI: 10.1021/jo00381a022

62 °C, 16h; v) Zn($COOCH_3$)·$2H_2O$, $CHCl_3$/MeOH (3:1), reflux, 2h; vi) dry DMF, MeI, 100 °C, 2h; vii) Cu($COOCH_3$)·$2H_2O$, $CHCl_3$/MeOH (3:1), reflux, 20h; viii) dry DMF, MeI, 100 °C, 2h.

Suitable crystals for diffraction of **Zn-*o*-VP**, **Cu-*o*-VP**, and **Cu-*o*-MVP** metalloporphyrins were obtained by the classical slow-evaporation method at room temperature (see Annex II for details). The three structures determined by X-ray analysis are illustrated in Fig. 2-14.

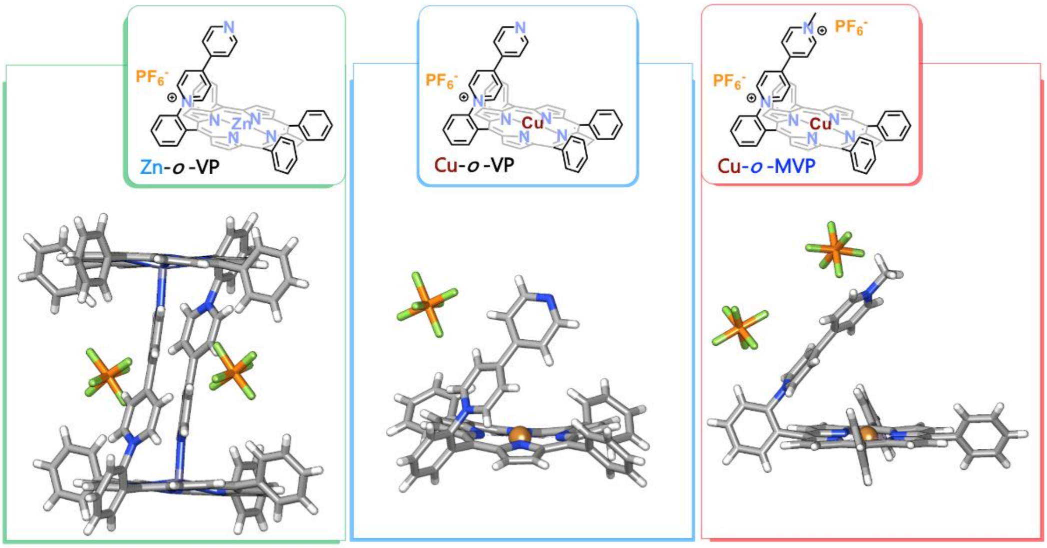

Fig. 2-14 Capped sticks representation of the X-ray crystal structures of **Zn-*o*-VP**, **Cu-*o*-VP**, and **Cu-*o*-MVP**.

Needle-shaped **Zn-*o*-VP** crystals revealed a dimeric complex. Two monomers of **Zn-*o*-VP** were found assembled in a cage-like configuration, with the free-pyridyl group of each monomer coordinated to the metal center of the other. A similar X-ray structure has been also reported by Sutton[101] for an analogous zinc porphyrin derivative bearing pendent pyridyl groups. **Cu-*o*-VP** on the other hand, crystallized as a monomer adopting a saddle-distorted porphyrin platform. The preference of **Zn-*o*-VP** over **Cu-*o*-VP** to bind the pyridyl ligand could be rationalized by the electronic structures of their metal centers and their frontier orbitals. Zn^{II} has a d^{10} electron configuration, while Cu^{II} exhibits a d^9 open-shell electronic state. Compared to the Zn^{II} closed-shell electronic structure, Cu^{II} offers a singly occupied $d_{x^2-y^2}$ molecular orbital.[102],[103] As commonly observed for zinc (II) porphyrin derivatives, the zinc ion can easily adapt with an axial ligand while the strong ligand field provided by the N_4 coordination scheme of the porphyrin macrocycle around the copper (II) centre in a square planar environment is reflected in the shorter bond lengths compared to the **Zn-*o*-VP** derivative (Table 2-3). Henceforth, this renders the binding of an axial ligand to the Cu(II) ion less likely although a few examples of copper porphyrins are known in the literature to crystallize as five[104],[105] - or six[106]-coordinated complexes. The crystal structure of **Cu-*o*-MVP** shows a more planar porphyrin platform and a slightly larger angle relative to **Cu-*o*-VP**.

---

[101] Bernad Jr, P.B., Guerin, A.J., Haycock, R.A., Heath, S.L., Hunter, C.A. *et al.*, *New J. Chem.*, **2008**, 32, 525-532, DOI: 10.1039/B704571A

[102] Liao, M-S.,Scheiner, S., *J. Chem. Phys.*, **2002**, 117, 205-219, DOI: 10.1063/1.1480872

[103] Büchner, R., Fondell, M., Haverkamp, R., Pietzsch, A. *et al.*, *Phys. Chem. Chem. Phys.*, **2021**, 23, 24765–24772, DOI: 10.1039/d1cp03944j

[104] Lipstman, S., Goldberg, I., *Cryst. Growth Des.*, **2010**, 10, 10, 4596-4606, DOI: 10.1021/cg1008973

[105] Cremers, J., Richert, S., Kondratuk, D.V., Claridge, T.D.W. *et al.*, *Chem. Sci.*, **2016**, 7, 6961 6968, DOI: 10.1039/c6sc01809b

[106] Zimmer, B., Hutin, M., Bulach, V., Hosseini, M.W., De Cianab, A., Kyritsakas, N., *New J. Chem.*, **2002**, 26, 1532-1535, DOI: 10.1039/B206661K

Furthermore, the presence of one PF_6 anion in **Cu-*o*-VP** and two PF_6^- anions in **Cu-*o*-MVP** confirms their mono-cationic and di-cationic nature, respectively.

Table. 2-3 Selected bond lengths obtained by the crystal structures of **Zn-*o*-VP**, **Cu-*o*-VP**, and **Cu-*o*-MVP**.

Bond Length (Å)	**Zn-*o*-VP**	**Cu-*o*-VP**	**Cu-*o*-MVP**
$M\text{-}N_{pyrrole}$	2.053	1.997	1.999
$M\text{-}N_{pyridyl}$	2.147	-	-

2.4 Electrochemical Characterization

The redox properties of **Cu-*o*-VP** and **Cu-*o*-MVP** were investigated by cyclic voltammetry (CV) and were compared to the non-functionalized **CuTPP** porphyrin, zinc derivatives **Zn-*o*-VP** and **Zn-*o*-MVP**, and reference complexes, viologen-appended free-base porphyrin (***o*-VPH₂**) and methyl viologen (**MV^{2+}**), as shown in Fig 2-15 and summarized in Table 2-4. The non-functionalized **CuTPP** is characterized by two reversible reduction processes, which are attributed to macrocycle-centered electron transfers.[107][108] The reduction potentials at -1.186 V and -1.708 V (*vs.* SCE) correspond to the formation of copper (II) porphyrin π-anion and dianion radicals, respectively.

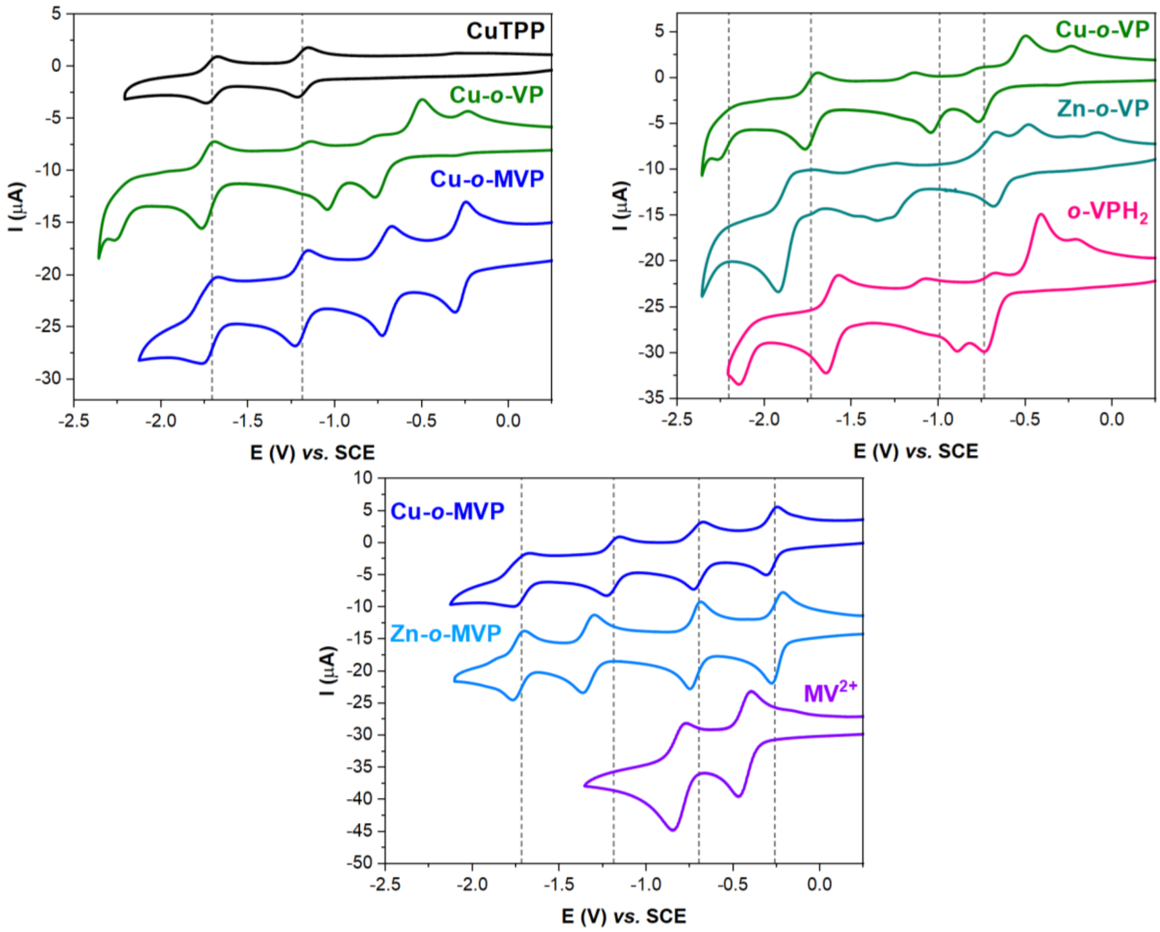

---

[107] Fang, Y., Senge, M.O., Van Caemelbecke, E., Smith, K.M., Medforth, C.J. *et al.*, *Inorg. Chem.*, **2014**, 53, 19, 10772–10778, DOI :10.1021/ic502162p

[108] Ye, L., Ou, Z., Fang, Y., Xue, S., Song, Y. *et al.*, *RSC Adv.*, **2015**, 5, 77088–77096, DOI: 10.1039/c5ra15593b

Fig. 2-15 CVs of 0.5 mM of **Cu-o-VP** and **Cu-o-MVP** compared to the parent **CuTPP** porphyrin recorded in Ar-degassed DMF/TBAPF$_6$ (0.1 M) solution at a scan rate of 100 mV/s. Comparison of the CVs with respective reference complexes.

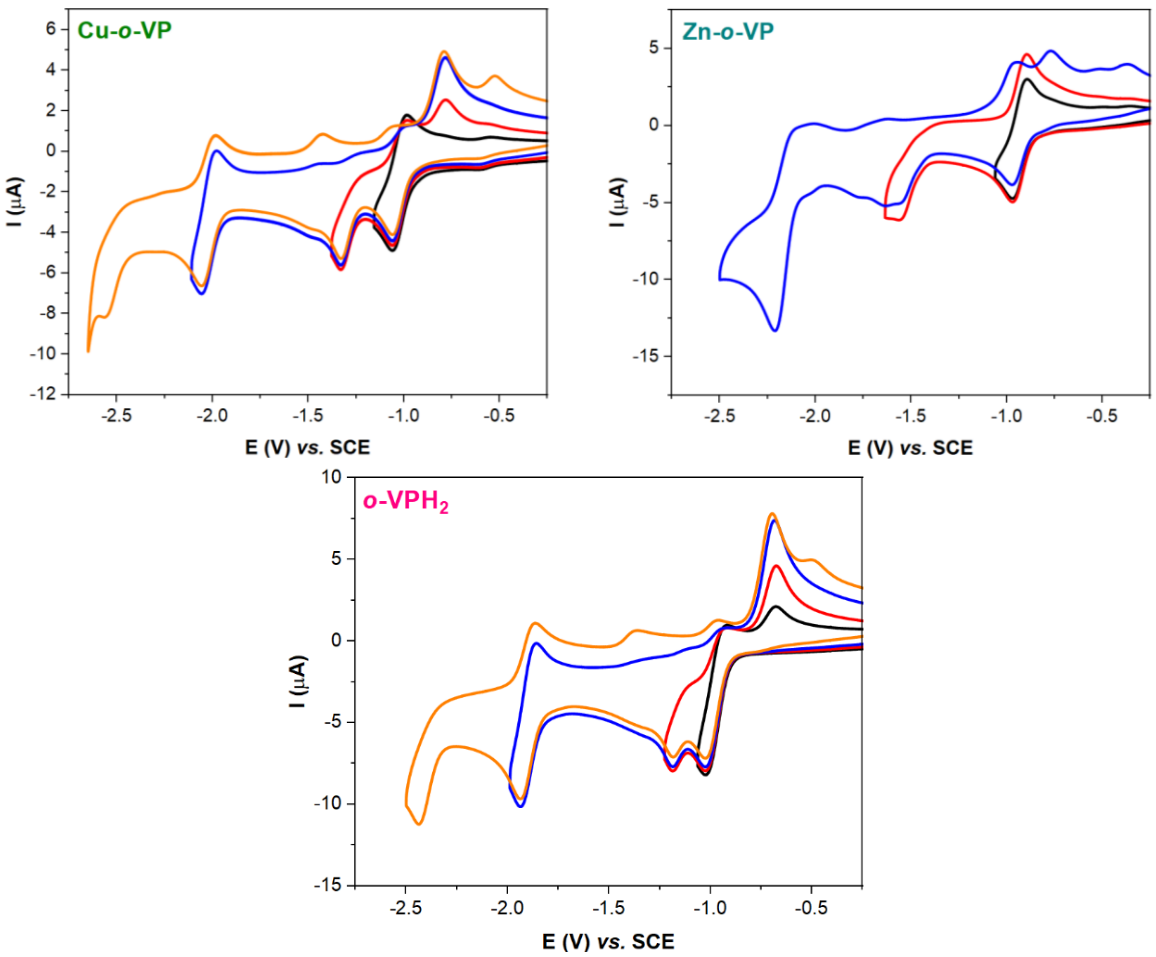

Fig. 2-16 CVs of 0.5 mM of **Cu-o-VP** (up-left) in Ar-degassed DMF/TBAPF$_6$ (0.1 M) solution at a scan rate of 100 mV/s with different potential windows to verify the reversibility for each reduction wave in comparison to the reference complexes **Zn-*o*-VP** (up-right) and c) ***o*-VPH$_2$** (bottom)

Table. 2-4 Redox potentials (*vs.* SCE) of the investigated copper porphyrins in Ar-degassed DMF/TBAPF$_6$ (0.1 M) solution at a scan rate of 100 mV/s.

Complex	MV^{2+}/MV$^{\bullet+}$	MV$^{\bullet+}$/MV	Por/Por$^{\bullet-}$	Por$^{\bullet-}$/Por^{2-}	Pyr/Pyr$^{\bullet-}$
CuTPP	-	-	-1.186	-1.708	-
Cu-*o*-VP	**-0.737**	**-**	**-0.991***	**-1.732**	**-2.206***
Zn-*o*-VP	-0.644	-	-1.192*	-1.858*	-1.858*
o-VPH$_2$	-0.687	-	-0.877*	-1.609	-2.087*
Cu-*o*-MVP	**-0.259**	**-0.697**	**-1.186**	**-1.718**	**-**
Zn-*o*-MVP	-0.247	-0.718	-1.335	-1.733	-
MV	-0.435	-0.815	-	-	-

**Irreversible reduction*: Potential reported for the half-wave of the cathodic peak

The functionalization of the porphyrin framework with viologen-like moieties, **Cu-o-VP** and **Cu-*o*-MVP** is accompanied by the presence of additional reduction waves compared to the parent **CuTPP**. **Cu-*o*-VP** exhibited a first reversible cathodic wave at -0.737 V *vs.* SCE, assigned to the reduction of the pyridinium group (Fig 2-17). This is based on similarities with the first reversible peak observed for reference complexes **Zn-*o*-VP** (-0.644 V) and ***o*-VPH$_2$** (-0.687 V), with differences arising from the nature of the metal center or its absence in the case of ***o*-VPH$_2$**, as shown in Fig 2-16. Further evidence comes from the comparison with methyl viologen, where it seems to coincide with the first reversible reduction peak at -0.435 V albeit with a cathodic shift of 300 mV for **Cu-*o*-VP** (Table 2-4).

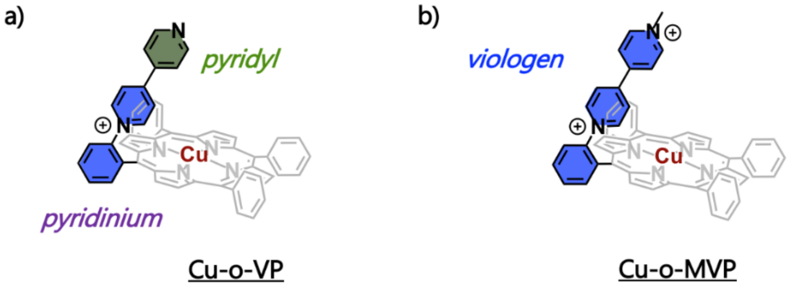

Fig. 2-17 Investigated copper catalysts highlighting the localization of charges in the pendant groups.

The second reduction peak at -0.991 V is irreversible, while the third reduction peak at -1.732 V is reversible, and both are attributed to the porphyrin-centered reductions, based on comparison with the free base ***o*-VPH$_2$** (-0.877 V and -1.609 V). Notably, the third reduction peak of **Cu-*o*-VP** coincides with the second reduction peak of **CuTPP**, indicating the formation of dianion porphyrin (P^{2-}), further confirming the initial attribution. These macrocycle-centered reductions seem to be significantly affected by the nature of the metal center as the **Zn-*o*-VP** showed a second irreversible reduction peak at -1.192 V (more cathodic than in **Cu-*o*-VP** or ***o*-VPH$_2$**) and a third two-electron irreversible reduction peak at -1.858 V, attributed to the merging of the porphyrin-centered dianion and pyridyl anion radical. The latter redox process is, however, well separated for the **Cu-*o*-VP** (appearing at -2.206 V) and ***o*-VPH$_2$** (appearing at -2.087 V). The irreversible second reduction of **Cu-*o*-VP** at -0.991 V creates a return oxidation wave peak at -0.786 V while the next irreversible peak at -2.206 V results in return oxidation waves at -1.428 V and -0.526 V. These irreversible peaks observed for **Cu-*o*-VP** indicate the high sensitivity of the ligand towards further chemical steps during the CV measurements. To confirm if these irreversible peaks arise from the possibility of dimer formation, as initially hinted by the solid-state crystal structure of **Zn-*o*-VP** (Fig 2-14), concentration-dependent studies were performed as shown in Fig 2-18. From the linear scaling between the concentration of the complexes (**Cu-*o*-VP** and **Zn-*o*-VP**) and the current response of the first reduction peak, dimer formation is not observed in the DMF/TBAPF$_6$ solution of the complexes, especially in the dilute concentration of 500 μM used in the CV studies.

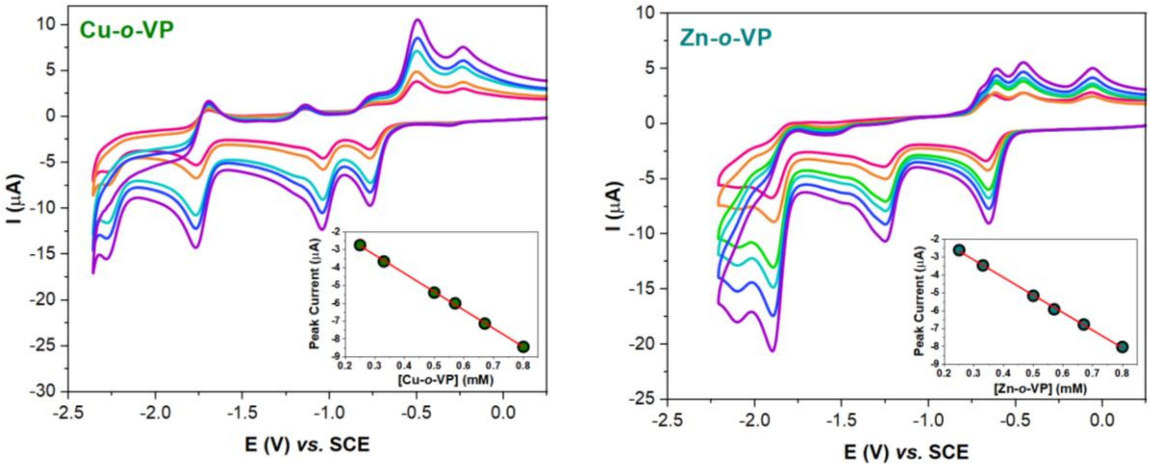

Fig. 2-18 CVs of increasing concentrations (250 μM to 800 μM) of **Cu-*o*-VP** and **Zn-*o*-VP** in Ar-degassed DMF/TBAPF$_6$ (0.1 M) solution at a scan rate of 100 mV/s. Inset: plot of the first reduction peak current as a function of concentration.

Unlike **Cu-*o*-VP**, **Cu-*o*-MVP** shows four reversible reduction waves that are easily comparable with the reference complexes **Zn-*o*-MVP** and **MV^{2+}** (Fig 2-15). The first and second reduction couples at -0.259 V and -0.697 V *vs.* SCE, respectively, correspond to the two mono-electronic reductions of the viologen ligand.[109] These appear to fit well with the first two reversible reductions in **Zn-*o*-MVP** (-0.247 V and -0.718 V), while it is observed to be anodically shifted by 120 - 170 mV in comparison with **MV** (-0.435 V and -0.815 V). This anodic shift indicates that the porphyrin macrocycle imposes an electron-withdrawing effect on the appended viologen moiety. The third and fourth reversible reduction waves at -1.186 V and -1.718 V, respectively, correspond to the porphyrin-centered reductions, as similarly observed for the reference complexes **Zn-*o*-MVP** (-1.335 V and -1.733 V) and **CuTPP** (-1.186 V and -1.708 V).

2.5 CO$_2$ Reduction under Anaerobic Conditions

Under CO$_2$ atmosphere in dry DMF solvent, notable differences are observed between the reactivities of the viologen-appended copper porphyrins, as shown in Fig 2-19. **Cu-*o*-MVP** showed a current increase (i_{cat} / $i_{p,0}$ = 1.68) only in the fourth reduction wave (that is, when the dianion porphyrin is formed). This indicates that (i) the doubly reduced macrocycle interacts and reduces CO$_2$ and (ii) the methyl viologen pendent in **Cu-*o*-MVP** is innocent in terms of CO$_2$ reduction activity. On the other hand, significant changes are observed for **Cu-*o*-VP** under CO$_2$ atmosphere: (i) there is a 135 mV anodic shift for the second reduction peak, (ii) a higher current increase (i_{cat} / $i_{p,0}$ = 2.33) is seen in the third reduction peak (when doubly-reduced porphyrin is formed) as compared to **Cu-*o*-MVP** at similar potentials, and (iii) an even higher current increase (i_{cat} / $i_{p,0}$ = 4.49) is observed for the fourth reduction peak (when the pyridyl radical is formed). All of these new observations for **Cu-*o*-VP** indicate that (i) again, the doubly reduced porphyrin interacts and reduces CO$_2$, and (ii) the pyridyl anion radical also interacts with CO$_2$. Indeed, **Cu-*o*-VP** bears a pyridinium and a pyridyl group, while the pendent ligand of **Cu-*o*-MVP** could be better described as a non-equivalent methyl viologen salt (Fig. 2-17). Pyridyl ligands can undergo one-electron reduction at high cathodic potentials (-2.3 V *vs.* Fc/Fc$^+$) to form their radical anions, which can reversibly trap and release CO$_2$ as proposed by

---

[109] Cook, S.K., Horrocks, B.R., *ChemElectroChem*, **2017**, 4, 320-331, DOI: 10.1002/celc.201600536

Gould[110] and Buttry[111] (Fig. 2-20). This reasonably occurs in **Cu-*o*-VP** bearing a similar pyridyl ligand and accounts for the unexpected current enhancements observed for the third and fourth reduction waves.

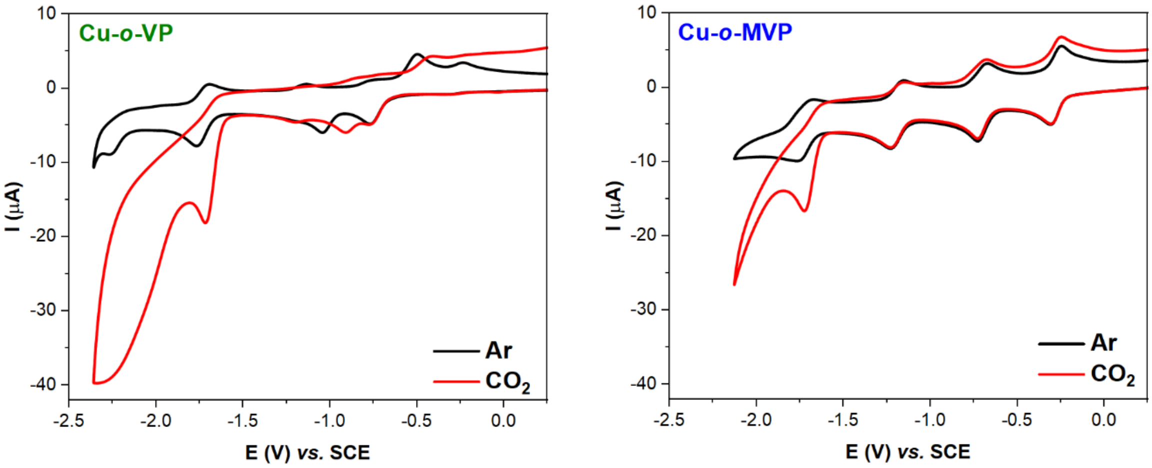

Fig. 2-19 CVs of 0.5 mM **Cu-o-VP** (left) and **Cu-o-MVP** (right) in Ar-degassed (black) and CO_2-saturated (red) dry DMF/$TBAPF_6$ (0.1 M) solution at a scan rate of 100 mV/s.

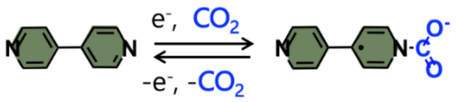

Fig 2-20 Reduction and interaction of bipyridyl ligands with CO_2.

Since protons are needed to perform CO_2 reduction, we then interrogated the effect of adding proton sources in CO_2-saturated solutions. In the presence of water as the proton source, all the investigated copper porphyrin derivatives (**Cu-*o*-VP**, **Cu-*o*-MVP**) exhibited an enhancement of the cathodic current at their $P^{\bullet -}/P^{2-}$ redox couple, which was also shifted to more positive potentials (Fig. 2-21). Such an increase in the current intensity is indicative of a catalytic CO_2 reduction behavior, as has been previously reported by Masaoka and co-workers.[68] While no other shifts in the reduction waves are observed for **Cu-*o*-MVP**, we observe new reduction peaks appearing at -0.75 V and -1.25 V for **Cu-*o*-VP**, again pointing to the high sensitivity of this ligand towards chemical reactivity.

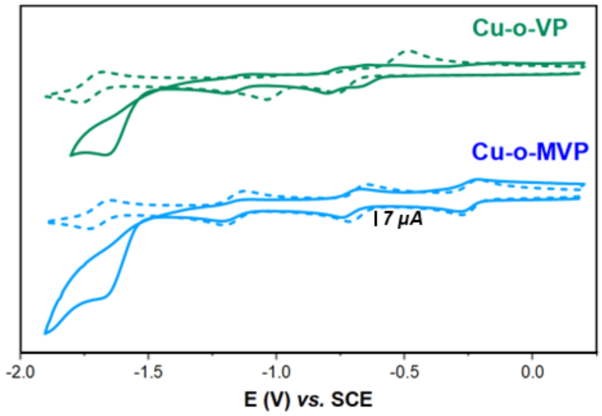

Fig. 2-21 CVs of 1 mM of **Cu-*o*-VP** and **Cu-*o*-MVP** catalysts under Ar atmosphere (dash lines) and under CO_2 with 5.5 M H_2O (solid lines) in DMF/$TBAPF_6$ (0.1 M) solution at a scan rate of 100 mV/s.

---

[110] Ranjan, R., Olson, J., Singh, P., Lorance, E.D., Buttry, D.A., Gould, R.I., *J. Phys. Chem. Lett.*, **2015**, 6, 4943−4946, DOI: 10.1021/acs.jpclett.5b02220

[111] Singh, P., Tarakeshwar, P., Buttry, D.A., *ChemElectroChem*, **2020**, 7, 2, 469-475, DOI: 10.1002/celc.201901884

We further interrogated the catalytic performance with a more acidic proton source, trifluoroethanol (p*K*a = 24.0 in DMF) as shown in Fig 2-22 compared to water (p*K*a = 31.5 in DMF), with the mindset that the possible oxygen reduction reaction of the complexes would need more acidic conditions to produce H_2O_2/H_2O. Following acid concentration studies in CO_2-saturated dry DMF, we could notice a similar anodic shift of the onset potentials occurring at the $P^{\bullet -}/P^{2-}$ redox couple, with more significant shifts for **Cu-*o*-MVP** than **Cu-*o*-VP** (120 mV *vs.* 100 mV with 2.5 M TFE). For **Cu-*o*-MVP**, addition of higher concentrations of TFE resulted in current enhancements at -2.0 V, however, for **Cu-*o*-VP**, this resulted in decreasing currents after the initial increase at 500 mM TFE. The trend observed for **Cu-*o*-MVP** is similar to reported systems in which CO_2 reduction depends on the protonation as the rate-determining step. On the other hand, even though the synergy of the porphyrin dianion radical and pyridyl radical was initially thought to be at work in **Cu-*o*-VP** in CO_2-saturated solutions and in the absence of proton sources, the decreasing currents for **Cu-*o*-VP** when protons were added might indicate the competition between HER and CO_2RR in the pyridyl-appended ligands. Even though the pendent methyl viologen unit in **Cu-*o*-MVP** is innocent in terms of CO_2 reduction activity, the dicationic character of the moiety resulted in greater current enhancements under CO_2 atmosphere and presence of TFE (as the proton source) relative to the non-functionalized **CuTPP** (Fig 2-23).

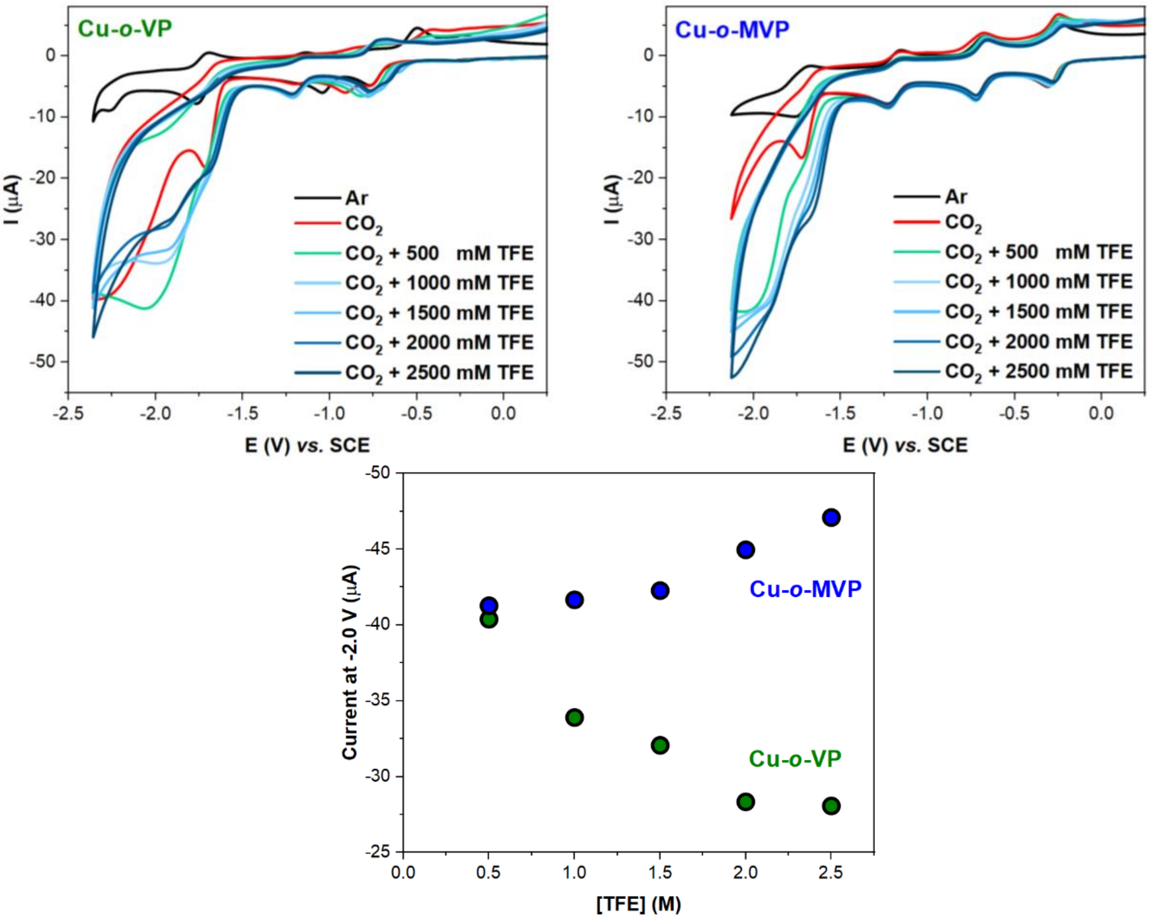

Fig. 2-22 CVs of 0.5 mM of **Cu-*o*-VP** (left) and **Cu-*o*-MVP** (right) catalysts under Ar atmosphere (black) and under CO_2 (red) with increasing concentrations of trifluoroethanol (shades of blue-green) in DMF/$TBAPF_6$ (0.1 M) solution at a scan rate of 100 mV/s. Bottom: Plot of current at -2.0 V as a function of TFE concentration.

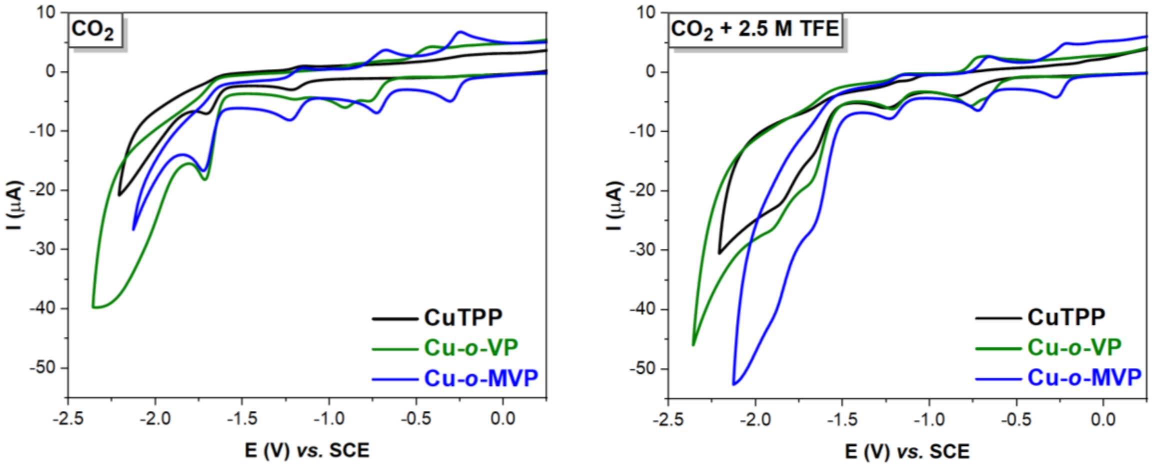

Fig. 2-23 Comparison of CVs of 0.5 mM **CuTPP** (black), **Cu-*o*-VP** (green), **Cu-*o*-MVP** (blue) under CO_2 atmosphere (left) and under CO_2 with 2.5 M TFE (right) in DMF/$TBAPF_6$ (0.1 M) solution at a scale rate of 100 mV/s.

2.6 O_2 Reduction Reaction

To investigate the potential of the viologen-appended systems for CO_2RR in presence of oxygen, the oxygen reduction reaction (ORR) activities of the complexes were first determined to set a background for eventual comparison. Oxygen (21% in air, corresponding to a partial pressure of 0.21 atm) is reduced reversibly at the glassy carbon electrode at -0.863 V (*vs.* SCE) in DMF, as shown in Fig 2-24 (left). In the presence of 2.5 M TFE, as the proton source, the reversibility is lost, the onset potential shifts anodically, and a catalytic current is observed ($i_{cat} / i_{p,0}$ = 1.66). This irreversible nature comes from the chemical reaction of the superoxide anion radical (formed after one-electron reduction of oxygen) with protons to form the uncharged hydroperoxyl radical ($HOO^•$).[112]

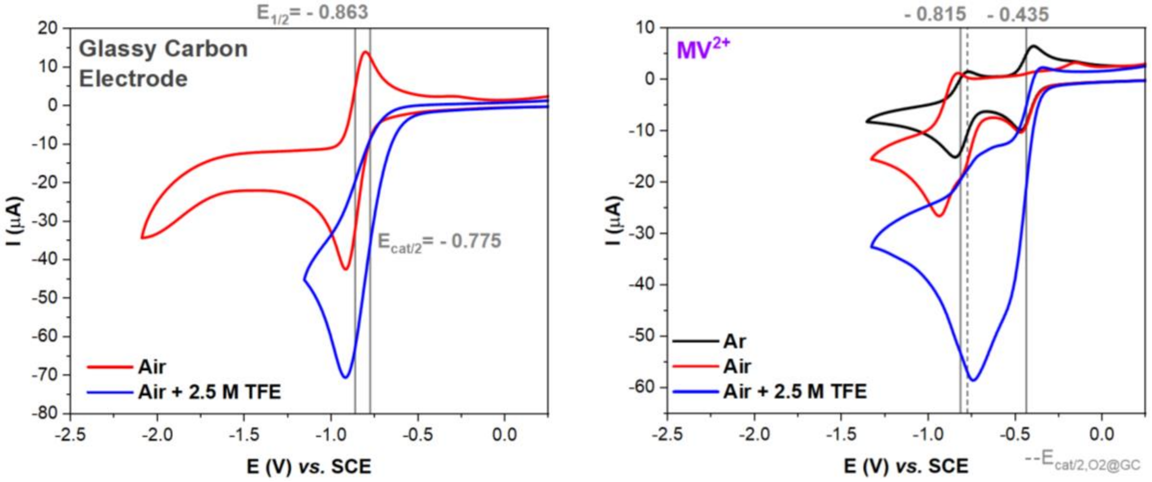

Fig. 2-24 Left: CVs of Air in DMF/$TBAPF_6$ (0.1 M) solution in the absence (red) and presence (blue) of 2.5 M TFE. Right: CVs of 0.5 mM methyl viologen in DMF/$TBAPF_6$ (0.1 M) solution under Ar-saturated (black) and Air-equilibrated conditions without (red) and with (blue) 2.5 M TFE.

Next we determined the ORR activity of methyl viologen as an important control for the viologen-appended copper porphyrins. Methyl viologen possesses two reversible reductions at -0.435 V and -0.815 V in Ar-saturated DMF (Fig 2-24 right, Table 2-4). In air-equilibrated

---

[112] Singh, P.S., Evans, D.H., *J. Phys. Chem. B*, **2006**, 110, 1, 637–644, DOI: 10.1021/jp055296f

solutions, we observe a slight current enhancement at the second reduction peak (i_{cat} / $i_{p,0}$ = 1.25), immediately followed by the background heterogeneous reduction of O_2 at the glassy carbon electrode (GC). However, in presence of a proton source such as TFE, we immediately observe catalytic current enhancements at the first reduction peak (i_{cat} / $i_{p,0}$ = 4), indicating that the $MV^{•+}$ can mediate homogenous ORR at acidic conditions, possibly forming hydroperoxyl radicals. This capability of $MV^{•+}$ to reduce O_2 has already been reported by Compton in ethanol (forming a superoxide radical anion).[113] More recently, it has been shown that when MV^{2+} is heterogeneously anchored to Nafion nanoparticles in the working electrode, it can realize the $2e^-/2H^+$ reduction of O_2 to H_2O_2.[114] .

The viologen-appended copper porphyrins were then investigated in air-equilibrated DMF solutions, as shown in Fig 2-25. It can be observed that the heterogeneous reduction of O_2 at the glassy carbon electrode at -0.863 V is dominating the CVs. Nevertheless, the interaction of **Cu-*o*-VP** and **Cu-*o*-MVP** with molecular O_2 can be observed with (i) anodic shifts of onset ORR potentials and (ii) slight current enhancements even in the absence of any proton source. Notably, O_2 interacts with the first reduced form of **Cu-*o*-VP** (pyridinium radical) giving catalytic enhancement of (i_{cat} / $i_{p,0}$ = 2.39) while it interacts with the second reduced form of **Cu-*o*-MVP** (viologen dianion) giving a weaker catalytic enhancement of (i_{cat} / $i_{p,0}$ = 1.49).

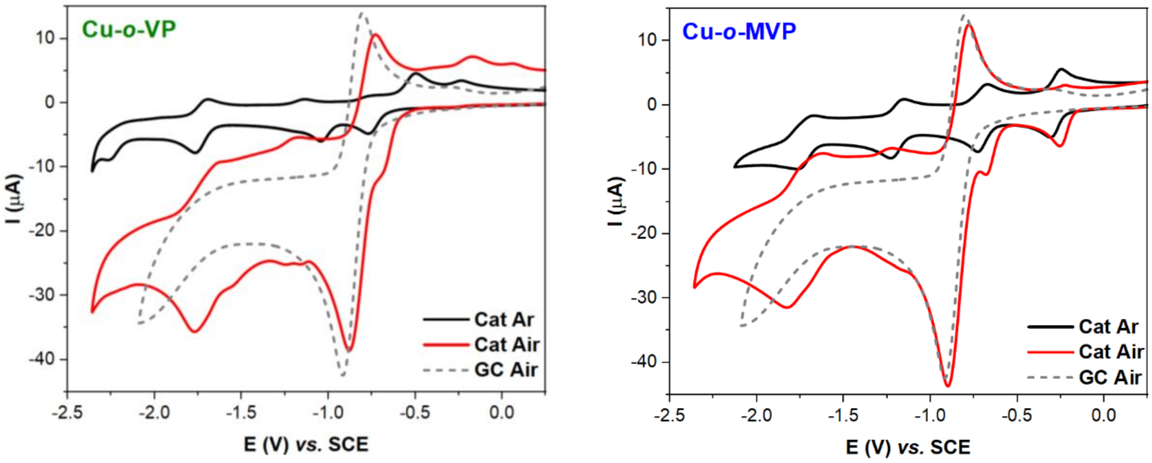

Fig. 2-25 Comparison of CVs of 0.5 mM **Cu-*o*-VP** (left) and **Cu-*o*-MVP** (right) in DMF/TBAPF$_6$ (0.1 M) solution in the absence (black) and presence (red) of air. O_2 reduction at glassy carbon electrode is shown as dotted grey lines for comparison.

As shown in Fig. 2-26, in the presence of increasing concentrations of an acidic proton source, trifluoroethanol (p*K*a = 24.0 in DMF), for both **Cu-*o*-VP** and **Cu-*o*-MVP**, it is observed that (i) the onset potential for ORR anodically shifts, and (ii) the catalytic current increases. Addition of 2.5 M TFE results in a catalytic current enhancement of (i_{cat} / $i_{p,0}$ = 20.1) for **Cu-*o*-VP**, and again, a much weaker increase for **Cu-*o*-MVP** (i_{cat} / $i_{p,0}$ = 10.9). Even though the differences in the potentials between the ORR active species of the viologen-appended copper porphyrins and the heterogeneous O_2 reduction at the surface of the glassy carbon electrode are not that far ($\Delta E_{Cu\text{-}o\text{-}VP}$ = 120 mV, $\Delta E_{Cu\text{-}o\text{-}MVP}$ = 160 mV in the absence of any proton source), the ORR catalytic enhancements uniquely occur homogenously through the viologen-appended copper porphyrins because of the much earlier onset potentials (Fig 2-27). However, compared to methyl viologen, they still occur at much more negative potentials under the same conditions. This arises mainly from the differences in the redox potential of the active

---

[113] Lin, Q., Li, Q., Batchelor-McAuley, C., Compton, R.G., *J. Electrochem. Sci. Technol.*, **2013**, 4, 2, 71-80, DOI: 10.5229/JECST.2013.4.2.71

[114] Chen, L., Lin, C., Compton, R.G., *Phys. Chem. Chem. Phys.*, **2018**, 20, 15795-15806, DOI: 10.1039/C8CP02311E

species (pyridinium radical for **Cu-*o*-VP,** viologen dianion for **Cu-*o*-MVP**, and viologen mono-anionic radical for **MV^{2+}**). Further reductions beyond -1.5 V (Fig 2-26, Fig 2-27) might come from further reduction of reduced oxygen species and/or (more probably) the competition for HER in which the **Cu-*o*-VP** complex shows higher catalytic enhancements than **Cu-*o*-MVP**. Bulk electrolysis experiments and product quantification may help distinguish the differences.

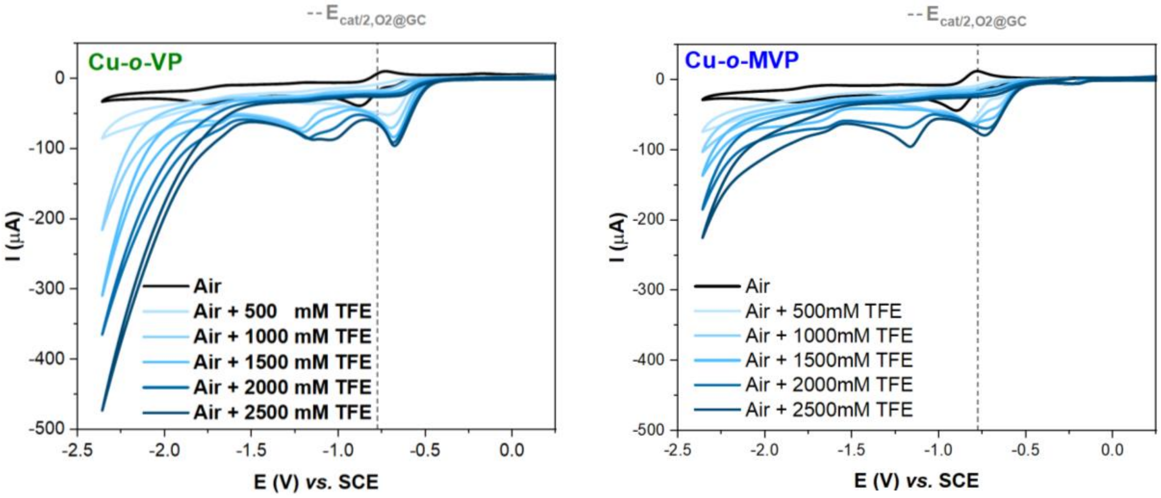

Fig. 2-26 Comparison of CVs of 0.5 mM **Cu-*o*-VP** (left) and **Cu-*o*-MVP** (right) in air-equilibrated DMF/TBAPF$_6$ (0.1 M) solution with increasing concentrations of trifluoroethanol. Dash grey lines indicate the E$_{cat/2}$ of O$_2$ at glass carbon electrode with 2.5 M TFE in DMF/TBAPF$_6$.

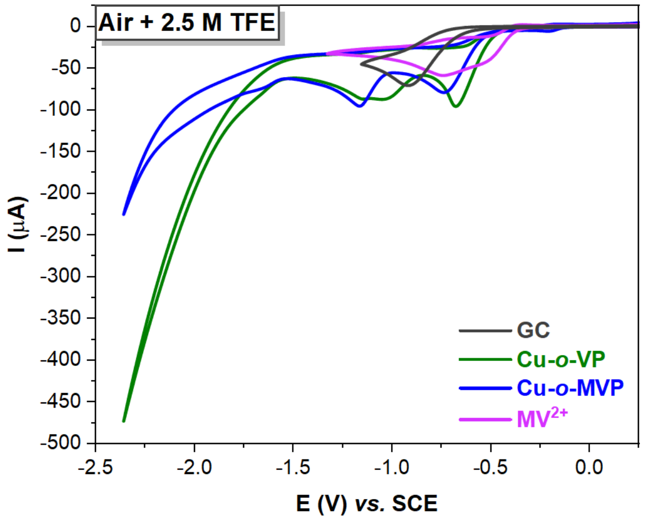

Fig. 2-27 Comparison of the CVs of 0.5 mM **Cu-*o*-VP** (green), **Cu-*o*-MVP** (blue), and methyl viologen (purple) in air-equilibrated DMF/TBAPF$_6$ (0.1 M) solution containing 2.5 M TFE relative to O$_2$ reduction at the glassy carbon electrode (black).

2.7 CO$_2$ Reduction in Presence of O$_2$

Taking leverage of the bifunctional catalytic activity of **Cu-*o*-VP** and **Cu-*o*-MVP** to reduce CO$_2$ and O$_2$ separately, qualitative electrocatalytic studies were also performed in CO$_2$-air mixtures, as shown in Fig 2-28. Comparing the catalytic currents due to ORR (~ -0.75 V), it can be observed that increasing the oxygen concentration (i) increases the catalytic ORR currents with much greater enhancements observed for **Cu-*o*-VP** than **Cu-*o*-MVP**, and (ii) anodically shifts the onset potentials. This is similarly observed in the previous section for the distinguished ORR activities of the viologen-appended copper porphyrins. Comparing the catalytic current changes in the CO$_2$RR potential domain (-2.0 V) in the presence of oxygen, it can be observed that with increasing oxygen concentration, the catalytic currents also apparently increase. To remove any contributions from the increase in the capacitive current because of the preceding ORR, the catalytic currents were corrected and a plot of corrected current enhancements is shown in Fig 2-29.

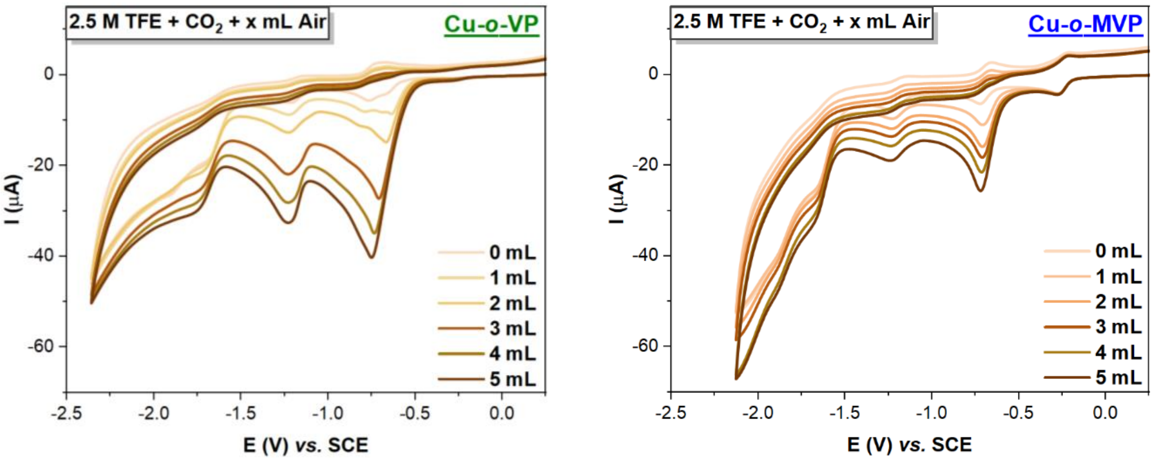

Fig. 2-28 Comparison of the CVs of 0.5 mM **Cu-*o*-VP** (left) and **Cu-*o*-MVP** (right) in CO_2-saturated DMF/$TBAPF_6$ (0.1 M) solution containing 2.5 M TFE and increasing amounts of air (shades of brown) bubbled through the solution.

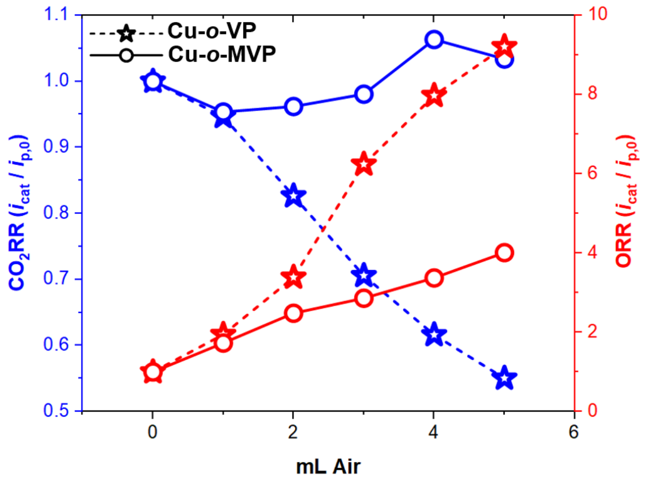

Fig. 2-29 Comparison of the CO_2RR (blue) and ORR activities of **Cu-*o*-VP** (star) and **Cu-*o*-MVP** (circle) in CO_2-saturated DMF/$TBAPF_6$ (0.1 M) solution containing 2.5 M TFE and 5mL Air. CO_2RR is calculated based on ($i_{cat@-2V}$ / $i_{p,0}$) subtracting any capacitive currents due to ORR. ORR is calculated based on (i_{cat}/ $i_{p,0}$) occurring at the first catalytic wave (~ -0.75 V). All $i_{p,0}$ indicate currents in presence of CO_2 + 2.5 M TFE but absence of air in the respective CO_2RR and ORR potentials.

It can be observed in Fig 2-29 that the catalytic currents at -2.0 V is actually decreasing for **Cu-*o*-VP**, but is not significantly changed for **Cu-*o*-MVP**. The observation that the catalytic current for CO_2RR is maintained for **Cu-*o*-MVP** while having moderate ORR activities indicates the promise that this complex has in realizing the CO_2RR in presence of oxygen. Comparison of the CO_2RR activities in the absence and presence of oxygen (Fig 2-30) indeed points to higher catalytic currents and earlier onset CO_2RR potentials for **Cu-*o*-MVP**. On the other hand, the greater ORR activity of **Cu-*o*-VP** and its poor CO_2RR performance in presence of O_2, which is similarly shown by the non-functionalized **CuTPP**, point out that these other complexes may not achieve aerobic CO_2RR. All of the comparisons were mostly based on catalytic current enhancements as initial investigations of this chapter.

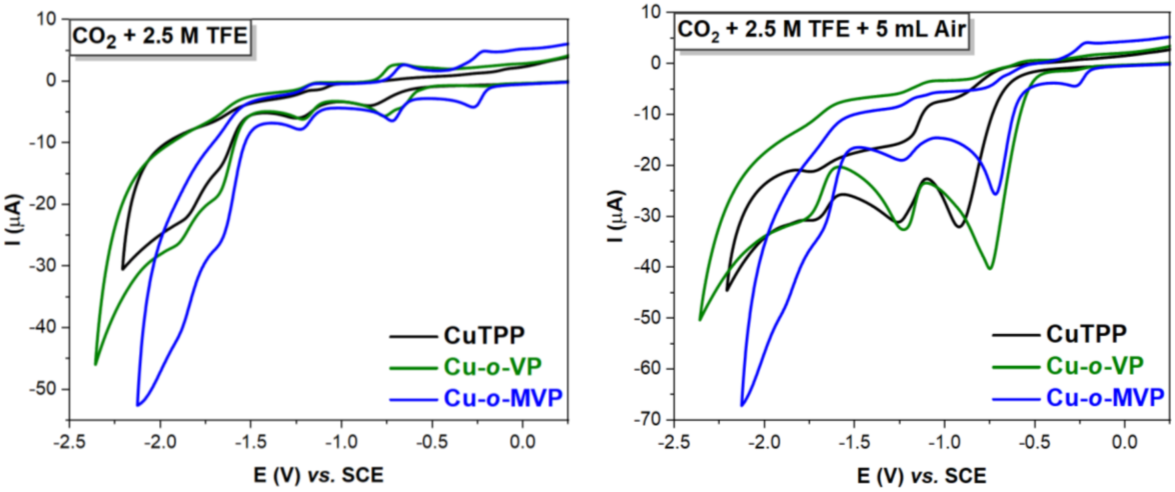

Fig. 2-30 Comparison of CVs of 0.5 mM **CuTPP** (black), **Cu-*o*-VP** (green), **Cu-*o*-MVP** (blue) under CO_2 atmosphere (left) and under CO_2 with 2.5 M TFE (right) in DMF/$TBAPF_6$ (0.1 M) solution at a scan rate of 100 mV/s.

Bulk electrolysis experiments and product quantification are still ongoing to solidify any selectivity changes that might occur due to the presence of oxygen. It is worthy to note that a recent study by Lu and co-workers showed that partially reduced oxygen species (PROS) can assist a higher conversion of CO_2RR towards C_1 and C_2 products by copper polycrystalline electrodes.[115]

2.8 Conclusions

In conclusion, we described a different approach to develop efficient copper porphyrins as CO_2RR electrocatalysts that can maintain their activity in the presence of O_2. In particular, we functionalized a copper porphyrin with a pendent methyl-viologen-like group (**Cu-*o*-MVP**) and investigated its electrocatalytic activity toward the reduction of CO_2 and molecular O_2. On the same line, we also synthesized its non-methylated analog (**Cu-*o*-VP**) and compared its CO_2RR and ORR performance with **Cu-*o*-MVP**.

Under 1 atm of CO_2 and in the presence of a weak proton source (5.5 M H_2O), the CVs of **Cu-*o*-VP** and **Cu-*o*-MVP** displayed a considerable enhancement of the current intensity at the anodically shifted $P^{\bullet -}/P^{2-}$ redox couple indicating the electrocatalytic reduction of CO_2 by the P^{2-} state of the copper catalysts. On the other hand, when 0.5 M of TFE was used as a stronger acid, a similar catalytic response at around – 2.0 V *vs.* SCE was obtained for both viologen-appended copper porphyrins. However, upon increasing the concentration of TFE to 2.5 M, the CO_2RR activity of **Cu-*o*-VP** was noticeably suppressed due to the competitive HER. In contrast, the opposite trend was observed for **Cu-*o*-MVP** implying that the rate-determining step involves the protonation of the activated CO_2 molecule. Compared to the non-modified **CuTPP** porphyrin and in the presence of 2.5 M of TFE, **Cu-*o*-VP** showed a slightly higher CO_2RR electrocatalytic activity, whereas it was greatly enhanced for **Cu-*o*-MVP**.

When **Cu-*o*-VP** and **Cu-*o*-MVP** were investigated as ORR electrocatalysts with 2.5 M of TFE as the proton source, the reduction of molecular O_2 was realized by the electrogenerated pyridinium radical, and the viologen dianion moiety, respectively. To our surprise, the first

---

[115] He, M., Li, C., Zhang, H., Chang, X., Chen, J.G. *Nat. Commun.*, **2020**, 11, 3844, DOI: 10.1038/s41467-020-17690-8

reduced state of **Cu-*o*-MVP**, *viz*. the formation of $MV^{\bullet+}$, was inactive towards ORR, which was not the case for the reference methyl viologen compound. The inability of the pendent $MV^{\bullet+}$ group on **Cu-*o*-MVP** to reduce O_2 derives from the fact that the $MV^{2+}/MV^{\bullet+}$ redox couple is shifted almost 180 mV anodically compared to the analogous reduction process in methyl viologen. Therefore, it seems that the $MV^{\bullet+}$ state in **Cu-*o*-MVP** is missing the reducing power to drive the ORR. Moreover, in contrast to the CO_2RR studies, **Cu-*o*-VP** displayed almost twice ORR catalytic current compared to **Cu-*o*-MVP** under the same conditions.

Moving one step forward and taking profit of the bifunctional catalytic character of **Cu-*o*-VP** and **Cu-*o*-MVP** to reduce CO_2 and O_2 separately, we also investigated their CO_2RR performance in the presence of O_2. Starting from a CO_2 saturated electrolytic solution containing 2.5 M TFE and upon addition of aliquots of O_2, both catalysts showed the same ORR catalytic trend as in the absence of CO_2. However, concerning their CO_2RR activity, **Cu-*o*-VP** displayed a decrease in the CO_2 reduction catalytic current at the $P^{\bullet-}$/ P^{2-} redox couple at -2.0 V. On the flip side, the increasing concentration of O_2 did not affect the activity of **Cu-*o*-MVP** to activate and reduce CO_2. Hence, although **Cu-*o*-MVP** was not as efficient ORR electrocatalyst as **Cu-*o*-VP**, it was the only one that could maintain its CO_2RR electrocatalytic performance even in the presence of O_2. In other words, the pendent methyl-viologen-like group served its proposed purpose to tackle the ORR, while the copper porphyrin catalyzes the CO_2 reduction.

2.9 Perspectives

Bulk electrolysis experiments for **Cu-*o*-VP** and **Cu-*o*-MVP** are on the way to quantify their CO_2 reduction products and to determine changes in the selectivity and Faraday efficiencies. Rotating Ring Disc Voltammetry (RRDV) will be performed to determine their selectivity over the $2e^-/2H^+$ or the $4e^-/4H^+$ ORR pathway. In addition, their iron analogs, **Fe-*o*-VP** and **Fe-*o*-MVP**, are currently under investigation as alternative CO_2RR/ORR electrocatalysts. Iron porphyrins are considered one of the most efficient and promising families of molecular electrocatalysts for the reduction of CO_2 Hence, it would be wise to explore the potential CO_2RR activity of **Fe-*o*-MVP** under aerobic conditions; yet, it might be quite challenging since iron porphyrins can equally efficiently perform the ORR, as it was extensively discussed in Chapter I.

Moreover, these preliminary results can pave the way for the development of photocatalytic systems capable of reducing CO_2 into valuable-added chemicals under aerobic conditions. Photocatalytic CO_2RR is considered a more sustainable alternative way to mitigate the accumulation of CO_2 in the atmosphere. In these systems, a photosensitizer (**PS**) harnesses the solar energy and translates it into high energy electrons that reduce the CO_2RR catalyst to its active state (**CAT$_{red}$**) to activate and further transform CO_2 into CO, CH_4, MeOH, etc., depending on its catalytic efficiency. A sacrificial electron donor (**SED**) is also present in the photocatalytic solution that "regenerates" the **PS**, so a new photocatalytic cycle can take place. Prompted by the X-ray crystallographic data, it would be worth exploring the photocatalytic activity of a binuclear system in which **Zn-o-VP** can potentially serve as the **PS** and an electron relay to the CO_2RR/ORR catalyst such as **Cu-*o*-MVP** or even its iron analog, **Fe-*o*-MVP**. Such systems can potentially replace the commonly established ruthenium and iridium photosensitizers with complexes based on earth-abundant metals such as zinc.

On the other hand, another perspective offered from the preliminary results of this study is to develop covalent organic frameworks (**COFs**) films and further deposit them on electrode surfaces since heterogenization of catalytic systems is more likely to meet industry standards.

This latter approach is already being investigated in our lab. Moreover, taking profit of the same porphyrin framework, we could also investigate the electrocatalytic HER activity of **Co-*o*-MVP** in the presence of O_2.

Annex II

Synthetic Procedure

Synthesis of *o*-NO_2PH_2

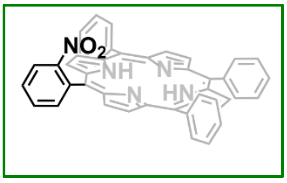

Benzaldehyde (10.10 mL, 0.099 mol) and 2-nitrobenzaldehyde (5 gr, 0.033 mol) were dissolved in 900 mL of $CHCl_3$/ EtOH 10% and the resulting solution was bubbled with Ar for at least 20 min under vigorous stirring. Then, pyrrole (9.3 mL, 0.134 mol) was added dropwise in the absence of light and the reaction mixture was purged with Ar for an additional period of 10 min before BF_3OEt_2 (5 mL, 0.041 mol) was added dropwise. After the addition of BF_3OEt_2, the mixture of the reaction was stirred at room temperature for ~3h under Ar atm and in the dark. Then, DDQ (45 g, 0.198 mol) was transferred to the solution which was left stirring for 1h at room temperature. Once, the reaction reached completion, the solution of the crude product mixture was filtered through a silica pad, and then it was further neutralized by extractions with $NaHCO_{3(aq)}$. The organic phase was collected and evaporated until dryness. ***o*-NO_2PH_2** was obtained as a purple solid after its purification via column chromatography (SiO_2, CH_2Cl_2/ cyclohexane (1:1 v/v)) (1.6 gr, 7.3 %).

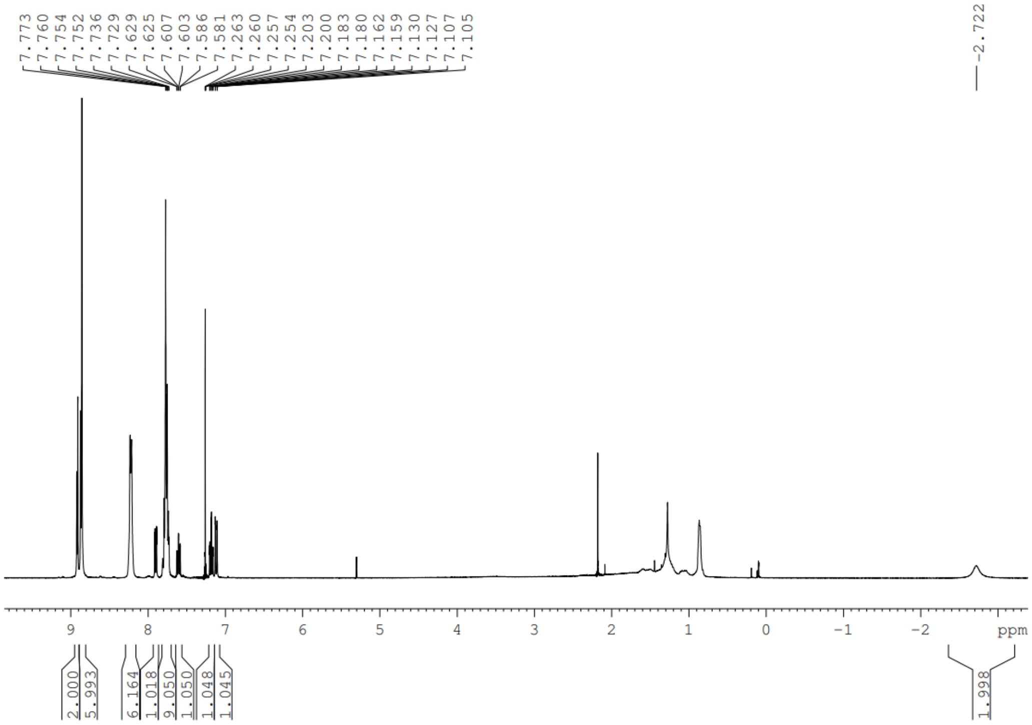

Figure S2-1 ^1H NMR spectrum of ***o*-NO_2PH_2** (360 MHz, $CDCl_3$).

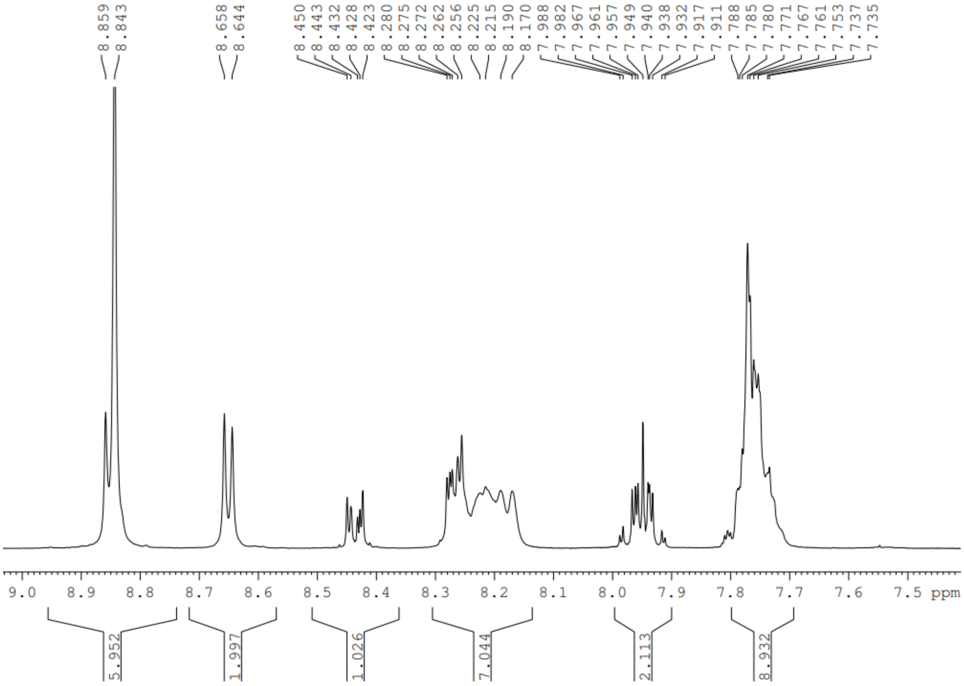

Figure S2-2 Zoom on the aromatic region of ^{1}H NMR spectrum of ***o*-NO$_2$PH$_2$** (360 MHz, CDCl$_3$).

Synthesis of *o*-NH$_2$PH$_2$

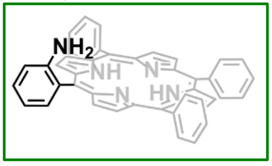

To a stirred solution of ***o*-NO$_2$PH$_2$** (744 mg, 1.13 mmol) in DCM (210 mL), 13 mL of c. HCl and SnCl$_2$·2H$_2$O (1.95 g, 8.64 mmol) are added at 0 °C and the mixture was left stirring at room temperature for 72 h. The progress of the reaction is monitored by thin layer chromatography (TLC, SiO$_2$, CH$_2$Cl$_2$/ Cyclohexane (3:2 v/v)). Upon reaction completion, 150 g of ice were transferred to the solution and the resulting solution was stirred for 15 min. Afterwards, the organic phase was collected, quenched with NaHCO$_{3(aq)}$, and washed thoroughly with H$_2$O. Then, the obtained organic layer is dried over MgSO$_4$ and evaporated until dryness. ***o*-NH$_2$PH$_2$** was obtained as a purple solid after silica column chromatography (CH$_2$Cl$_2$ /Cyclohexane (3:2 v/v)) purification and recrystallization from MeOH (655 mg, 92 %).

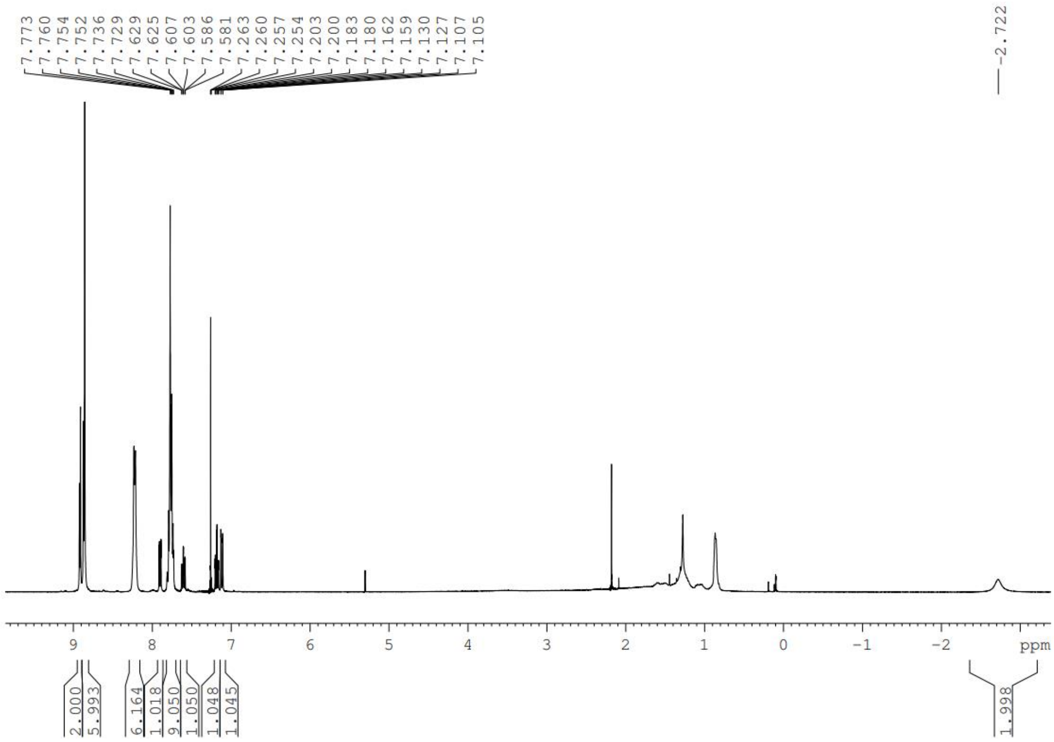

Figure S2-3 ^{1}H NMR spectrum of ***o*****-NH$_2$PH$_2$** (360 MHz, CDCl$_3$).

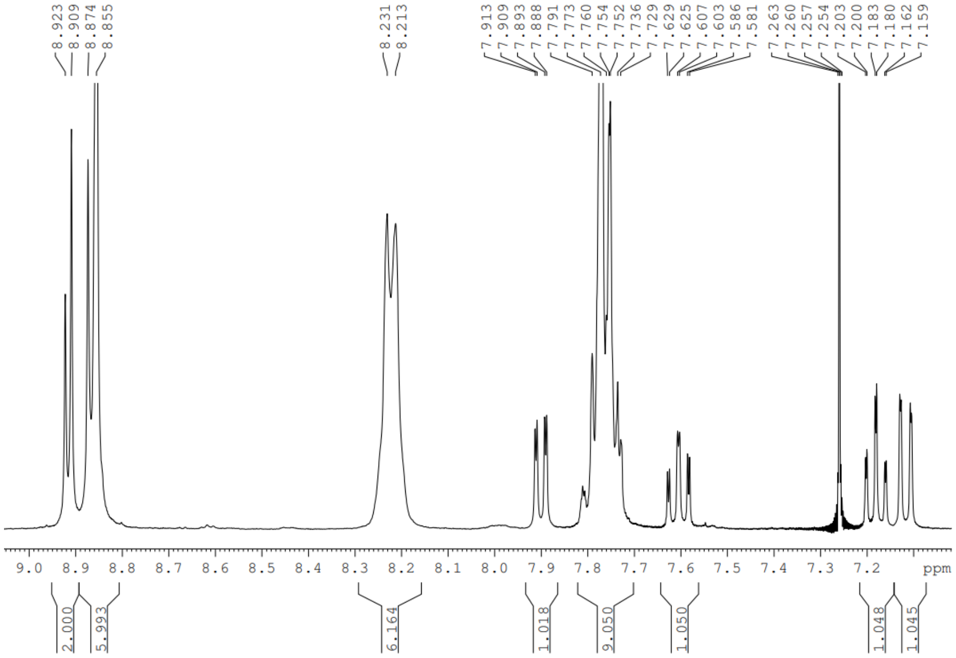

Figure S2-4 Zoom on the aromatic region of ^{1}H NMR spectrum of ***o*****-NH$_2$PH$_2$** (360 MHz, CDCl$_3$).

Synthesis of Zincke-salt

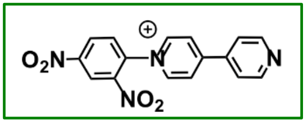

4,4 bipyridine (830 mg, 5.3 mmol) was dissolved in acetone (6 mL) and 1-chloro-2,4-dinitrobenzene (1g, 4.9 mmol) was added. The reaction mixture was heated up to 53 °C for 16 h in the dark. Upon completion of the reaction, the white-grey precipitate was filtered and was washed firs with acetone (50 mL) and then with pentane (50 mL). **Zincke-salt** was obtained as a pale grey-white solid (902.6 mg, 51%).

^{1}H NMR (360 MHz, MeOD): δ 9.42 (d, J= 7.1Hz 2H), 9.31 (d, J= 2.5 Hz, 1H), 8.94 (dd, J1= 8.7 Hz, J2= 8.5 Hz, 1H), 8.91 (dd, J_1= 6.3 Hz, J_2= 2.8 Hz, 1H), 8.82 (d, J= 7.1, 2H), 8.34 (d, J= 8.7 Hz, 1H), 8.13 (dd, J_1= 6.3 Hz, J_2= 2.8 Hz 1H) ppm.

ESI-HRMS: calc. for chemical formula $C_{16}H_{11}N_4O_4$ $[M]^+$ = 323.0775, found 323.0773

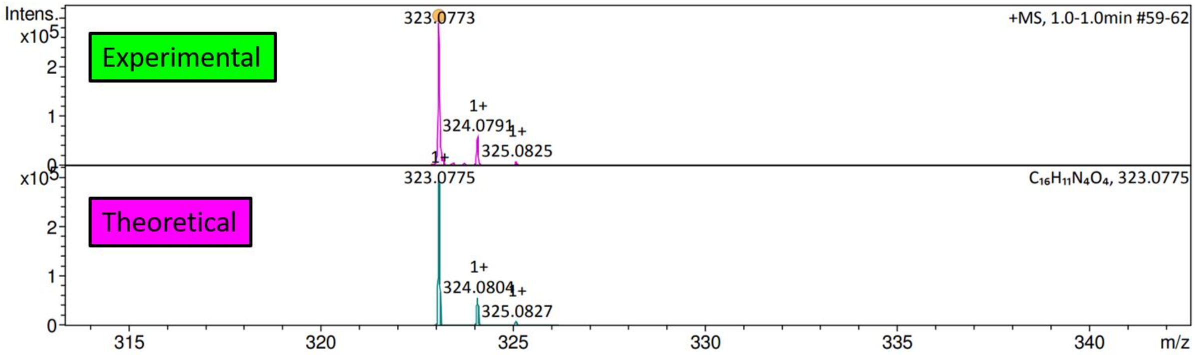

Synthesis of *o*-VPH$_2$

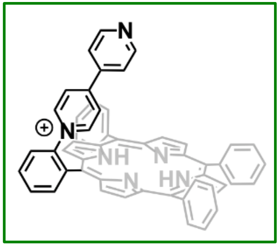

***o*-NH$_2$PH$_2$** (200 mg, 0.316 mmol) was dissolved in $CHCl_3$ (10 mL) and a solution of **Zincke-salt** (460 mg, 1.28 mmol) in EtOH (7 mL) was added. The reaction was heated to reflux (65 °C) for 20 h in the dark. Once the reaction was completed, the volatiles were evaporated under reduced pressure and the crude solid was purified via column chromatography (SiO2, ACN/H_2O/sat. KNO_3 (aq) (8:1:1) v/v) providing ***o*-VPH$_2$** as a purple solid. ***o*-VPH$_2$** was dissolved in the minimum amount of MeOH (4 mL) and a saturated NH_4PF_6 aqueous solution was added dropwise (5mL). The formed precipitate was filtered, washed thoroughly with H_2O (400 mL), and dried under vacuum to afford 280 mg of the desired porphyrin (97%).

^{1}H NMR (360 MHz, $CDCl_3$): δ 9.20 (d, J= 6.4 Hz, 2H), 8.92 (d, J= 4.8 Hz, 2H), 8.83 (s, 4H), 8.77 (d, J= 4.8 Hz, 2H), 8.70 (d, J= 8.1 Hz, 1H), 8.44 (d, J= 7.5 Hz, 1H), 8.36 (d, J= 5.0 Hz, 2H), 8.17 (m, 4H), 8.08 (m, 4H), 7.78 (m, 9H), 7.56 (d, J= 6.8 Hz, 2H), 6.98 (dd, J_1= 6.2 Hz, J_2= 3.2 Hz, 2H), -2.91 (br s, 2H) ppm.

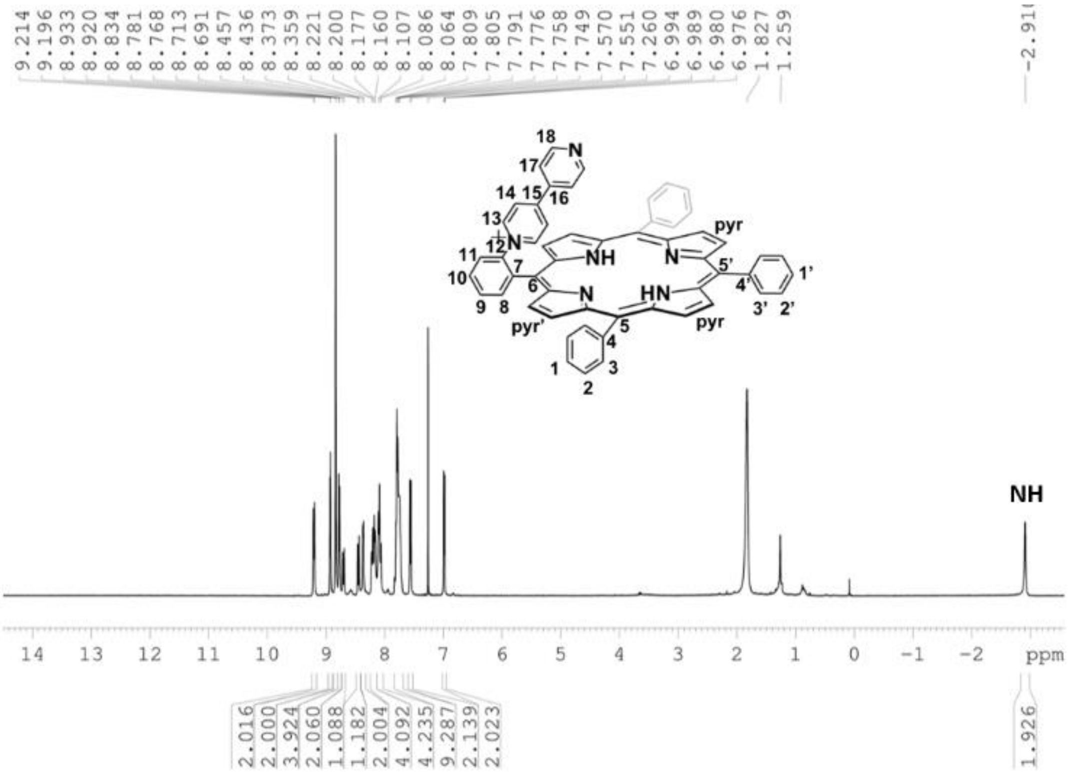

Figure S2-5 ^{1}H NMR spectrum of *o*-VPH$_2$ (360 MHz, CDCl$_3$).

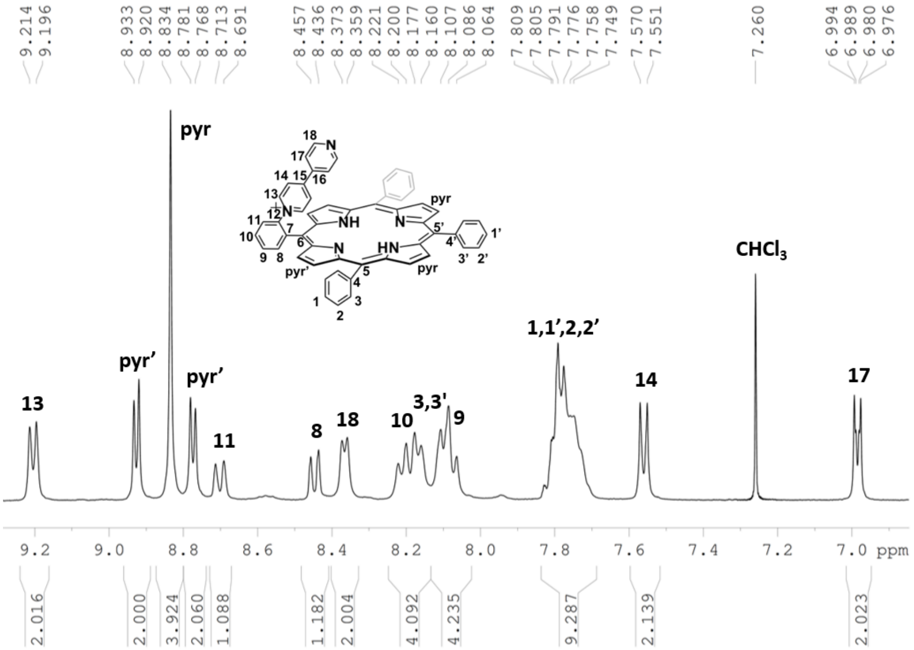

Figure S2-6 Zoom on the aromatic region of ^{1}H NMR spectrum of *o*-VPH$_2$ (360 MHz, CDCl$_3$).

^{13}C NMR (75 MHz, CDCl$_3$): δ 153.7, 151.0, 146.2, 144.0, 141.6, 141.3, 139.9, 136.4, 134.7, 134.6, 133.4, 131.9, 130.7, 129.3, 128.3, 128.2, 127.1, 127.0, 126.8, 125.1, 122.2, 121.5, 121.2, 109.5 ppm.

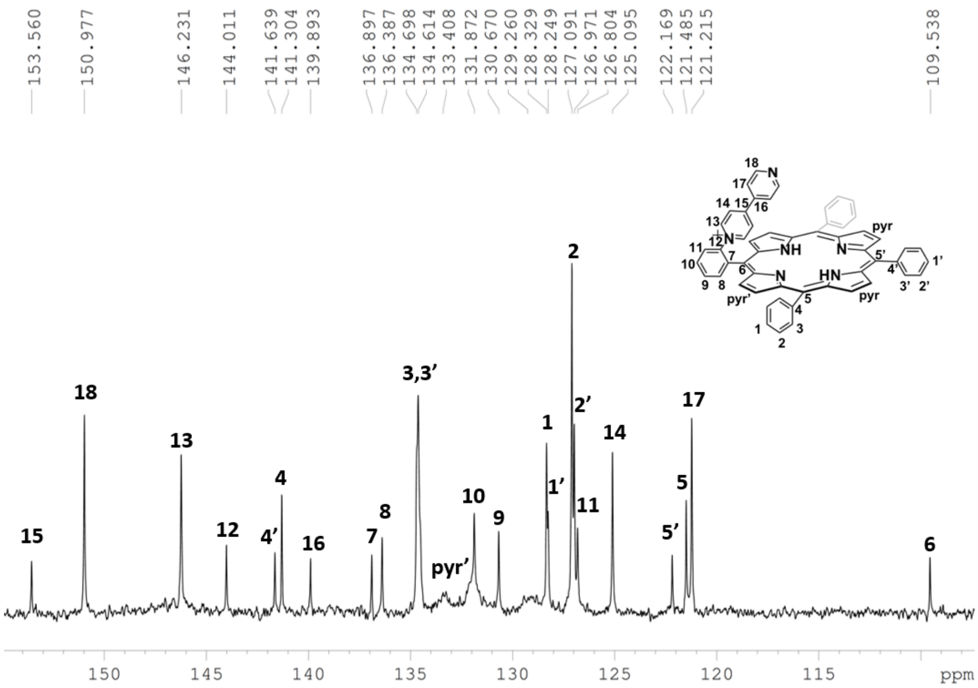

Figure S2-7 ^{13}C NMR spectrum of ***o*-VPH₂** (75 MHz, $CDCl_3$).

ESI-HRMS: calc. for chemical formula $C_{54}H_{37}N_6$ $[M]^+$ = 769.3074, found 769.3043.

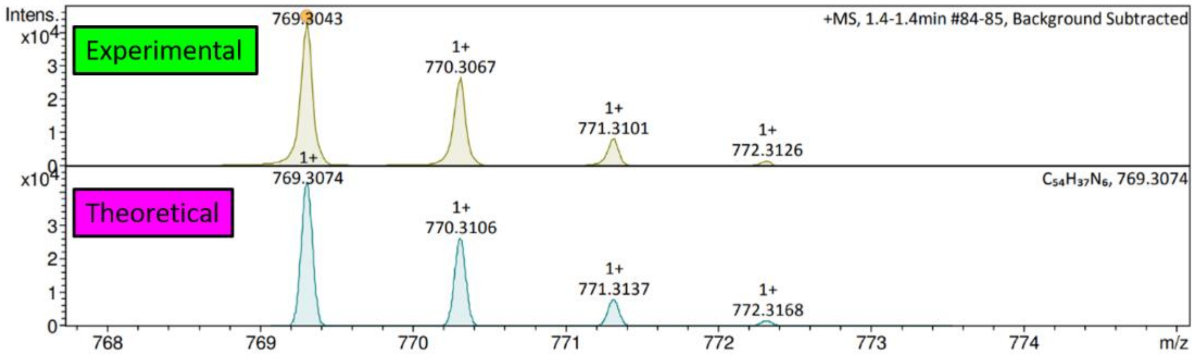

Synthesis of Zn-*o*-VP

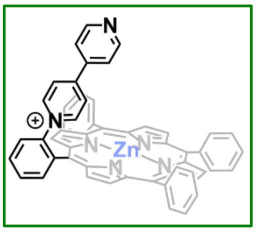

A methanolic solution (7 mL) of $Zn(OAc)_2 \cdot 2H_2O$ (61.2 mgr, 0.279 mmol) to a stirred solution of ***o*-VPH₂** (60.6 mg, 0.066 mmol) in $CHCl_3$ (15 mL), and the reaction mixture was heated to reflux for 2 h. After cooling down to room temperature, diethyl ether (200 mL) was added and the formed precipitate was filtered and dried under vacuum. The obtained solid was dissolved in the minimum amount of a MeOH/DMF (3 mL, 2:1) mixture and a saturated NH_4PF_6 aqueous solution was added dropwise (6mL). The precipitate was filtered, washed thoroughly with H_2O (300 mL) and dried under vacuum. Finally, **Zn-*o*-VP** was recrystallized from MeOH (51.5 mg, 80 %).

^{1}H NMR (360 MHz, DMSO-*d₆*): δ 9.29 (d, J= 6.6 Hz, 2H), 8.96 (d, J= 4.6 Hz, 2H), 8.77 (d, J= 4.6 Hz, 2H), 8.74 (s, 4H), 8.46 (d, J= 7.4 Hz, 1H), 8.31 (m, 4H), 8.15 (m, 6H), 8.04 (d, J= 6.8 Hz, 1H), 7.94 (d, J= 6.6 Hz, 2H), 7.81 (m, 9H), 7.32 (d, J= 5.8 Hz, 2H) ppm.

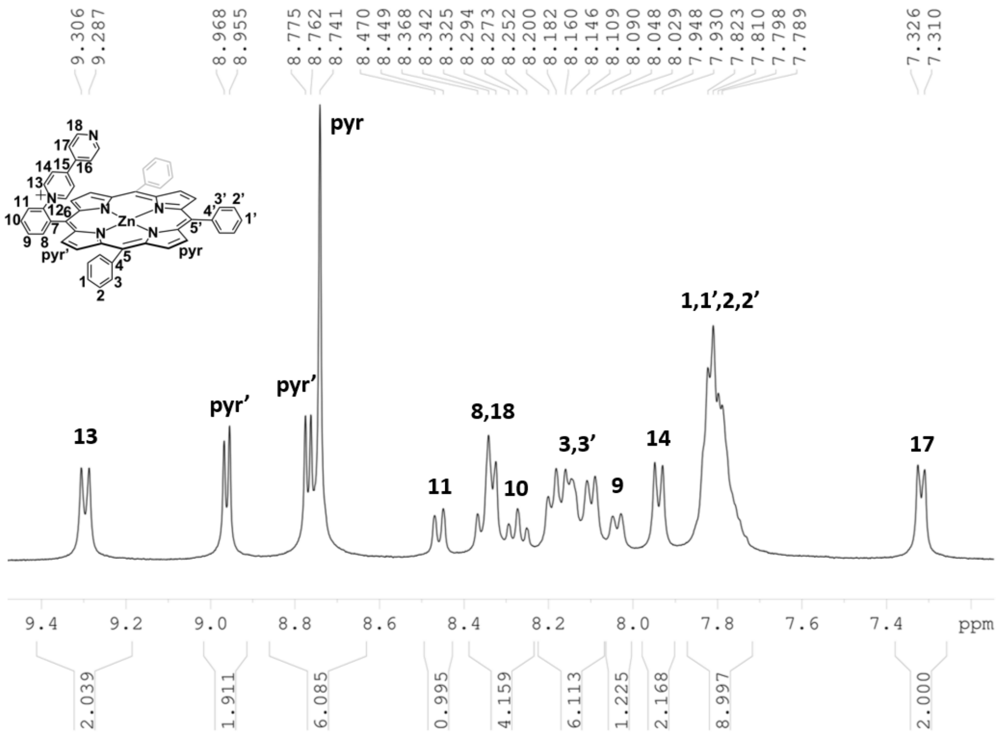

Figure S2-8 Zoom on the aromatic region of ^{1}H NMR spectrum of **Zn-*o*-VPH$_2$** (360 MHz, DMSO- *d$_6$*).

^{13}C NMR (75 MHz, DMSO- *d$_6$*): δ 152.2, 150.5,149.7, 149.4, 149.2, 148.8, 146.6, 143.5, 142.3, 142.2, 139.1, 137.6, 136.3, 134.3, 134.0, 132.6, 132.0, 131.8, 130.8, 130.4, 129.9, 127.7, 126.6, 126.3, 123.7, 121.6, 121.2, 120.8, 110.9 ppm.

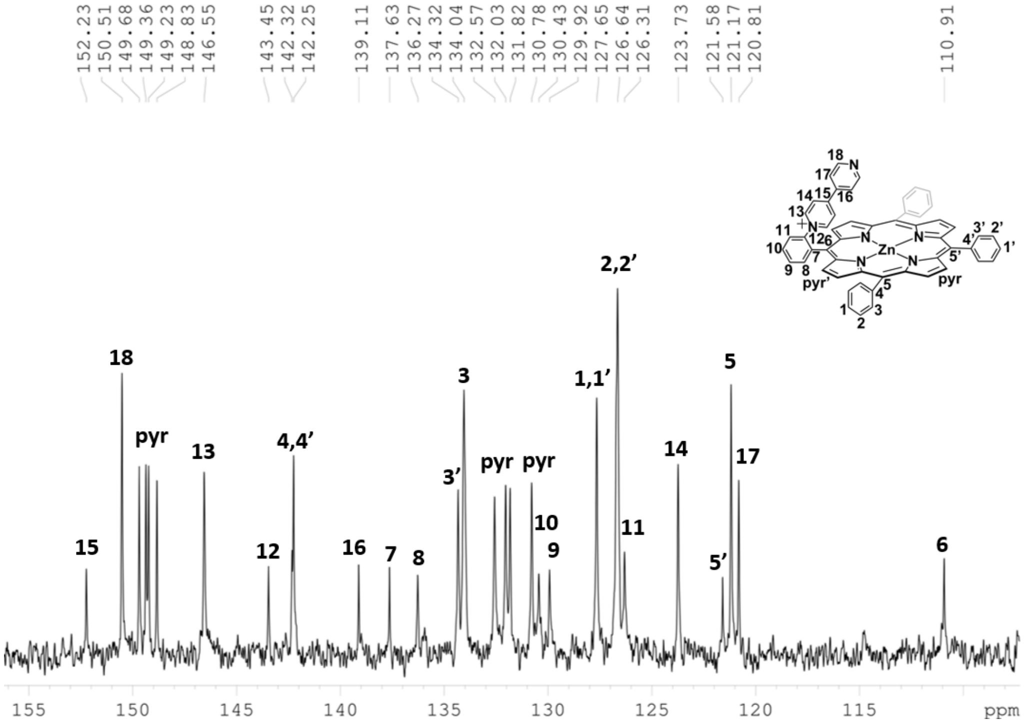

Figure S2-9 ^{13}C NMR spectrum of **Zn-*o*-VPH$_2$** (75MHz, DMSO- *d$_6$*).

ESI-HRMS: calc. for chemical formula $C_{54}H_{35}ZnN_6$ $[M]^+$ = 831.2209, found 831.2195.

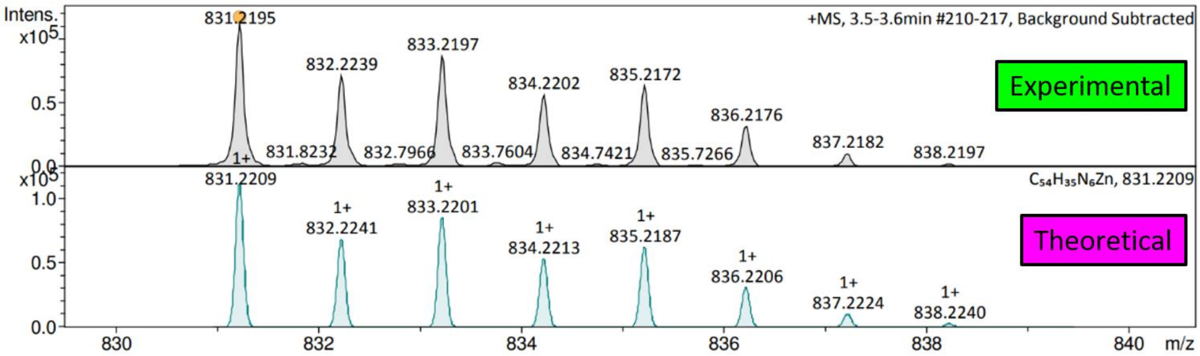

Synthesis of Zn-*o*-MVP

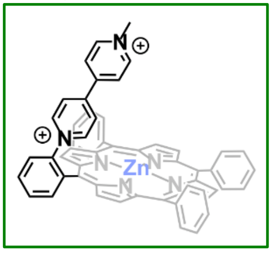

Zn-*o*-VP (20 mg, 0.020 mmol) was dissolved in dry DMF (7 mL) and MeI (50 μL, 0.82 mmol) was transferred into the solution, under Ar atmosphere. The reaction mixture was heated to 100 °C under stirring for 2 h. Once the reaction was completed, diethyl ether (150 mL) was added and the precipitate was filtered and washed with diethyl ether. Further purification was with column chromatography was not needed. The precipitate was then dissolved in the minimum amount of MeOH (2 mL) and a saturated NH_4PF_6 aqueous solution was added dropwise (3mL). Once again, the precipitate was filtered, washed thoroughly with H_2O (100 mL), and dried under vacuum to afford 22 mg of the **Zn-*o*-MVP** (97.2%).

ESI-HRMS: calc. for chemical formula $C_{55}H_{38}ZnN_6$ $[M]^{2+}$ = 423.1219, found 423.1199

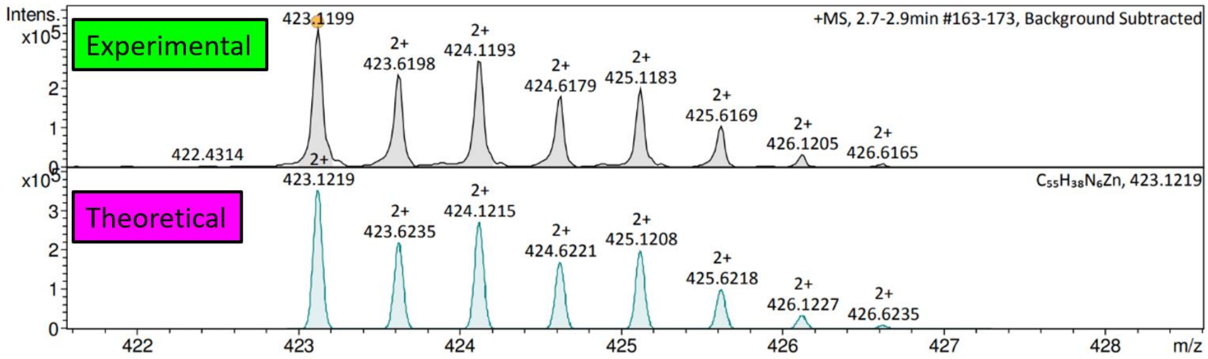

Synthesis of Cu-*o*-VP

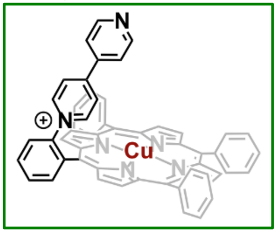

***o*-VPH₂** (50 mg, 0.062 mmol) was dissolved in $CHCl_3$ (12 mL) and a solution of $Cu(COOCH_3)_2 \cdot H_2O$ (41 mg, 0.205 mmol) in $CHCl_3$/ MeOH (8 mL, 3:5) mixture, was added. The resulting solution was heated to reflux for 20 h. Upon reaction completion, the solvents were evaporated under reduced pressure and the crude solid was purified via column chromatography (SiO_2, ACN/H_2O/sat. KNO_3 (aq) (8:1:1) v/v) providing **Cu-*o*-VP** as a purple-orange solid. **Cu-*o*-VP** was dissolved in the minimum amount of MeOH (2 mL) and a saturated NH_4PF_6 aqueous solution was added dropwise (3mL). The formed precipitate was filtered, washed thoroughly with H_2O (600 mL), and dried under vacuum to afford 55.3 mg of the desired porphyrin (91%).

ESI-HRMS: calc. for chemical formula $C_{54}H_{35}ZnN_6$ $[M]^+$ = 830.2214, found 830.2188.

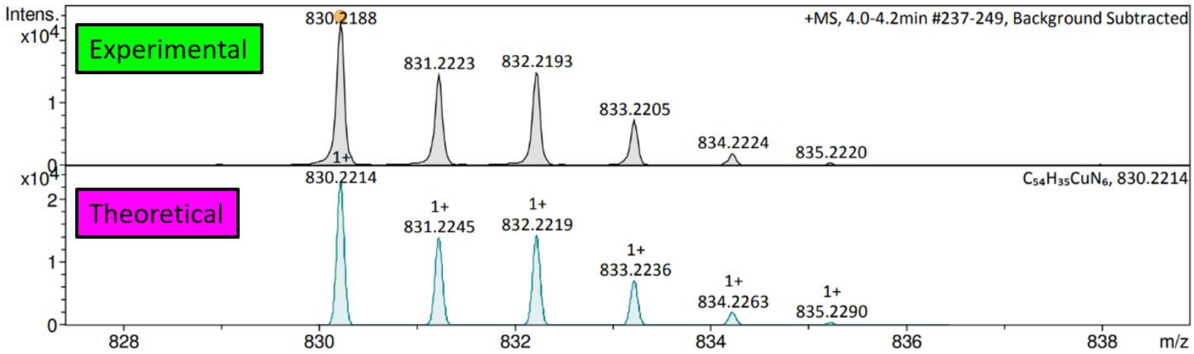

Synthesis of Cu-*o*-MVP

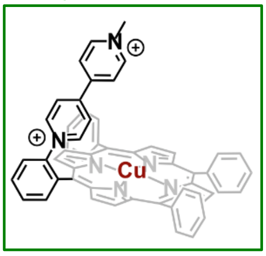

Cu-*o*-VP (49 mg, 0.050 mmol), dry DMF (7mL) and MeI (50 μL, 0.82 mmol) were transferred in a two-neck round bottom flask, under Ar atmosphere. The resulting solution was heated to 100 °C under stirring for 2 h. Once the reaction was completed, diethyl ether (200 mL) was added and the precipitate was filtered and collected. The crude solid was purified by column chromatography (SiO_2, ACN/H_2O/sat. KNO_3 (aq) (9:0.5:0.5) v/v) providing **Cu-*o*-MVP** as a purple-orange solid. Ion exchange with PF_6^- was carried out by dissolving **Cu-*o*-MVP** in the minimum amount of MeOH/ACN (2 mL) and adding a saturated NH_4PF_6 aqueous solution dropwise (3mL). The precipitate was filtered, washed thoroughly with H_2O (400 mL), and dried under vacuum to afford 55.4 mg of the desired porphyrin (98%).

ESI-HRMS: calc. for chemical formula $C_{55}H_{38}CuN_6$ $[M]^{2+}$ = 422.6221, found 422.6204

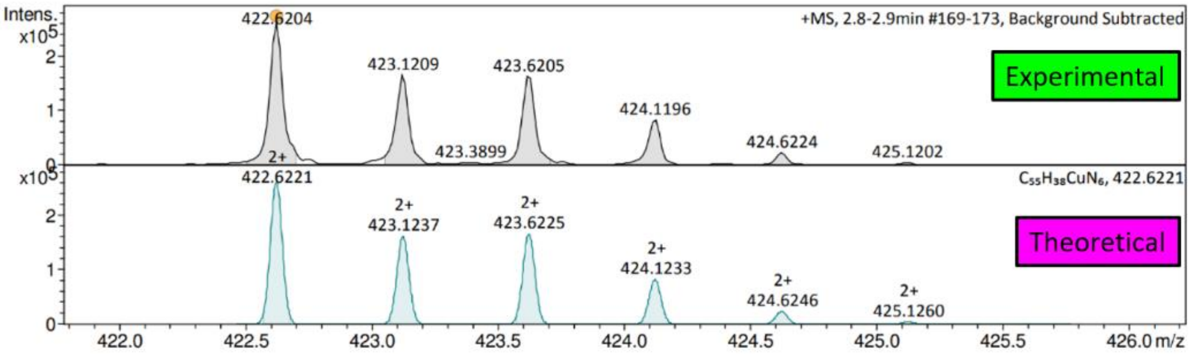

Chapter III

Water Activation by a Manganese Fused Imidazole-Phenol Porphyrin Derivative

3.1 Introduction

Carbon-based energy sources constitute the majority of the global energy supply; yet, their over-exploitation is inextricably linked to the ever-increasing concentration of greenhouse gases, which are responsible for the climatic change that planet Earth is experiencing as a result of global warming. Therefore, one of the primary scientific challenges of the 21st century is to mitigate climate change by replacing fossil fuels with carbon-neutral alternatives that can equally meet the demands of the modern world in energy. Among the available renewable sources, solar energy is the most abundant, clean, and inexhaustible. Indeed, if only less than 0.2 % of Earth's surface is covered with solar panels that can harvest the sunlight and convert it into electricity with an efficiency of nearly 10 %, then almost around 20 TW of energy could be produced, a quantity that exceeds by far the world's energy demands. [1],[2]

Nature, for more than a million years, captures the sunlight and translates it into chemical energy via photosynthesis. Plants, algae, and most oxygenic bacteria utilize solar energy to drive water splitting and produce high-energy electrons and protons which are required to fixate CO_2 into sugars (glucose). The way such organisms harvest solar energy has been a source of inspiration for the development of artificial photosynthetic systems that can reduce protons into H_2 and CO_2 into renewable solar fuels and valuable chemicals.[3]

3.1.1 Photosynthesis: Water-Splitting

The initial process in oxygenic photosynthesis is the light-driven water-splitting reaction through which four electrons and four protons are liberated, while O_2 is produced as a by-product. As shown in Scheme 3-1, the solar light is harvested in photosystem II (**PSII**) by a special pair of chlorophylls α (**P_{680}**) noted as the reaction center. Photon absorption leads to the excitation of the reaction center to yield its excited state, **P_{680}^***. At the same time, sunlight is absorbed by "antenna" pigments (chlorophyll and carotenoid molecules) that also transmit the excitation energy to **P_{680}** via an inductive resonance mechanism. **P_{680}^*** reduces an adjacent pheophytin (**$Pheo_A$**) followed by an electron transfer to a bound plastoquinone (**QA**) which serves as an electron mediator between **PSII** and photosystem I (**PSI**).[4] These sequences of electron transfer events lead to the **$P_{680}^{\bullet+}$/ $QA^{\bullet-}$** charge-separated state which is long-lived enough (~ $t_{1/2}$= 1.7 ms) to drive water-splitting.[5]

3.1.1.1 Crystal structure of Oxygen Evolution Complex (OEC)

Oxidation of water in **PSII** is catalyzed by the oxygen evolution complex (**OEC**). It consists of four manganese metal centers (**Mn**) and one calcium atom (**Ca**) interconnected with five oxygen (**O**) bridges in a distorted chair conformation, as shown in Scheme 3-1. **Mn4** and **O4** atoms comprise the top of the back of the chair in which two water molecules (**W_1**, **W_2**) are bound to the **Mn_4** center. The remaining **3Mn**, **Ca** and **4O** atoms constitute the base of the chair adopting a cubane-like conformation where **Ca** is coordinated with two additional water molecules (**W_3**, **W_4**).[6], [7]

---

[1] Hosenuzzaman, M., Rahim, N.A., Selvaraj, J., Hasanuzzaman, M., Malek, A.B.M.A., Nahar, A., *Renew. Sust. Energ. Rev.*, **2015**, 41, 284-297, DOI: 10.1016/j.rser.2014.08.046

[2] Service, R.F., *Science*, **2005**, 309, 5734, 548-551, DOI :10.1126/science.309.5734.548

[3] Zhang, B., Sun, L., *Chem. Soc. Rev.*, **2019**, 48, 2216-2264, DOI: 10.1039/C8CS00897C

[4] Hou, H.J.M., Najafpour, M.M., Moore, G.F., Allakhverdiev, S.I., *Photosynthesis: Structures, Mechanisms, and Applications*, Springer Cham **2017**, Ch. 1., 1-9, ISBN: 978-3-319-48873-8, DOI: 10.1007/978-3-319-48873-8

[5] Reinman, S., Mathis, P., *Biochim. Biophys. Acta Bioenerg.*, **1981**, 635, 2, 249-258, DOI: 10.1016/0005-2728(81)90024-4

[6]Umena, Y., Kawakami, K., Shen, J.-R., Kamiya, N., *Nature*, **2011**, 473, 55−60, DOI: 10.1038/nature09913

[7]Kawakami, K., Umena, Y., Kamiya, N., Shen, J.-R., *J. Photochem. Photobiol. B*, **2011**, 104, 1-2, 9-18, DOI: 10.1016/j.jphotobiol.2011.03.017

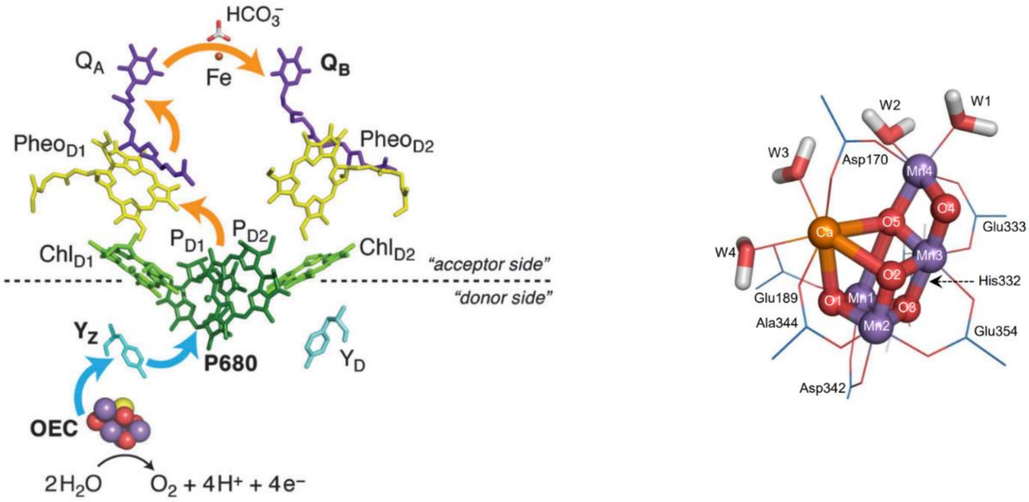

Scheme 3-1 Left: Schematic representation of the electron transfer steps between the cofactors of **PSII** after the photoexcitation of the reaction center (**P_{680}**).[8] Right: Crystal structure of the **OEC** taken from ref. [9].

3.1.1.2 Proposed Catalytic Mechanism of H_2O oxidation

The mechanism of water-splitting involves five intermediate redox states (S_n, n= 0-4)[10], which differ in the number of the oxidizing equivalents held by **Mn_4CaO_5**. Each sequential transition from the **S_0** to the **S_4** state is initiated by the absorption of a photon (*hv*). In total four photons are required for the **Mn_4CaO_5** to oxidize two H_2O molecules into O_2, as was first proposed by Joliot in 1969[11]. Each flash induces the formation of **$P_{680}^{\bullet+}$** that is oxidizing enough (~1.2 V *vs.* SHE) [12] to extract electrons from H_2O via a tyrosine residue (**Tyr_{161}**) laying close to the **Mn_4CaO_5** cluster. Crystallographic data have shown that **Tyr_{161}** is hydrogen-bonded to a nearby histidine (**His_{190}**), as shown in Scheme 3-2.[13] Reduction of **$P_{680}^{\bullet+}$** by **Tyr_{161}** generates the **P_{680}** and the cationic radical of **Tyr_{161}** (**$Tyr_{161}^{\bullet+}$**) accompanied by the concomitant transfer of the hydroxyl proton to **His_{190}**, forming the **$Tyr_{161}^{\bullet}$- His_{190}^{+}** pair.[14],[15],[16] Once **$Tyr_{161}^{\bullet}$** is formed (~ 0.937 *vs.* SHE, pH=7)[17], it removes electrons and protons from the **Mn_4CaO_5** cluster through proton-coupled-electron-transfer (**PCET**) steps before the O-O bond is formed and O_2 is released.

The proposed redox processes taking place during water-splitting by **Mn_4CaO_5** were first described by Kok in 1970. [18] Recently, the so-called Kok's cycle has been revised by Cox and

---

[8] Retegan, M., Cox, N., Lubitz, W., Neese, F., Pantazis, D.A, *Phys. Chem. Chem. Phys.*, **2014**, 16, 11901—11910 DOI: 10.1039/c4cp00696h

[9] Vogt, L., Vinyard, D.J., Khan, S., Brudvig, G.W., *Curr. Opin. Chem. Biol.*, **2015**, 25, 152-158, DOI: 10.1016/j.cbpa.2014.12.040

[10] "S" symbolizes the "state" and not the electron spin quantum number S

[11] Joliot, P., Barbieri, G., Chabaud, R., *Photochem. Photobiol.*, **1969**, 10, 5, 309-329, DOI: 10.1111/j.1751-1097.1969.tb05696.x

[12] Kato, Y., Sugiura, M., Oda, A., Watanabe, T., *PNAS USA*, **2009**, 106, 41, 17365–17370, DOI: 10.1073pnas.0905388106

[13] Guskov, A., Kern, J., Gabdulkhakov, A., Broser, M., Zouni, A., Saenger, W, Nat. Struct. Mol. Biol., **2009**, 16, 334-342, DOI : 10.1038/nsmb.1559

[14] Chu, H.A, Nguyen, A.P, Debus, R.J., *Biochemistry*, **1995**, 34, 17, 5839–5858, DOI: 10.1021/bi00017a016

[15] Berthomieu, C., Hienerwadel, R., Boussac, A., Breton, J., Diner, B.A., *Biochemistry*, **1998**, 37, 30, 10547–10554, DOI: 10.1021/bi980788m

[16] Saito, K., Shen, J.R, Ishida, T., Ishikita, H., *Biochemistry*, **2011**, 50, 45, 9836–9844, DOI: 10.1021/bi201366j

[17] Ishikita, H., Knapp, E.W., *Biophys. J.*, **2006**, 90, 11, 3886–3896, DOI: 10.1529/biophysj.105.076984

[18] Kok, B., Forbush, B., McGloin, M., *Photochem. Photobiol.*, **1970**, 11, 457–475, DOI: 10.1111/j.1751-1097.1970.tb06017.x

co-workers based on a series of spectroscopic and theoretical calculations (Scheme 3-2).[19],[20] The first step of the proposed water-splitting model involves the photo-induced oxidation of the **S_0** state (**$3Mn^{III}$-$1Mn^{IV}$**) by **$Tyr_{161}^{\bullet}$**. This oxidation process is accompanied by the deprotonation of the **-OH** ligand giving rise to the **S_1** intermediate state (**$2Mn^{III}$-$2Mn^{IV}$**). Further oxidation of the **$2Mn^{III}$-$2Mn^{IV}$** cluster can be realized in the **Mn^{III}_1** or **Mn^{III}_4** center affording a low-spin open-cubane (**S_2^A**) or a high-spin close-cubane (**S_2^B**) state, respectively. It is proposed that only the **S_2^B** conformation can promote the transition to the **S_3'** state since this one-electron oxidation step is coupled with a loss of a proton from **W1** that requires a manganese atom which can be oxidized by **$Tyr_{161}^{\bullet}$**, *viz.*, **Mn^{III}**. During the **S_2^B** → **S_3'** transition, a new H_2O molecule enters the catalytic cycle and binds to the **Mn_4^{IV}** leading to the exchange of its **-OH** ligand with the bridging **O** atom of the **Mn_3^{IV}** and **Mn_1^{IV}** centers. Once the **OEC** has reached its higher oxidation state (**S_4**), O_2 is released on the lumenal side of **PSII** and **OEC** returns to its resting **S_0** state with the insertion of a second water molecule.

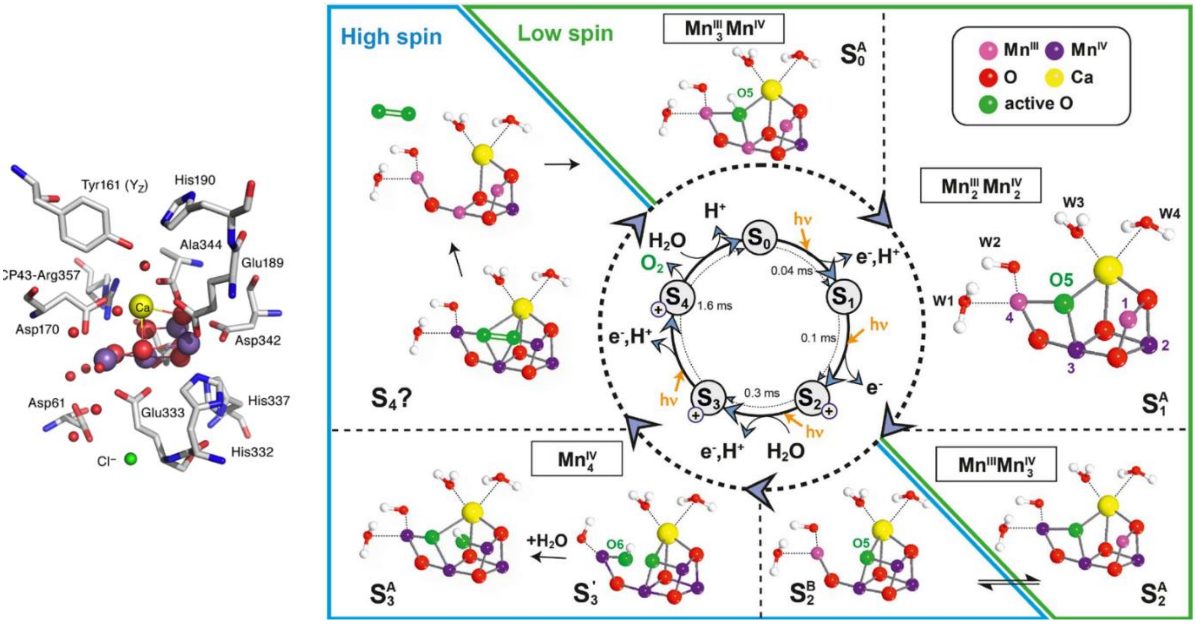

Scheme 3-2 Left: **Tyr_{161}-His_{190}** pair in **OEC** [21] Right: Proposed model for water-splitting realized in **PSII** by **OEC**.[22]

However, the nature of the exact intermediates involved in the **S_3^A** → **[S_4]** → **S_0** transition is still a matter of debate due to the short lifetime of the transient **S_4** state which makes its experimental characterization difficult. There are two main proposed intermediates responsible for the O-O bond formation in the **S_4** state: (i) a **Mn^V=O** intermediate or (ii) a **Mn^{IV}-$O^{\bullet}$** species, both of them produced upon further one-electron oxidation of the **S_3** state. As shown in Fig. 3-1a, the O-O bond in the first scenario is formed upon nucleophilic attack of the calcium's bound water molecule (**W3**) to the **Mn_4^V=O** center. On the other hand, when a **Mn^{IV}-$O^{\bullet}$** intermediate is involved, O-O bond formation proceeds via a coupling between the

---

[19] Cox. N., Pantazis, D.A., Neese, F., Lubitz, W., *Interface Focus*, **2015**, 5, 3, 20150009, DOI: 10.1098/rsfs.2015.0009

[20] Krewald, V., Retegan, M., Neese, F., Lubitz, W., Pantazis, D.A., Cox, N., *Inorg. Chem.*, **2016**, 55, 488–50, DOI: 10.1021/acs.inorgchem.5b02578

[21] Pantazis, D.A., *ACS Catal.*, **2018**, 8, 9477−9507, DOI: 10.1021/acscatal.8b01928

[22] Lubitz, W., Chrysina, M., Cox, N., *Photosynth. Res.*, **2019**, 142, 105–125, DOI: 10.1007/s11120-019-00648-3

Mn_1^{IV}-O$^{\bullet}$ radical species and the **Mn_4^{IV}=O** metal center, according to the proposed mechanism by Siegbahn[23] (Fig. 3-1b).

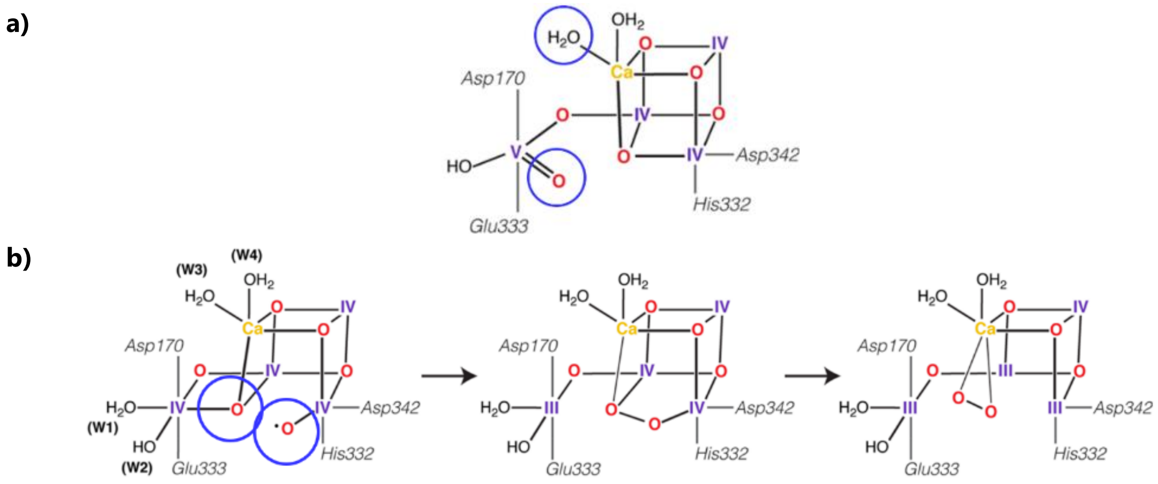

Fig. 3-1 Possible intermediates involved in the final catalytic step of **OEC** in **PSII**. a) O-O bond formation upon nucleophilic attack of the H_2O water molecule bound on the **Ca** atom to the **Mn^V=O** species; b) Proposed mechanism by Siegbahn concerning a radical coupling between a **Mn^{IV}-O$^{\bullet}$** and **Mn^{IV}=O** species.[21]

It is worth noting that the one-electron oxidation steps involved in the **S_0** → **S_1**, **S_2^B** → **S_3^A**, and **S_3^A** → **S_4** transitions by **$Tyr_{161}^{\bullet}$** are all coupled with the expulsion of a proton from the **OEC** cofactor. In other words, all of them refer to as **PCET** processes. The reason why Nature employs **PCET** steps is mainly to prevent the accumulation of more positive charges in the **S_4** state that can potentially lead to the collapse of **OEC** and its deactivation. Such successive **PCET** steps allow each of the four oxidations of the cluster to happen along an isoenergetic pathway and make them thermodynamically favorable.[24] At the same time, crystallographic data of **PSII** has highlighted the importance of H-bond water networks (e.g., O_4-water chain) that permit the movement of the expelled protons from **OEC** to the bulk of **PSII**, by lowering the p*K*a of the proton donors resulting in a downhill proton transfer.[25],[26]

3.1.2 Synthetic Models of the Tyr_{161}-His_{190} pair

Studies on **OEC** model systems can help to gain better insights into the discrete activation steps in the water-splitting reaction and especially how the redox active **Tyr_{161}-His_{190}** pair is involved in the **OEC** mechanism. Hammarström and Styring have developed over the years a series of ruthenium complexes appended with **Tyr_{161}(-His_{190})** analogs coupled or not with dinuclear manganese complexes in an effort to understand the **PCET** steps upon oxidation of the phenol function. Some representative examples of their work are provided below.

As shown in Fig. 3-2. Hammarström developed a biomimetic model of the **P_{680}-Tyr_{161}-His_{190}** sequence in **PSII** by functionalizing a ruthenium complex with a phenol unit appended to two dipicolylamine ligands (**Ru- PhOH- dpa**), in which the phenolic proton formed strong hydrogen bonds with the **dpa** groups.

---

[23] Siegbahn, P.E.M., *Acc. Chem. Res.*, **2009**, 42, 12, 1871–1880, DOI: 10.1021/ar900117k
[24] Brudvig, G.W., *Philos. Trans. R. Soc. B: Biol. Sci.*, **2008**, 363, 1494, 1211–1219, DOI: doi.org/10.1098/rstb.2007.2217
[25] Takaoka, T., Sakashita, N., Saito, K., Ishikita, H., *J. Phys. Chem. Lett.*, **2016**, 7, 10, 1925–1932, DOI: 10.1021/acs.jpclett.6b00656
[26] Narzia, D., Bovia, D., Guidoni, L., *PNAS USA*, **2014**, 111, 24, 8723–8728, DOI: 10.1073/pnas.1401719111

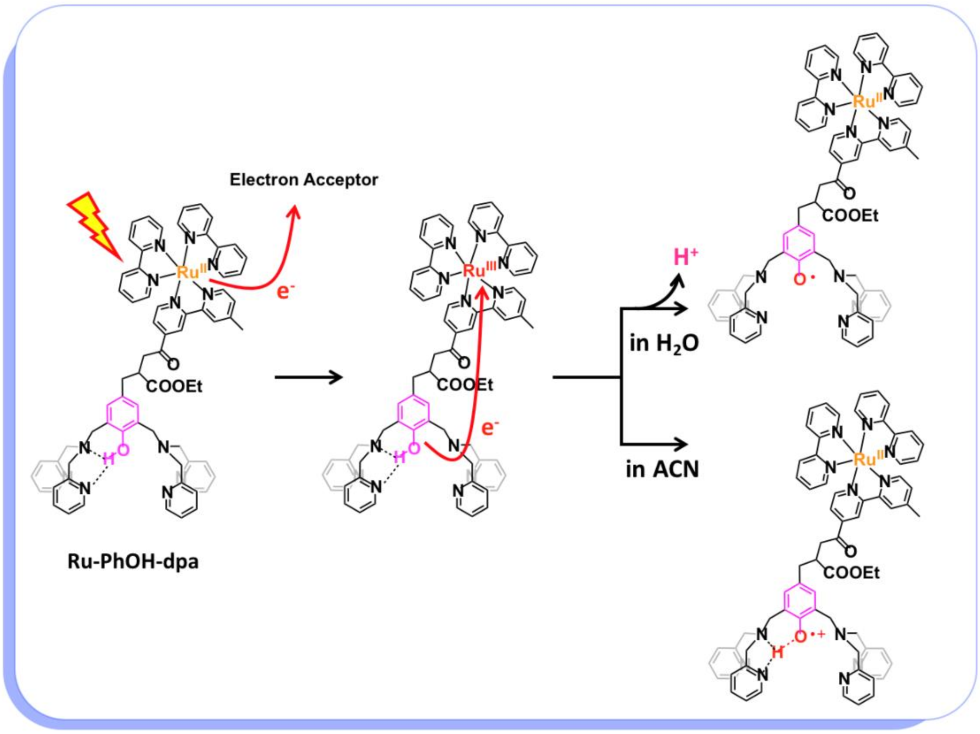

Fig. 3-1 Proposed Electron Transfer induced by photoexcitation of **Ru-PhOH-dpa** in the presence of an electron acceptor in an aqueous or ACN solution.

Excitation of the Ru unit generated its excited state which was quenched by an electron acceptor in an attempt to resemble the electron transfer step from the excited reaction center of **PSII** to the nearby **QA**. Upon this electron transfer **Ru^{III}** was formed that oxidized the covalently linked **PhOH**. When these studies were conducted in a polar aprotic solvent, the **PhOH** unit was rapidly oxidized to its cationic radical which was suggested to be hydrogen-bonded to the **dpa** ligand. However, this was not the case in aqueous solutions in which H_2O acted as a base thus mediating the proton transfer from the cationic phenoxyl radical generating its neutral tyrosyl radical mimicking the first photo-induced events in **PSII**. Interestingly, when a similar complex lacking the **dpa** fractions was investigated the rate of the electron transfer was considerably suppressed. Hence, their results demonstrated that the hydrogen bond between **PhOH** and **dpa** accelerates the electron transfer to the Ru^{III} complex, like in the **Tyr$_{161}$-His$_{190}$** pair upon oxidation from **$P_{680}$$^{\bullet+}$**.[27]

Moving one step forward with their studies, they synthesized a μ-oxo bridged Mn^{III} dinuclear complex (**$Mn^{III}_2OL_2$**) that was already known in the literature that it could store up to two oxidizing equivalents at a potential of around 1.5 V *vs.* SCE. [28] When a solution of a **Ru(bpy)$_3$** complex covalently linked with a PhOH group containing **$Mn^{III}_2OL_2$** was photoexcited in the presence of an electron acceptor they observed that **Ru^{III}(bpy)$_3$** removed one electron from the **$Mn^{III}_2OL_2$** giving rise to the initial **Ru(bpy)$_3$** moiety and a mixed-valence (**Mn^{III} – Mn^{IV}OL$_2$**) complex. Spectroscopic studies indicated that mediator of this electron

---

[27]Sun, L., Burkitt, M., Tamm, M., Raymond, M.K., Abrahamsson, M. *et al.*, *J. Am. Chem. Soc.*, **1999**, 121, 29, 6834–6842, DOI: 10.1021/ja984048c

[28]Horner, O., Anxolabéhère-Mallart, E., Charlot, M.-F., Tchertanov, L., Guilhem, J. *et al.*, *Inorg. Chem.*, **1999**, 38, 6, 1222–1232, DOI: 10.1021/ic980832m

transfer was the PhOH moiety which was initially oxidized by **$Ru^{III}(bpy)_3$** and rapidly reduced by **$Mn^{III}{}_2OL_2$** (Fig. 3-3 left).[29]

A similar study by Hammarström and Styring was also carried out concerning the supramolecular complex of Fig. 3-3 right. In particular, they covalently linked a dinuclear **Mn^{II}-Mn^{II}** complex with **$Ru(bpy)_3$** via a L-tyrosine and investigated its photochemical response in the presence of an electron acceptor. In the presence of 10% H_2O, the photogenerated **$Ru^{III}(bpy)_3$** oxidized the **Mn^{II}-Mn^{II} (L-tyrosine)** complex, but this time three electrons were removed from the **Mn^{II}-Mn^{II} (L-tyrosine)** resulting in a mixed-valence **Mn^{III}-Mn^{IV}** center that could store up to three oxidizing equivalents. The authors speculated that the tyrosine mediated these electron transfer processes in a concomitant manner. The photo-induced events taking place within this triad are summarized in Fig. 3-3 right.[30]

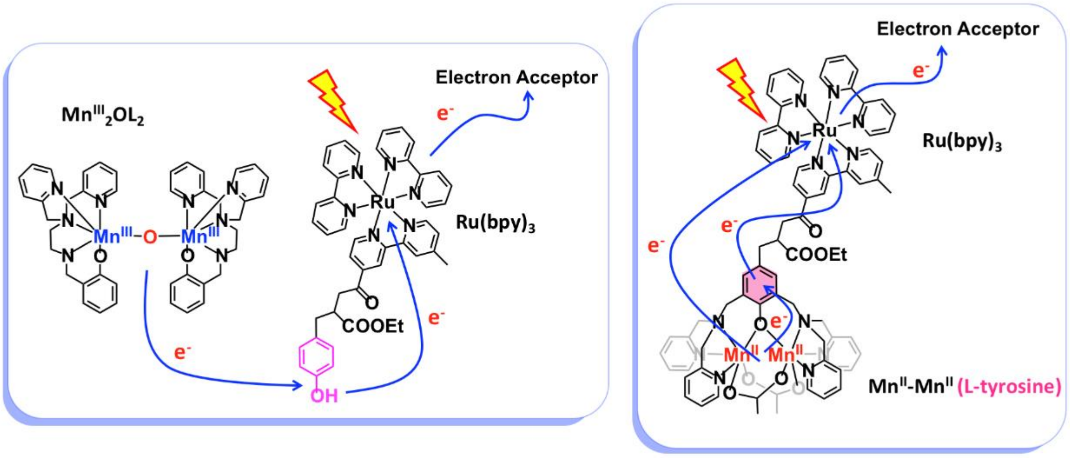

Fig. 3-3 Proposed Electron Transfer induced by photoexcitation of Left: a solution containing **$Mn^{III}{}_2OL_2$** and **$Ru(bpy)_3$** covalently attached to a phenol group; Right: the dyad comprised of **Mn^{II}-Mn^{II} (L-tyrosine)** linked to a **$Ru(bpy)_3$** photosensitizer.

Our group has also developed **P_{680}-Tyr_{161}-His_{190}** mimics by the attachment of benzimidazole-phenol moiety to a phenanthroline ligand coordinated to a Ru complex bearing two additional bipyridines, as shown in Fig. 3-4. Cyclic voltammetry experiments proposed that the oxidation the phenol group was realized at considerable low positive potentials, *viz.* 0.52 *vs*. SCE, while the one-electron oxidation of the **Ru^{II}** complex **Ru^{III}** took place at 1.29 *vs*. SCE. Intrigued by the electrochemical properties of the dyad, a series of spectroscopic studies were conducted in an attempt to investigate the photoinduced **PCET** process. Our finding demonstrated that the photo-generated **Ru^{II}** excited state was quenched by a reversible electron acceptor to form **Ru^{III}**. **Ru^{III}** subsequently oxidized intramolecularly the phenol group of the benzimidazole-phenol ligand and yielded the phenoxyl radical, as shown in Fig. 3-4 However, no intramolecular proton transfer to the imidazole fragment was realized upon oxidation suggesting that a base is required to unlock the **PCET**.[31]

---

[29]Magnuson, A., Frapart, Y., Abrahamsson, M., Horner, O., Åkermark, B. *et al., J. Am. Chem. Soc.*, **1999**, 121, 1, 89–96, DOI: 10.1021/ja981494r

[30]Huang, P., Magnuson, A., Lomoth, R., Abrahamsson, M., Tamm, M. *et al., J. Inorg. Biochem.*, **2002**, 91,1, 159-172, DOI: 10.1016/s0162-0134(02)00394-x

[31]Lachaud, F., Quaranta, A., Pellegrin, Y., Dorlet, P., Charlot, M.-F. *et al., Angew. Chem., Int. Ed.*, **2005**, 117, 10, 1560-1564, DOI: 10.1002/ange.200461948

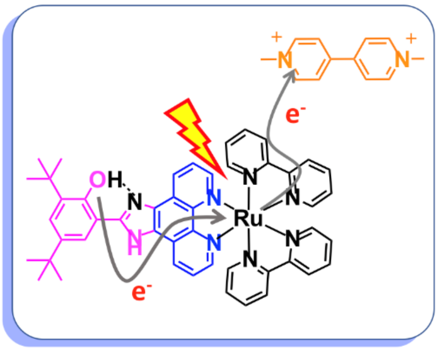

Fig. 3-4 Photo-induced electron transfer steps upon excitation of the ruthenium complex ligated to a phenanthroline ligand functionalized with a benzimidazole-phenol group.

As shown in Fig. 3-5, Megiatto *et al.* developed a molecular dyad (**Bi-PhOH-PF$_{10}$-TCNP-2tBut**), as shown in Fig. 3-X. This supramolecular complex was comprised of phenol-imidazole moiety (**Bi-PhOH**) as a mimic of the **Tyr$_{161}$-His$_{190}$** pair, which was appended on a non-metallated porphyrin bearing electron-withdrawing groups (**PF$_{10}$**). In addition, **PF$_{10}$** was covalently linked to a free base tert-butyl porphyrin bearing– CN groups on the β-pyrrolic positions (**TCNP-2tBut**), in an effort to resemble the **P$_{680}$** reaction center. Time-resolved spectroscopic analysis revealed that upon selective excitation of **TCNP-2tBut**, the singlet excited of **TCNP-2tBut** was rapidly quenched due to the one-electron transfer from **PF$_{10}$** followed by the reduction of the oxidized **PF$_{10}$** by **Bi-PhOH** yielding the **BiH^{+}-PhO$^{•}$ -PF$_{10}$-TCNP-2tBut $^{•−}$** charge-separated. **BiH^{+}-PhO$^{•}$ -PF$_{10}$- TCNP-2tBut $^{•−}$** exhibited a lifetime of 3.8 μs and it was placed ~1.35 eV higher than its ground state. Hence, the authors postulated that **Bi-PhOH-PF$_{10}$- TCNP-tBut** could potentially be coupled with water oxidation catalysts since the activation of H_2O and its further oxidation would be thermodynamically favorable from the **BiH^{+}-PhO$^{•}$ -PF$_{10}$- TCNP-2tBut $^{•−}$** state.[32] Interestingly, when **TCNP-2tBut** was replaced by **TCNP-tBut** (Fig. 3-Xb), the **Bi-PhOH-PF$_{10}$$^{•+}$ TCNP-tBut$^{•−}$** transient intermediate decayed rapidly to its ground state **Bi-PhOH-PF$_{10}$-TCNP-tBut**, and the detection of an analogous **BiH^{+}-PhO$^{•}$ -PF$_{10}$- TCNP-tBut$^{•−}$** charge-separated state was not feasible.[33]

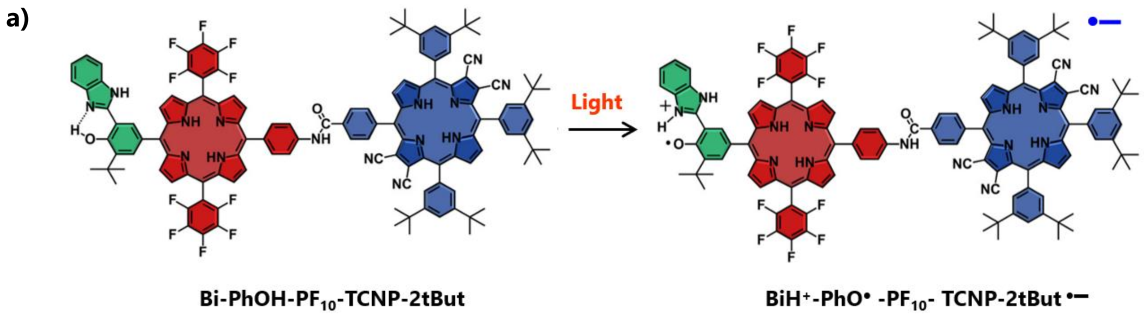

---

[32]Megiatto, J.D., Antoniuk-Pablant, A., Sherman, B.D., Kodis, G., Gervaldo, M. *et al*, *PNAS USA*, 2012, 109, 39, 15578–15583, DOI: 10.1073/pnas.1118348109

[33] Ravensbergen, J., Antoniuk-Pablant, A., Sherman, B.D., Kodis, G., Megiatto, J.D. *et al.*, *J. Phys. Chem. B*, **2015**, 119, 12156−12163, DOI: 10.1021/acs.jpcb.5b05298

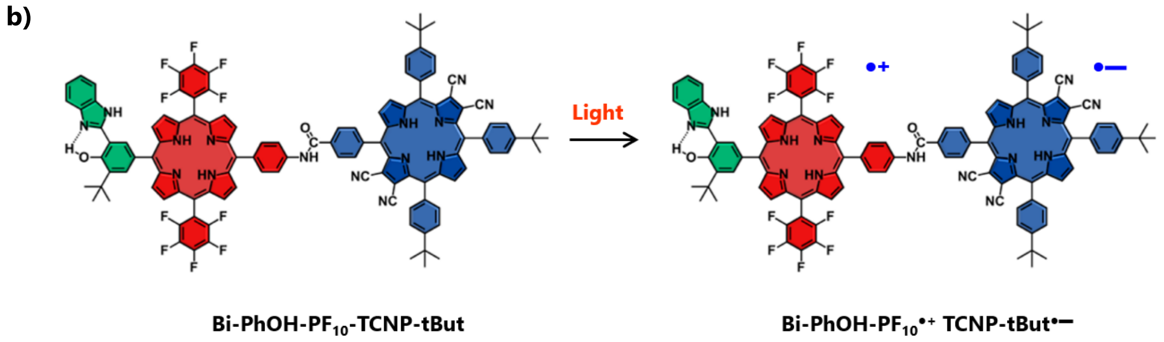

Fig. 3-5 P$_{680}$-Tyr$_{161}$-His$_{190}$ mimics investigated by Moore and co-workers; a) **Bi-PhOH-PF$_{10}$-TCNP-2tBut** and b) **Bi-PhOH-PF$_{10}$-TCNP-tBut** dyads

On a similar note, Moore and co-workers synthesized a free-base porphyrin bearing an imidazole-phenol and modified with -COOH groups as anchoring sites to SnO_2 nanoparticles (**Bi-PhOH-TCP-SnO$_2$**) (Fig. 3-6a). Excitation of **TCP** resulted in the injection of an electron into the conduction band of **SnO$_2$** giving rise to the **Bi-PhOH-TCP$^{\bullet+}$-SnO$_2$$^{\bullet-}$** state that finally evolved to the **BiH$^+$-PhO$^{\bullet}$-TCP-SnO$_2$$^{\bullet-}$** charge-separated state with a lifetime of ~93 μs.[34] The same team in collaboration with the group of Mallouk, also investigated the photoelectrochemical oxidation of H_2O by modifying TiO_2 electrodes with a ruthenium complex as the photosensitizer and iridium oxide nanoparticles as the catalyst. The catalyst was also functionalized with an imidazole-phenol group as an electron relay (Fig. 3-6b). The incorporation of the imidazole-phenol moiety greatly enhanced the electron transfer from the catalyst (IrO_x) to the photosensitizer and the new artificial photocatalytic H_2O-oxidation system exhibited a quantum efficiency of almost 2.3%.[35]

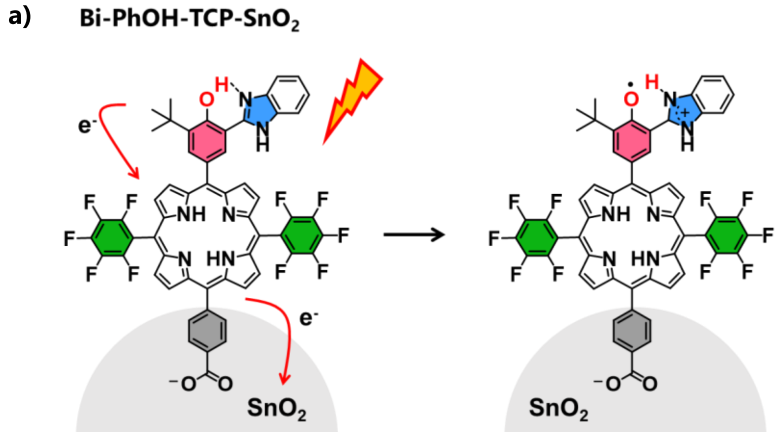

---

[34] Mora, S.J., Odella, E., Moore, G.F., Gust, D., Moore, T.A., Moore, A.L., *Acc. Chem. Res.*, **2018**, 51, 2, 445–453, DOI: 10.1021/acs.accounts.7b00491

[35] Zhao, Y., Swierk, J.R.,Megiatto, J.D., Sherman, B., Youngblood, W.J. *et al.*, *PNAS USA*, **2012**, 109, 39, 115612–15616, DOI: 10.1073/pnas.1118339109

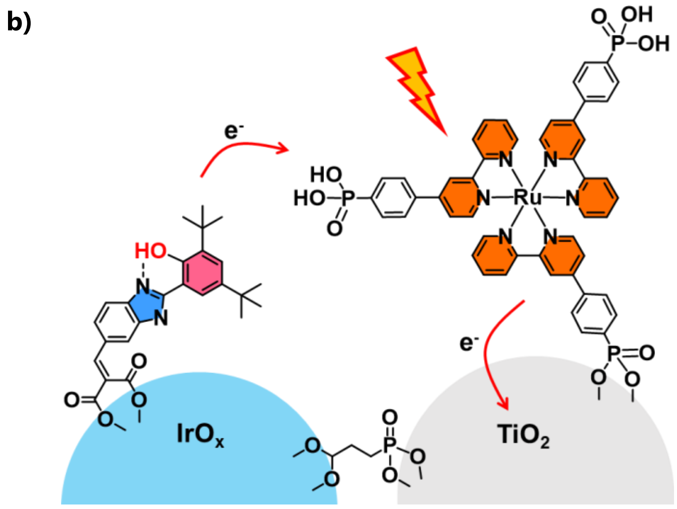

Fig. 3-6 Supramolecular assemblies of **Tyr$_{161}$-His$_{190}$** mimics attached on the surface of nanoparticles; a) adsorbed on SnO_2, arrows indicate the flow of the electron upon excitation of the porphyrin; b) adsorption of a Ru photosensitizer and IrO_x H_2O-oxidation catalyst on a TiO_2 electrode. IrO_x was modified with an imidazole-phenol moiety serving as an electron relay upon catalysis.

In contrast to the **PCET** mechanisms carried out by the models described above, the number of synthetic analogs of the **Tyr$_{161}$-His$_{190}$** pair that couple the one-electron oxidation of the phenol group with multi-proton transfer steps is quite limited. Most of these mimics have been developed by the group of Moore and mostly concern properly modified imidazole-phenol derivatives bearing basic residues, as shown in Fig. 3-7. Although, these "proton-wires" can transfer more than one proton upon one-electron oxidation of the phenol (phOH), due to the presence of the basic groups the redox potential of the PhOH/PhO$^\bullet$ redox couple is considerably shifted to less positive values.[36],[37],[38]

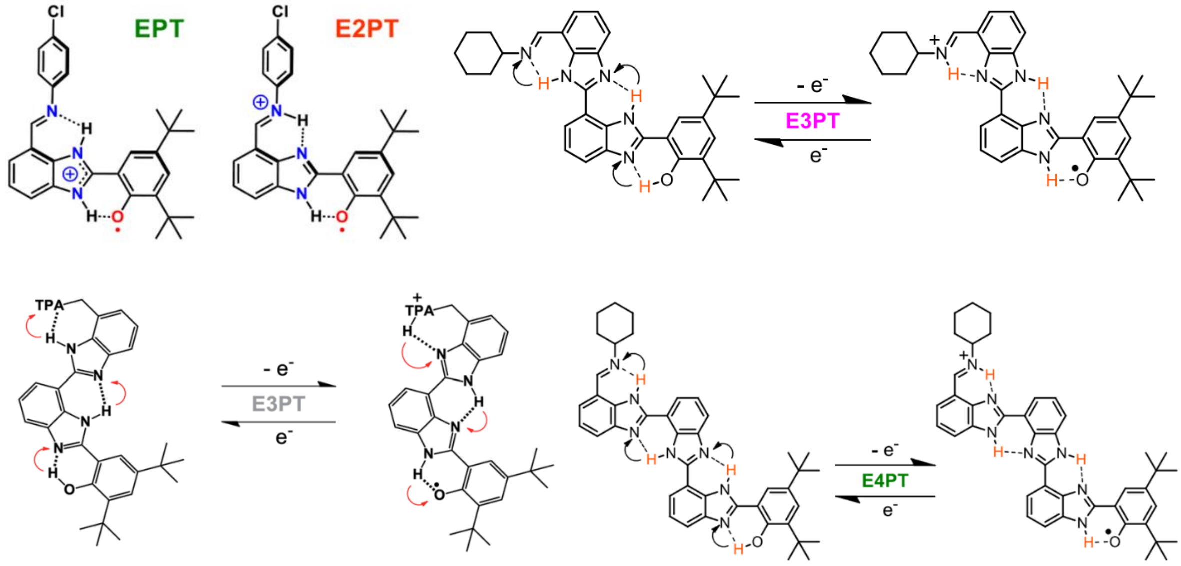

---

[36]Odella, E., Mora, S.J., Wadsworth, B.L., Huynh, M.T., Goings, J.J. *et al.*, *J. Am. Chem. Soc.*, **2018**, 140, 45, 15450–15460, DOI: 10.1021/jacs.8b09724

[37]Odella, E., Wadsworth, B.L., Mora, S.J., Goings, J.J., Huynh, M.T. *et al.*, *J. Am. Chem. Soc.*, **2019**, 141, 14057−14061, DOI: 10.1021/jacs.9b06978 8

[38]Odella, E., Mora, S.J., Wadsworth, B.L., Goings, J.J., Gervaldo, M.A. *et al.*, *Chem. Sci.*, **2020**, 11, 3820–3828, DOI: 10.1039/c9sc06010c

Fig. 3-7 Proton benzimidazole-phenol wires developed by Moore's groups capable of realizing one-electron coupled with multiple proton transfers.

Recently, we developed a biomimetic model of the **P_{680}-Tyr_{161}-His_{190}** sequence in **PSII** and we showed for the first time that the **Tyr_{161}-His_{190}** pair serves both as an electron and proton relay between the **P_{680}** and the **OEC**, realizing the expulsion of protons from the **OEC**.

Indeed, we evinced that the photo-induced oxidation of the **Tyr_{161}-His_{190}** pair is controlled by water molecules that trigger a photo-induced one electron two-proton coupled transfer (**E2PT**) process along an isoenergetic pathway (~1.0 V *vs.* SCE), as shown in Fig. 3-8.[39]

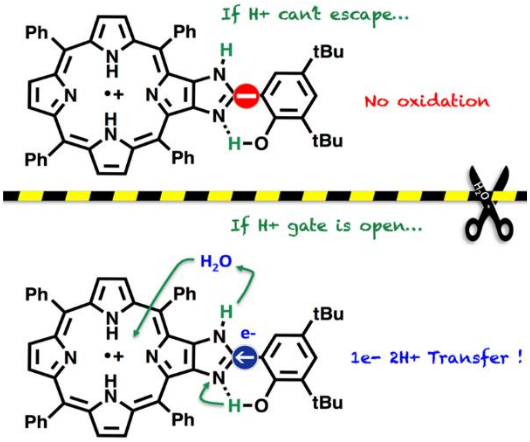

Fig. 3-8 Biomimetic model of the **P_{680}-Tyr_{161}-His_{190}** sequence in **PSII** showing the crucial role of H_2O to unlock the oxidation of the phenol group in a concentrated **E2PT** process.

3.2 Objectives and Scope

Taking leverage of the same fused-imidazole porphyrin framework, this chapter aims to investigate its manganese derivative (**MnPPhOH**) as a potential H_2O activation and oxidation catalyst (Scheme 3-3). Based on our previous findings concerning its free analog we would like to examine whether, upon oxidation of **MnPPhOH** either chemically or/and from the activation of a bound water molecule, the oxidation power could be also held on the oxidized phenol moiety thus alleviating the metal center.

3.3 Synthetic approach and X-ray Crystallography Studies

MnPPhOH and reference compound, **MnPPh**, were obtained following the multi-step synthetic approach illustrated in Scheme 3-3. In particular, selective mono-nitration of one of four pyrrole units of tetraphenyl copper porphyrin (**CuTPP**) afforded the **CuTPP-β-NO_2** derivative which was further demetallated to yield the free base analog, H_2TPP-β-NO_2. Subsequent reduction of the -NO_2 group gave the **H_2TPP-β-NH_2** intermediate compound which was further oxidized to **H_2TPP-Dione**. The diketone porphyrin was used as the starting complex for the synthesis of **H_2PPh** and **H_2PPhOH** via a Debus-Radziszewski condensation reaction with 3,5-Di-tert-butylbenzaldehyde and 3,5-Di-tert-butyl-2-hydroxybenzaldehyde, respectively. In the next and final step, metallation of **H_2PPh** and **H_2PPhOH** with a manganese salt afforded the final **MnPPh** and **MnPPhOH** compounds. The experimental details and the characterization of the synthesized intermediates and final products are gathered in Annex III at the end of Chapter 3.

---

[39] Charalambidis, Das, S., Trapali, A., Quaranta, A., Orio, M. *et al.*, *Angew. Chemie – Int. Ed.*, **2018**, 57, 29, 9013-9017, DOI: 10.1002/anie.201804498

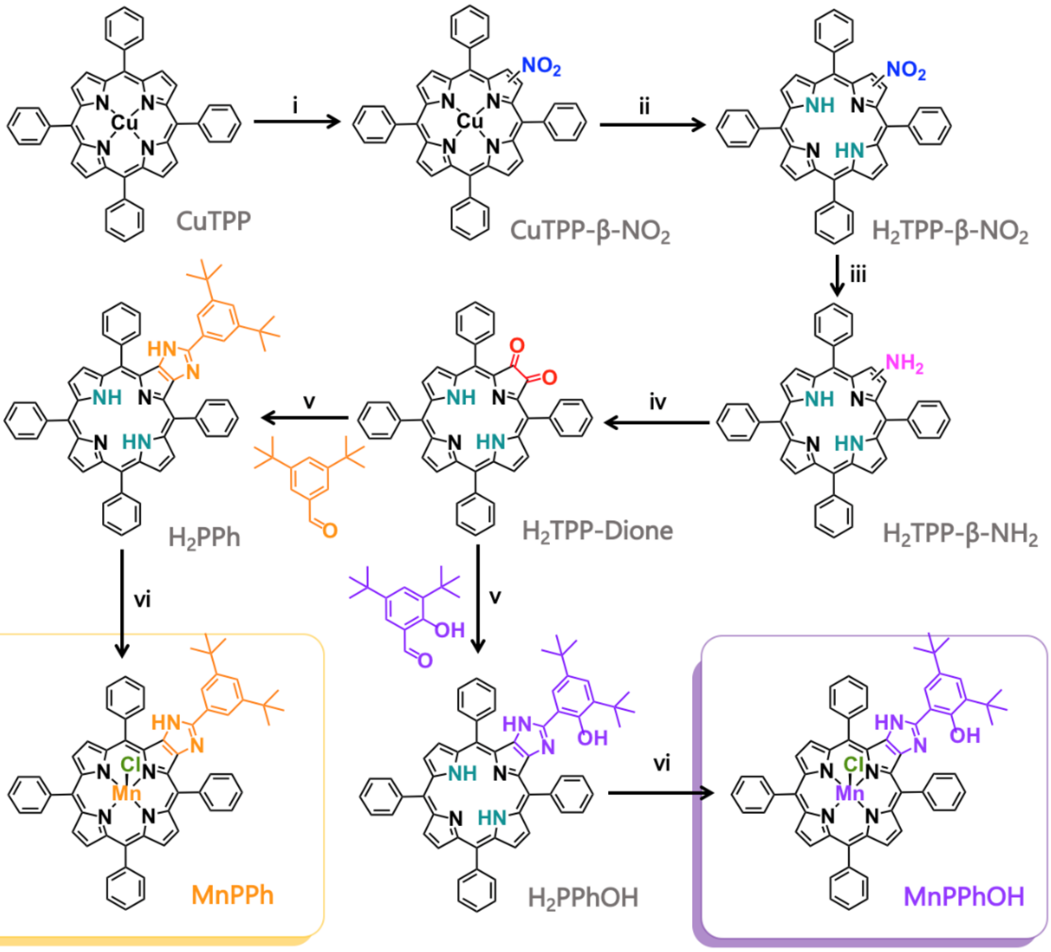

Scheme 3-3 General experimental approach for the synthesis of the **MnPPh** and **MnPPhOH** manganese porphyrins. Experimental conditions: i) NO_2 (g), CH_2Cl_2 , RT; ii) CH_2Cl_2, c. H_2SO_4, RT, 8 min; iii) CH_2Cl_2, c. HCl; iv) CH_2Cl_2, SiO_2, O_2, *hv*, RT; v) $CHCl_3$, CH_3COOH, NH_4OAc, 100 °C, 3-4 h; vi) $MnCl_2 \cdot 4H_2O$, THF/MeOH, DIPEA, reflux, 15 h.

MnPPh and **MnPPhOH** were also structurally characterized via X-ray diffraction studies. Needle-shaped crystals of **MnPPh** and **MnPPhOH** porphyrins suitable for diffraction were attained by slow evaporation of their corresponding saturated ACN solutions at room temperature and 5°C, respectively. X-ray analysis of the two obtained structures revealed that the manganese-porphyrin-imidazole and the phenyl in **MnPPh**, or phenol moiety in **MnPPhOH**, were coplanar. More importantly, in **MnPPhOH** the -OH group was found hydrogen-bonded to the imidazole unit with an N---H distance of 1.850 Å, as illustrated in Fig. 3-9.

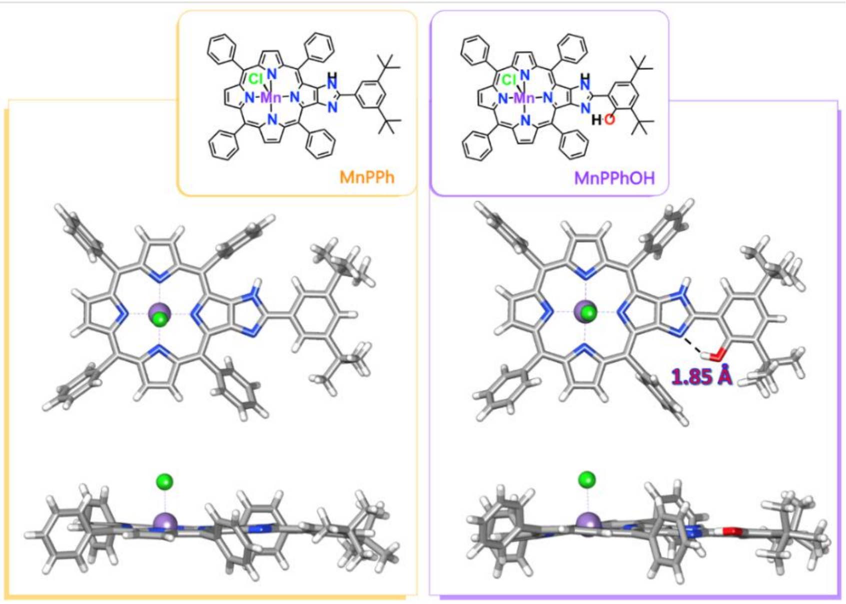

Fig. 3-9 Capped sticks representation of the X-ray crystal structures of **MnPPh** (left) and **MnPPhOH** (right).

3.4 Electrochemical Characterization in the absence of H_2O

Moving forward with the characterization of the two manganese porphyrins, the redox properties of **MnPPhOH** and **MnPPh** were studied via cyclic voltammetry and were compared to the parent **MnTPP** complex. The cyclic voltammogram (CV) of the non-modified **MnTPP** exhibited three quasi-reversible redox waves at -0.23, -1.45, and -1.77 V *vs*. SCE, which were assigned to the $Mn^{III/II}$, $Mn^{II}P$/ $Mn^{II}P^{\bullet-}$, and $Mn^{II}P^{\bullet-}$/ $Mn^{II}P^{2-}$ couples, respectively, where P stands for the porphyrin macrocycle[40], [41], [42]. **MnPPhOH** and **MnPPh** displayed similar one-electron reduction processes; yet, they appeared at more positive potentials, as shown in Fig. 3-10.

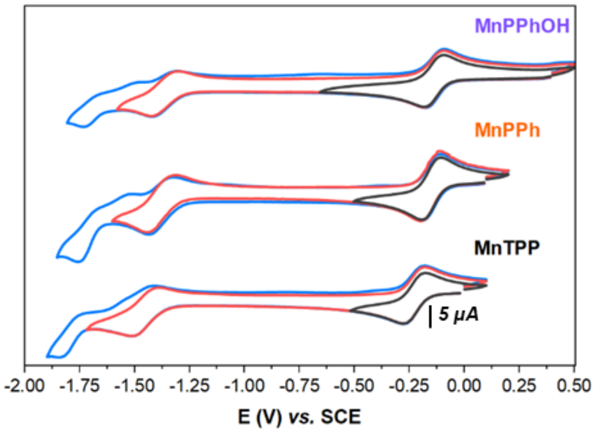

Fig. 3-7 CVs of 0.5 mM of **MnPPhOH**, **MnPPh**, and parent **MnTPP** recorded under Ar atmosphere in an ACN/$TBAPF_6$ 0.1 M solution at a scan rate of 100 mV/s

Within the positive potential limit of the solvent, the CV of **MnTPP** showed two quasi-reversible anodic waves at $E_{1/2}$ = 1.20 V and 1.55 V *vs.* SCE, corresponding to the two consecutive one-electron oxidations of the porphyrin ligand to yield $Mn^{III}P^{\bullet+}$ and $Mn^{III}P^{2+}$,

---

[40] Giraudeau, A., Callot, H.J., Jordan, J., Ezhar, I., Gross, M., *J. Am. Chem. Soc.*, **1979**, 101, 14, 3857–3862, DOI: 10.1021/ja00508a024
[41] Kelly, S.L., Kadish, K.M., *Inorg. Chem.*, **1982**, 21, 10, 3631–3639, DOI: 10.1021/ic00140a010
[42] Boucher, L.J., Garber, H.K., *Inorg. Chem.*, **1970**, 9, 12, 2644–2649, DOI: 10.1021/ic50094a004

respectively [41], [43]. For **MnPPh**, the Mn^{III}/ $Mn^{III}P^{\bullet +}$ and $Mn^{III}P^{\bullet +}$/ $Mn^{III}P^{2+}$ redox couples were shifted to more anodic potentials, viz., $E_{1/2}$ = 1.41 V and 1.69 V *vs.* SCE, respectively. On the other hand, for **MnPPhOH**, the Mn^{III}/ $Mn^{III}P^{\bullet +}$ oxidation process took place at a less positive potential compared to **MnTPP** and **MnPPh** (1.31 V *vs.* SCE), while the $Mn^{III}P^{\bullet +}$/ $Mn^{III}P^{2+}$ redox couple was found at 1.53 V *vs.* SCE; a half-wave potential close to the one obtained with **MnTPP** for the same oxidation process. Moreover, in the case of **MnPPhOH**, an additional anodic wave with an $E_{1/2}$= 1.05 V *vs.* SCE was observed, which was absent for **MnPPh** and **MnTPP** (Fig. 3-11).

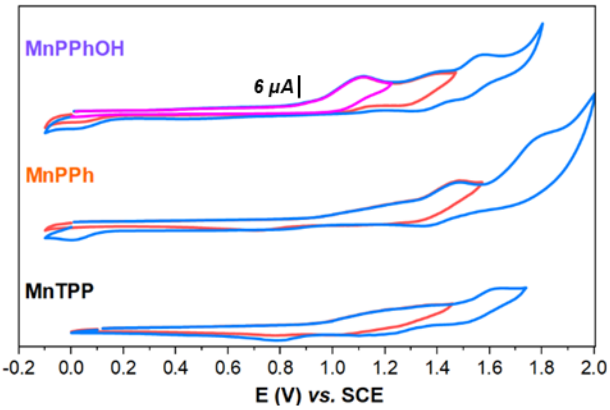

Fig. 3-8 CVs of 0.5 mM of **MnPPhOH**, **MnPPh**, and parent **MnTPP** recorded under Ar atmosphere in an ACN/$TBAPF_6$ 0.1 M solution at a scan rate of 100 mV/s.

Based on our previous electrochemical findings on the non-metallated H_2PPhOH porphyrin, a similar anodic wave was detected at 0.98 V *vs.* SCE, and it was attributed to the reversible one-electron oxidation of the macrocycle ring followed by the oxidation of the phenol group (PhOH) accompanied by a proton transfer (PT) to the imidazole unit to yield the corresponding hydrogen bonded phenoxyl radical (imi-H^+-- $PhO^\bullet$) [39]. Potential coulometric studies for **MnPPhOH** revealed that the oxidation at $E_{1/2}$= 1.05 V *vs.* SCE involved only one electron. Hence the anodic wave at 1.05 V *vs.* SCE could be also ascribed to the MnPPhOH/ $MnPPhO^\bullet$ redox couple, as has been also reported for 2-(3′,5′-di-tert-butyl-2′-hydroxyphenyl)benzimidazole (BIP) and other metalloporphyrins fused with an imidazole-phenol moiety.[44] Yet, in our case, the **MnPPhOH/ $MnPPhO^\bullet$** redox couple was irreversible compared to the **H_2PPhOH/ $H_2PPhO^\bullet$**. Irreversible oxidation of PhOH is well-established for 2-(3′,5′-di-tert-butyl-4′-hydroxyphenyl)benzimidazole compounds, in which the -OH group is not hydrogen-bonded to the imidazole unit and it has been shown to take place at a less positive potential (E_a = ~0.8-0.9 V *vs.* SCE) than the hydrogen-bonded analogs.[44][45]However, with **MnPPhOH** such a scenario was unlikely since X-ray analysis in the solid state revealed a strong hydrogen bond interaction between the PhOH and the imidazole ring. Therefore, we can attribute in the first place that the irreversibility is rather related to a slow reduction of the electrogenerated $MnPPhO^\bullet$ species.

---

[43] Fukuzumi, S., Mizuno, T., Ojiri, T., *Chem. Eur. J.*, **2012**, 18, 15794 – 15804, DOI: 10.1002/chem.201202041

[44] Moore, G.F., Hambourger, M., Gervaldo, M., Poluektov, O.G., Rajh, T. *et al.*, *J. Am. Chem. Soc.*, **2008**, 130, 32, 10466–10467, DOI: 10.1021/ja803015m

[45] Orio, M., Jarjayes, O., Baptiste, B., Philouze, C., Duboc, C. *et al.*, *Eur., J., Chem.*, **2012**, 18, 17, 5416-5429, DOI : 10.1002/chem.201102854

3.5 Spectroelectrochemical Studies

To further characterize the species formed upon oxidation of the **MnPPhOH** species, we performed a series of spectroelectrochemical studies and followed the evolution of the UV-Vis spectrum upon electrolysis at ~ 1.0 V *vs*. SCE, at which we suspect that the one-electron oxidation of the phenol group occurs. Before electrolysis, the UV-Vis spectrum of **MnPPhOH** in extra dry ACN and under anaerobic conditions displayed a set of Soret bands at 379 nm and 478 nm, and Q bands at 577 nm and 623 nm, as depicted in Fig. 3-12 (**blue** trace). Such UV-Vis features are quite unique compared to other metalloporphyrin compounds and are indicative of chloro-porphyrinato Mn^{III} complexes [46]. Upon electrolysis at 1.0 V *vs*. SCE, noticeable changes were observed both in the Soret and Q bands regions, suggesting the formation of new species (Fig. 3-12, red trace). In particular, the absorption of the Soret peaks substantially decreased, while a new band with strong absorption at 390 nm was attained. The two Q bands, on the other hand, shifted from 577 nm to 567 nm and 623 nm to 609 nm. Moreover, a slight absorption between 700-900 nm was observed.

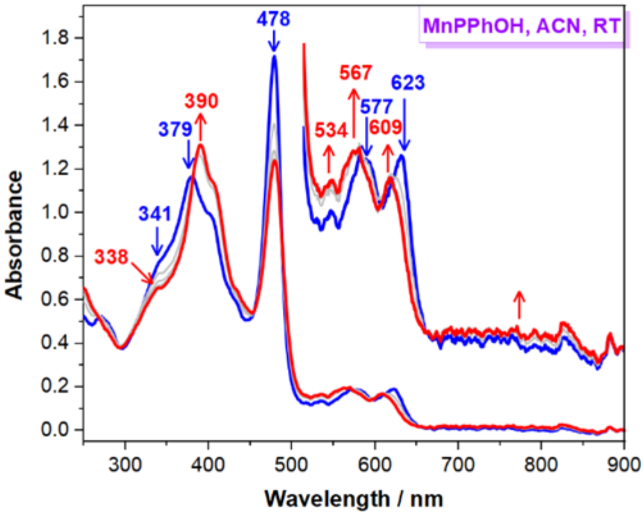

Fig. 3-12 Evolution of UV-Vis spectra of **MnPPhOH** upon electrolysis at 1.0 V in dry and deaerated ACN/TBAPF$_6$ 0.1 M solution.

It has been reported that benzimidazole-phenoxyl radicals, **PhO**$^{\bullet}$ and **PhOH**$^{\bullet+}$, absorb at 350-480 nm and 790-910 nm.[45] However, because of the strong absorption of the **MnPPhOH** Soret bands, we could not attribute any of the observed UV-Vis changes to the formation of a possible **MnPPhO**$^{\bullet}$ or **MnPPhOH**$^{\bullet+}$ species. In addition, due to the low concentration of the electrolyzed solution, it was also hard to follow the absorption changes between the 700-900 nm region, at which benzimidazole-PhO$^{\bullet}$ and PhOH$^{\bullet+}$ species also absorb. Hence, to gain a more clear picture of the UV-Vis spectrum evolution at those wavelengths upon electrolysis, we repeated the experiment with a more concentrated solution of **MnPPhOH**. As shown in Fig. 3-13 below, the Q band region evolved similarly to that of the previously investigated less concentrated solution. Interestingly, additional distinguishable UV-Vis features were detected at approximately 710 nm, 790 nm, and 833 nm which might indicate that upon electrolysis at 1.0V we form a **MnPPhO**$^{\bullet}$ species.

---

[46] Boucher, L.J., *J. Am. Chem. Soc.*, **1970**, 92, 9, 2725–2730, DOI: 10.1021/ja00712a024

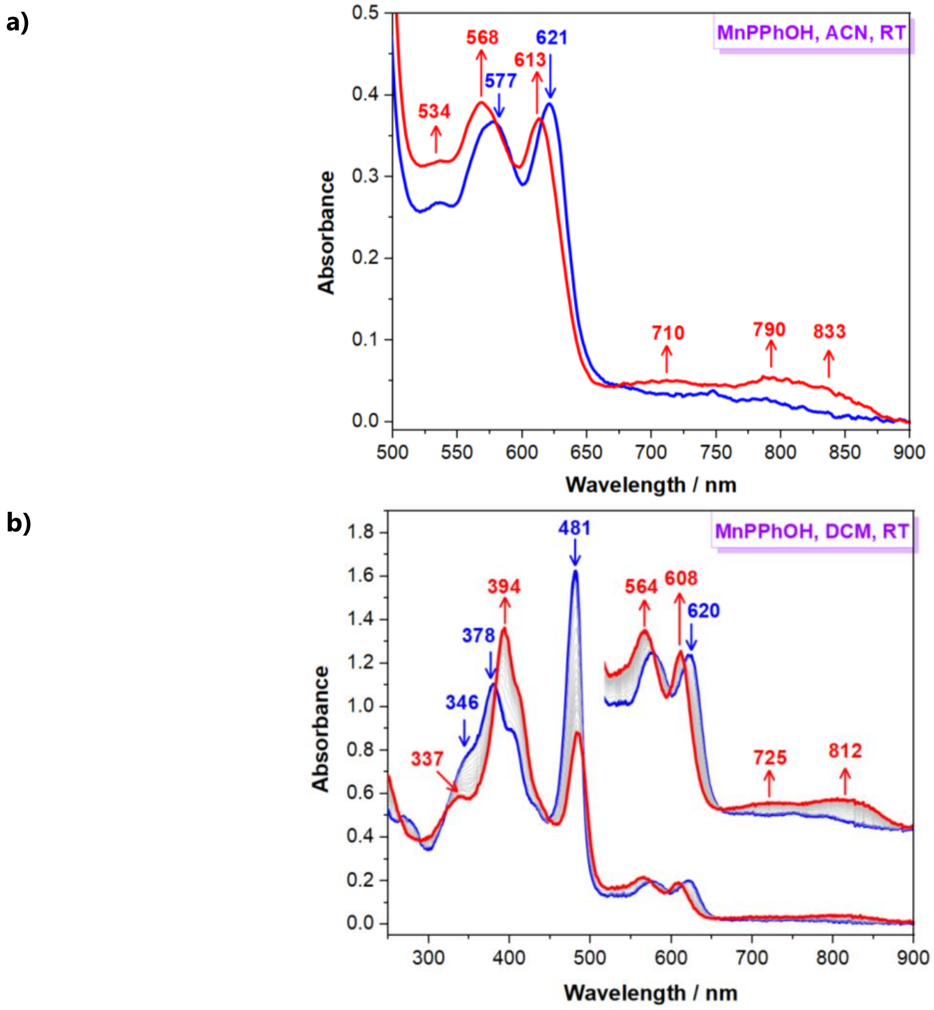

Fig. 3-13 a) UV-Vis spectra changes in the Q region of **MnPPhOH** before (blue trace) and during electrolysis (red trace) at 1.0 V *vs.* SCE in dry and deaerated ACN/TBAPF$_6$ 0.1 M solution; b) evolution of the UV-Vis spectrum of MnPPhOH upon electrolysis at 1.0V *vs.* SCE in dry and anaerobicDCM/TBAPF$_6$ 0.1 M solution

Similar changes were also observed when the electrolysis was realized in CH$_2$Cl$_2$ (DCM) (Fig. 3-13b. The generation of an organic radical upon electrolysis at 1.0 V *vs.* SCE was further corroborated by EPR spectroscopy studies. The X-band EPR spectra of the oxidized **MnPPhOH** solution at 1.0 V *vs.* SCE showed an isotropic signal with a *g* tensor value of 2.005 (Fig. 3-14), indicative of an organic radical species, in which the unpaired electron can be delocalized on a carbon or oxygen atom. In other words, it could correspond to a porphyrin π-cationic radical ($P^{\bullet +}$) [47], [48],[49],[50] or a phenoxyl, ($PhO^{\bullet}$ [51],[45], $PhOH^{\bullet +}$ [45]) radical. Moreover, the EPR spectra of the electrogenerated $H_2PPhO^{\bullet}$ species exhibited a *g*= 2.0056 which is in good accordance with the value obtained for the electrolyzed solution of **MnPPhOH**. As such, we could assume that upon electrolysis at 1.0 V *vs.* SCE, **MnPPhOH** is singly-oxidized to **MnPPhO$^{\bullet}$**. However, under

---

[47] Gasyna, Z., Browett, W.R., Stillman, M.J., *Inorg. Chem.*, **1984**, 23, 3, 382–384, DOI: 10.1021/ic00171a024

[48] Spreer, L.O., Maliyackel, A.C., Holbrook, S., Otvos, J.W., Calvin, M., *J. Am. Chem. Soc.*, **1986**, 108, 8, 1949–1953, DOI: 10.1021/ja00268a037

[49] Méndez-Hernández, D.D., Baldansuren, A., Kalendra, V., Charles, P., Mark, B. *et al.*, *iScience*, **2020**, 23, 8, 101366, DOI: 10.1016/j.isci.2020.101366

[50] Kaustov, L., Tal, M.E., Shames, A.I., Gross, Z., *Inorg. Chem.*, **1997**, 36, 16, 3503–3511, DOI: 10.1021/ic961207p

[51] Megiatto, J.D., Méndez-Hernández, D.D., Tejeda-Ferrari, M.E., Teillout, A.-L., Llansola-Portolés, M.J. *et al.*, *Nature Chem.*, **2014**, 6, 423–428, DOI: 10.1038/nchem.1862

the applied experimental conditions we could not draw any conclusions about whether these radical species could be possible coupled with the **Mn^{III}** center. DFT calculations will be helpful to investigate such a scenario. In addition, further EPR investigations for the oxidized **MnPPhOH** porphyrin as well as for the reference **MnPPh** are ongoing.

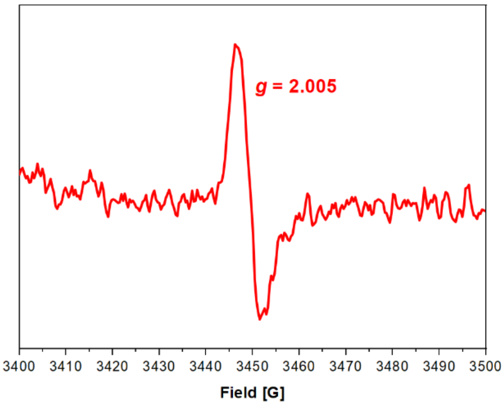

Fig. 3-14 X-band EPR spectra of **MnPPhOH** recorded upon electrolysis at 1.0 V *vs.* SCE at room temperature in a DCM/$TBAPF_6$ solution.

3.6 Electrochemical Characterization in the presence of H_2O or/and base

3.6.1 In the presence of H_2O

To investigate the oxidation of H_2O by **MnPPhOH** and **MnPPh**, their CVs were recorded in an ACN/H_2O (2M) solution under anaerobic conditions. The addition of H_2O resulted in major changes in their CVs. In particular, in the case of **MnPPhOH**, the putative **MnPPhOH/ $MnPPhO^{\bullet}$** redox couple shifted from $E_{1/2}$= 1.05 V to 0.93 V *vs.* SCE, while the one-electron oxidation of the macrocycle ring occurred more easily. Interestingly, an increase in the current intensity at the **$Mn^{III}P$/ $Mn^{III}P^{\bullet+}$** level was observed (Fig. 3-15). Similar behavior has also been reported by D' Eramo[52] and Ikeda[53] and it was attributed to the activation of H_2O by a water-soluble manganese porphyrin. The authors suggested that activation of H_2O afforded a **PMn^{IV}=O** intermediate that was further oxidized to the **PMn^{V}=O** species at approximately 1.3 V *vs.* SCE. In addition, both CVs of **MnPPhOH** and **MnPPh** exhibited a considerable enhancement of the current intensity at ~ 1.8 V *vs.* SCE, mightily suggesting further activation of H_2O by a **PMn^{V}=O** intermediate to yield H_2O_2 or/and O_2[54]. However, for our systems, further investigation is required before reaching any conclusions on such oxidation processes.

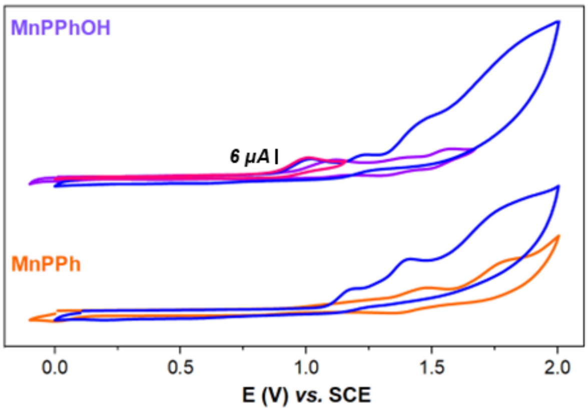

---

[52] Luna, M.A., Moyano, F., Sereno, L., D'Eramo, F., *Electrochim. Acta*, **2014**, 135, 301-310, DOI: 10.1016/j.electacta.2014.04.157
[53] Trofimova, N.S., Safronov, A.Y., Ikeda, O., *Electrochim. Acta*, **2005**, 50, 4637–4644, DOI: 10.1016/j.electacta.2005.02.014
[54] Naruta, Y., Sasayama, M., Sasaki, T., *Angew. Chem. Int. Ed.*, **1994**, 33, 18, 1839-1841, DOI: 10.1002/anie.199418391

Fig. 3-15 CVs of 0.5 mM of **MnPPhOH** and **MnPPh** recorded under Ar atmosphere in an ACN/TBAPF$_6$ 0.1 M solution at a scan rate of 100 mV/s in the absence (purple and orange line) and presence of 2M H_2O (blue line).

3.6.2 In the presence of H_2O and base

Addition of tetrabutylammonium hydroxide (TBAOH) to a **MnPPhOH** ACN/H_2O (2M) solution slightly shifted the **MnPPhOH/ MnPPhO$^{\bullet}$** redox couple to less positive potentials, while no significant changes were observed within 1.2 V-1.8 V, except a small enhancement of the current intensity at ~ 1.6 V. Moreover, a new anodic wave was observed with a peak current at 0.44 V *vs*. SCE, which was reversible ($E_{1/2}$= 0.4 V *vs.* SCE), as shown in Fig. 3-16. D' Eramo and co-workers have reported a similar CV response at ca. 0.5 V *vs*. SCE for a manganese porphyrin in alkaline aqueous solutions (pH=10). According to their studies, such an oxidation process was attributed to the adsorption of the **Mn^{III}P** at the surface of the glassy carbon electrode (GC) whose oxidation to their corresponding **PMn^{IV}=O** species was realized at substantially less positive potentials compared to the non-adsorbed Mn^{III}P [52]. At the same time, we also need to take into consideration that TBAOH may deprotonate the phenol group yielding a **MnPPhO^{-}** species, as suggested by Concepcion for a Ru^{II} complex bearing a phenanthroline imidazole-PhOH ligand. Electrochemical studies showed that the corresponding phenolate derivative was oxidized at considerably lower potentials, 0.23 V *vs*. SCE, compared to the phenol analog, 1.13 V *vs*. SCE.[55] On a similar note, Moore and co-workers have also proposed for a free base porphyrin appended with an imidazole-PhOH group in which the deprotonation of **PhOH** by TBAOH yielded **PPhO^{-}** in which the oxygen atom was hydrogen-bonded to the imidazole unit. The oxidation of these species was realized at 0.26 V *vs*. SCE and it was a reversible process.[56]

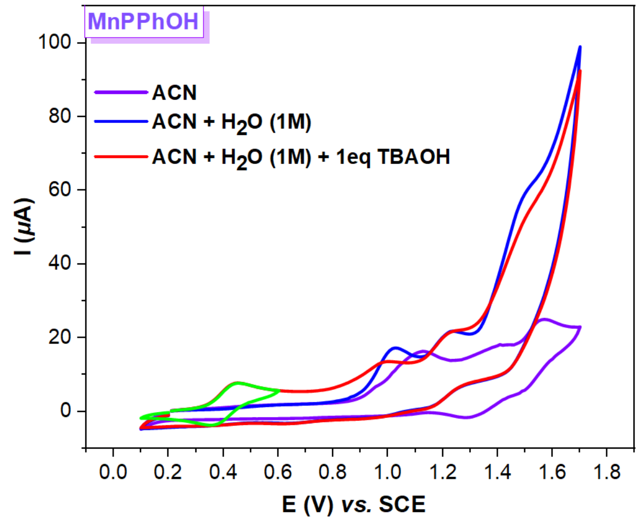

Fig. 3-16 CVs of 0.5 mM of **MnPPhOH** recorded under Ar atmosphere in an ACN/TBAPF$_6$ 0.1 M solution at a scan rate of 100 mV/s in the absence (purple line), presence of 2M H_2O (blue line) and presence of 2M H_2O + 0.5 mM of TBAOH.

---

[55] Manbeck, G.F., Fujita, E., Concepcion, J.J., *J. Am. Chem. Soc.*, **2016,** 138, 11536−11549, DOI: 10.1021/jacs.6b03506

[56] Moore, G.F., Hambourger, M.,Kodis, G., Michl, W., Gust, D. *et al.*, *J. Phys. Chem. B*, **2010**, 114, 14450–14457, DOI: 10.1021/jp101592m

3.7 Spectroscopic evidence of High-Valent Manganese-oxo species

3.7.1 UV-Vis Spectroscopy Studies

The generation of high-valent **Mn**-oxo species was realized by treatment of a **MnPPhOH** or **MnPPh** dry and deaerated ACN solution with oxidants, e.g., meta-Chloroperoxybenzoic acid (mCPBA) and iodosobenzene diacetate (PhI(OAc)$_2$). Attempts to oxidize **MnPPhOH** with iodosobenzene (PhIO) were unsuccessful due to its very low solubility in the investigated solutions. As shown in Fig. 3-17a., addition of mCBPA into the **MnPPhOH** ACN solution resulted in significant changes in the UV-Vis spectra at -35°C under Ar atmosphere, suggesting the formation of a new species. In particular, the absorption of the Soret band at 478 nm substantially decreased, while a maxima absorption was observed at 421 nm. At the same time, the Q bands located at 577 nm and 621 nm disappeared and shoulders were detected at 520 nm and 674 nm. Similar changes were also obtained when PhI(OAc)$_2$ was used as an oxidant at 25°C (Fig. 3-17b). These new UV-Vis absorption features fit well with other Mn^{IV}=O porphyrin derivatives reported in the literature.[57], [58] However, in our case we cannot exclude the possibility that we might as well generate the **Mn^{III}-O PPhO$^{\bullet}$** species since it is the tautomeric form of **Mn^{IV}=O PPhOH**.

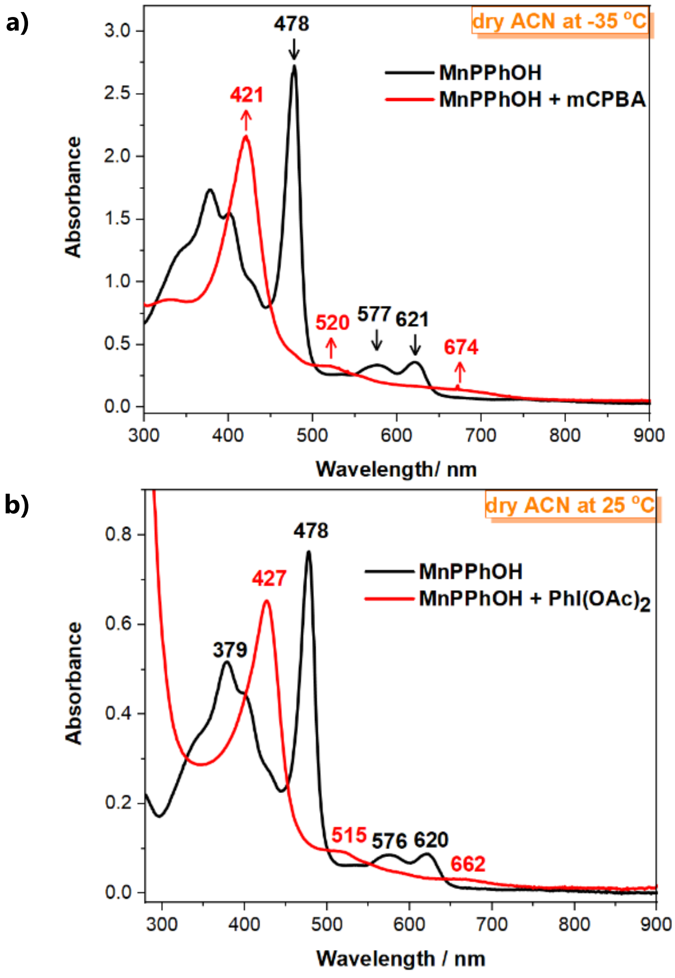

Fig. 3-17 UV-Vis evolution spectra upon addition a) of mCPBA (2 eq) in a **MnPPhOH** ACN solution at -35 °C; b) PhI(OAc)$_2$ (50 eq) in **MnPPhOH** ACN solution at 25 °C

---

[57] Groves, J.T., Stern, M.K., *J. Am. Chem. Soc.*, **1988**, 110, 26, 8628–8638, DOI: 10.1021/ja00234a009

[58] Liu, W., Groves, J.T., *Acc. Chem. Res.*, **2015**, 48, 6, 1727–1735, DOI: 10.1021/acs.accounts.5b00062

3.7.2 EPR Studies

Moving ahead with the characterization of the putative $Mn^{IV}=O$ of **MnPPhOH** formed upon oxidation with mCPBA, we generated the high-valent manganese-oxo species in situ in the EPR tube and recorded the EPR spectrum at 90 K. For comparison, **MnPPh** was also investigated as a reference. As shown in Fig. 3-18, the EPR spectrum of an oxidized **MnPPh** ACN solution displayed a weak signal with a tensor value of 3.81. Interestingly, for the oxidized **MnPPhOH** solution a strong isotropic signal with a *g* tensor value of 2.005 and a weak one with *g*= 3.81 were observed. For both manganese porphyrins, the signals with *g*= 3.81 might correspond to a Mn^{IV} metal center, suggesting that the oxidation of **MnPPhOH** and **MnPPh** with mCPBA produces a $Mn^{IV}=O$ intermediate. However, in the case of **MnPPhOH** the additional signal with *g*= 2.005 indicates the formation of an organic radical that can be either located on the porphyrin macrocycle ($Mn^{IV}=O\ P^{\bullet +}PhOH$) or on the oxidized PhOH moiety (($Mn^{IV}=O\ PPhO^{\bullet}$).

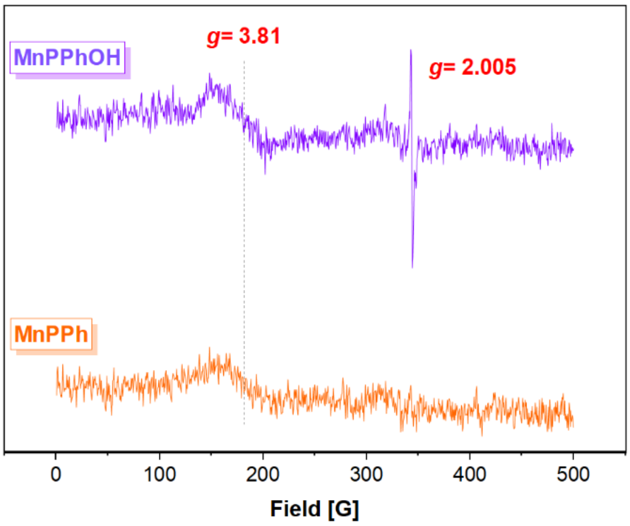

Fig. 3-15 X-band EPR spectra of an ACN solution of **MnPPhOH** (purple trace) and **MnPPh** (orange trace) in the presence of 5 eq of mCPBA recorded at 90 K.

3.7.3 Time-resolved UV-Vis spectroscopy

As discussed above, manganese (III) porphyrins exhibit high molar extinction coefficients in the visible region. However, their excited states are short-lived (~10^{-12} s)[59], and therefore their participation in biomolecular photo-redox reactions is suppressed. Hence, the activation of **MnPPhOH** and **MnTPP** was realized photochemically by the excitation of a ruthenium tris-bipyridine photosensitizer, denoted as **$[Ru(bpy)_3]^{+2}$** or **Ru^{II}**, at 460 nm, in the presence of an (ir)reversible electron acceptor (EA). In particular, diazonium sodium chloride (**Diaz**) and sodium persulfate (**Per**) were used as irreversible EAs, while methyl viologen (**MV^{+2}**) as a reversible EA. In all the experiments, the concentration of **MnPPhOH** and **MnTPP** was at 10 µM, while the concentration of **Ru^{II}** and **EA** was at 30 µM and 10-20 mM, respectively.

---

[59] Jung, J., Ohkubo, K., Goldberg, D.P., Fukuzumi, S., *J. Phys. Chem. A*, **2014**, 118, 6223−6229, DOI: 10.1021/jp505860f

3.7.3.1 Photochemical Oxidation (Oxidative Pathway)

In presence of an irreversible electron acceptor: a diazonium salt (**Diaz**) or persulfate salt (**Per**)

Under 1 atm of Ar and in the presence of **Diaz**, excitation of **Ru^{II}** at 463 nm with light led to the formation of the oxidized ruthenium complex, **Ru^{III}**. **Ru^{III}** subsequently oxidized **MnPPhOH** and gave rise to a new species that exhibited a strong absorbance at 427 nm, while the characteristic Soret band of **MnPPhOH** at 480 nm disappeared (Fig. 3-19a). Interestingly, this difference-absorption spectrum was almost identical to the one obtained upon chemical oxidation of **MnPPhOH** with (PhIOAc)$_2$ (Fig. 3-19b). Hence, it can be suggested that a Mn^{IV}=O species is also generated under the investigated conditions, probably due to the activation of a bound H_2O molecule on the **MnPPhOH** porphyrin.

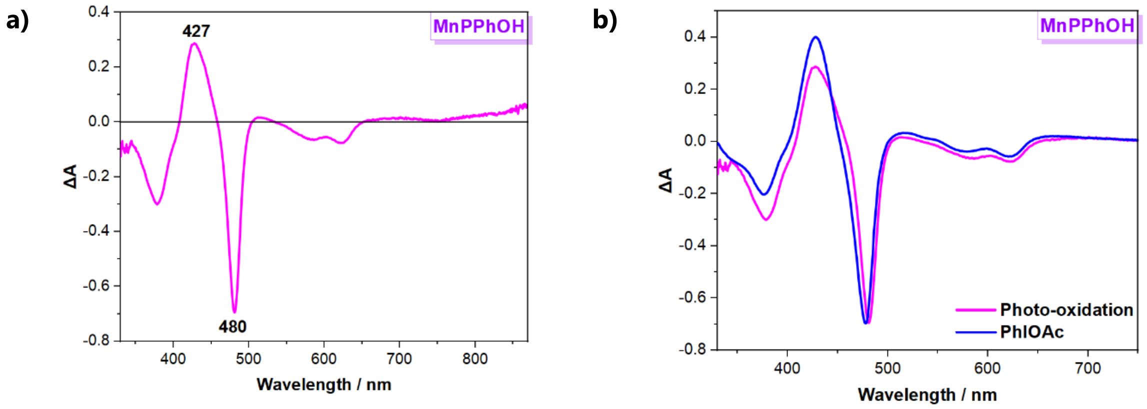

Fig. 3-19 a) Absorption changes induced by irradiation of a **MnPPhOH** ACN/H_2O 2% solution at pH =8 containing **Ru^{II}** and **Diaz** as irreversible EA; b) Comparison of the difference spectra obtained by chemical oxidation of **MnPPhOH** with PhI(OAc)$_2$ and by irradiation in presence of diazonium as irreversible EA.

Similar absorption changes were obtained when the **MnPPhOH**/ **Ru^{II}** solution was excited with a laser pulse at 460 nm in the presence of **Per** at pH=4, suggesting once again the formation of a Mn^{IV}=O intermediate (Fig. 3-20a). The addition of an excess of a water-soluble substrate as styrene sulfonate increased the stability of the laser-flash induced formation of the Mn^{IV}=O species, as shown in Fig. 3-20b. The fact that the transient absorption spectra did not change indicated that **Mn^{III}PPhOH** was regenerated between the successive flashes, presumably by oxidation of the substrate from the Mn^{IV}=O species, and subsequently activated again by **Ru^{III}**. This finds further support from the faster kinetics of the flash-induced Mn^{IV}=O intermediate formation in the presence of styrene sulfonate (Fig. 3-20c).

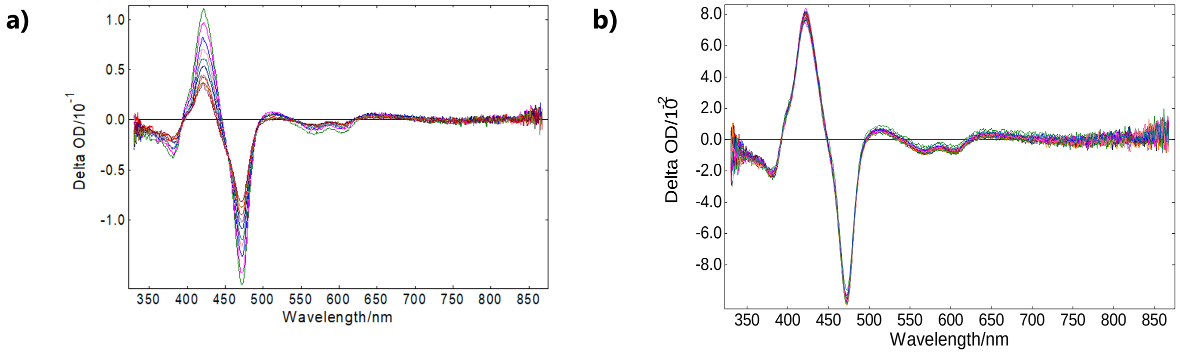

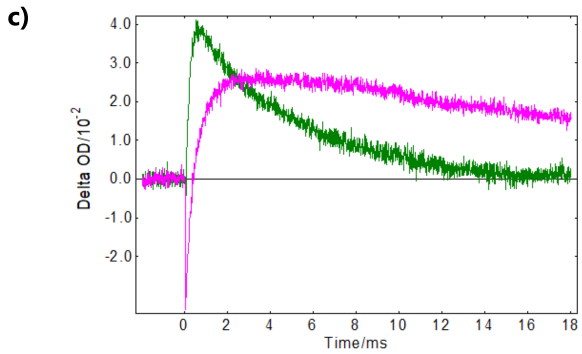

Fig. 3-20 Flash-induced difference spectra recorded 1 ms after the flash a) in a series of 10 successive laser flashes (spaced by 2 s) leading to progressive loss of signal due to the depletion of **Mn^{III}PPhOH** species and accumulation of **Mn^{IV}=O** at 427 nm in the absence of styrene sulfonate; b) in a series of 20 successive laser flashes (spaced by 2 s) in the presence of 25 mM styrene sulfonate; c) transient absorption kinetics at 422 nm with **MnPPhOH** at pH=4 in the absence (magenta) and presence (green) of 25 mM styrene sulfonate.

The non-functionalized **MnTPP** was also investigated under identical conditions. Like in the case of **MnPPhOH**, excitation of a **MnTPP** ACN/ H_2O solution at pH=4 containing **Ru^{III}** and **Per** as an irreversible EA resulted in the formation of the corresponding transient Mn^{IV}=O species that was able to oxygenate styrene sulfonate and displayed a broad absorption band at ~ 420 nm (Fig. 3-21a).[60] (Anything about the kinetics?) On the other hand, in the absence of a manganese porphyrin, **Ru^{III}** was formed upon successive laser flashes via the oxidative quenching of its triplet excited state by **Per**. **Ru^{III}** was able to realize the oxidation of styrene sulfonate through an intermolecular electron transfer process to form an alkenyl radical cation[61], [62]. However, the formation of **Ru^{III}** was not that reversible compared to that of the Mn^{IV}=O species for **MnPPhOH** and **MnTPP** (Fig. 3-21b).

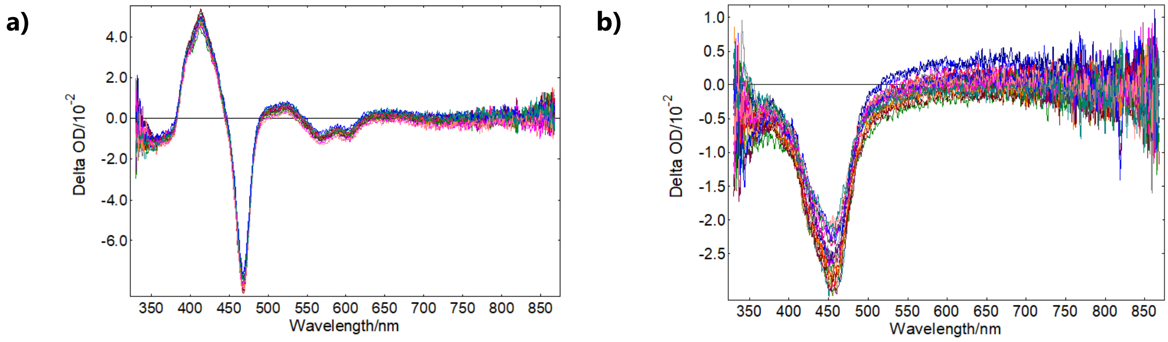

Fig. 3-21 Flash-induced difference spectra recorded 1 ms after the flash Flash-induced difference spectra recorded 1 ms after the flash in a series of 20 successive laser flashes (spaced by 2 s) in the presence of styrene sulfonate a) in the presence of **MnTPP**; b) in the absence of a manganese porphyrin.

The catalytic activity of **MnPPhOH** and **MnTPP** towards styrene sulfonate oxidation was also studied at pH=8 with **Per** as irreversible EA. Laser flash photolysis experiments revealed that only **MnPPhOH** was able to realize the oxygen atom transfer to the substrate via the photochemically-generated Mn^{IV}=O intermediate (Fig. 3-22).

---

[60] Zhang, R., Horner, J.H., Newcomb, M., *J. Am. Chem. Soc.*, **2005**, 127, 18, 6573–6582, DOI: 10.1021/ja045042s

[61] Ischay, M.A., Lu, Z., Yoon, T.P., *J. Am. Chem. Soc.*, **2010**, 132, 25, 8572–8574, DOI: 10.1021/ja103934y

[62] Vo, N.T., Mekmouche, Y., Tron, T., Guillot, R., Banse, F. *et al.*, *Angew. Chem. Int. Ed.*, **2019**, 58, 45, 16023-16027, DOI: 10.1002/anie.201907337

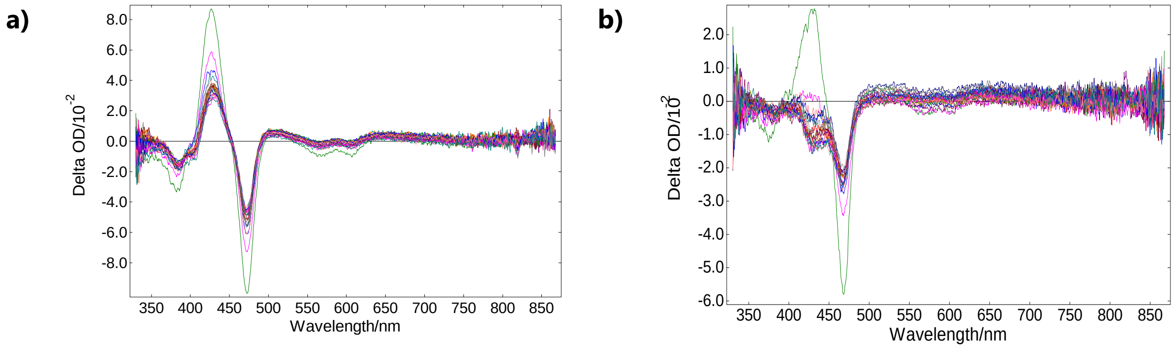

Fig. 3-22 Flash-induced difference spectra recorded 1 ms after the flash in a series of 20 successive laser flashes (spaced by 2 s) at pH 8 in presence of 25 mM styrene a) **MnPPhOH**; b) **MnTPP**.

However, the activity of **MnPPhOH** was lower compared to that observed in acidic media This might be ascribed to the deprotonation of the imidazole group at pH=8. Indeed, a [(Mn^{IV}=O)(PPhO$^{\bullet}$)] species might not be oxidizing enough to activate the C=C double bond of styrene sulfonate. Hence, these findings might suggest that at pH=4 a putative transient [(Mn^{IV}=O)(PPhOH$^{\bullet +}$)]could be possibly involved in the oxidation of the substrate.

3.7.3.2 Photochemical Reduction (Reductive Pathway)

Reversible Electron acceptor: MV^{2+}

Replacement of the EA, **Diaz**, or **Per** with a reversible EA e.g., **MV^{2+}**, resulted in a different photochemical pathway. When a **MnPPhOH/Ru^{II}** ACN/ H_2O (1:1) solution at pH=4 containing **MV^{2+}**, was excited with a flash-pulse, a concomitant depletion of the **MnPPhOH** Soret band at 479 nm and the appearance of a maximum absorption at 436 nm were observed. Such changes were attributed to the reduction of **MnPPhOH** to its **Mn^{II}** state via the singly reduced EA (Fig. 3-23a)[63], 64. Interestingly, the photoexcitation of the same solution in the presence of air led to a different transient absorption spectrum which fits well with the one obtained under anaerobic conditions at pH=4 and in the presence of **Diaz** or **Per**, as shown in Fig. 3-23b-c, suggesting the formation of a Mn^{IV}=O species. In aerated ACN/ H_2O acidic solutions, the **MV$^{\bullet +}$** formed by the reduction of **MV^{2+}** by the excited triplet state of **Ru^{II}**, **[Ru^{II}]***, can rapidly reduce molecular O_2 to give a hydroperoxyl radical $^{\bullet}$OOH (p*K*a ($^{\bullet}$OOH/ $O_2^{\bullet -}$)= 4.7). [65] Hence, it is possible that **Mn^{II}** can interact with $^{\bullet}$OOH to form finally an Mn^{IV}=O intermediate.

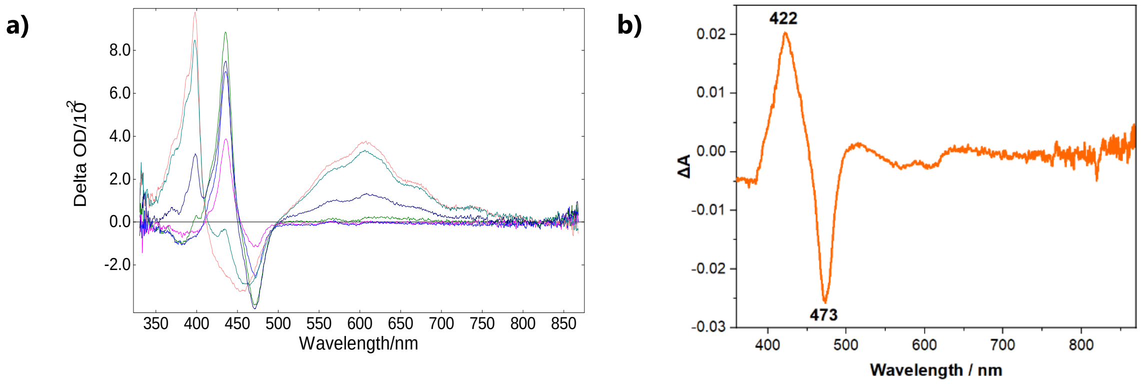

---

[63] Klaine, S., Bratcher, F., Winchester, C.M., Zhang, R., *J. Inorg. Biochem.*, **2020**, 204, 110986, DOI: 10.1016/j.jinorgbio.2019.110986

[64] Hoshino, M., Nagashima, Y., Seki, H., *Inorg. Chem.*, **1998**, 37, 2464-2469, DOI: 10.1021/ic971517n

[65] Sawyer, D.T., Valentine, J.S., *Acc. Chem. Res.*, **1981**, 14, 12, 393–400, DOI: 10.1021/ar00072a005

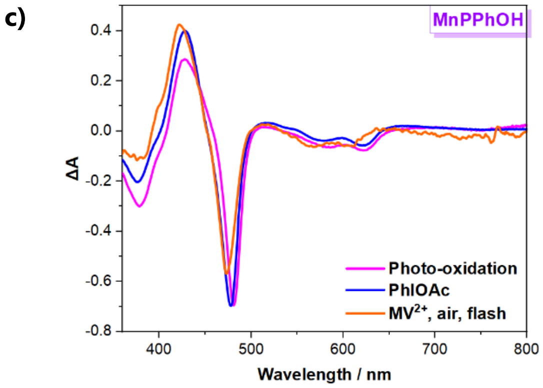

Fig. 3-23 Time evolution of flash-induced absorption difference spectra in a) an anaerobic; b) an aerobic ACN/H_2O solution of **MnPPhOH** at pH=4; c) Comparison of the flash-induced absorption difference (3 ms after flash) (x30) with difference spectra obtained by (photo)chemical oxidation.

Like in the case of the oxidative pathway described previously, the addition of styrene sulfonate made the system more stable, and thus we were able to investigate more deeply the photochemical processes taking place upon photoexcitation of the **MnPPhOH** aerated solution. As shown in Fig. 3-24a, 10 µs after excitation with the flash, the absorption at 436 nm indicated the formation of **Mn^{II}** by the reduction of **Mn^{III}** from the photochemically reduced EA, **MV$^{\bullet+}$**, followed by the oxidation of **Mn^{II}** to **Mn^{IV}=O** indicated by the appearance of an absorption band at ~ 425 nm. Upon successive flashes, the transient spectra did not change, suggesting that between the laser flashes **Mn^{III}PPhOH** is regenerated via the oxidation of styrene sulfonate by **Mn^{IV}=O**, as was proposed for the oxidative pathway (Fig. 3-24b). Saturation of the solution with O_2 seems to have no effect on the kinetics of **Mn^{IV}=O**, further supporting that the hydroperoxyl radical is interacting with **Mn^{II}** (Fig. 3-24c).

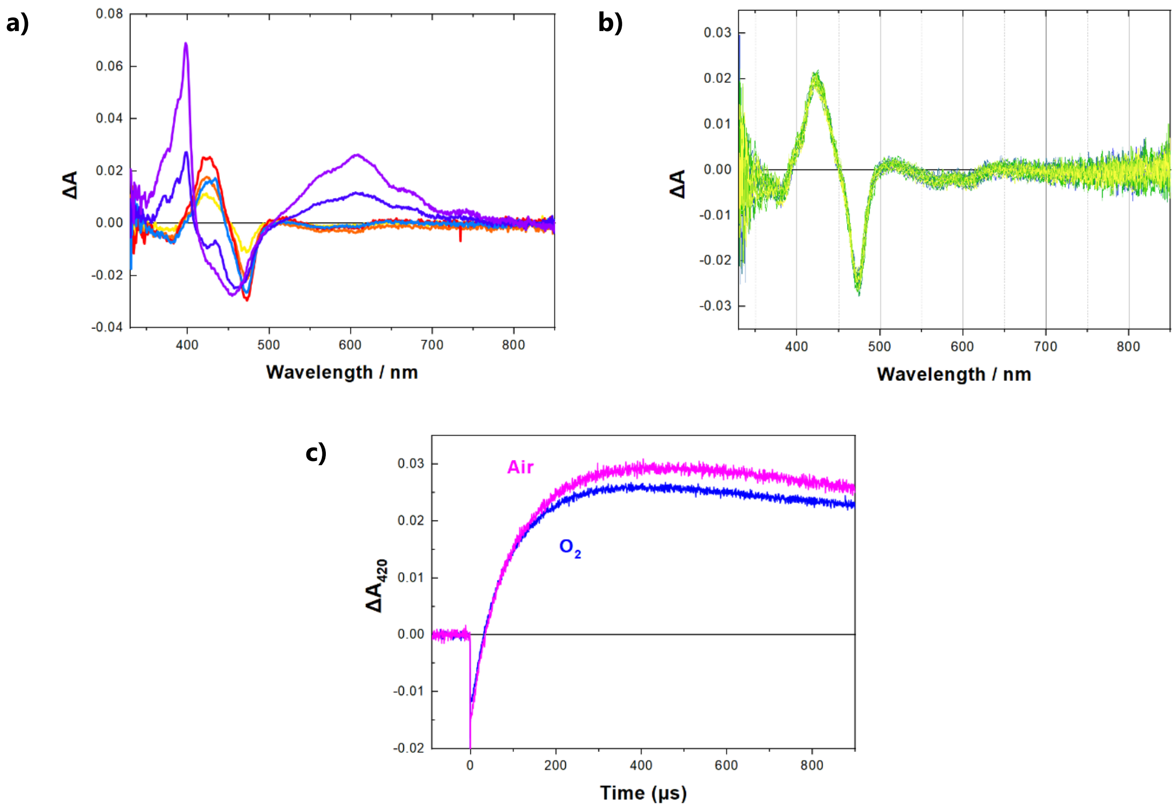

Fig. 3-24 a) Time evolution of flash-induced absorption difference spectra of an aerobic **MnPPhOH**; b) Flash-induced difference spectra recorded 1 ms after the flash in a series of 20 successive laser flashes (spaced by 2 s) in the presence of $MV^{2+}$and 50 mM in an air-equilibrated ACN/H_2O (1:1) solution at pH=4; c) Comparison of the transient absorption kinetics at 420 nm of **MnPPhOH** ACN/H_2O (1:1) solution at pH=4 in presence of $MV^{2+}$and 50 mM of styrene sulfonate in air (magenta trace) and in O_2 saturated (blue trace) solution.

3.8 Conclusions and Perspectives

In conclusion, we successfully synthesized a manganese fused-imidazole-phenol porphyrin (**MnPPhOH**) in an effort to mimic the **Tyr_{161}/ His_{190}** pair in **OEC**. X-ray analysis of suitable **MnPPhOH** crystals for diffraction revealed that the phenol group was coplanar with regard to the manganese fused-imidazole-porphyrin, while the phenolic proton was engaged in a strong hydrogen-bond with the imidazole unit exhibiting an N---H distance of 1.850 Å.

The electrochemical properties of **MnPPhOH** were investigated by cyclic voltammetry in a dry ACN solution and were compared with the reference **MnPPh** and non-functionalized **MnTPP** porphyrins. The CVs of **MnPPhOH** showed two anodic waves at 1.31 V *vs.* SCE and 1.53 V *vs.* SCE which were attributed to the successive one-electron oxidations of the macrocycle ring, *viz.* **Mn^{III}/ $Mn^{III}P^{\bullet+}$** and **$Mn^{III}P^{\bullet+}$/ $Mn^{III}P^{2+}$** redox couples. More importantly, the CV of **MnPPhOH** displayed an additional anodic wave at 1.05 V *vs.* SCE which was absent for **MnPPh** and **MnTPP**. Such an oxidation process was attributed to the one-electron oxidation of the phenol moiety accompanied by an intramolecular proton transfer to the imidazole unit to form a phenoxyl radical species (**$MnPPhO^{\bullet}$**). The generation of such species was further supported by spectroelectrochemical studies upon electrolysis at 1.0 V *vs.* SCE coupled with EPR spectroscopy. Addition of H_2O (2M) to the electrolytic solution of **MnPPhOH** and **MnPPh** resulted in an enhancement of the anodic wave at the level of the **$Mn^{III}P$/ $Mn^{III}P^{\bullet+}$** redox couple which might suggest the activation of a bound H_2O molecule to give high-valent **Mn-oxo** species that can further oxidize H_2O at approximately 1.8 V *vs.* SCE where also a considerable increase of the current intensity was observed.

To gain better insights into the formation of **Mn-oxo** species we performed a series of spectroscopic studies in which the high-valent **Mn-oxo** were generated this time chemically by the addition of a strong oxidant in an ACN solution. Oxidation of **MnPPhOH** resulted in major changes in its UV-Vis footprints with absorption features that fit well with **Mn^{IV}=O** porphyrins reported in the literature. However, due to the presence of the phenol group we couldn't exclude the possibility that we might also form the tautomeric **Mn^{III}-O $PPhO^{\bullet}$** species. To investigate such a scenario, we also characterized the oxidized **MnPPhOH** species via EPR spectroscopy. The oxidized **MnPPh** derivative was also studied as a reference. The EPR spectra of **MnPPhOH** and **MnPPh** in the presence of mCPBA exhibited a tensor value of 3.81 which might correspond to **Mn^{IV}** metal center. Interestingly, in the case of **MnPPhOH** an additional signal with g=2.005 was also observed suggesting the formation of an organic radical that can be either located on the porphyrin macrocycle (**Mn^{IV}=O $P^{\bullet+}$PhOH**) or on the oxidized PhOH moiety (**Mn^{IV}=O $PPhO^{\bullet}$**). EPR simulations would be helpful to interpret the obtained EPR spectra for the oxidized **MnPPhOH**.

The generation of **Mn-oxo** species upon water activation was also interrogated via time-resolved UV-Vis spectroscopy in an ACN/ H_2O mixture at pH=4 and pH=8. At acidic conditions under Ar atmosphere and in the presence of an irreversible electron acceptor, excitation of a **MnPPhOH**/ **Ru^{II}** solution gave rise to a transient UV-Vis spectrum with absorption bands similar to those of the putative **Mn^{IV}=O** species. Addition of styrene sulfonate to the investigated solution increased the stability of the **Mn^{IV}=O** intermediate suggesting that **Mn^{III}PPhOH** was regenerated between the successive flashes, presumably by oxidation of the substrate from the **Mn^{IV}=O** species. The same behavior was also observed for the non-functionalized **MnTPP**. However, under basic conditions only the **MnPPhOH** was able to realize the oxidation of the substrate; however, its activity seemed to be considerably suppressed compared to the one at pH=4.

The replacement of the irreversible electron acceptor with a reversible one led to a different photochemical pathway in which **Mn^{III}PPhOH** was reduced to **Mn^{II}PPhOH** at pH=4 under anaerobic conditions. When the solution was exposed to air the obtained transient absorption spectra proposed the formation of **Mn^{IV}=O** species that could realize the oxidation of styrene sulfonate. This time the formation of the high-valent **Mn-oxo** species was attributed to the interaction of the laser-induced **Mn^{II}PPhOH** with $^{\bullet}$OOH.

At this moment, photocatalytic experiments concerning the **MnPPhOH** and reference **MnPPh** are ongoing in order to evaluate their performance in the oxidation of styrene sulfonate. Moreover, we have also synthesized the copper and iron analogs of **MnPPhOH** in an attempt to (i) investigate the activation of H_2O and O_2, respectively, and (ii) follow the formation of high-valent tyrosyl radical species via the oxidation of organic substrates.

Annex III

Synthetic Procedure

Synthesis of CuTPP-β-NO_2

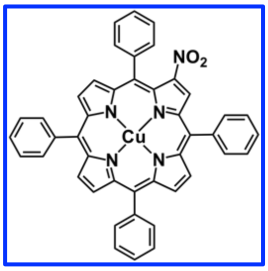

$Pb(NO_3)_2$ (1 gr, 3 mmol) was added into a schlenk tube and it was heated above 205 °C. Once $NO_{2(g)}$ (reddish-brown gas) was produced, it was injected with a syringe in portions of 12 mL into a stirring solution of CuTPP (500 mg, 0.740 mmol) in CH_2Cl_2 (150 mL). The progress of the reaction was monitored by thin layer chromatography (TLC, SiO_2, CH_2Cl_2/ Hexane (6:4 v/v)). Upon reaction completion, the solvent was distilled off and the crude product was used without any further purification for the synthesis of H_2TPP-β-NO_2.

Synthesis of H_2TPP-β-NO_2

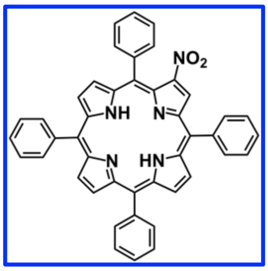

The crude mixture of CuTPP-β-NO_2 (500 mg) was dissolved in CH_2Cl_2 (60 mL) and conc. H_2SO_4 (2.3 mL) was added dropwise, under vigorous stirring. The reaction mixture was stirred at room temperature for 8 min. Then, ice-cold water (100 mL) was added and the mixture was stirred for an additional 15 min. The organic layer was washed with a sat. $NaHCO_{3(aq)}$ solution (2 x 100 mL) and H_2O (2 x 200 mL). The combined organic extracts were evaporated under vacuum and the obtained crude product was used without any further purification for the synthesis of H_2TPP-β-NH_2.

Synthesis of H_2TPP-β-NH_2

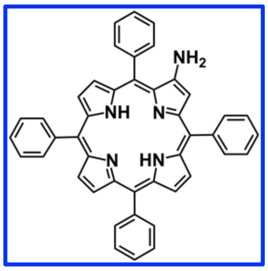

$SnCl_2{\cdot}2H_2O$ (1 gr, 4.4 mmol) and conc. HCl (3 mL) were added to a solution of H_2TPP-β-NH_2 (500 mg) in CH_2Cl_2 (100 mL). The resulting reaction mixture was stirred at room temperature for 72 h. Once the reaction was completed, H_2O (100 mL) was added to the solution and the mixture was stirred for an additional 30 min. The organic layer was neutralized with a sat. $NaHCO_{3(aq)}$ solution (2 x 80 mL) and then washed with H_2O (3 x 30 mL). The combined organic phases were dried over Na_2SO_4, filtered, and evaporated until dryness. The obtained crude residue was used without any further purification for the synthesis of H_2 TPP-Dione.

Synthesis of H_2TPP-Dione

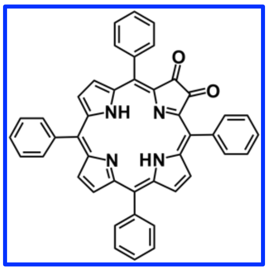

The crude product mixture of H_2TPP-β-NH_2 (500 mg) was dissolved in CH_2Cl_2 (100 mL) and silica gel (10 gr) was added. The reaction mixture was stirred under irradiation (white led lamp) in an open flask for 24 h at room temperature. The progress of the reaction was monitored by thin layer chromatography (TLC, SiO_2, CH_2Cl_2/ Hexane (6:4 v/v)). Upon reaction completion, silica gel was filtered and washed thoroughly, first with CH_2Cl_2 (200 mL) and then with THF (100 mL). The filtrate was collected and the volatiles were evaporated under reduced pressure. The crude solid was purified via column chromatography (SiO_2, CH_2Cl_2/ Hexane (6:4 v/v)) providing H_2TPP-Dione as a purple solid (262 mg, total yield of three steps 55%).

^{1}H NMR (500 MHz, $CDCl_3$): δ 8.76 (dd, J_1 = 4.9 Hz, J_2 = 1.6 Hz, 2H), 8.62 (dd, J_1 = 4.9 Hz, J_2 = 1.8 Hz, 2H), 8.58 (s, 2H), 8.15 (m, 4H), 7.91 (m, 4H), 7.74 (m, 12H), -2.00 (br s, 2H) ppm.

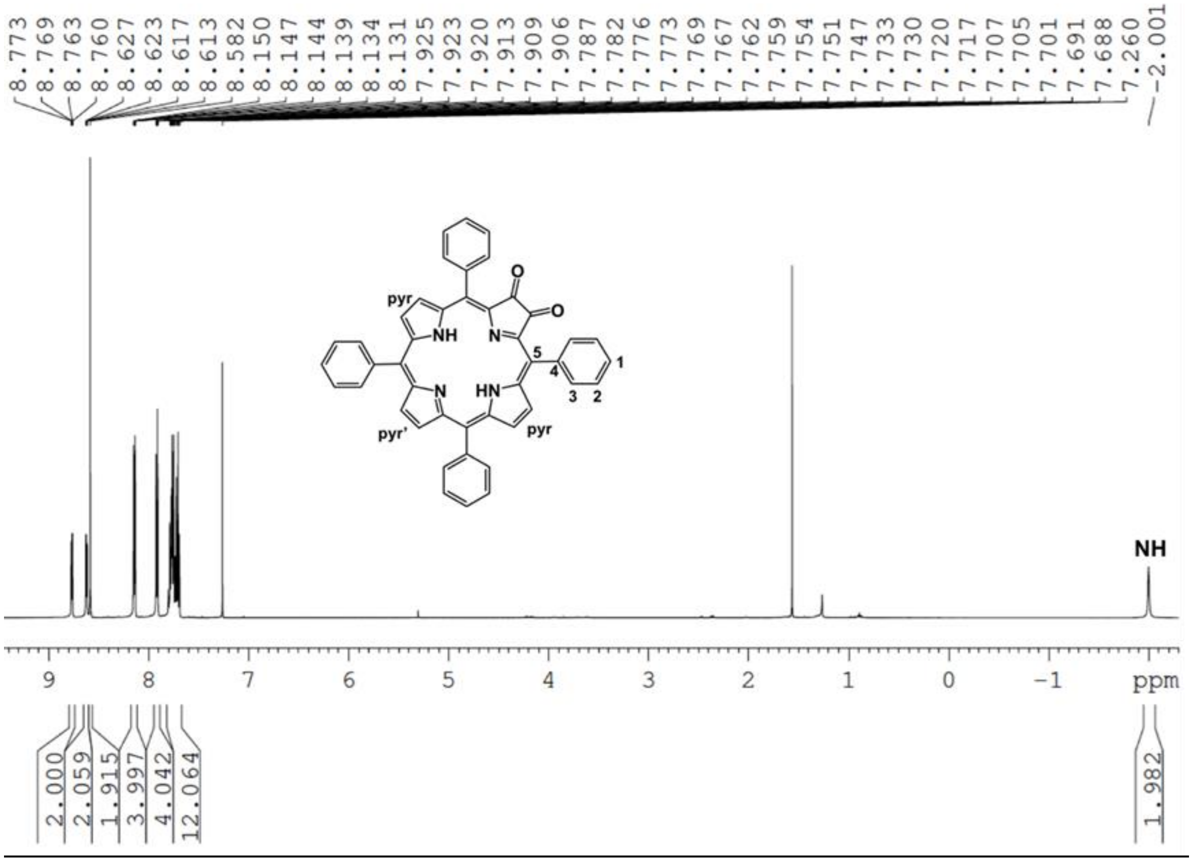

Figure S3-1 ^{1}H NMR spectrum of H_2TPP-Dione (360 MHz, $CDCl_3$).

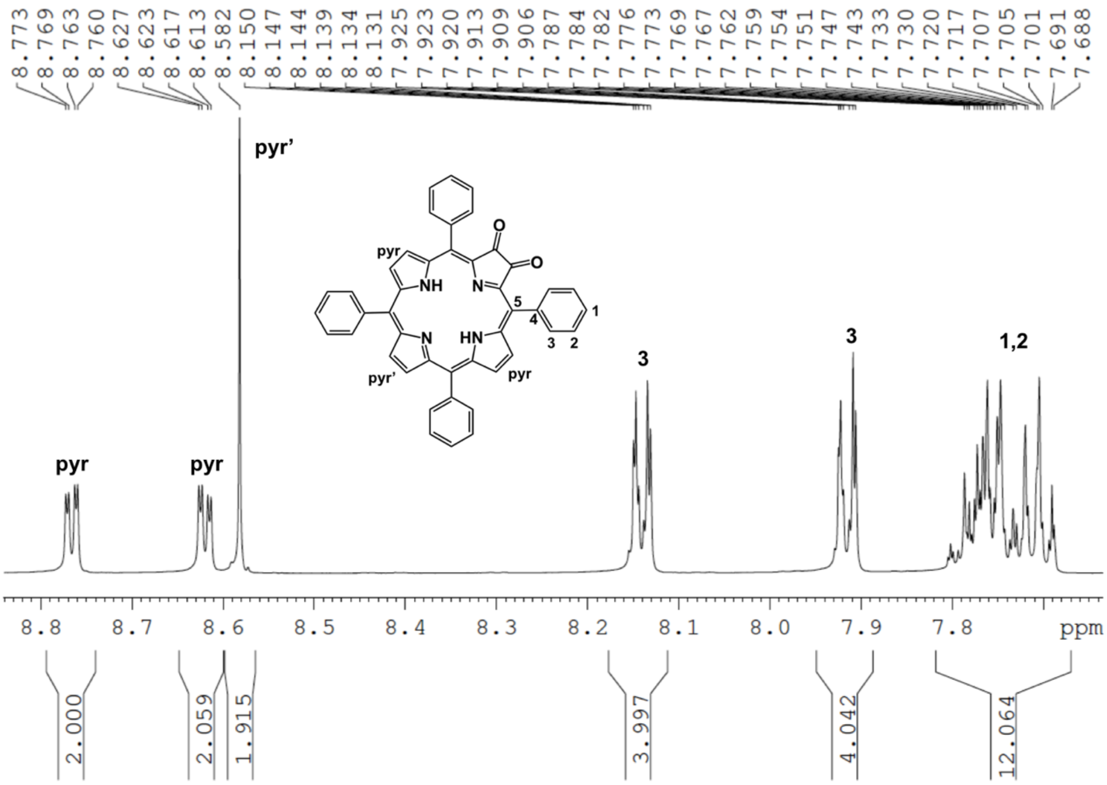

Figure S3-2 Zoom on the aromatic region of ^{1}H NMR spectrum of **H_2TPP-Dione** (500 MHz, $CDCl_3$).

Synthesis of H_2PPh

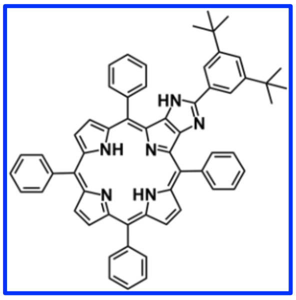

H_2TPP-Dione (35 mg, 0.054 mmol) was dissolved in $CHCl_3$ (8 mL, stabilized with amylene) and CH_3COOH (1.6 mL) was added. To this stirring solution, an excess of NH_4OAc (18.8 mg, 0.244 mmol) and a solution of 3,5-Di-tert-butylbenzaldehyde (65.2 mg, 0.299 mmol) in $CHCl_3$ (8 mL, stabilized with amylene) were added. The resulting reaction mixture was heated to 100 °C for 3h. Once the reaction was completed, the solution was quenched with sat. $NaHCO_{3(aq)}$ solution and washed with H_2O (3 x 15 mL). The organic layer was dried over Na_2SO_4, filtered, and evaporated under reduced pressure. Finally, H_2PPh was purified by column chromatography (SiO_2, CH_2Cl_2/ Hexane (9:1 v/v)) and obtained as a dark red-orange solid (36 mg, 80%).

^{1}H NMR (500 MHz, $CDCl_3$): δ 9.02 (d, J = 4.8 Hz, 1H), 8.97 (m, 2H), 8.94 (d, J = 4.8 Hz, 1H), 8.81 (m, 2H), 8.49 (br s, 1H), 8.32 (m, 4H), 8.25 (m, 4H), 7.98 (m, 3H), 7.84-7.76 (m, 9H), 7.61 (d, J = 1.8 Hz, 2H), 7.48 (t, J = 1.8 Hz, 1H), 1.44 (s, 18H), -2.88 (br s, 2H) ppm.

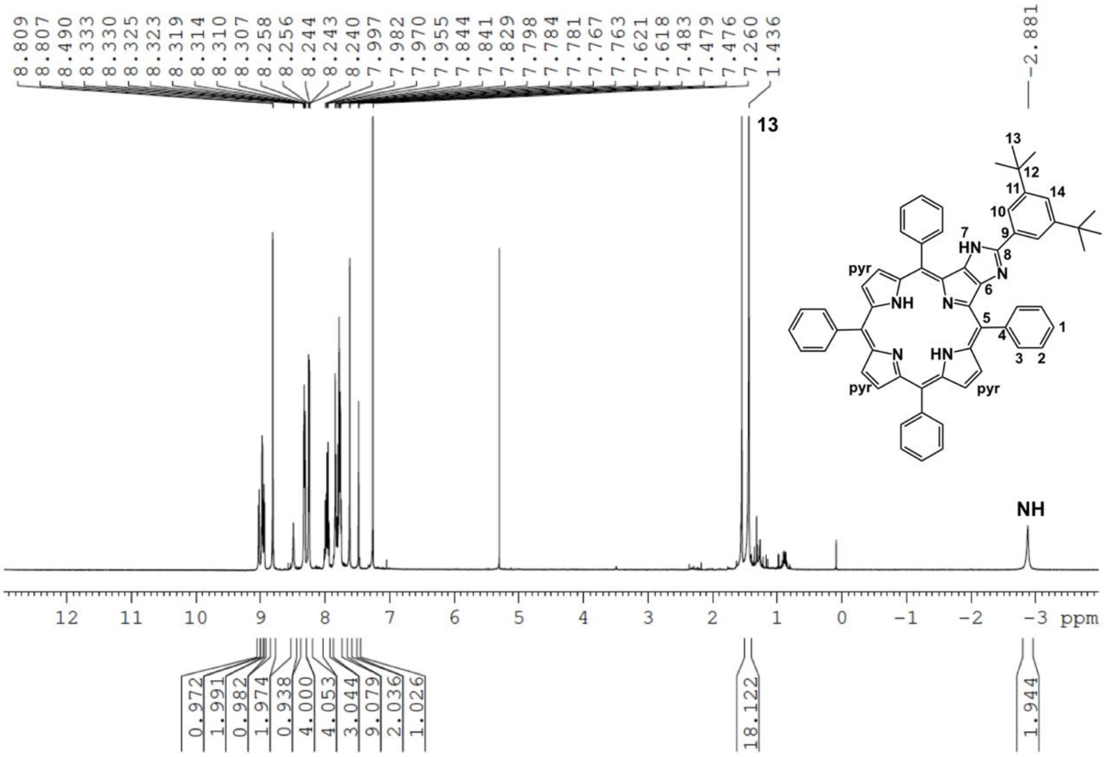

Figure S3-3 ^{1}H NMR spectrum of **H_2PPh** (500 MHz, $CDCl_3$)

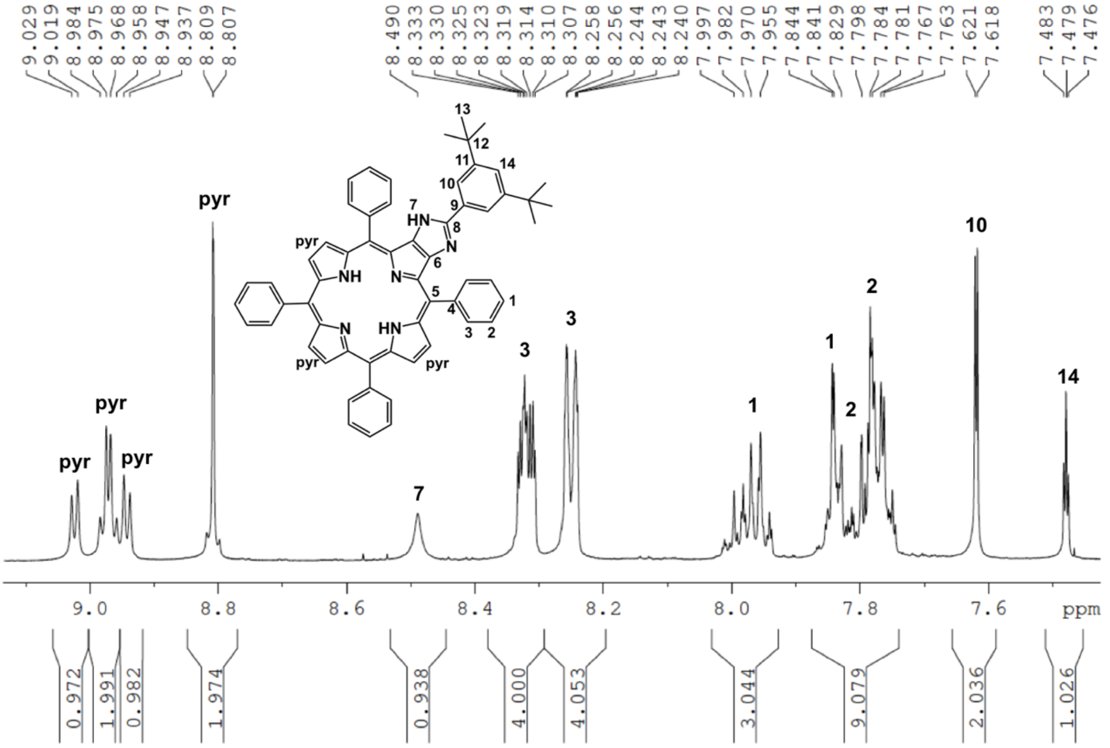

Figure S3-4 Zoom on the aromatic region of ^{1}H NMR spectrum of **H_2PPh** (500 MHz, $CDCl_3$).

^{13}C NMR (75 MHz, $CDCl_3$): δ 153.1, 151.5, 143.0, 142.5, 142.3, 141.1, 140.9, 134.7, 133.3, 132.6, 130.2, 129.8, 128.9, 128.2, 127.9, 127.7, 127.1, 126.8, 123.6, 121.3, 121.0, 120.1, 118.1, 114.7, 35.1, 31.5 ppm.

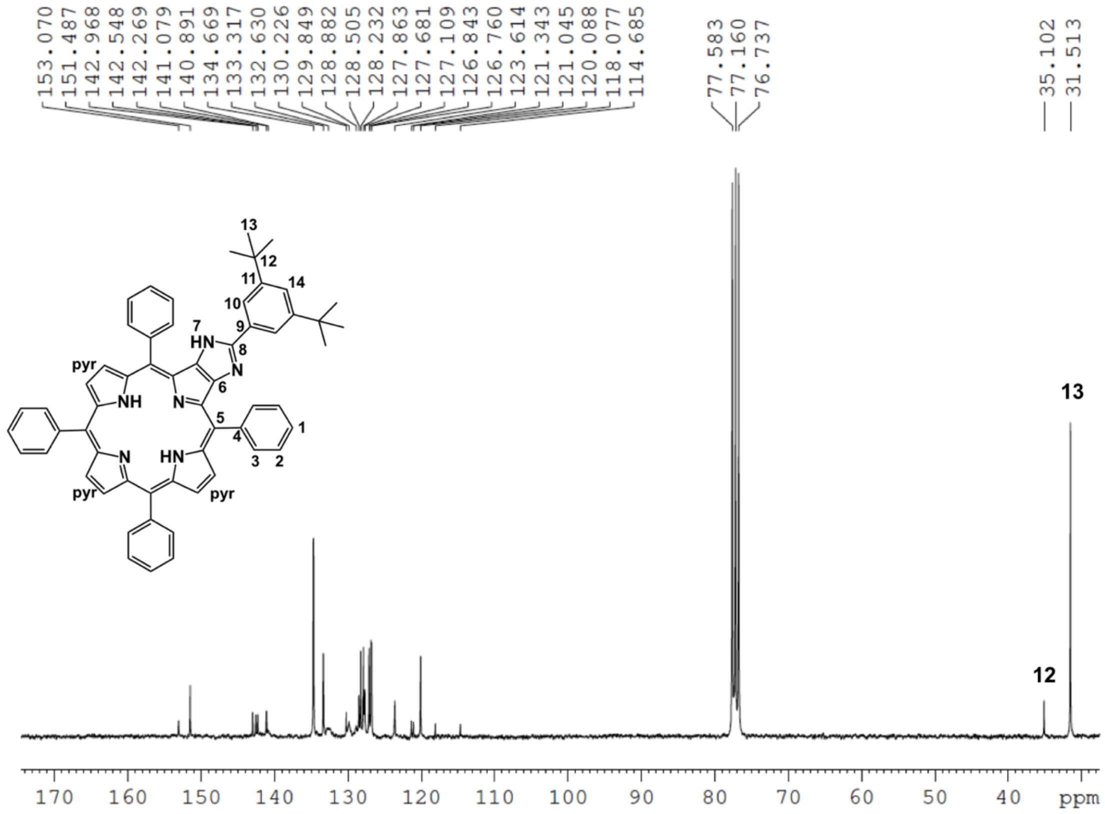

Figure S3-5 ^{13}C NMR spectrum of **H_2PPh** (75 MHz, $CDCl_3$).

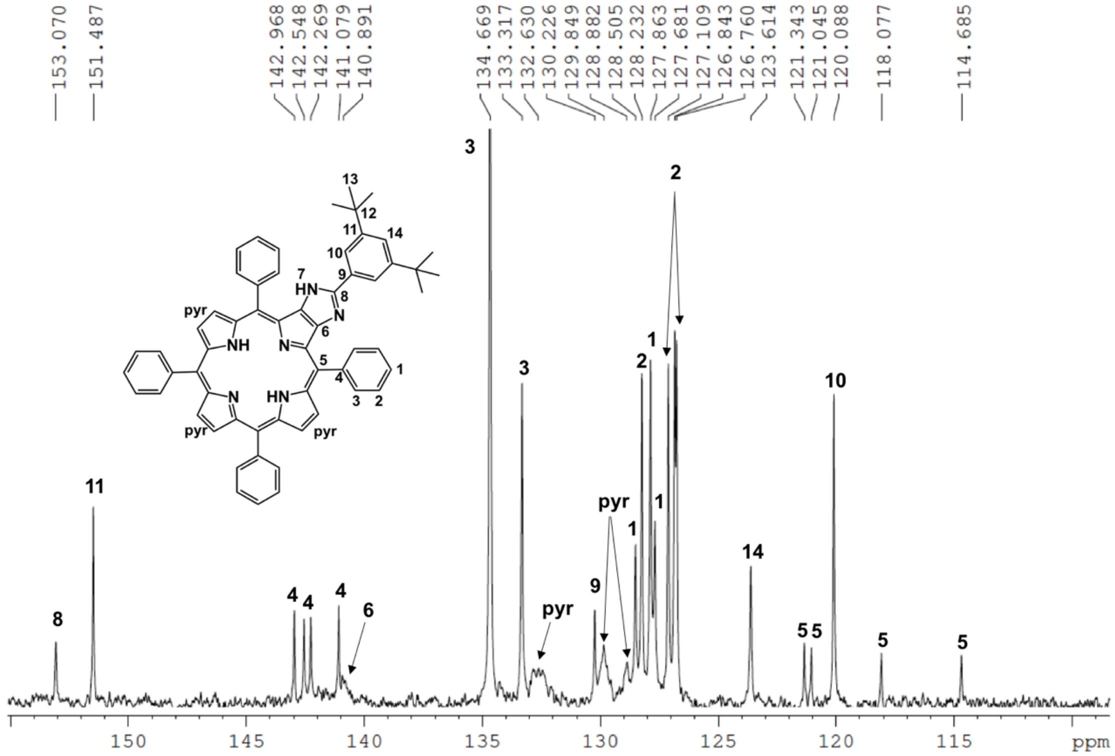

Figure S3-6 Zoom of the ^{13}C NMR spectrum of **H_2_TPP_imi_phenyl** (75 MHz, $CDCl_3$).

Synthesis of H_2PPhOH

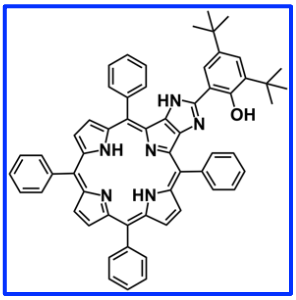

To a stirring solution of H_2TPP-Dione (70 mg, 0.109 mmol) in $CHCl_3$ (16 mL, stabilized with amylene), an excess of dry NH_4OAc (38 mg, 0.491 mmol) and CH_3COOH (3.2 mL) were added. 3,5-Di-tert-butyl-2-hydroxybenzaldehyde (140.5 mg, 0.600 mmol) was dissolved in $CHCl_3$ (16 mL, stabilized with amylene) and the resulting solution was transferred to the solution of H_2TPP-Dione. The reaction mixture was heated to 100 °C for 4 h. Upon completion of the condensation, the reaction mixture was quenched with sat. $NaHCO_{3(aq)}$ solution and washed with H_2O (3 x 30 mL). The organic extract was dried over Na_2SO_4, filtered and evaporated under vacuum. The crude residue was purified via column chromatography on silica gel and using a CH_2Cl_2/Hexane (1:1 v/v) mixture as the eluent to give H_2PPhOH as a dark red-orange solid (30 mg, 32%).

^{1}H NMR (500 MHz, $CDCl_3$): δ 12.19 (s, 1H), 9.07 (d, J = 4.8 Hz, 1H), 9.01 (s, 2H), 8.99 (d, J = 4.8 Hz, 1H), 8.81 (s, 2H), 8.46 (br s, 1H), 8.32 (m, 1H), 8.26 (m, 6H), 8.03 (m, 1H), 7.98 (m, 2H), 7.93 (m, 1H), 7.86 (m, 2H), 7.78 (m, 6H), 7.37 (d, J = 2.0 Hz, 1H), 7.01 (d, J = 2.0 Hz, 1H), 1.54 (s, 9H), 1.41 (s, 9H), -2.95 (br s, 2H) ppm.

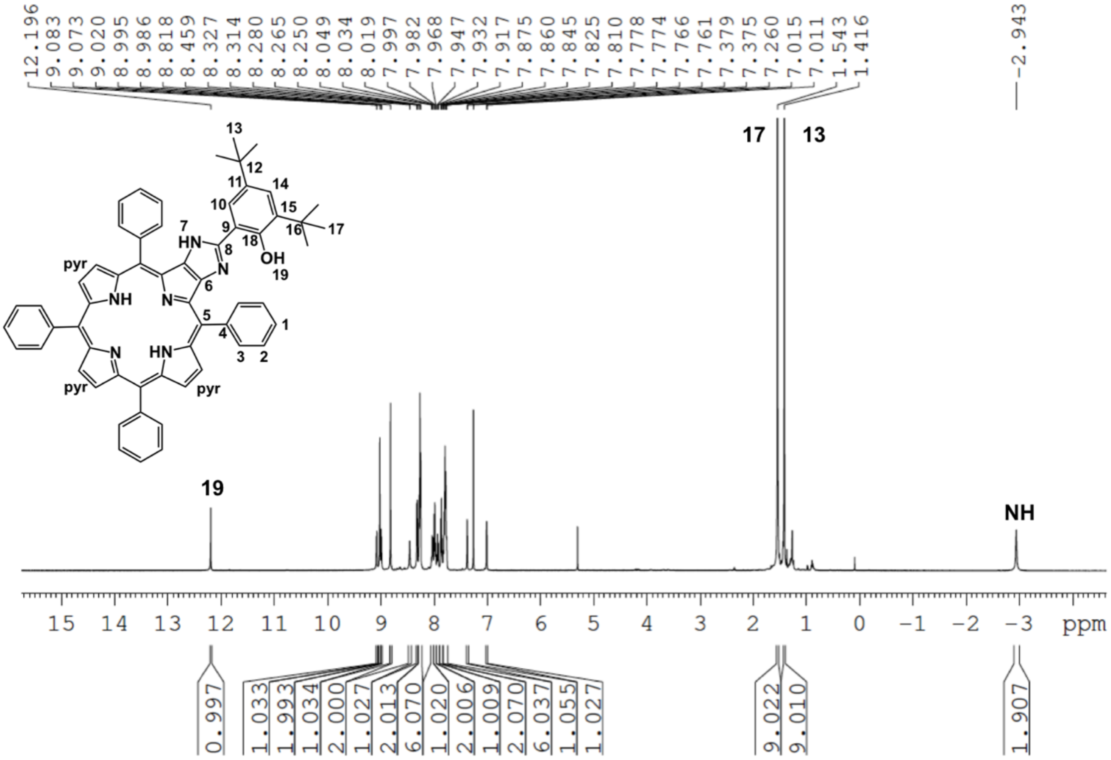

Figure S3-7 ^{1}H NMR spectrum of **H_2PPhOH** (500 MHz, $CDCl_3$).

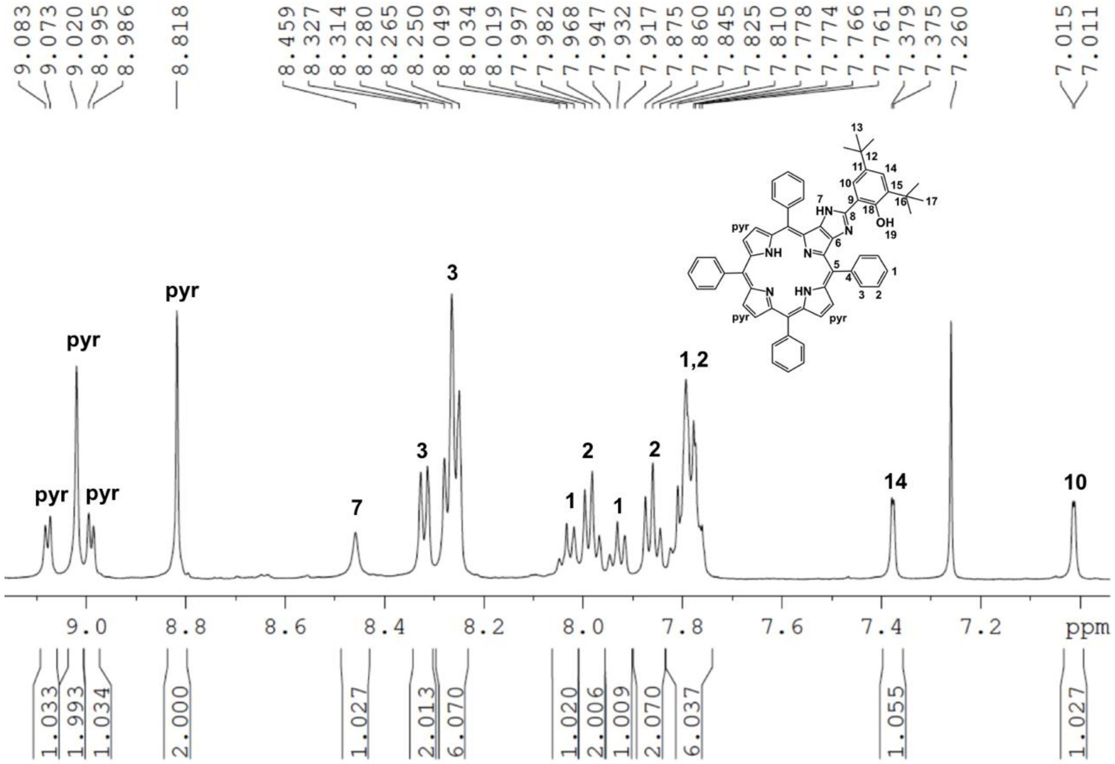

Figure S3-8 Zoom on the aromatic region of ^{1}H NMR spectrum of **H₂PPhOH** (500 MHz, CDCl₃).

^{13}C NMR (75 MHz, CDCl₃): δ 155.2, 152.9, 142.7, 142.2, 140.9, 140.1, 139.7, 137.8, 134.7, 134.0, 133.6, 133.3, 129.3, 128.7, 128.3, 127.9, 127.4, 126.9, 126.8, 125.8, 121.5, 121.2, 118.1, 117.5, 115.0, 112.2, 35.5, 34.3, 31.6, 29.6 ppm.

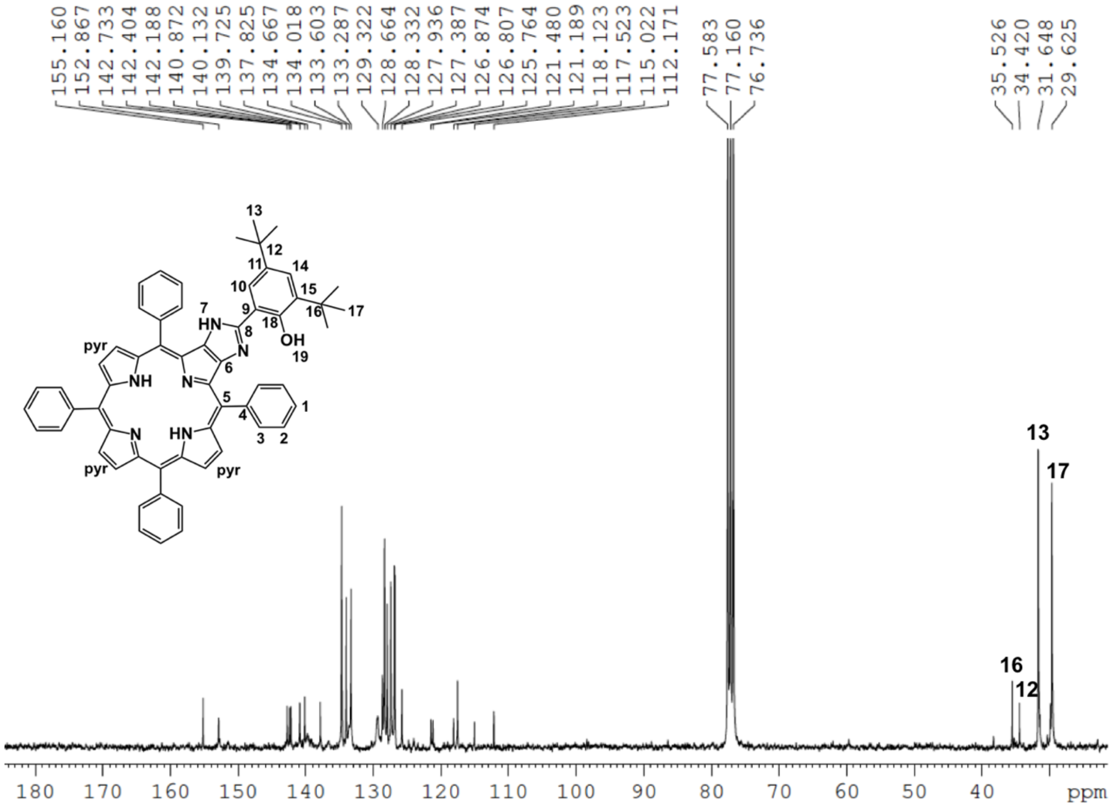

Figure S3-9 ^{13}C NMR spectrum of **H_2PPhOH** (75 MHz, $CDCl_3$).

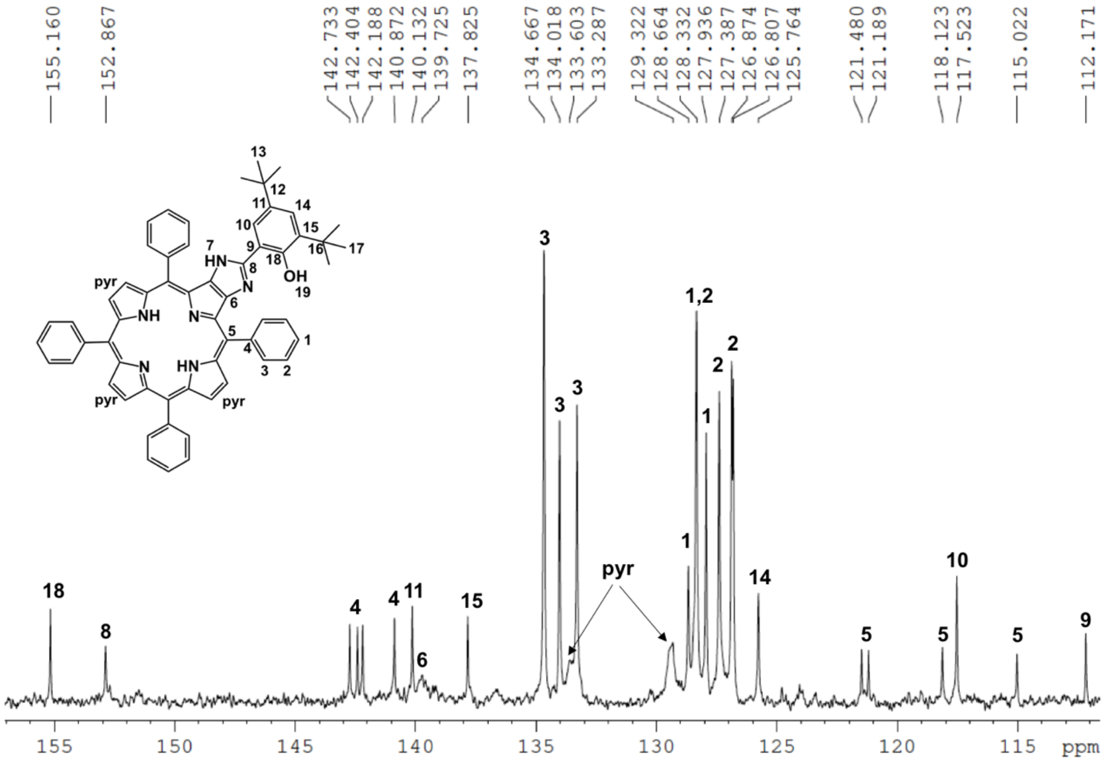

Figure S3-10 Zoom of the ^{13}C NMR spectrum of **H_2PPhOH** (75 MHz, $CDCl_3$).

Synthesis of MnPPh

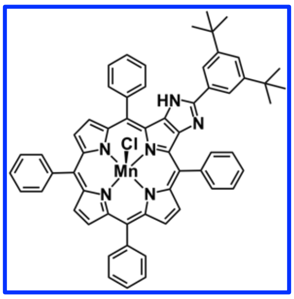

To a stirred solution of H_2PPh (100 mg, 0.20 mmol) in THF (10 mL), a solution of manganese chloride tetrahydrate (1.17 gr, 5.90 mmol) in THF/MeOH (15 mL, 3:2 v/v) and DIPEA (0.5 mL, 2.98 mmol) were added. The resulting solution was heated to reflux for 15 h. Upon reaction completion and after cooling down to room temperature, the excess of the manganese salt was precipitated by the addition of diethyl ether. The manganese salt was filtered, washed with CH_2Cl_2 and the filtrate was evaporated under reduced pressure. The obtained crude residue was purified by silica column chromatography (CH_2Cl_2/MeOH (99:1)) providing Mn(Cl)_TPP_imi_phenyl as a green solid (91.7 mg, 86%).

MALDI-TOF: calc. for chemical formula $C_{59}H_{48}ClN_6Mn$ $[M+H]^+$ = 931.3270, found 930.3076

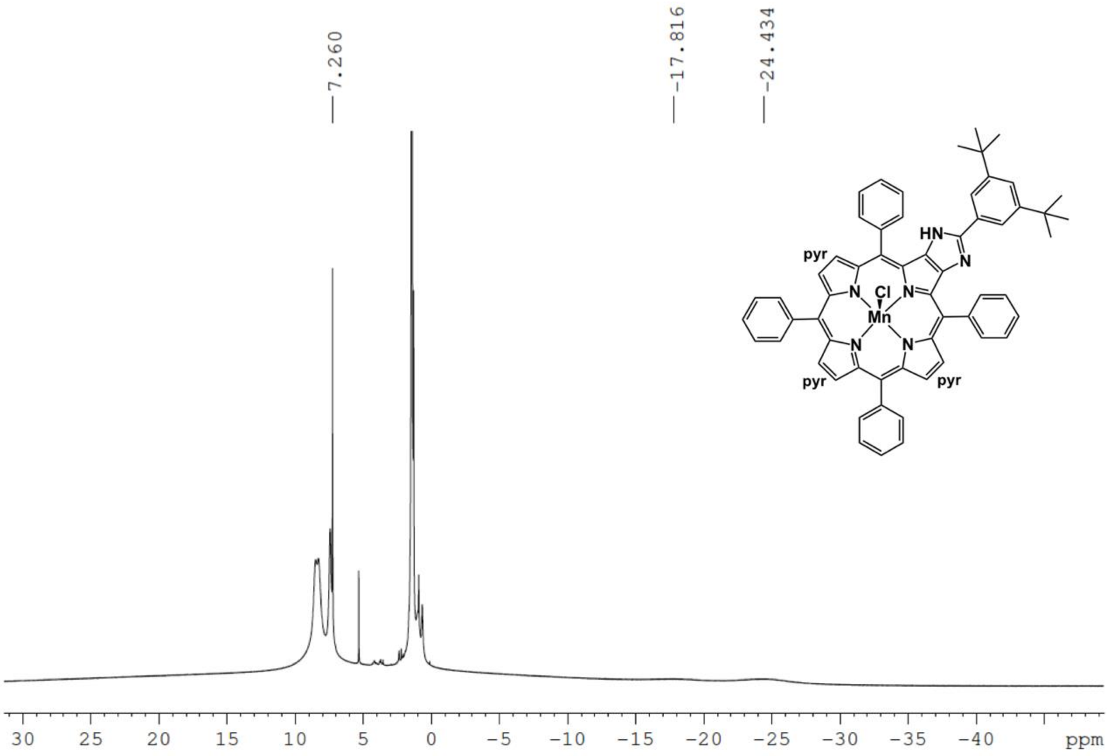

Figure S3-11 Paramagnetic ^{1}H NMR spectrum of **MnPPh** (500 MHz, $CDCl_3$).

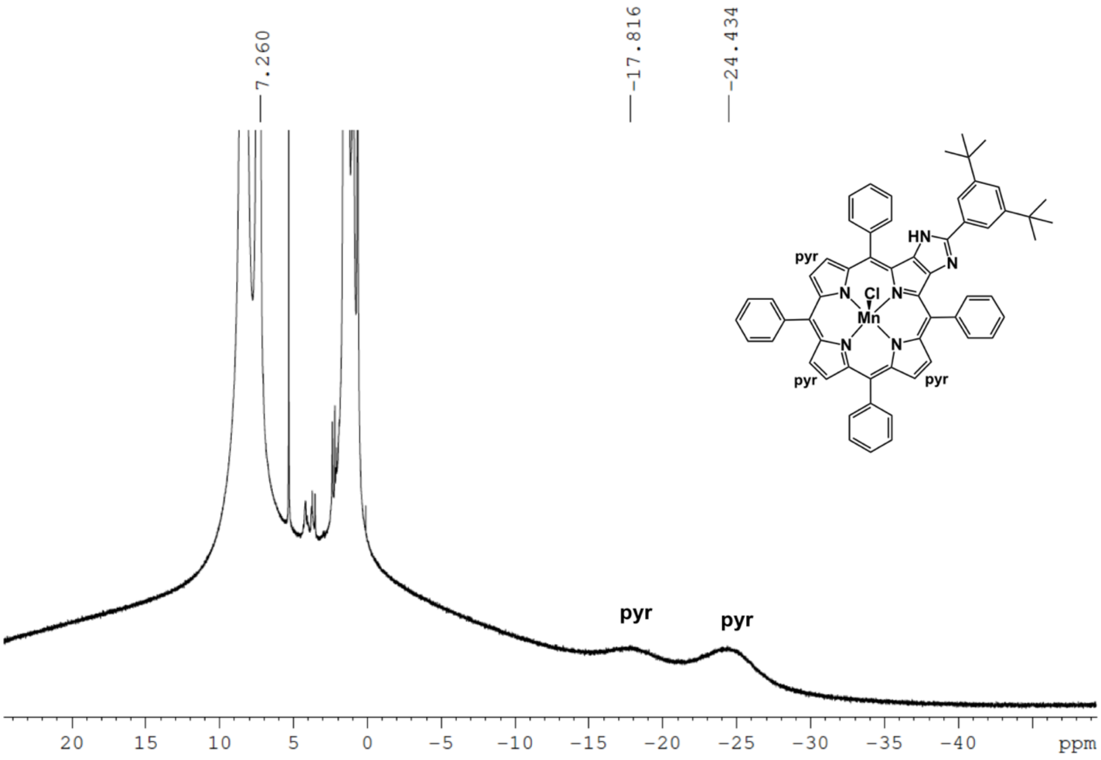

Figure S3-12 Zoom on the pyrrolic region of ^{1}H NMR paramagnetic spectrum of **MnPPh** (500 MHz, $CDCl_3$).

Synthesis of MnPPhOH

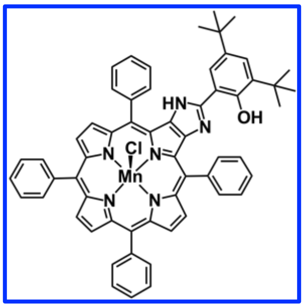

Manganese chloride tetrahydrate (410 mg, 2.1 mmol) was dissolved in a mixture of THF/MeOH (5 mL, 3:2 v/v). The resulting solution was added to a stirred solution of H_2PPhOH (21 mg, 0.024 mmol) in THF (2 mL). Afterwards, DIPEA (0.1 mL, 0.57 mmol) was added and the reaction mixture was heated to reflux under stirring for 15 h. After cooling to room temperature, the excess of the manganese salt was precipitated by the addition of diethyl ether and filtered. The filtrate was then distilled under reduced pressure to provide the crude product. The crude residue was purified via column chromatography (SiO_2, CH_2Cl_2/MeOH (98:2)) to obtain MnPPhOH as a green solid (17.3 mg, 79%).

MALDI-TOF: calc. for chemical formula $C_{59}H_{49}N_6OMn$ $[M+H]^+$ = 911.3270, found 911.3276 , calc. for chemical formula $C_{59}H_{49}ClN_6OMn$ $[M+H]^+$ = 946,2959, found 946.

UV-Vis (CH_2Cl_2): λ_{max}/nm (10^{-3} ε. L mol^{-1} cm^{-1}) : 348 (37.6), 380 (54.3), 405 (42.9), 434 (26.8), 482 (81.6), 537 (5.7), 575 (8.7), 621 (9.0).

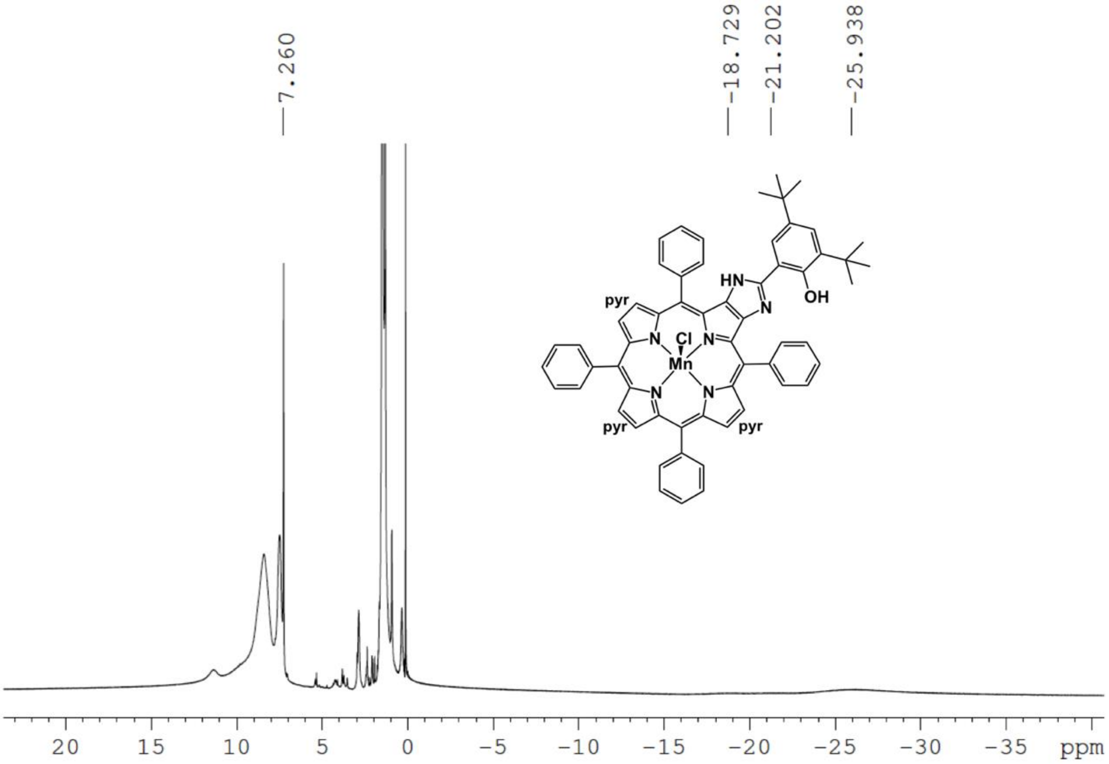

Figure S3-13 Paramagnetic ^{1}H NMR spectrum of **MnPPhOH** (500 MHz, $CDCl_3$).

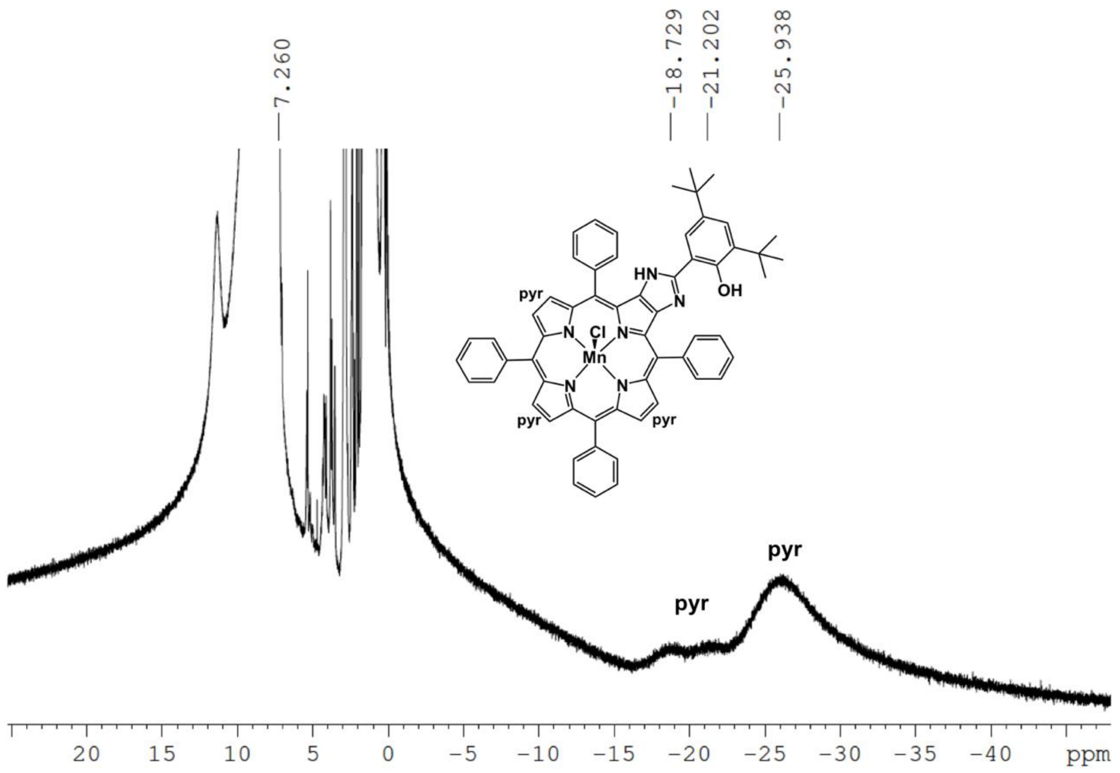

Figure S3-14 Zoom on the pyrrolic region of ^1H NMR spectrum of **MnPPhOH** (500 MHz, $CDCl_3$).

Synthesis of ZnPPhOH

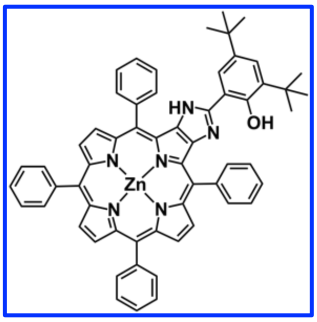

A solution of zinc acetate dihydrate (77 mg, 0.350 mmol) in MeOH (5 mL) was added to a stirred solution of H_2PPhOH (32 mg, 0.037 mmol) in $CHCl_3$ (15 mL). The reaction was kept in dark and it was heated to reflux for 2 h. After cooling down to room temperature, the solvents were removed under reduced pressure. The obtained crude mixture was dissolved in CH_2Cl_2 (50 mL), washed with saturated aqueous solution of sodium bicarbonate (50 mL) and then with deionized H_2O (100 mL). The combined organic layers were evaporated under reduced pressure and the desired compound was purified using silica column chromatography (CH_2Cl_2/Hexane (1:1)). ZnPPhOH was obtained as a magenta-red solid (33 mg, 97%).

^1H NMR (360 MHz, $CDCl_3$): δ 12.24 (s, 1H), 9.10 (d, J = 4.7 Hz, 1H), 9.05 (s, 2H), 9.02 (d, J = 4.7 Hz, 1H), 8.97 (s, 2H), 8.60 (br s, 1H), 8.31 (m, 2H), 8.26 (m, 6H), 7.92 (m, 6H), 7.78 (m, 6H), 7.38 (d, J = 2.0 Hz, 1H), 7.05 (d, J = 2.0 Hz, 1H), 1.54 (s, 9H), 1.42 (s, 9H) ppm.

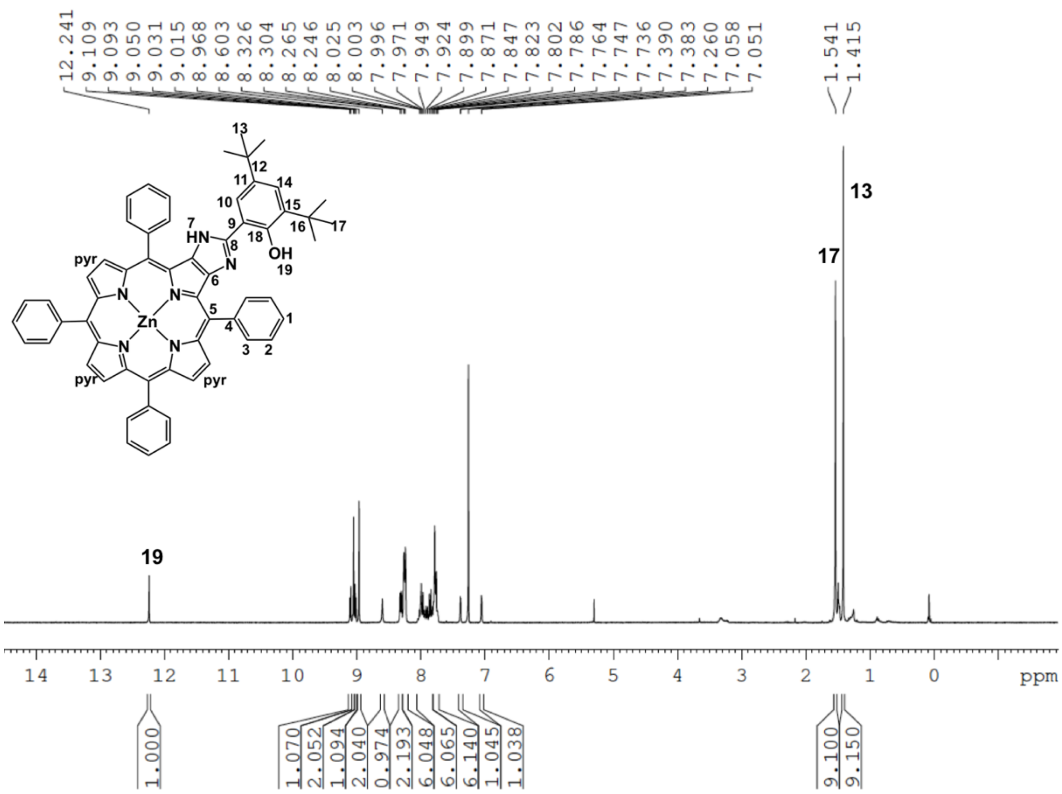

Figure S3-15 ^{1}H NMR spectrum of **ZnPPhOH** (360 MHz, $CDCl_3$).

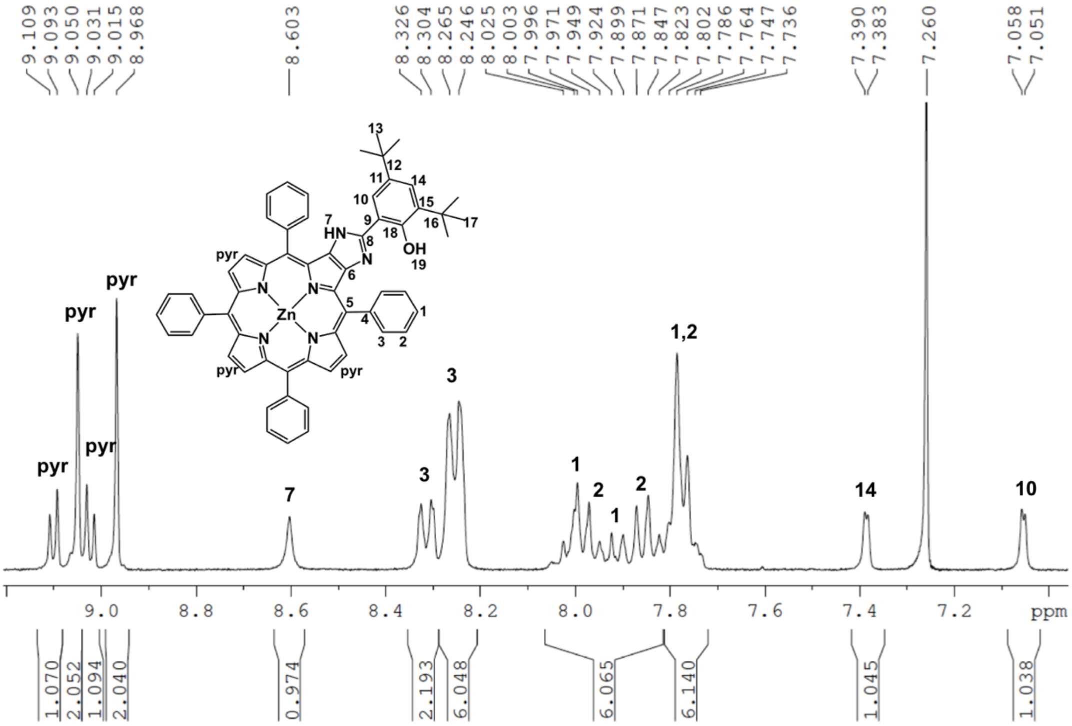

Figure S3-16 Zoom on the aromatic region of ^{1}H NMR spectrum of **ZnPPhOH** (360 MHz, $CDCl_3$).

UV-Vis (CH_2Cl_2): λ_{max}/nm (10^{-3} ε. L mol^{-1} cm^{-1}) : 421 (391.0), 512 (4.5), 547 (24.7), 584 (9.9).

MALDI-TOF: calc. for chemical formula $C_{59}H_{49}N_6OZn$ [M+H] $^+$ = 921.3254, found 921.3202
calc. for chemical formula $C_{59}H_{48}N_6NaOZn$ [M+Na] $^+$ = 943.3073, found 943.3028.

Synthesis of CuPPhOH

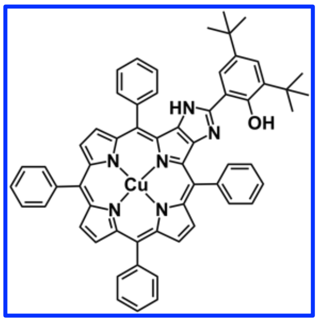

To a stirred solution of copper (II) acetate monohydrate (32 mg, 0.160 mmol) in MeOH (5 mL), a solution of H_2_TPP_imi_phOH (50 mg, 0.058 mmol) in $CHCl_3$ (15 mL) was added and the resulting solution was refluxed for 20 h. After cooling down to room temperature, the solution was washed with brine and extracted with CH_2Cl_2. The organic extracts were combined, dried over Na_2SO_4, filtered and distilled to dryness. The crude product was purified via column chromatography on silica gel using CH_2Cl_2/Cyclohexane (1:1) mixture as eluent to give Cu_TPP_imi_phOH_as a purple solid (42.5 mg, 79%).

UV-Vis (CH_2Cl_2): λ_{max}/nm (10^{-3} ε. L mol^{-1} cm^{-1}) : 418 (329.7), 505 (5.5), 538 (23.6), 575 (10.0).

ESI-HRMS: calc. for chemical formula $C_{59}H_{49}N_6OCu$ [M+H] $^+$ = 920.3258, found 920.3212
calc. for chemical formula $C_{59}H_{48}N_6CuONa$ [M+Na] $^+$ = 942.3078, found 942.3030.

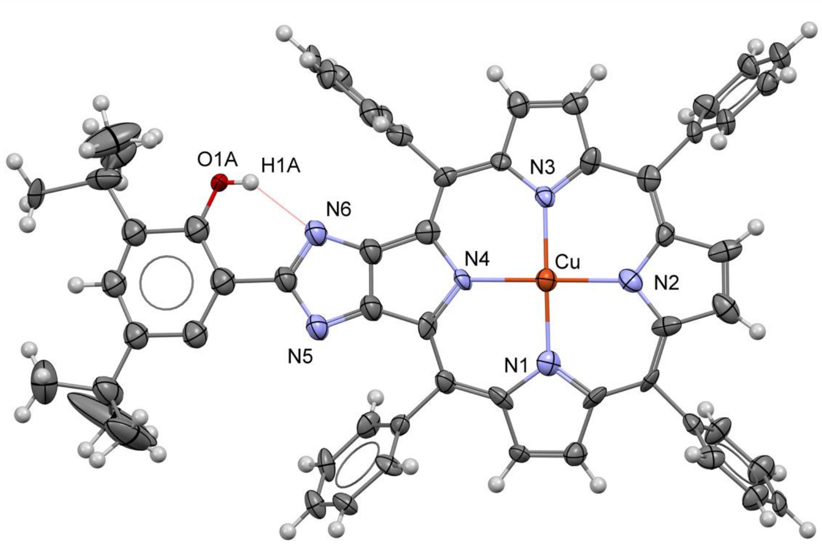

Fig. S3-17 Capped sticks representation of the X-ray crystal structure of CuPPhOH

Synthesis of CuPPh

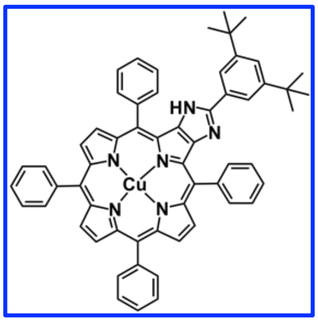

Copper (II) acetate monohydrate (205 mg, 1.25 mmol) was dissolved in MeOH (10 mL) and a solution of H_2_TPP_imi_phenyl (102 mg, 0.121 mmol) in $CHCl_3$ (30 mL) was added. The mixture was heated to reflux for 16 h. After cooling down to room temperature, the solution was washed with brine and extracted with CH_2Cl_2. The combined organic layers were dried over Na_2SO_4 and the solvents were removed under reduced pressure. The residue was purified by silica column chromatography (CH_2Cl_2/Hexane (6:4 v/v)) to give Cu_TPP_imi_phenyl_as a purple solid (105.3 mg, 96 %).

UV-Vis (CH_2Cl_2): λ_{max}/nm (10^{-3} ε. L mol^{-1} cm^{-1}) : 419 (351.0), 507 (9.3), 539 (25.2), 576 (13.0).

MALDI-TOF: calc. for chemical formula $C_{59}H_{49}N_6OCu$ $[M+H]^+$ = 904.3200, found 903.3200

Synthesis of CoPPhOH

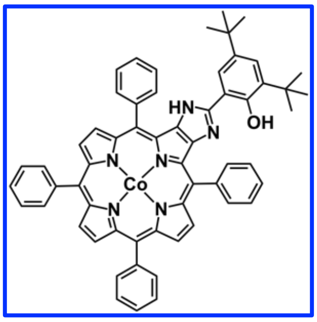

H_2_TPP_imi_phOH (60 mg, 0.070 mmol) was dissolved in $CHCl_3$ (20 mL) and a solution of cobalt (II) acetate tetrahydrate (106 mg, 0.36 mmol) in $CHCl_3$/MeOH (25 mL, 4:1) was added. The reaction was left under stirring and it was heated to reflux for 1.5 h. After the reaction reached completion, the volatiles were evaporated under reduced pressure and the obtained product was purified by column chromatography on silica gel using as eluent a mixture of CH_2Cl_2/Hexane (1:1 v/v). Finally, Co(II)_TPP_imi_phOH was further purified by recrystallization from hexane (48.3 mg, 76%).

^{1}H NMR (500 MHz, $CDCl_3$): δ 15.88 (m, 7H), 14.80 (br s, 1H), 13.13 (m, 8H), 9.97 (m, 12H), 8.52 (br s, 2H), 2.39 (m, 18H) ppm.

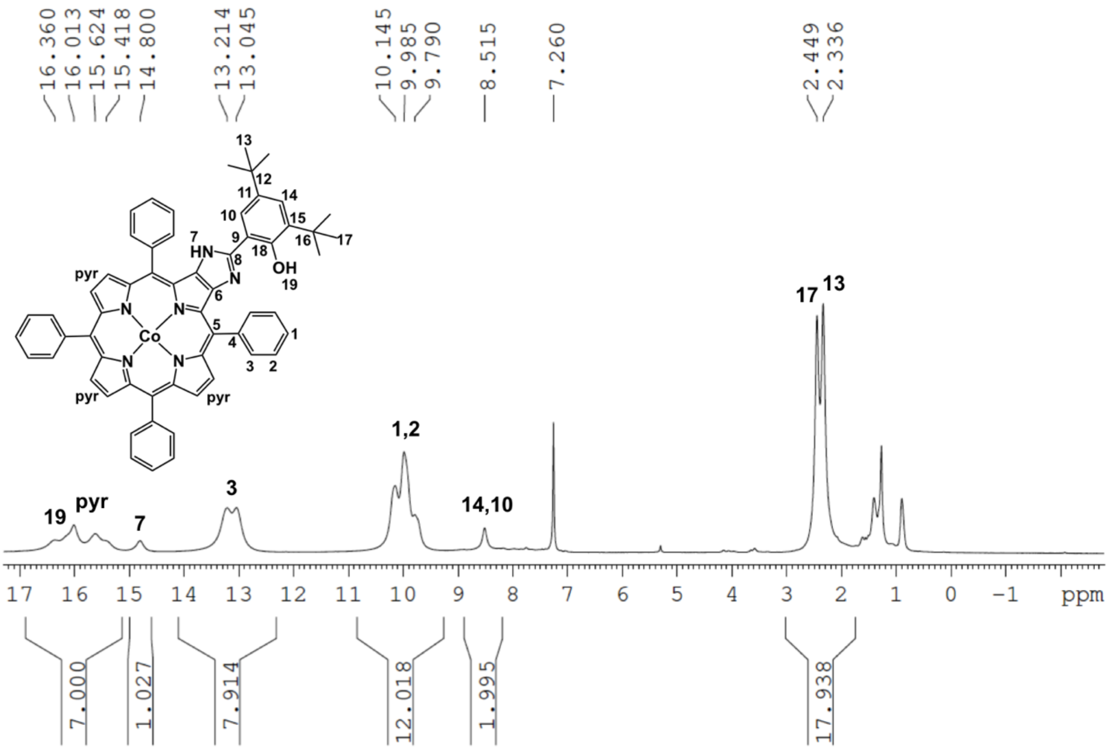

Figure S3-18 Paramagnetic ^{1}H NMR spectrum of **CoPPhOH** (500 MHz, $CDCl_3$).

Synthesis of CoPPh

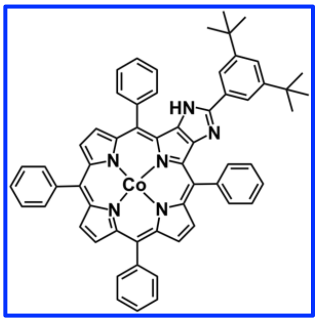

Cobalt (II) acetate tetrahydrate (175 mg, 0.600 mmol) was dissolved in $CHCl_3$/MeOH (40 mL, 3:1 (v/v)) and the resulting solution was added into a solution of H_2_ TPP_imi_phenyl (104 mg, 0.123 mmol) in $CHCl_3$ (30 mL). The reaction mixture was heated to reflux under stirring for 2h. Once metallation was completed, the volatiles were distilled under vacuum. The crude solid was dissolved in CH_2Cl_2 and the remaining precipitate was filtered off and washed thoroughly with CH_2Cl_2. The filtrate was collected and concentrated under reduced pressure. The obtained crude product was purified via column chromatography (SiO_2, CH_2Cl_2/Hexane (6:4)) providing the desired cobalt porphyrin. Finally, CoPPh was further purified by recrystallization from MeOH (92.7 mg, 84%).

^{1}H NMR (500 MHz, $CDCl_3$): δ 16.36 (m, 2H), 15.65 (m, 4H), 14.80 (br s, 1H), 13.14 (m, 8H), 10.61 (br s, 2H), 9.97 (m, 11H), 8.59 (br s, 2H), 2.35 (br s, 18H) ppm.

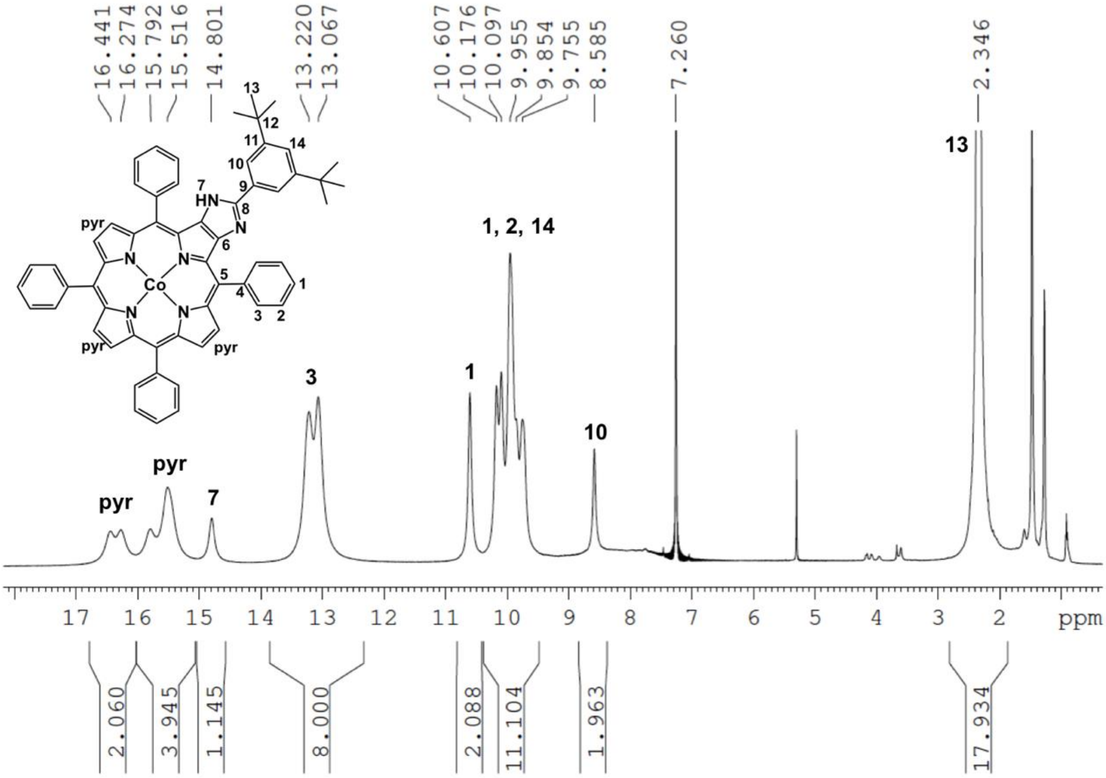

Figure S3-19 Paramagnetic ^{1}H NMR spectrum of **CoPPh** (500 MHz, $CDCl_3$).

Synthesis of FePPhOH

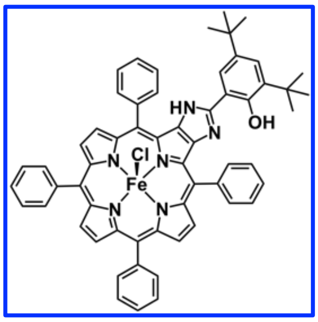

In a schlenk tube, under Ar atmosphere, H_2_TPP_imi_phOH (75 mg, 0.087 mmol) was dissolved in dry-degassed THF (8 mL) and $FeBr_2$ (94 mg, 0.435 mmol) was added to the solution. The reaction mixture was heated up to 55 °C overnight. After 16 h, the solvent was evaporated in vacuo and the obtained residue was dissolved in CH_2Cl_2 (50 mL). The resulting solution was washed with 2N HCl (2 x 200 mL), dried over Na_2SO_4, filtered and concentrated under reduced pressure. The desired iron porphyrin was purified via column chromatography on silica gel using a CH_2Cl_2/EtOH (97:3 v/v) mixture as the eluent. Finally, Fe(Cl)_TPP_imi_phOH was further purified by recrystallization from MeOH (54 mg, 66%).

MALDI-TOF: calc. for chemical formula $C_{59}H_{49}ClFeN_6O$ $[M+H]^+$ = 948.29, found 947.29

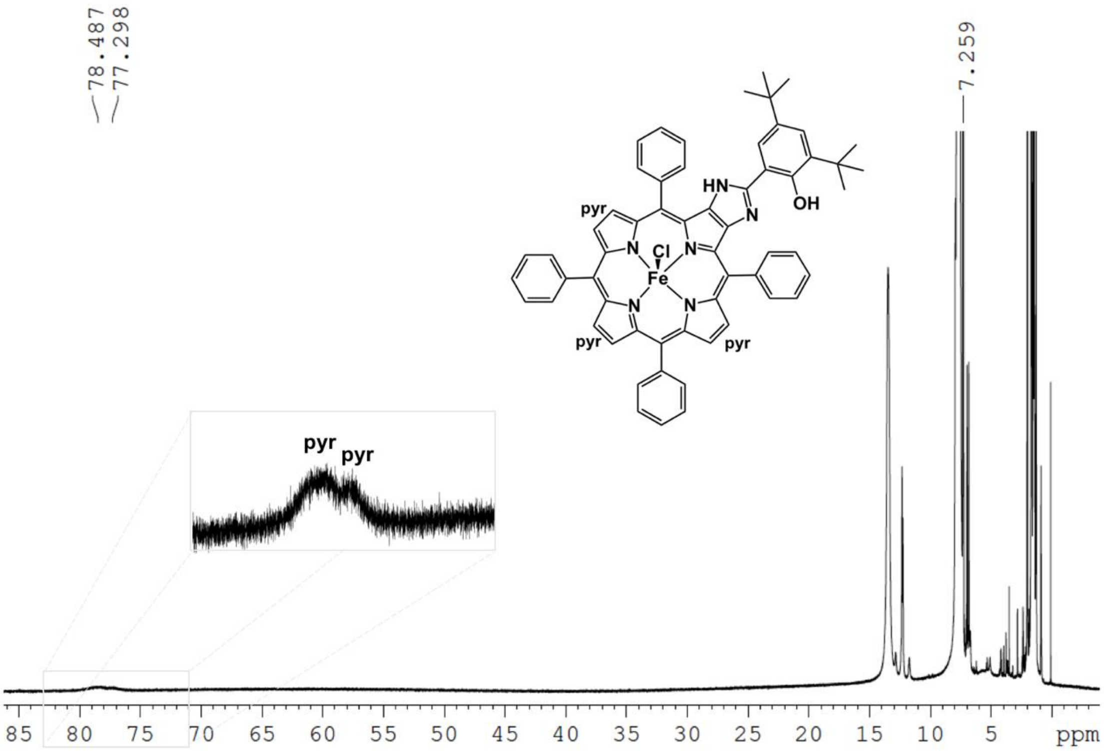

Figure S3-20 ^{1}H NMR paramagnetic spectrum of **FePPhOH** (500 MHz, $CDCl_3$).

Synthesis of FePPh

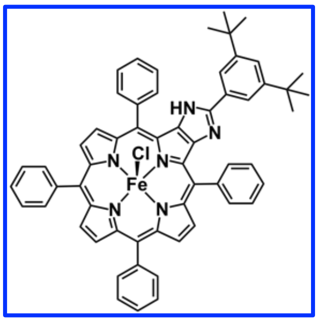

H_2_TPP_imi_phenyl (93 mg, 0.110 mmol) was dissolved in dry-degassed THF (10 mL), under Ar atmosphere, and $FeBr_2$ (120 mg, 0.550 mmol) was added to the solution. The reaction mixture was heated up to 55 °C for 18 h and upon reaction completion, the solvent was distilled off. The obtained solid was dissolved in CH_2Cl_2 (50 mL), washed with 2N HCl (2 x 200 mL), dried over Na_2SO_4, filtered and evaporated in vacuo. The crude residue was purified via column chromatography (SiO_2, CH_2Cl_2/EtOH (98:2 v/v)) providing Fe(Cl)_TPP_imi_phenyl as a purple solid which was further purified by recrystallization from MeOH (50 mg, 49%).

MALDI-TOF: calc. for chemical formula $C_{59}H_{48}ClFeN_6$ $[M+H]^+$ = 932.30, found 931.30

Les trois sujets principaux de cette thèse portent sur la conception de métalloporphyrines bio-inspirées et l'évaluation de leur réactivité envers (i) la réduction de l'O_2 moléculaire, (ii) la réduction du CO_2 en conditions aérobies, et (iii) l'activation de l'H_2O.

Concernant le premier axe de ce travail de thèse, nous avons caractérisé via des études spectroscopiques UV-Vis, EPR, et rRaman les premiers intermédiaires impliqués dans la réduction de l'O_2 moléculaire catalysé par deux atropisomères de fer-porphyrine fonctionnalisés dans leur deuxième sphère de coordination avec des groupes urée comme donneurs de liaisons hydrogène multipoints.

Les propriétés électrochimiques du **Fe-αα-2Urea** et du **Fe-αβ-2Urea** ont été étudiées par voltampérométrie cyclique en solution dans des conditions anaérobies et aérobies en l'absence d'une source de protons. Sous une atmosphère d'Argon, les deux dérivés de porphyrine de fer ont présenté trois vagues d'oxydoréduction réversibles successives lors du balayage dans la fenêtre de potentiel négatif, qui ont été attribuées au couple $Fe^{III/II}$ et aux couples formels $Fe^{II/I}$ et $Fe^{I/0}$. Nous avons également noté un décalage positif des potentiels par rapport au FeTPP parent, dû aux fonctions urée qui retiennent les groupes $-CF_3$ qui retirent les électrons. Lorsque la solution électrolytique était saturée en O_2, le couple redox $Fe^{III/II}$ devenait irréversible, avec un léger gain de l'intensité du courant. Une telle réponse indique une liaison de l'O_2 au centre ferreux du fer, suivie d'un transfert simultané d'électrons du métal à la molécule d'O_2 liée pour donner un Fe^{III}-$O_2^{\bullet-}$ noté comme intermédiaire superoxo *(S)*. Les CV du **Fe-αα-2Urea** et du **Fe-αβ-2Urea** ont montré une nouvelle onde cathodique avant le couple redox $Fe^{II/I}$, et la réduction de l'O_2 à la surface de l'électrode GC. Ce processus redox semblait quasi-réversible, et il était absent dans le FeTPP non-modifié. Cette onde supplémentaire a été attribuée à la réduction supplémentaire des espèces **Fe-αα-2Urea** *(S)* et **Fe-αβ-2Urea** *(S)* à leurs intermédiaires Fe^{III}-O_2^{2-} *(P)* correspondants. Il est intéressant de noter qu'à un taux de balayage de 5 mV/sec, la réduction des espèces *(S)* en *(P)* devient un processus quasi-réversible pour les deux **porphyrines Fe-αα-2Urea** et **Fe-αβ-2Urea.** Nous avons donc déterminé le potentiel redox du couple (S)/(P) à E= -0.796 V *vs.* $Fc^{+/0}$, qui était le même pour les deux atropisomères. Il est à noter qu'il s'agit du premier exemple de couple redox *(S)/(P)* de porphyrine de fer déterminé par voltampérométrie cyclique. De plus, ce processus redox a été réalisé à un potentiel considérablement plus positif que les autres dérivés de porphyrines de fer documentés dans la littérature. Nos modèles de porphyrines de fer soulignent le rôle essentiel des unités d'urée sur la deuxième sphère de coordination pour stabiliser les intermédiaires *(S)* et rendre la réduction de l'espèce (S) en (P) thermodynamiquement plus favorable.

Pour caractériser davantage les premiers intermédiaires impliqués dans l'activation et la réduction de l'O_2 moléculaire, nous avons également généré les espèces *(S)*, *(P)* et *(HP)* de **Fe-αα-2Urea** et de **Fe-αβ-2Urea** par voie chimique à basse température. Les intermédiaires *(S)* ont montré une stabilité remarquable à -20°C pendant plus de 30 min pour le **Fe-αα-2Urea** *(S)* par rapport à l'espèce **Fe-αβ-2Urea** correspondante. Cependant, ils étaient tous les deux sensiblement plus stables que le FeTPP *(S)* parent. Ces résultats corroborent davantage nos conclusions initiales de voltampérométrie cyclique selon lesquelles l'incorporation de bras d'urée dans la deuxième sphère de coordination améliore considérablement la stabilité des adduits Fe- O_2. De plus, la topologie des fonctions urée influence également la stabilité des espèces superoxo indiquant que les intermédiaires superoxo sont mieux stabilisés lorsque les deux groupes urée sont sur le même plan de la porphyrine. En avançant d'un pas, après la formation réussie des espèces **Fe-αα-2Urea** *(S)* et **Fe-αβ-2Urea** *(S)*, nous les avons réduites chimiquement à leurs intermédiaires *(P)* correspondants à -80°C. Leurs spectres UV-Vis présentaient des bandes d'absorption caractéristiques des espèces peroxo latérales. De plus, la conversion des espèces *(S)* en *(P)* était un processus réversible, comme l'indiquaient également nos études électrochimiques initiales à de faibles vitesses de balayage. Les spectres RPE de **Fe-αα-2Urea** *(P)* et **Fe-αβ-2Urea** *(P)* corroborent les résultats de l'UV-Vis concernant la formation d'espèces peroxo à spin élevé. Cependant, d'autres signaux étaient également présents, qui pourraient être attribués à des espèces ferriques *(P)* et/ou ferreuses *(P)* à faible spin. Des études de simulation RPE sont actuellement en cours pour étudier les différents modes de coordination possibles du ligand peroxo. Enfin, les espèces **Fe-αα-2Urea** *(HP)* et **Fe-αβ-2Urea** *(HP)* ont été générées par l'addition d'un acide fort ou faible à une solution des intermédiaires *(P)* correspondants, et caractérisées par des études de spectroscopie UV-Vis à basse température. Le fait qu'un acide faible puisse protoner les espèces *(P)* démontre qu'il est possible de générer et de stabiliser les intermédiaires ferriques *(HP)* en modifiant de manière appropriée la seconde sphère de coordination avec des fonctions urée donneuses de liaisons H appropriées sans avoir besoin d'une base axiale forte. Ici aussi, des études EPR et rRaman sont en cours. Actuellement, l'activité électrocatalytique ORR des atropisomères de **Fe-2Urea** est étudiée dans des conditions homogènes et hétérogènes.

Dans le second axe de recherche, nous avons décrit une approche différente pour développer des électrocatalyseurs à base de porphyrines de cuivre pour une réduction efficace du CO_2 qui présentent une grande tolérance à la présence de l'O_2. Plus précisément, nous avons fonctionnalisé une porphyrine de cuivre avec un groupe pendentif de type méthyl-viologène et étudié en premier lieu son activité électrocatalytique vers la réduction du CO_2 et de l'O_2 moléculaire, séparément. Les expériences électrocatalytiques ont non seulement montré que le nouveau catalyseur de cuivre pouvait réaliser à la fois la réduction du CO_2 et de l'O_2 individuellement, mais aussi qu'il pouvait maintenir son activité de réduction du CO_2 même dans des conditions aérobies. Ainsi, le groupe pendentif de type méthyl-viologène a rempli son rôle en s'attaquant à la réduction de l'O_2 en même temps que la porphyrine de cuivre catalyse la réduction du CO_2.

Sous 1 atm de CO_2 et en présence d'une faible source de protons (H_2O), le CV de **Cu-o-MVP** a affiché une augmentation considérable de l'intensité du courant au couple redox $P^{\bullet-}/P^{2-}$ décalé anodiquement, indiquant la réduction électrocatalytique du CO_2 par l'état P^{2-} des catalyseurs de cuivre. D'autre part, lorsque du TFE a été utilisé comme acide plus fort, une réponse catalytique similaire à environ – 2.0 V *vs.* SCE a été obtenue. Lorsque le **Cu-o-MVP** a été étudié en tant qu'électrocatalyseur ORR avec du TFE comme source de protons, la réduction de l'O_2 moléculaire a été réalisée par le radical pyridinium électrogénéré, et la partie dianion viologène, respectivement. À notre grande surprise, le premier état réduit de **Cu-o-MVP**, à savoir la formation de $MV^{\bullet+}$, était inactif vis-à-vis de l'ORR, ce qui n'était pas le cas pour le composé méthyl-viologène de référence. L'incapacité du groupe $MV^{\bullet+}$ pendant sur le **Cu-o-MVP** à réduire l'O_2 découle du fait que le couple redox $MV^{2+}/MV^{\bullet+}$ est décalé de près de 180 mV anodiquement par rapport au processus de réduction analogue dans le méthyl viologène. Il semble donc que l'état $MV^{\bullet+}$ dans le **Cu-o-MVP** manque de pouvoir réducteur pour entraîner l'ORR.

Nous avons ensuite tiré profit du caractère catalytique bifonctionnel du **Cu-o-MVP** pour réduire le CO_2 et l'O_2 séparément et nous avons également étudié ses performances de réduction du CO_2 en présence d'O_2. A partir d'une solution électrolytique saturée en CO_2 contenant du TFE et après ajout d'aliquots d'O_2, la concentration croissante d'O_2 n'a pas affecté l'activité du **Cu-o-MVP** pour activer et réduire le CO_2. Par conséquent, bien que le **Cu-o-MVP** ne soit pas un électrocatalyseur ORR efficace, il peut maintenir ses performances électrocatalytiques CO_2RR même en présence d'O_2. En d'autres termes, le groupe pendentif de type méthyl-viologène a rempli son rôle en s'attaquant à l'ORR, tandis que la porphyrine de cuivre catalyse la réduction du CO_2.

Dans la dernière partie de cette thèse, nous avons présenté nos résultats préliminaires sur l'activation de l'H_2O par une porphyrine manganèse fusionnée-imidazole-phénol. Ce dérivé a été conçu pour mimer la paire Tyr_{161} / His_{190} dans le photosystème II (PSII) dans le but d'étudier son rôle dans la dernière étape catalytique de la division de l'eau par le complexe d'évolution de l'oxygène (OEC) pendant la photosynthèse oxygénique.

La CV de **MnPPhOH** a montré une onde anodique à 1.05 V contre SCE dans des conditions sèches a été attribuée à l'oxydation à un électron de la fraction phénol accompagnée d'un transfert intramoléculaire de proton à l'unité imidazole pour former une espèce de radical phénoxyle ($MnPPhO^{\bullet}$). La génération de ces espèces a été étayée par des études spectroélectrochimiques lors de l'électrolyse à 1.0 V par rapport au SCE, couplées à la spectroscopie RPE. L'ajout d'H_2O à la solution électrolytique de **MnPPhOH** a entraîné une augmentation de l'onde anodique au niveau du couple redox $Mn^{III}P$/ $Mn^{III}P^{\bullet +}$, ce qui pourrait suggérer l'activation d'une molécule d'H_2O liée pour donner des espèces Mn-oxo de haute valence qui peuvent ensuite oxyder l'H_2O à environ 1.8 V par rapport à la SCE, où une augmentation considérable de l'intensité du courant a également été observée.

Pour mieux comprendre la formation des espèces Mn-oxo, nous avons réalisé une série d'études spectroscopiques dans lesquelles les Mn-oxo de haute valence ont été générés, cette fois chimiquement par l'addition d'un oxydant fort dans une solution ACN. L'oxydation du **MnPPhOH** a entraîné des changements majeurs dans ses empreintes UV-Vis avec des caractéristiques d'absorption qui correspondent bien aux porphyrines Mn^{IV}=O rapportées dans la littérature. Cependant, en raison de la présence du groupe phénol, nous ne pouvions pas exclure la possibilité de former également l'espèce tautomère Mn^{III}-O $PPhO^{\bullet}$. Pour étudier un tel scénario, nous avons également caractérisé l'espèce oxydée **MnPPhOH** par spectroscopie RPE. Les spectres RPE du **MnPPhOH** en présence de mCPBA ont présenté une valeur de tenseur de 3.81 qui pourrait correspondre au centre métallique Mn^{IV}. De manière intéressante, un signal supplémentaire avec g=2.005 a également été observé, suggérant la formation d'un radical organique qui peut être soit situé sur le macrocycle de la porphyrine (Mn^{IV}=O $P^{\bullet +}$PhOH), soit sur le fragment PhOH oxydé (Mn^{IV}=O $PPhO^{\bullet}$). Des simulations RPE seraient utiles pour interpréter les spectres RPE obtenus pour le **MnPPhOH** oxydé.

La génération d'espèces Mn-oxo lors de l'activation de l'eau a également été interrogée par spectroscopie UV-Vis à résolution temporelle dans un mélange ACN/ H_2O à pH=4 et pH=8. Dans des conditions acides sous atmosphère d'Argon et en présence d'un accepteur d'électrons irréversible, l'excitation d'une solution de **MnPPhOH**/ Ru^{II} a donné lieu à un spectre UV-Vis transitoire avec des bandes d'absorption similaires à celles de l'espèce Mn^{IV}=O putative. L'ajout de sulfonate de styrène à la solution étudiée a augmenté la stabilité de l'intermédiaire Mn^{IV}=O, suggérant que le Mn^{III}PPhOH a été régénéré entre les flashs successifs, probablement par oxydation du substrat à partir de l'espèce Mn^{IV}=O. Le même comportement a également été observé pour le MnTPP non fonctionnalisé. Cependant, dans des conditions basiques, seul le **MnPPhOH** a été capable de réaliser l'oxydation du substrat ; cependant, son activité semble être considérablement réduite par rapport à celle à pH=4.

Le remplacement de l'accepteur d'électron irréversible par un accepteur réversible a conduit à une voie photochimique différente dans laquelle le Mn^{III}PPhOH a été réduit en Mn^{II}PPhOH à pH=4 dans des conditions anaérobies. Lorsque la solution a été exposée à l'air, les spectres d'absorption transitoires obtenus ont proposé la formation d'espèces Mn^{IV}=O qui pourraient réaliser l'oxydation du sulfonate de styrène. Cette fois, la formation de l'espèce Mn-oxo de haute valence a été attribuée à l'interaction du Mn^{II}PPhOH induit par laser avec le $^{\bullet}$OOH. Actuellement, des expériences photocatalytiques concernant le **MnPPhOH** sont en cours afin d'évaluer ses performances dans l'oxydation du sulfonate de styrène.